Bioinspired Fluid Dynamic Designs and Implementation of Soft Computing Techniques in Savonius Wind Turbine Rotors

A Thesis
Submitted in Partial Fulfilment of the Requirements for the Award of the Degree of

Doctor of Philosophy

By

Umang H. Rathod
Reg. No. 196103025

Department of Mechanical Engineering
Indian Institute of Technology Guwahati
Guwahati – 781039, Assam, India

June, 2024

Dedicated to My Beloved Grandparents ...

Late Shree Manilal Maganlal Hirani

&

Late Srimati Mangalaben Manilal Hirani

Declaration

I hereby certify that the work compiled in this dissertation entitled **'Development of Bioinspired Blade Designs and Performance Prediction Techniques for Savonius Vertical Axis Wind Turbine'** is the outcome of my research work under the guidance of Professor Vinayak Kulkarni and Professor Ujjwal K. Saha in the Department of Mechanical Engineering, Indian Institute of Technology Guwahati, India.

Any part of this work has not earlier been submitted for the award of any degree, diploma, associate-ship, fellowship or its equivalent to any University or Institution.

Date: June 7, 2024

(Umang H. Rathod)
Registration No. 196103025
Department of Mechanical Engineering,
Indian Institute of Technology Guwahati.

Department of Mechanical Engineering
Indian Institute of Technology Guwahati
Guwahati – 781039
India

Certificate

It is certified that the work contained in the thesis entitled **'Development of Bioinspired Blade Designs and Performance Prediction Techniques for Savonius Vertical Axis Wind Turbine'** submitted by **Umang H. Rathod** to the Indian Institute of Technology Guwahati for the award of the degree of Doctor of Philosophy has been carried out under my supervision in the Department of Mechanical Engineering, Indian Institute of Technology Guwahati. This work has not been submitted elsewhere for the award of any other degree or diploma.

Date: June 7, 2024

(Vinayak Kulkarni)
Professor
Department of Mechanical Engineering,
Indian Institute of Technology Guwahati.

Date: June 7, 2024

(Ujjwal K. Saha)
Professor
Department of Mechanical Engineering,
Indian Institute of Technology Guwahati.

Acknowledgement

I take this opportunity to sincerely acknowledge the Indian Institute of Technology Guwahati for providing me with such an excellent environment for conducting my research. I owe my deepest gratitude to my supervisors Prof. Vinayak Kulkarni and Prof. Ujjwal K. Saha for their continuous support, encouragement, and active guidance at every stage of this endeavour.

I would like to express special appreciation to my doctoral committee members Prof. Niranjan Sahoo, Dr. Pranab K. Mondal and Prof. Rajib K. Bhattacharjya for their productive suggestions and advises towards my research findings. My sincere acknowledgment goes to Prof. K. S. R. Krishna Murthy (HOD, Mechanical Engineering Department) and Prof. Vimal Katiyar (Dean, R & D) for providing all the research facilities and financial support. A word of appreciation goes to the senior technician of Mechanical Engineering Department Mr. Monoj K. Baishya for their assistance in the fabrication of wind turbine blades.

I am indebted to Ministry of Human Resource Development (MHRD), Govt. of India, for providing me scholarship for the entire PhD programme to fulfil my financial requirements. Further, I would like to gratefully acknowledge the ASME (The American Society of Mechanical Engineers) for offering me the prestigious SACTA (Student Advisory Committee Travel Award) award which made me possible to attend and present my work at the ASME Turbo Expo 2023 conference held at Boston, MA, USA, during June 26 – 30, 2023.

I am also thankful to my seniors, co-workers, and friends Dr. Parag K. Talukdar, Dr. Md. Nur Alom, Dr. Ojing Siram, Mr. Anand Verma, Mr. Bastav Borah, Mr. Ravi Kumar, Ms. Kabita Naik for their friendship and unforgettable moments.

Finally, I am deeply grateful to my beloved parents, wife, in-laws, my brother for their continuous encouragement and blessings. Without their support, the completion of my PhD would remain a dream for me.

June 7, 2024
Guwahati, India

Umang H. Rathod

Abstract

To address the problem of imminent energy crisis, pollution from fossil fuels, and global warming, it is necessary to incorporate the renewable technologies. In that context, the drag-based Savonius wind turbine has tremendous potential to extract wind energy and can be operated as a standalone system at remote areas where the conventional electricity cannot be provided. With such merits in mind, literature review is presented in this thesis besides the research directions and research gaps. It is found that the ongoing research directions are the bioinspired Savonius rotor designs, surrogate modelling, and optimization using soft computing techniques. Concise literature review on the reported bioinspired and nature-inspired blade design of the Savonius rotor is presented. Furthermore, applicability of using soft computing techniques for wind turbines, and especially for the Savonius rotor, is discussed. The potential research gaps are identified and are addressed in this thesis.

In the present thesis, the biomimetic blade design for the Savonius rotor is developed. The novel *priori* flow physics analysis and principal flow conditions are proposed. A marine bio-organism named 'Orange sea-pen (*Ptilosarcus gurneyi*)' is found to be suitable for the novel blade design. An analogy is established between the torque mechanism of the Savonius rotor and feeding mechanism of the sea-pen. A blade shape is derived from the body shape of the Orange sea-pen. A rotor models having sea-pen and conventional semicircular blades are fabricated, and then assessed numerically and experimentally. The results show that the sea-pen bladed rotor performs better than the semicircular bladed rotor in terms of rotor power and starting torque. As an extension of this approach, another novel blade profile inspired from the corrugations found on the dragonfly wings is developed. The numerical findings reveal that the corrugation has a capability of improving the rotor performance.

Further, the surrogate model is created by training Artificial Neural Network (ANN) and Genetic Expression Programming (GEP) consisting rotor's design and operating parameters as input and the performance as output parameter. The Golden Section Method (GSM) is then merged with the trained surrogate models to predict the optimum performance of the rotor having a given design and operating conditions. A parametric study is also conducted to check the capability of the surrogate model. A graphical user interface is then developed as a predictive tool for providing ease to the user.

Contents

Nomenclature

English Symbols

A	Swept area (product of H and D)	[m^2]
AR	Aspect ratio	-
A_{wt}	Cross-sectional area of wind tunnel test section	[m^2]
c	Chord length of an airfoil/hydrofoil	[m]
C_D	Drag coefficient	-
C_L	Lift coefficient	-
C_P	Power coefficient	-
$C_{P,\,Opt}$	Optimum power coefficient	-
C_{Pr}	Pressure coefficient	-
C_{ST}	Static torque coefficient	-
C_T	Torque coefficient	-
D	Rotor diameter	[m]
d	Blade chord length (≈ blade diameter for semicircular blade)	[m]
D_{in}	Diameter of inner circle in rotors having fish-shaped blades	[m]
dl	Elemental blade length	-
D_o	End plate diameter	[m]
D_P	Diameter of braking pulley	[m]
e	Overlap length	[m]
F	Force	[N]
F_D	Drag force	[N]
F_L	Lift force	[N]
f_{max}	Maximum camber	[m]
F_N	Normal force	[N]
F_R	Resultant force	[N]
F_S	Spring tension	[N]
F_T	Thrust force	[N]
F_x	x-component of force	[N]
F_y	y-component of force	[N]
g	Growth factor of spiral	-
H	Height of rotor	[m]
h	Representative cell size	-
k	Turbulent kinetic energy	[m^2/s^2]

N	RPM, rotation per minute	-
n	Approximation order	-
n_b	Number of blades	-
n_h	Number of hidden neurons	-
n_i	Number of input variables	-
n_o	Number output variables	-
n_s	Number of stages	-
O_c	Apparent order of convergence	-
p	Length of blade straight arm as per blade parametrization scheme	[m]
p/q	Shape factor	-
P_F	Fluid power	[J/s]
P_{out}	Power output	[W]
pr	Pressure	[N/m^2]
pr_∞	Free stream pressure	[N/m^2]
P_T	Turbine power	[J/s]
q	Radius of blade arc as per blade parametrization scheme	[m]
r	Radius in polar co-ordinates	-
R	Correlation coefficient	-
R^2	Coefficient of determination	-
R_d	Discriminating ratio	-
Re	Reynolds number	-
RF	Refinement factor	-
r_{log}	Radius of logarithmic spiral	[m]
r_Φ	Radius of the Golden spiral	[m]
s	Gap length	[m]
T	Torque	[N·m]
T_L	Local torque	[N·m]
T_L*	Non-dimensional local torque	-
T_S	Static torque	[N·m]
U	Free stream velocity	[m/s]
U_C	Corrected wind velocity	[m/s]
U_{rel}	Relative velocity	[m/s]
W	Dead weight	[kg]
x	x-coordinate	-
x_{est}	Estimated value of variable, which is estimated either by ANN or GEP	-
x_i	i^{th} value of variable x	-

X_{max}	Location of maximum camber	[m]
x_{mean}	Arithmetic mean value of data	-
x_{norm}	Normalized value of the data	-
x_{tar}	Target value of variable, which is collected from experimental data	-
y	y-coordinate	-
$y+$	Non-dimensional distance	-

Greek Letters

α	Curtain angle at advancing blade	[°]
β	Curtain angle at returning blade	[°]
δ	Blade twist angle	[°]
ε_t	Correction factor	-
θ	Rotor angle	[°]
θ_1	Shape angle 1 as per blade parametrization	[°]
θ_2	Shape angle 2 as per blade parametrization	[°]
λ	Tip-speed ratio	-
λ_{LB}	Lower bound of tip-speed ratio	-
λ_{Opt}	Tip-speed ratio at $C_{P,\,Opt}$	-
λ_{UB}	Upper bound of tip-speed ratio	-
μ	Viscosity	[Ns/m^2]
ρ	Density of air	[kg/m^3]
ΣC_{LT}	Total local torque coefficient	-
φ	Angle of spiral	[rad]
Φ	Golden ratio	-
ϕ	Azimuthal angle	-
ϕ_A	Advancing blade azimuthal angle	[°]
ϕ_R	Returning blade azimuthal angle	[°]
Ψ	Setting angle of fish-shaped blade in rotor	[°]
ω	Rotational speed	[rad/s]

Abbreviations

2D	Two dimensional	-
3D	Three dimensional	-
ANFIS	Adaptive neuro-fuzzy inference system	-
ANN	Artificial neural network	-
CART	Classification and regression trees	-
CFD	Computational fluid dynamics	-
DES	Detached eddy simulation	-
ET	Expansion tree	-
FIS	Fuzzy inference system	-
GA	Genetic algorithm	-
GAN	Generative adversarial network	-
GCI	Grid convergence index	-
GEP	Genetic expression programming	-
GEP-RNC	Genetic expression programming- randomly generated numerical constant	-
GP	Genetic programming	-
GR	Gap ratio	-
GSM	Golden section method	-
GUI	Graphical user interface	-
HAWT	horizontal axis wind turbine	-
LE	Leading edge	-
LEV	Leading edge vortex	-
LISP	List processing	-
LM	Levenberg Marquardt learning algorithm	-
MAE	Mean absolute error	-
MARS	Multiple adaptive regression splines	-
MLP	Multilayer perceptrons	-
MSE	Mean squared error	-
NN	Neural network	-
OR	Overlap ratio	-
RANS	Reynolds averaged Navier Stokes	-
RBF	Radial basis function	-
RMS	Root mean squared error	-
RPM	Rotations per minute	-
SCG	Scaled conjugate gradient	-
SIMPLE	Semi-implicit method for pressure-linked equation	-
SST	Shear stress transport	-
SVM	Support vector machine	-
TE	Trailing edge	-
VAT	Vertical-axis turbine	-
VAWT	Vertical-axis wind turbine	-

List of Figures

List of Tables

Chapter – 1

Introduction

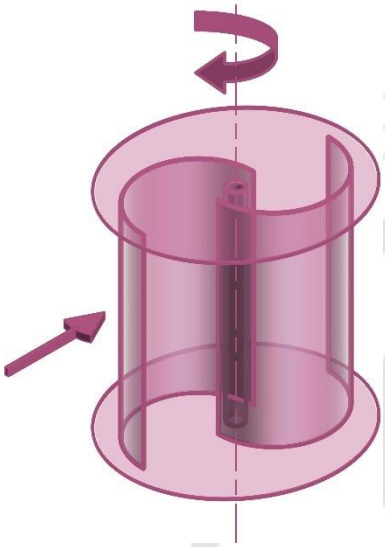

Chapter Layout:

Overview

This chapter showcases the wind energy as cost-effective, one of the most abundant and highly contributing source among other renewable energy sources. The present energy scenario is surveyed through the global viewpoint as well as Indian perspective. The indications of future dependability on the wind energy and the surge in the installation of the wind energy extractors are highlighted in this chapter. The wind turbines, their categorization, and current states are then examined. It is realized that small-scale wind energy systems in the form of vertical-axis wind turbine (VAWTs) has a promising future even though the off-shore/on-shore horizontal-axis wind turbines and floating turbines are the most prevalent ones. This chapter provides the reason behind choosing the Savonius rotor as a research focus, objectives and overall roadmap of the research work undertaken.

1.1 Motivation

From the commencement of industrialization, the fossil fuels became the backbone of modern economics. Thereafter, the scientific advancements have adapted fossil fuels in technologies belonging to various sectors such as transportation, manufacturing, home appliances and other sophisticated value-added services. However, the harmful effects of unlimited and uncontrolled use of fossil fuels have led to depletion of their reserves and CO_2 emission, which is the main player behind the global warming and climate change. The climate scientists and environmentalists have observed sudden increment in CO_2 concentration (in parts per million) in the atmosphere and global average temperature after the start of industrial era in 1769 (Mackay, 2009). In addition to this, the fossil fuels are continuously depleting which may create the energy market of the future very volatile.

In light of this, the renewable energy sources can be the game changer since they are abundant in nature and have no direct CO_2 emission. Solar energy, the main source and its derivatives such as wind, biomass, tidal and hydro; have their own merits and demerits. For example, the solar energy has the largest share among the renewable energy sources, however, it is in low grade and non-concentrated form. The solar photovoltaic technology converts solar radiation directly into electricity, however, it still requires sophisticated and expensive semi-conducting materials. Some of the remaining sources such as hydro, wave, tidal, and geo-thermal have pseudo-constant supply of energy besides the specific requirement of expensive infrastructure. The biomass energy is also referred as the renewable energy that is actually the biological form of the solar energy. The bioenergy is traditionally being used since ancient times and still it is in practice in the form of biogas plant, biofuels, and others. However, their production and post-processing demand considerable time and efforts. Last but not the least, the wind energy has attracted many researchers due to multiple ways by which it can be extracted. For example, wind turbines, airborne wind energy systems, flying kite, oscillating objects based on vortex induced vibrations, floating wind turbines, diffuser augmented wind turbines, hybrid turbines, multi-rotor systems are the notable ones (Watson et al., 2019). Moreover, such wind energy systems can be used either in the form of centralized or standalone formats. Among these, the most prevalent technologies are the wind turbines. They convert the kinetic energy of the wind into rotary motion of their blades, which is then delivered to the generator to produce electricity or hydraulic pump or other devices based on the requirements.

Taking the aforementioned facts into consideration, the author of the current PhD thesis had decided to conduct research in the field of wind energy and that too into wind turbines. There are wide range of wind turbine variants suitable for specific operating conditions and energy requirements of a specific region or nation. Thus, it is necessary to appraise the present energy scenario (Section 1.2) and then select an appropriate type of wind turbine from the pool of their numerous types (Section 1.3).

1.2 Present Energy Scenario

As per the latest report of IEA (International Energy Agency), total energy supply required for the world is 624 EJ (1 EJ = 10^{18} J) in the year of 2021 (IEA, 2022). Out of the total, approximately 12% energy was supplied by the renewable energy. Wind energy sector, however, contributed 10% of the total renewable energy supply, which is anticipated to be doubled by 2050 as per net-zero emission scenario proposed by IEA. As per the statistics published by the GWEC (Global Wind Energy Council), the global wind power capacity has reached to 837 GW in 2021 (GWEC, 2022). Further, the WWEA (World Wind Energy Association) predicted that the global installed wind power capacity would be around 956 GW by the end of 2022 (WWEA, 2022). This trend indicates emerging dependence on wind energy sources worldwide in response to the global energy need.

From the Indian perspective, the total consumption in 2021 was close to 27 EJ that is 6% of the worldwide energy consumption (IEA, 2022). For the nation like India, despite having a large population of over 1.3 billion people, per capita energy consumption is substantially lower than the developed countries both presently as well as historically (IEA, 2022; Mackay, 2009). Further, energy imports of India in 2021 constituted 40% of the total energy consumption (IEA, 2021), which is not promising from the point of view of energy independency and energy security for the country. The imports are dominated by conventional energy sources *viz.*, coal, crud oil, and natural gas. To mitigate this besides reducing the net CO_2 emission, energy shift towards the renewable energy is the need of the hour for India. Renewable energy sources in India are utilized particularly for electricity generation contributing 21% out of total electricity consumption of 1583 TWh (1 TWh = 10^{12} Wh) as per the 2019 records (IEA, 2021). Although the hydro-sources dominates almost half of the electricity generation in 2019 followed by wind-sector (20%) as of now, the relative trend would be inverted by 2040 as per the predictions by state policy of India. This indicates the growing emphasis on the wind sector in the future. India has achieved the total installed wind

power capacity of 41.93 GW till the end of 2022 (MNRE, 2023). The electricity generation in the wind sector is dominated by the on-shore wind farms. The Ministry of New and Renewable Energy India has determined various potential sites for wind farm development based on wind speed distribution. According to global wind atlas (DTU, 2023), the average wind speed of India at 100 meter in height (for 10% of windiest areas) is 6.5 m/s with 7-9 m/s velocity for the states like Tamilnadu, Gujarat, and Jammu & Kashmir. North-eastern states including Assam have mean wind speed of nearly 4 m/s, which is very low. Based on these wind energy potentials and the energy requirements, types of the wind turbines are selected, which are classified in Section 1.3.

1.3 Types of Wind Turbines

The wind turbines are classified based on the orientation of rotating axis with respect to the free stream wind direction (Manwell et al., 2009). If the rotor's axis is parallel to the wind direction, the turbine is called horizontal-axis wind turbines (HAWTs). On other hand, if the rotation axis is perpendicular to the wind direction, then it is known as vertical-axis wind turbine (VAWTs). The HAWTs work on the principle of the lift generation, whereas the VAWTs can be lift-based or the drag-based turbines. In order to maximize the energy extraction from the incoming wind energy, the axis of the HAWT should be aligned parallel to the ever-changing wind direction. It creates a requirement of yaw mechanism for the turbines and hence the additional energy is needed to perform this task. The VAWTs can operate irrespective to the incoming wind direction, thereby it is referred as direction independent turbines. This advantage of VAWTs over HAWTs results into relatively simpler design and easy manufacturing of VAWTs. HAWTs require high velocity wind to avoid atmospheric boundary layers, which makes the nacelle to be placed at some specific height away from the ground. This necessitates the turbine tower to be established which increases the capital cost of the. However, the VAWTs do not need this type of structure as it can be operated in lower wind velocity and even in wind shear layer. Moreover, the generators and other auxiliary instruments can be placed at the ground in the case of VAWTs enabling ease of installation and maintenance. Further, VAWTs demonstrate lower noise levels as compared to the HAWTs.

Even though the HAWTs provide higher efficiency of 45%-50% at higher rotational speeds as compared to the VAWT, the VAWTs are still preferred over the HAWTs due to their aforementioned merits. These attributes have facilitated the implementation of the VAWTs as small-scale power generators at location such as high-rise buildings in urban environment,

public places, highways, communication base-stations, off-shore oil-fields, islands, border areas, and other remote locations (Li et al., 2022). Among the different variants of the VAWTs, the lift-based Darrius and the drag-based Savonius rotors are the most prevalent and thoroughly studied. Usually, the former is superior to the latter in terms of performance, however, the Savonius rotor can be operated in low wind velocity conditions as it requires a low starting torque despite its small size (Blanco Damota et al., 2022). This quality makes the Savonius rotor one of the potential candidates for the urban environment. Additionally, the blade design does not require inclusion of airfoil and this results its ease of fabrication. The design of the Savonius rotor can also be extended to the hydrokinetic rotor without any major modification. In account of such peculiar attributes of the Savonius rotor, the author of the present thesis chose the same for PhD research investigations.

1.4 The Savonius Wind Turbine

The design of the Savonius rotor was proposed by a Finnish engineer S. J. Savonius in 1930. As shown in Fig. 1.1, the Savonius rotor is originally the flettner's rotor modified by dividing it into two semicircular halves and then placing them diametrically away from the rotor center besides their concavities facing each other (Paraschivoiu, 2002). The overall shape of the rotor looks like 'S-shaped' when viewed from the top. The blade with its concavity facing upstream side is called an advancing blade while the remaining one is referred as a returning blade.

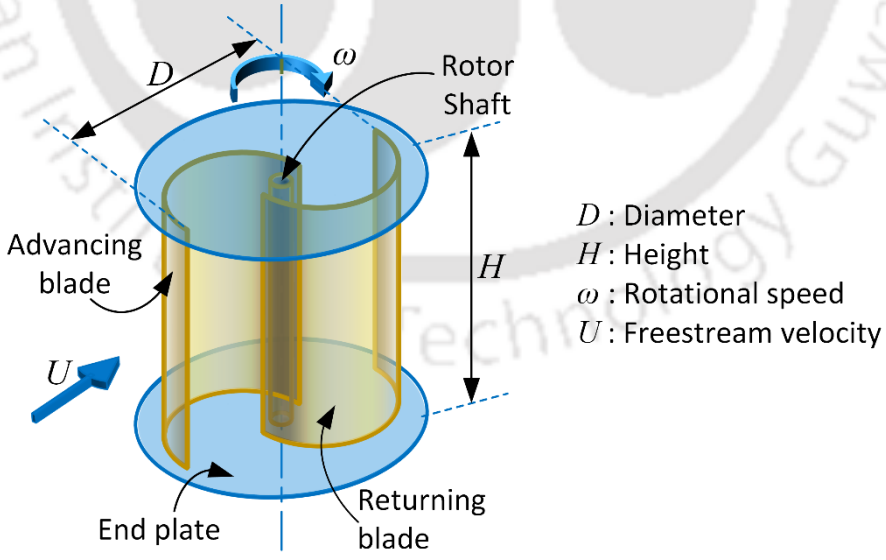

Figure 1.1 Conventional Savonius rotor

As the advancing blade is having its concavity facing the upstream, it experiences higher drag than the returning blade having its concavity facing the upstream. The drag force induces useful

torque for the advancing blade, whereas retarding torque is induced by the returning blade. The direction of the net-torque is however congruent with that of the advancing blade *i.e.*, clockwise direction in the present case of Fig. 1.1. Therefore, the Savonius rotor is considered as the drag-based turbine. As mentioned earlier, the performance of the Savonius rotor is less than the Darrius turbine, thereby the researchers are in constant effort to improve its performance for more than nine decades since its ideation (Alom and Saha, 2019a, 2018a). As per the literature, the methodologies adopted by the researchers are the augmentation techniques, design modifications, soft-computing techniques, bioinspired designs, and experimental and numerical investigations. With this in background, the objective of the present PhD research work had been decided.

1.5 Present Objective and Road Map

In the open literature, it is reported that the blade shape can substantially influence the rotor performance (Alom and Saha, 2019a). The traditional blade shapes such as Bach, modified Bach, Benesh, elliptical blades have shown higher performance than the conventional semicircular shape. Recently, several bioinspired and nature-inspired blades have been proposed to improve the rotor performance, *e.g.*, Fibonacci spiral blades (Blanco Damota et al., 2022; Blanco et al., 2021; Damota et al., 2022), nautilus blade (Gao et al., 2020), Koi-fish shaped blade (Hashem and Zhu, 2021), sand-eel shaped blade (Abdelghafar et al., 2023; Hashem et al., 2022), fish-ridge shaped blade (Ma et al., 2017; Song et al., 2013), barnacle inspired blade surface (Ashwindran et al., 2022), and others. Motivated by such trend, one of the objectives for the present study is to search for novel bioinspired blades. Two novel bio-inspired blades, namely, the seapen and corrugated blades have been developed for the anticipated performance improvement in comparison with the conventional semicircular blade. After establishing similarities between the torque mechanism of the Savonius rotor and corresponding biological phenomena of the bio-organisms, the novel blades have been designed and fabricated. The fabricated rotors are then subjected to wind tunnel experimentation for accurate performance assessment. Numerical analyses are also conducted to gain insights into the modification of the torque mechanism.

Parallelly, as a second objective, surrogate models using soft computing techniques *viz.*, artificial neural network (ANN) and genetic expression programming (GEP), have been developed. The aim is to predict the rotor performance based on the design and operating parameters of the rotor. The reported data have been utilized to train the surrogate models.

Thereafter, the golden section method (GSM) combined with the ANN model has been developed to search for the optimum performance of the rotor in question. Using this model, a suitable graphical user interface (GUI) is then developed. Furthermore, a parametric study has been conducted to demonstrate the influence of design and operating parameters on the rotor performance. There are several surrogate models based reported studies, for example, Mohammadi et al. (2018) used the ANN with genetic algorithm for blade shape optimization, (Sargolzaei and Kianifar, 2009) formulated six different ANN models for six different Savonius variants, Storti et al. (2019) combined ANN and CFD (computational fluid dynamics), and Debnath and Das (2010) used ANN for function approximation. However, unlike these examples, the ANN model trained in the present work deals with comparatively higher numbers of input variables.

Overall, as depicted in Fig. 1.2, a thorough literature review has been conducted to find the research gaps and then to set the objectives. Thence, the bioinspired blades have been developed aided by experimental and numerical investigation. Thereafter, surrogate models are formulated using soft computing techniques. Lastly, the conclusions have been drawn besides pointing out the future scopes.

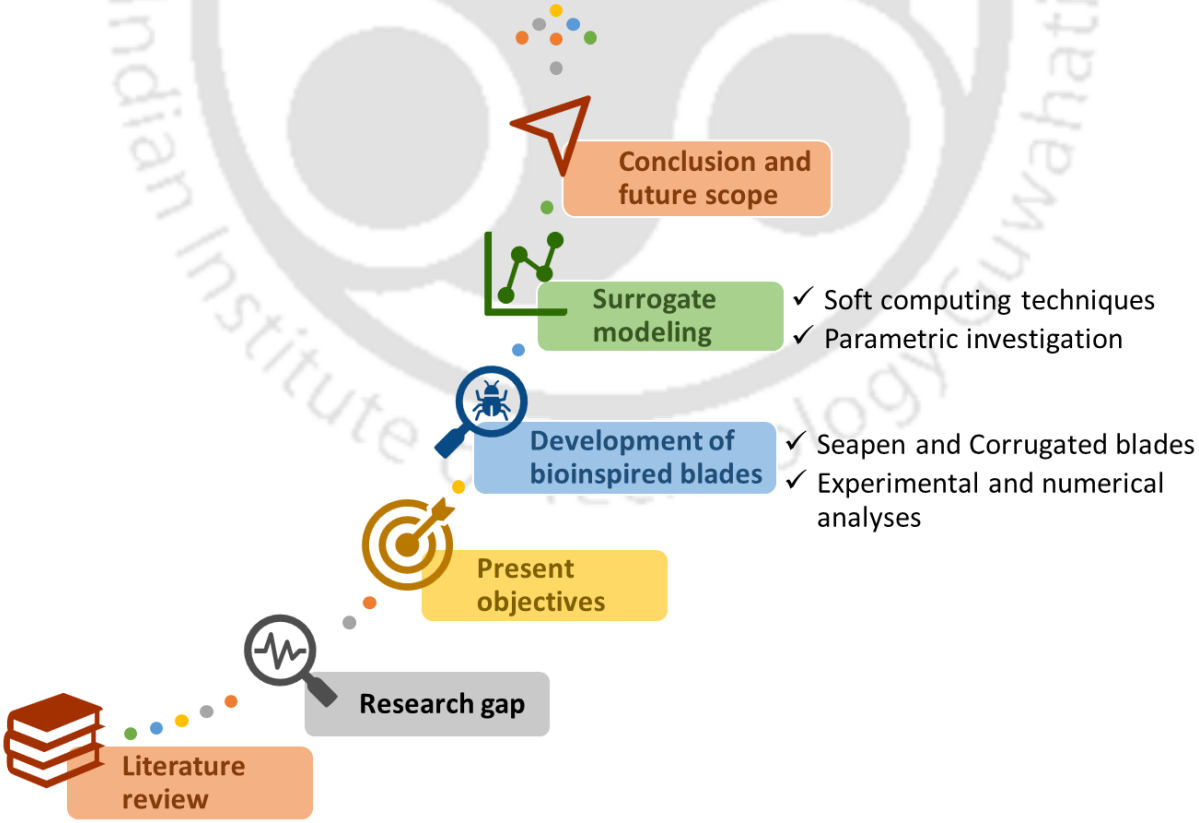

Figure 1.2 Road map of the present investigation

1.6 Thesis Organization

The present thesis has been organized by concentrating on the improvement and the prediction of the Savonius rotor performance. **Chapter 1** offers the motivation behind the work in the field of wind energy and a brief introduction of the present energy scenario and Savonius rotor. **Chapter 2** introduces the basic concepts of Savonius rotor, performance parameters, classification of augmentation techniques, reported bioinspired blades, and the soft computing techniques. **Chapter 3** discusses the experimental and numerical setups. **Chapter 4** elaborates on the development of novel seapen blade and its experimental as well as numerical assessment. **Chapter 5** continues the bioinspired blade design approach and discussion on the novel corrugated blade and its numerical assessment is presented. **Chapter 6** elaborates the development of surrogate model to predict the rotor performance using soft computing techniques such as artificial neural network (ANN) and genetic expression programming (GEP). **Chapter 7** highlights the methodology of finding optimum performance for a given rotor, parametric study, and development of graphical user interface to use surrogate models. Lastly, **Chapter 8** summarizes conclusions and possible future scopes.

Chapter – 2

Literature Review

Chapter Layout:

Overview

Since the conceptualization of the Savonius rotor, a host of augmentation techniques and design modification approaches have been introduced by the researchers for the purpose of performance improvement. All these approaches are focused around modifying the torque mechanism of the rotor. This chapter classifies all these approaches in detail including their working principles, whether they are successful in performance improvement or not, the reason behind their failure, whether the experimental and numerical analyses were performed or not, and many other aspects. Bioinspired designs introduced in the blade design together with its prevalent terminologies are discussed. The use of the soft computing techniques in the field is also described in the chapter. The current research trend is also provided in this chapter so as to find out the research gaps that need to be addressed. Accordingly, the research objectives are then set and discussed meticulously.

2.1 Torque Mechanism and Performance Parameters

As briefly mentioned in Section 1.4, a typical Savonius rotor as shown in Fig. 2.1, consists of two cylindrical halves acting as rotor blades with their concavity oriented face-to-face. The blades are then supported by either shaft or endplates (Fig. 2.1a). The design parameters in detail are depicted in Fig. 2.1(b). The blade having its concavity facing the upstream wind velocity (U) is named as advancing blade, while the other one is named as the returning blade. The concavity of the advancing blade induces a higher drag force than convexity of the returning blade due to their fundamental difference of shapes. The difference between both the drag forces results into a net positive torque as per the sign convention provided in Fig. 2.1(b).

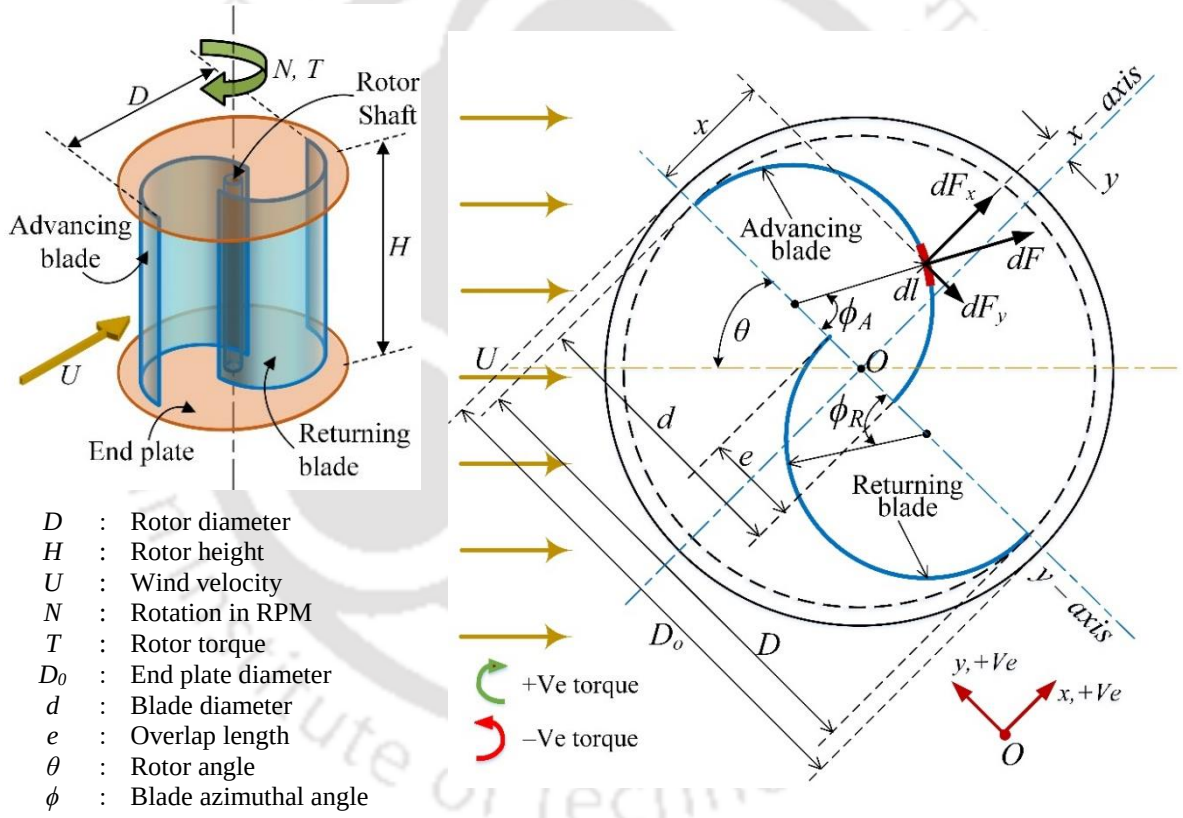

(a) Illustration of rotor parts **(b)** Geometric details

Figure 2.1 A typical two-bladed Savonius rotor

The drag force acting on advancing and returning blades is governed by the pressure distribution over their concave and convex surfaces. The pressure can be quantified in the form of non-dimensional pressure coefficient (C_{Pr}) as expressed by Eq. (2.1). As shown in Fig. 2.1(b), the pressure difference (Δpr) between upstream and downstream sides of an infinitesimal blade element (dl) produces a force (dF) perpendicular to dl (Eq. 2.2). The

elemental force dF induces a differential local torque (dT_L) with respect to rotor centre O. The dT_L can be calculated by Eq. (2.3) using the values of force components (dF_x and dF_y) and the coordinates of dl with respect to rotor's x and y axes. The necessary sign convention for torque and rotor's Cartesian coordinates system are provided in Fig. 2.1(b).

$$\text{Pressure Coefficient, } C_{\text{Pr}} = \frac{pr - pr_{\infty}}{\frac{1}{2}\rho U^2}$$
$$\therefore \Delta C_{\text{Pr}} = \frac{\Delta pr}{\frac{1}{2}\rho U^2} \tag{2.1}$$

Now, the force acting on length dl,

$$dF = \Delta pr\,(H\,dl) = \tfrac{1}{2}\rho U^2 \Delta C_{\text{Pr}}\,(H\,dl) \tag{2.2}$$

$$\begin{aligned}\therefore dT_L &= (x\,dF_y) + (y\,dF_x) \\ &= \{x\,(dF\cos\phi_A)\} + \{y\,(dF\sin\phi_A)\} \\ &= \tfrac{1}{2}\rho U^2 \Delta C_{\text{Pr}}\,(x\cos\phi_A + y\sin\phi_A)(H\,dl)\end{aligned} \tag{2.3}$$

The dT_L is then converted into non-dimensional quantity dT_L*, which can be defined mathematically as Eq. (2.4) (Fujisawa, 1992; Fujisawa and Gotoh, 1994). It can be expressed with the help of differential – $d\phi$ and integrand – C_{LT} (coefficient of local torque), which is fundamentally a function of ϕ. An integration of dT_L* over ϕ = 0° to 180° (π) has to be performed in order to obtain the total non-dimensional local torque (T_L*) exerted by the blade. This approach is applicable for the advancing as well as the returning blades. Moreover, it can be stated from Eq. (2.5) that the T_L* is proportional to ΣC_{LT}. Here, it is worth noting that the C_{LT} can be approximated as a constant over dl, when the integration is approximated as a summation in Eq. (2.5).

$$\therefore dT_L^* = \frac{dT_L}{\left(\frac{1}{2}\rho AU^2\right)\left(\frac{D}{2}\right)}$$

$$\therefore dT_L^* = \frac{\left(\frac{1}{2}\rho U^2\right)\left[\Delta C_{\text{Pr}}\left(x\cos\phi_A + y\sin\phi_A\right)\right](Hdl)}{\left(\frac{1}{2}\rho U^2\right)(H)(D)\left(\frac{D}{2}\right)} \quad \left[\because \text{ rotor area, } A = (H)(D)\right]$$

$$\therefore dT_L^* = \frac{\left[\Delta C_{\text{Pr}}\left(x\cos\phi_A + y\sin\phi_A\right)\right]\left[\left(\frac{d}{2}d\phi\right)\right]}{(D)\left(\frac{D}{2}\right)} \quad \left[\because dl = \frac{d}{2}d\phi\right]$$

$$\therefore dT_L^* = \underbrace{\left[\left(\frac{d}{D^2}\right)\left\{\Delta C_{\text{Pr}}\left(x\cos\phi_A + y\sin\phi_A\right)\right\}\right]}_{C_{LT}} d\phi$$

$$\therefore dT_L^* = C_{LT}\,d\phi \tag{2.4}$$

$$
\begin{aligned}
T_L^* &= \int dT_L^* = \int_0^{\pi} C_{LT}(\phi)\, d\phi \\
&\approx T_L^* \approx \left(\sum\nolimits_n C_{LT}\right) d\phi \quad \left[\text{Consider '}n\text{' number of } dl \text{ in a blade}\right] \\
&\approx T_L^* \propto \left(\sum C_{LT}\right)
\end{aligned} \tag{2.5}
$$

The ΣC_{LT} value for advancing blade usually remains positive, while it becomes negative for the returning blade. By adding up the ΣC_{LT} values of both the advancing and returning blades, the total torque of the rotor is obtained corresponding to rotor angle (θ). In entire $\theta = 0°$ to 360° (one revolution of rotor) interval, the overall positive ΣC_{LT} value for the major part of the interval ensures a net positive rotation of the rotor. A time averaged value of these ΣC_{LT} values over a rotation can provide an estimation of torque coefficient (C_T) of the rotor (Eq. 2.5). It is worth noting that the discussion of the torque mechanism in terms of C_{Pr} and C_{LT} is just an alternative approach to that of the conventional drag force-based discussion. However, the former one emphasizes more on elementary *dl* (peripheral length of blade) and its location with respect to the rotor center, while the latter one focuses more on cumulative effect of the entire blade. Therefore, the former approach is more insightful in order to know which shapes or segments of the blades are more important for the improvement of the C_{LT} values. Contrarily, this approach is very cumbersome to measure C_T by this way, experimentally. Instead, a mechanical dynamometer setup can be utilized to measure the rotor torque (T) experimentally and thereafter Eq. (2.6) is applied to calculate C_T. In order to assess the rotor performance, the power coefficient (C_P) as given by Eq. (2.7) can be calculated, which requires the value of C_T and the non-dimensional rotational speed, also known as tip-speed ratio (λ) (Eq. 2.8). As per the conventions, two different rotor designs are compared in terms of performance using C_P vs. λ characteristic performance curves. This performance trend can provide optimum power coefficient ($C_{P,\,Opt}$) corresponding to optimum tip-speed ratio (λ_{Opt}).

$$
C_T = \frac{T}{\frac{1}{2}\rho A U^2 \left(\frac{D}{2}\right)} \tag{2.6}
$$

$$
C_P = \lambda C_T = \frac{T\omega}{\frac{1}{2}\rho A U^3} \tag{2.7}
$$

$$
\lambda = \frac{\omega D}{2U} = \frac{\pi D N}{60 U} \tag{2.8}
$$

In case of starting torque characteristic of the rotor, the static torque (T_S) in non-rotary condition is measured and then it is converted into dimensionless parameter known as static torque coefficient (C_{ST}) as per Eq. 2.9. The starting capability of any two rotors are compared by their

C_{ST} vs. θ trends. Further, Reynolds number (Re) is an important dimensionless quantity as defined in Eq. 2.10, which is used to express the operating condition of the rotors. Here, the ρ is the fluid density and μ is the dynamic viscosity of the rotor.

$$C_{ST} = \frac{T_S}{\frac{1}{2}\rho A U^2 \left(\frac{D}{2}\right)} \tag{2.9}$$

$$\mathrm{Re} = \frac{\rho U D}{\mu} \tag{2.10}$$

2.2 Classification of Augmentation Techniques and Design Modification Strategies

In order to improve the performance of Savonius rotor, researchers have proposed various augmentation techniques and design modification strategies that attempt to improve and diminish the drag forces experienced by the advancing and returning blades, respectively. Based on the flow manipulation by the augmentation techniques and multiple rotor design parameters, they can be broadly classified in two categories (Fig. 2.2):

(a) Manipulation of upstream fluid flow : Additional attachments are mounted to the rotor to manipulate the incoming upstream flow without any substantial design modifications of the base rotor.

(b) Modification in rotor design : The rotor designs are modified without perturbing the upstream flow.

Each of these categories can be further sub-divided into two groups *viz.*, **Groups I** and **II** (catogory (a)), and **Groups III** and **IV** (category (b)). The key strategies implemented I each category aiming rotor performance enhancement are elucidated below. The augmentation techniques belonging to each and every groups are listed in Fig. 2.2 based on literature review.

- **Group-I :** The flow impingement on the returning blade is blocked and then diverted it towards the advancing blade.
- **Group-II :** In addition to the strategy of **Group I**, the concentration of upstream flow is facilitated towards the rotor inlet or the advancing blade.
- **Group-III :** The structure of the rotor is transformed in such a way that the fluid can flow through the rotor blades, and especially, through the returnnng blade.
- **Group-IV :** Modifications in terms of rotor shape, blade shape, relative dimensions and overall rotor design.

It is to be noted that the all the reported augmentation techniques and design modification strategies do not gaurantee the performance improvement. Nevertheless, such failed techniques are still included in this thesis to find out the missing link in their working principles and further developing a proper understanding. The augmentation techniques and design modification strategies listed in Fig. 2.2 are thoroughly discussed in the subsequent sub-sections.

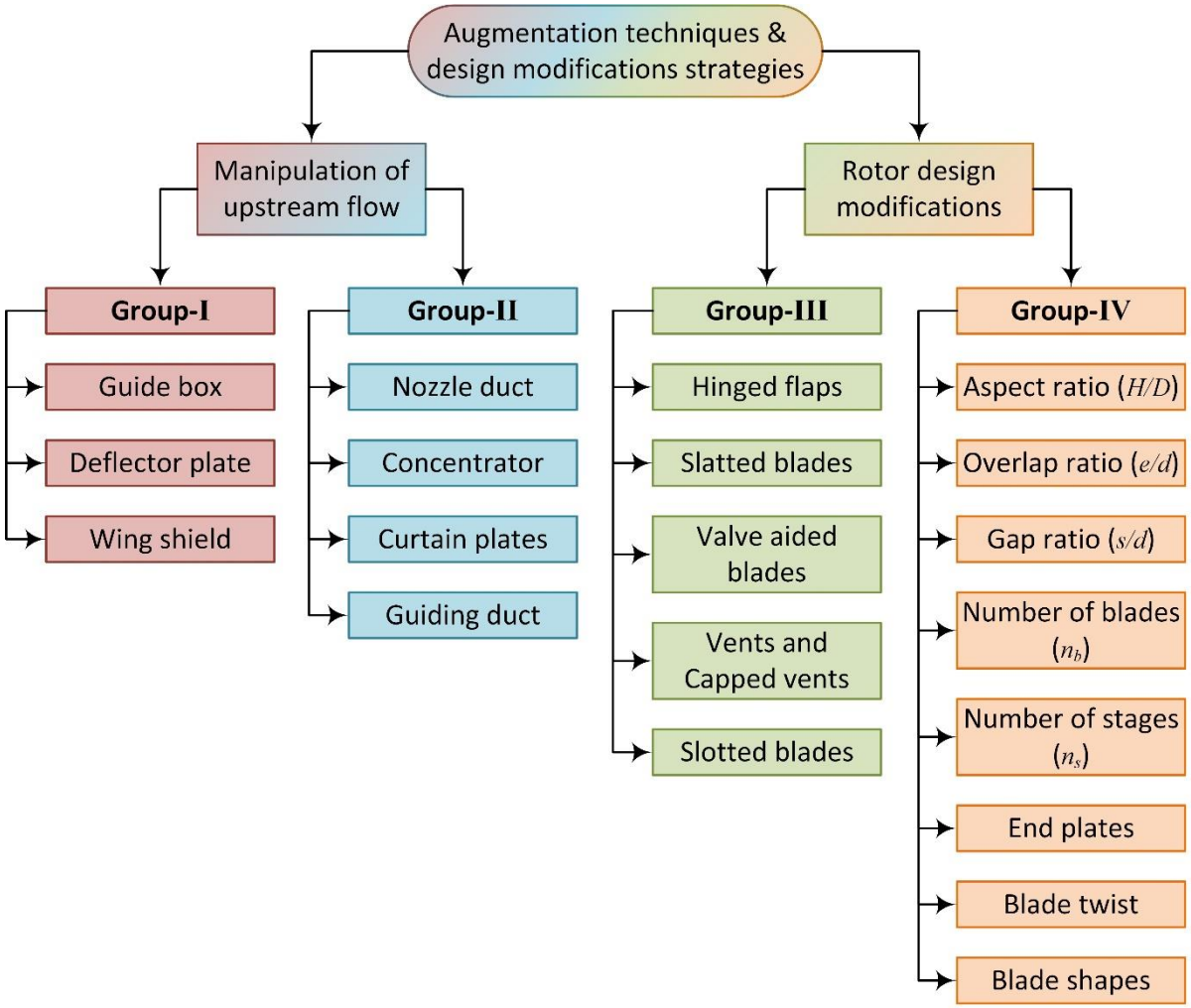

Figure 2.2 Classification of augmentation techniques and design modification strategies

2.2.1 Group-I

The basic designs of augmentation techniques *viz.*, guide box, deflector plate, and wind shield, belonging to Group-I are illustrated in Fig. 2.3. The working principle of the guide box (Fig. 2.3a) is to block the upstream flow to the returning blade while allowing the upstream flow to impinge on the advancing blade. In addition to that, the downstream flow is diverted from advancing blade to the concave side of the returning blade. The purpose is to decrease the negative torque produced by the returning blade (Irabu and Roy, 2007). The area ratios between

the inlet and exit of the guide box were set in the range of 0.3 to 0.7 to adjust the inlet mass flow rate and fluid energy. With the implementation of guide box, the $C_{P,\,Opt}$ values of two and three bladed rotors were found 1.5 and 1.2 times higher than the base rotor

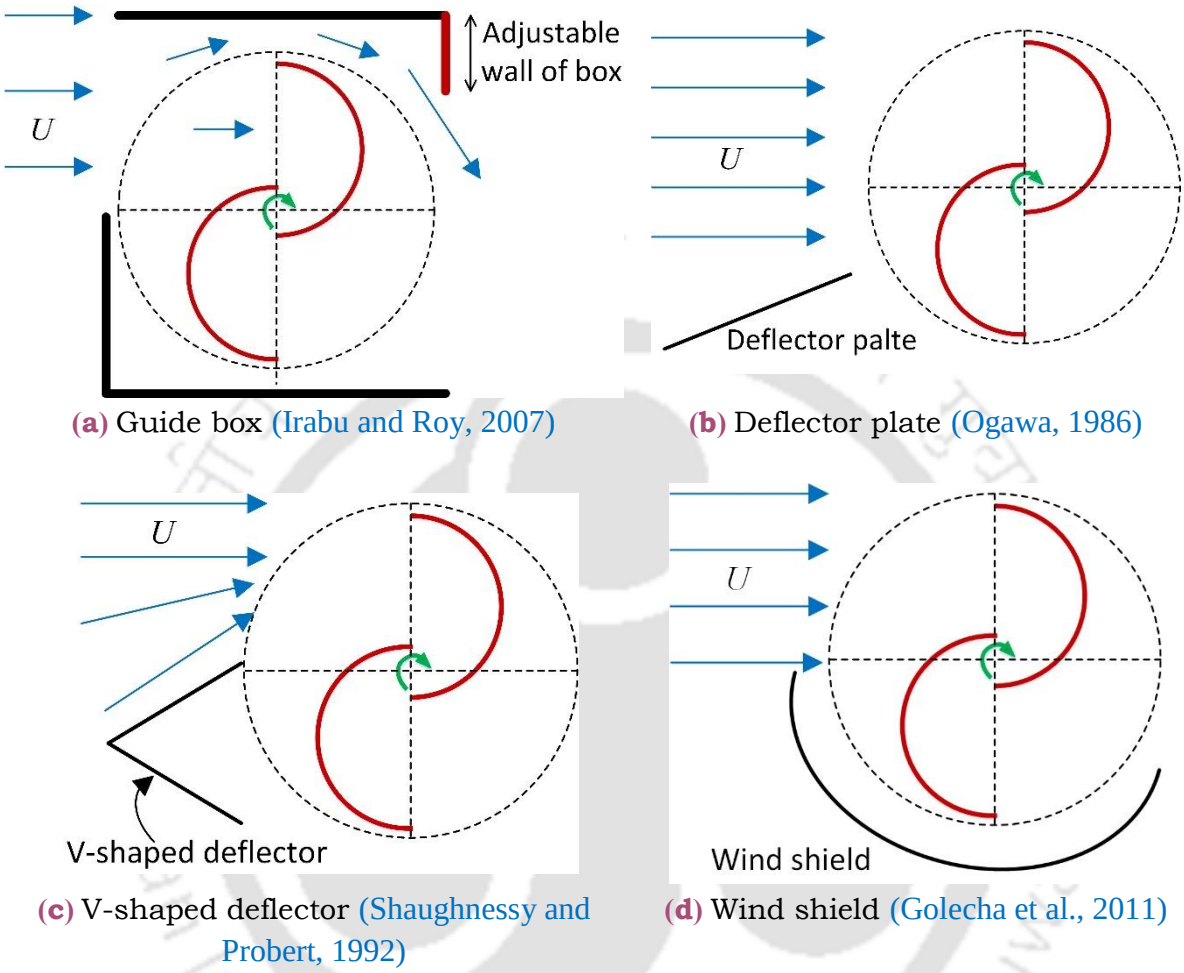

(a) Guide box (Irabu and Roy, 2007) **(b)** Deflector plate (Ogawa, 1986)

(c) V-shaped deflector (Shaughnessy and Probert, 1992) **(d)** Wind shield (Golecha et al., 2011)

Figure 2.3 Group-I augmentation techniques

Deflector plate shown in Fig. 2.3(b), hinders the upstream flow impingement on the returning blade and deflects it towards the advancing blade. Ogawa (1986) tested several deflector plate shapes *viz.*, circular, V-shaped, flat plate. For optimum performance, the suitable orientations and positions were found out for each deflector plate shape. Similarly, a V-shaped deflector (Fig. 2.3c) was investigated by changing the angle between the two arms of the V-shaped deflector (Shaughnessy and Probert, 1992). The angle equals to 37° was found to be the optimum improving $C_{P,\,Opt}$ by 20% as compared to non-augmented rotor. (Golecha et al., 2011) tested different orientations of flat plate deflector for all the single-stage, two-stage and three-stage rotors. The flat deflector plates improved the performance of single-stage as well as multi-stage rotors.

The concept of wind shield (Fig. 2.3d) is similar to that of the deflector plates except the former does not divert the flow from the returning blade to the advancing blade (Emmanuel and Jun, 2011; Hu et al., 2009; Mohamed et al., 2011). The results showed the performance improvement with an implementation of wind shields as augmentation technique. Thus, the guide box, deflector plates, and wind-shields are considered as the performance improving augmentation techniques.

2.2.2 Group-II

The augmentation techniques of Group-II include nozzle duct, concentrator, curtain plates, and guiding duct. Shikha et al. (2003) experimented on Savonius rotor with convergent nozzle as shown in Fig. 2.4(a). It concentrates wind on advancing blade and simultaneously shields the returning blade from the upstream flow. It was observed that when the blades are aligned with the airflow, no torque is produced. To mitigate this shortcoming, it was suggested to use four or six bladed rotors. The nozzle design for a particular rotor depends primarily on two factors, namely, the length of nozzle and the ratio of inlet to outlet nozzle areas. It was concluded that Savonius rotor with six blade and nozzle attachment enhances the performance.

The design of the concentrator (Fig. 2.4b) is similar to that of nozzle duct but the outlet of the former faces both the advancing and the returning blades, unlike the nozzle duct that faces only the advancing blade. The aim of the concentrator is to maximize the use of upstream fluid flow for energy extraction by the rotor. Roy et al. (2014) mounted the concentrator on the Bach-bladed rotor and then optimized its design, experimentally. By investigating different values of the face angles of the concentrators, the optimum design was found to be the one consisted of the upper and the lower faces orientating at 40° and 20° with respect to upstream wind direction, respectively. The $C_{P,\,Opt}$ of the augmented rotor was improved by 50% as compared to the non-augmented rotor.

Altan et al. (2008) conducted experimental and numerical analyses of semicircular bladed Savonius rotor with curtaining as shown in Fig. 2.4(c). The curtain located at the returning blade hinders the interaction of the upstream flow with the returning blade and diverts it towards the advancing blade. On the other hand, the curtain located at the advancing blade diverts the maximum available upstream flow toward the advancing blade. Both of these curtains try to divert and concentrate the upstream flow towards the advancing blade. The higher the length of curtain, the better the rotor performance was observed. For a given curtain length, the optimum value of α (angle of a curtain at advancing blade with respect to upstream)

and β (angle of a curtain at returning blade with respect to upstream) were found to be 45˚ and 15˚, respectively. Without curtaining, the maximum C_{ST} was obtained at $\theta = 45^{\circ}$, but with the implementation of the curtains, it was shifted to $\theta = 60^{\circ}$.

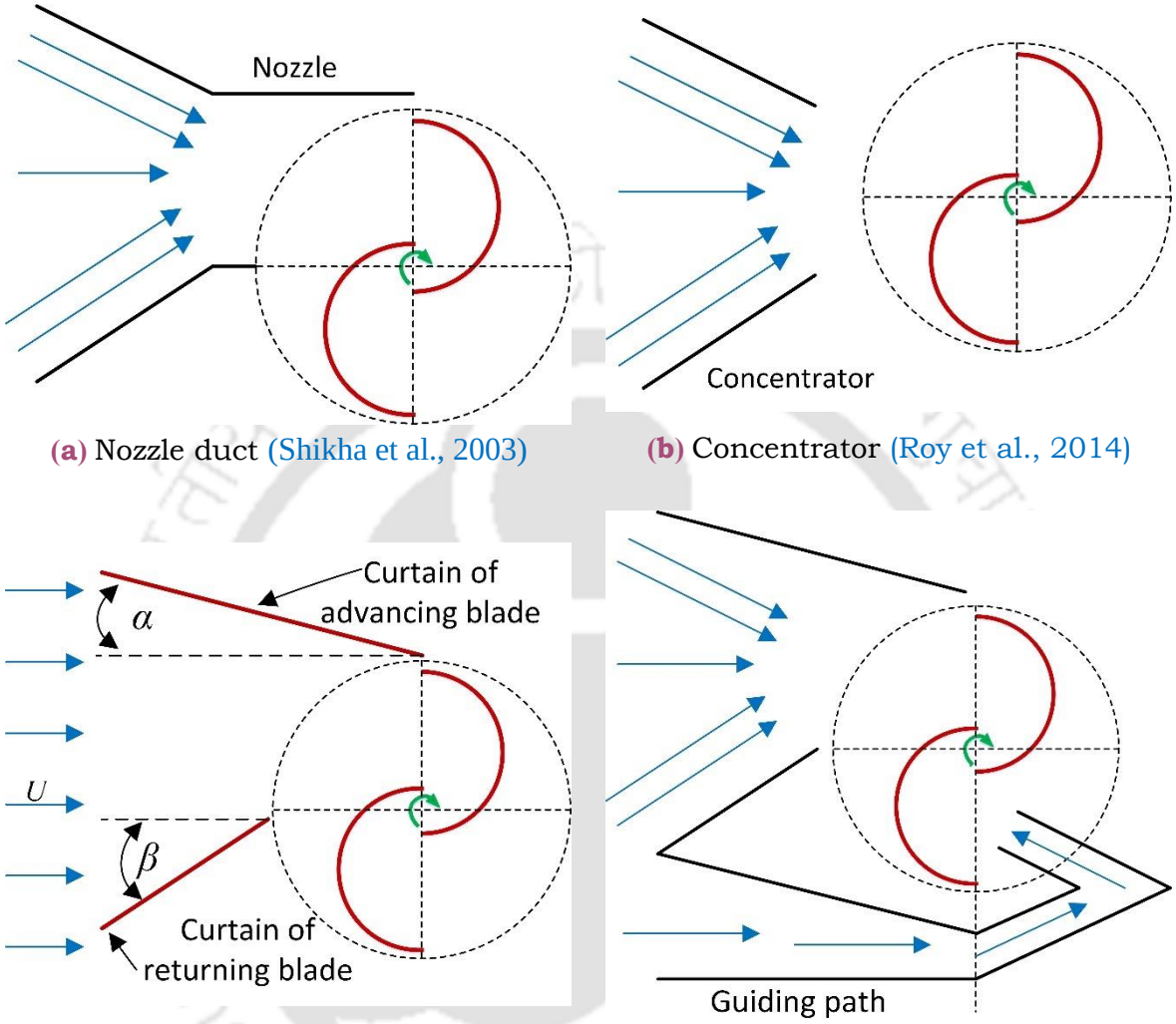

(a) Nozzle duct (Shikha et al., 2003) **(b)** Concentrator (Roy et al., 2014)

(c) Curtain plates (Altan et al., 2008) **(d)** Guiding duct (El-Askary et al., 2015)

Figure 2.4 Group-II augmentation techniques

The design of the guiding duct (Fig. 2.4d) synthesized by El-Askary et al. (2015) is nothing but a conceptual design extensions of the curtaining plates proposed by Altan et al. (2008). The placement of the curtains is identical besides an addition of a guiding path extending from the upstream of the returning to its concave side. The extension of the duct restricts the incoming air flow from impinging on the convex side of the returning blade and then diverts it towards its concave side. Three different designs of the guiding ducts were tested, and then, it was concluded that the curved guiding path with the outlet cross-section of a duct exactly facing the concave side of the returning blade provides maximum performance. Both the experimental and numerical methodologies were used to arrive at this conclusion.

2.2.3 Group-III

The augmentation techniques (Fig. 2.5) such as hinged flaps on blade, slatted blade, vents and capped vents on the blade, valve-aided blade, and slotted blade belong to Group-III. Tabassum and Probert (1987) experimented with circular flaps (Fig. 2.5a) hinged vertically on the end plates by such a way that they remain open when blade acts as returning blade, otherwise remain closed. The objective was to reduce drag on the returning blade by letting the upstream flow pass through the flap openings. These flaps, however, deteriorated the rotor performance with slightly improved performance limited to the short range of λ and U. Nonetheless, improvement in starting torque was observed with hinged flaps. The flaps with smaller width and light weight are beneficial for their efficient opening and closing. By limiting the opening span and angles of the flaps, its influence on the starting torque was examined. Opening angle of 60° provided the optimum static/starting torque for Bach type blade since it diminishes the negative torque produced by the returning blade. The improvement was roughly 30% as compared to the base rotor. Still this augmentation technique is not so prevalent because of its inferior performance in the rotating condition. The similar structure of the hinged flaps (referred as slatted blade) was studied by Reupke and Probert (1991). Two blades divided into 8 and 16 hinged flaps were fabricated and then tested experimentally. The findings were identical to those of Tabassum and Probert (1987).

Instead of using multiple flaps, Rathod et al. (2019) tested a single flap (also known as valve aided blades) with different widths at maximum drag point on the returning blade (Fig. 2.5b). Similar to the findings reported above, a single flap reduced the $C_{P,\,Opt}$ by 10%-15% for all its tested widths. According to Saha et al. (2008), performance improvement was reported with valve addition, however, limited to the three-bladed rotor and not beneficial to the two-bladed rotor. It was suggested to use valve materials with lower density to eliminate the hinderance caused by the centrifugal force in opening and closing of the valves. As the λ increase, the centrifugal force does not let the valves/flaps to remain open, which looks identical to the semicircular blade. Hence, at higher λ, the performance trend of valve aided/flapped blade resembles the trend of semicircular blades.

The remaining techniques, namely, the vents (Fig. 2.5c), capped vents (Fig. 2.5d), and slots (Fig. 2.5e) on the blades allow the leakage of the upstream flow through both the advancing and the returning blades. Like the hinged flaps and slatted blades, these techniques are unsuccessful in performance improvement of the rotors having semicircular blades (Alaimo et

al., 2013; Rathod et al., 2019). The reason behind such outcomes is believed to be the severe deterioration of the pressure distribution over the advancing blade surfaces. On the other hand, the vents have demonstrated the performance improvement in case of the elliptical bladed rotor, however, not so substantial (Abraham et al., 2012; Alom and Saha, 2018b; Plourde et al., 2012). In summary, all the augmentation techniques in this section are not so successful in terms of performance improvement.

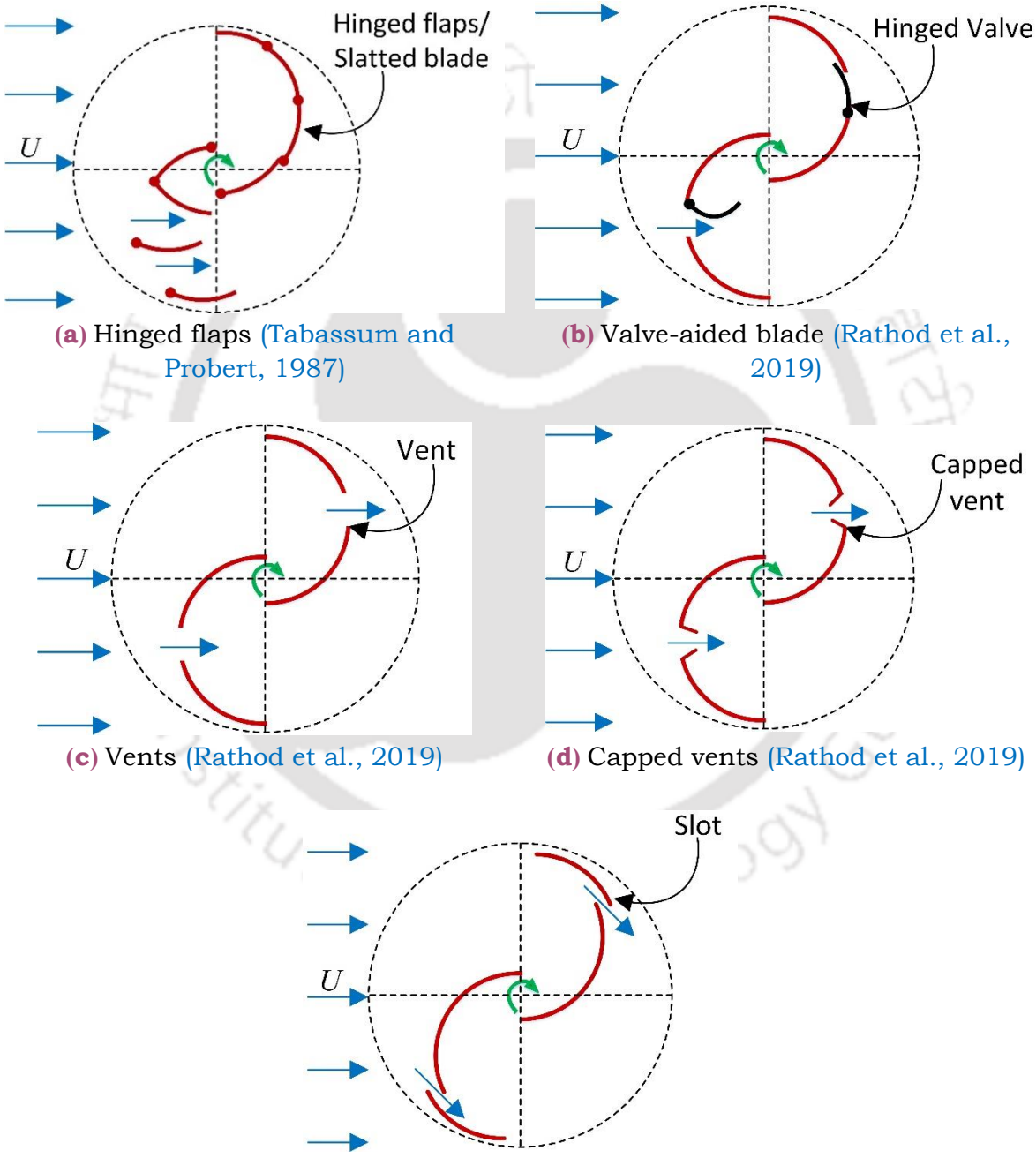

(a) Hinged flaps (Tabassum and Probert, 1987)

(b) Valve-aided blade (Rathod et al., 2019)

(c) Vents (Rathod et al., 2019)

(d) Capped vents (Rathod et al., 2019)

(e) Slotted blade (Alaimo et al., 2013)

Figure 2.5 Group-III augmentation techniques

Table 2.1 Key observations regarding augmentation techniques of Group-IV

Design Parameter	Investigators	Key observations
Aspect ratio ($AR = H/D$)	Alexander and Holownia (1978)	• Increment in AR improves the rotor performance.
	Ushiyama et al. (1986)	• Optimum AR = 4.29 was obtained among the tested values.
	Roy and Saha (2013c)	• Higher AR deteriorates the starting torque characteristics.
	Modi et al. (1984)	• Optimum AR = 0.77 for Bach-blades rotor.
Overlap ratio (e/d)	Sheldahl et al. (1978); Ushiyama et al. (1986)	• Optimum overlap ratio = 0.15 for semicircular bladed rotor.
	Alexander and Holownia (1978); Mojola (1985)	• Optimum overlap ratio = 0.22 for semicircular bladed rotor.
	Chen et al. (2012)	• Optimum overlap ratio = 0.167 for semicircular bladed rotor.
	Liang et al. (2020); Zhao et al. (2009b)	• Optimum overlap ratio = 0.19 for semicircular bladed rotor.
Gap ratio (s/d)	Alexander and Holownia (1978)	• Optimum gap ratio = 0.07 for semicircular bladed rotor.
	Ushiyama et al. (1986)	• Optimum gap ratio = 0 for semicircular bladed rotor.
	Kamoji et al. (2009)	• Optimum gap ratio = 0.05 for Bach bladed rotor.
Number of blades (n_b)	Wenehenubun et al. (2015)	• Tested rotors with n_b = 2 to 5. C_P of n_b = 3 > C_P of n_b = 2 and 4.
	Sheldahl et al. (1978); Ushiyama et al. (1986)	• Rotation condition: C_P of n_b = 2 > n_b = 3. • Starting condition: C_{ST} of n_b = 3 > n_b = 2.
	Saha et al. (2008); Saha and Rajkumar (2006)	• Rotation condition: C_P of n_b = 2 > n_b = 3 for twisted blade.
Number of stages (n_s)	Sheldahl et al. (1978); Ushiyama et al. (1986)	• Optimum design: n_s = 2 with 90° phase difference.
	Kamoji et al. (2009)	• Rotating condition: multi-staging improves C_P. • Starting condition: multi-staging deteriorates C_{ST}. • Improved starting torques with multi-staging.
	Hayashi et al. (2005)	• Performance of rotor with n_s = 3 < ns = 1.
End plates	Sheldahl et al. (1978); Zhao et al. (2009b)	• Performance improvement with D_o = 1.1D.
Twisted/helical blades	Grinspan et al. (2004)	• C_{ST} of twisted blade > C_{ST} of straight blade.
	Saha and Rajkumar (2006)	• Twisting improves C_{ST} at lower U.
	Zhao et al. (2009a)	• Optimum twist angle = 180°.

2.2.4 Group-IV

The key observations pertaining to the overall rotor design parameters belonging to Group-IV are summarized in Table 2.1. These recommendations are considered while designing the rotors of the present work. The primary advantage of the Group-IV augmentation techniques over other groups is that the direction independence of the rotor. This is also applicable to the Group-III augmentation techniques. The most important design parameter of Group-IV is the blade shape. The blade shape tends to manipulate the C_{Pr} close to the blade surfaces instead of purturbing the entire upstream flow as found in Group-I and Group-II techniques. Thereby, it is capable of directly influencing the torque mechanism of the rotor. Moreover, the recent trend indicates that the development of novel blade shapes has received an attention of the research community. Various blade shapes such as Bach (Modi et al., 1984; Modi and Fernando, 1989), Benesh (Benesh, 1996), modified Bach, elliptical (Alom and Saha, 2019b), arc-elliptical (Talukdar et al., 2022), parabolic and others have been introduced since the ideation of the traditional semicircular blade (Alom and Saha, 2019a). Among them, Bach type blade exhibits a high C_P values only in the range of lower λ (Chen et al., 2018), while the other blades such as arc-elliptical and modified Bach have demonstrated consistent improvement of C_P over the entire range of λ (Roy and Saha, 2015; Talukdar et al., 2022). The most superior blade shapes *viz*., elliptical and bach, are depicted in Fig. 2.6 in comparison with the conventional semicircular blade.

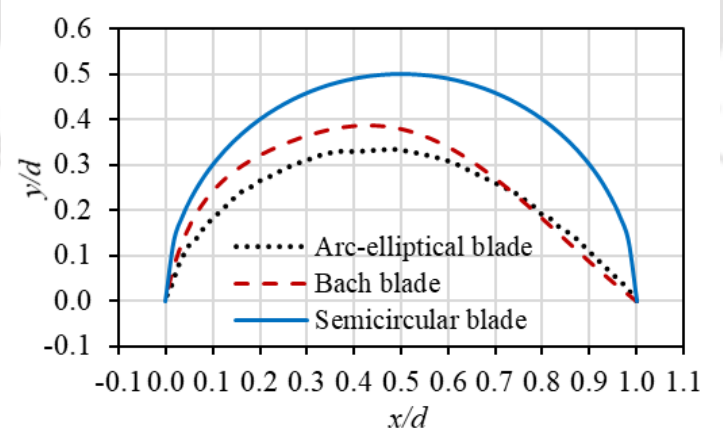

Figure 2.6 Reported high performing blades

Further, in the pursuit of finding a superior blade shape, researchers have also explored new directions by using (a) shape optimization with the help of numerical optimization techniques, (b) different aerodynamic shapes which are already prevalent, (c) novel bioinspired/nature-inspired shapes and many others. Using soft computing techniques like genetic algorithm together with CFD (computational fluid dynamics) solver, the optimum blade shape can be

obtained corresponding to the unique value of λ and U (Chan et al., 2018; Ramadan et al., 2018). Using existing aerodynamic shapes, Tian et al. (2015) numerically investigated the blade shape designed by Myring equation, which is widely used to design nose of underwater vehicles to minimize the drag. The aim was to shape a returning blade into Myring curve so that it could provide a low drag and a lower magnitude of negative ΣC_{LT}. It was found that an approximate parabolic curve, among the sets of curves expressed by Myring equation, showed a higher performance than the semicircular shape. The remaining blade design approach, known as bioinspired/nature-inspired blade designing, has acquired a tremendous attention of the blade designers in the recent times. Its development is elucidated in the next Section 2.3.

2.3 Bio/Nature-inspired Blade Designs of Savonius Rotor

2.3.1 Terminologies in Nature-inspired/Derived Research Activities

In the field of nature-inspired/derived research activities, there are wide range of prevalent glossary terms *viz.*, bio-inspiration, biomimicry, biomimetics, bionics, biomorphism, biophilia, bio-utilization, biotechnology, biomechanics and others. Historically, the word 'biomimetics' was the first to be used by an engineer and physicist Otto Schmitt in 1957 to describe his new instrument that mimics the electrical action of a nerve (Speck et al., 2017; Verbrugghe et al., 2023). Shortly after this, in the next year of 1958, a medical doctor Jack Steele coined the term 'bionics' for the first time in the context of aerospace medical research (Speck et al., 2017; Verbrugghe et al., 2023). On the other hand, the word 'biomimicry' was introduced later in 1997 by Janine M. Benyus in her famous book 'Biomimicry: Innovation Inspired by Nature' (Benyus, 2009). In 2015, George M. Whitesides, a chemist, proposed the term 'bio-inspiration' in the context of chemistry (Whitesides and Whitesides, 2015). This trend indicates the use of the aforementioned terms by the thinkers belonging to different professional backgrounds and the timelines indicate the possibility of unidentical interpretation of the same terms.

Even though the above-mentioned terms are prevalent for a long time, the meaning of these words are often ambiguous regarding where and in what context they should be used. To bring a clarification, a decision tree (Fig. 5) is developed by the authors of this thesis as a tool to decide a correct use of the word for a given specific application or research activity. The basis of this decision tree in Fig. 5 is established based on the insights provided by (Speck et al., 2017). The overall cluster of nature-inspired/derived activities were classified into 13 distinct classes. However, in the present thesis, only 7 classes of the activities are categorized as illustrated in Fig. 5 *viz.*, biotechnology, parallelly developed technologies, biophilia, bio-

utilization, bio-inspiration, biomorphism, biomimetics, and biomimicry. The purpose is to focus on the core idea behind the classification rather than creating a confusion by throwing multiple keywords and definitions. Nevertheless, the remaining categories can be made up by forming these 7 classes as a base.

As per the decision tree, the starting point is the mother nature herself showcasing plethora of natural designs, phenomena, products, and bio-organisms. The reason why the nature can be the ultimate guide is that the natural products and models are the result of evolutionary process that has been continued for a very long time (Benyus, 2009). As a next step, the main differentiating factor among the 7 categories is the step of the biological idea generation (Blasiak et al., 2022; Speck et al., 2017; Verbrugghe et al., 2023). If the generation of the biological idea is emphasized more, it leads to an actual concept of the bio-inspiration. For example, an aircraft, in which an idea of avian flight is incorporated. The lift and thrust are intertwined in the flapping avian flight, however, both are separated in the aircraft *i.e.* lift is generated by static rigid wing and thrust by engine. Overall, in both the cases, the idea of the thrust and lift is similar with separate ways of their execution nonetheless. The same logic can be applied to the reinforced cement in relation with the biological composite material (Speck et al., 2017). The fibers having relatively higher strength embedded in the base material found in the former is analogous to the steel-cement matrix present in the later one. However, neither the actual structure (morphology) nor the working principles of reinforcement are analogous between the both. Thereby, the concept further ought to be meticulously developed as' biomorphism' and 'biomimetics' by introducing an activity of the additional knowledge transfer. If the in-depth knowledge of the morphology of the bio-organism is incorporated, the 'bio-inspiration' can be sub-categorized into 'biomorphism'. In other words, 'biomorphism' is having a visual resemblance of technology identical to the natural life forms. The valid example of 'biomorphism' is the architecture of 'Lotus temple' that imitates only the morphology of lotus flower without carrying forward any probable structural principles.

On the other hand, if the working principles observed in the biological or natural phenomena are emulated, the sub-category of 'biomimetics' can be formulated. In other words, the actual functionality of the natural/biological phenomenon is emphasized rather than morphology (ISO, 2015). The suitable example of this is the gecko tape, which is developed based on the functionality of the surface structure found in the gecko feet to improve the adhesiveness of the tape. Alternatively, the term 'bionics' is considered synonymous to 'biomimetics' when the biological functionalities are emulated in the field of electronics.

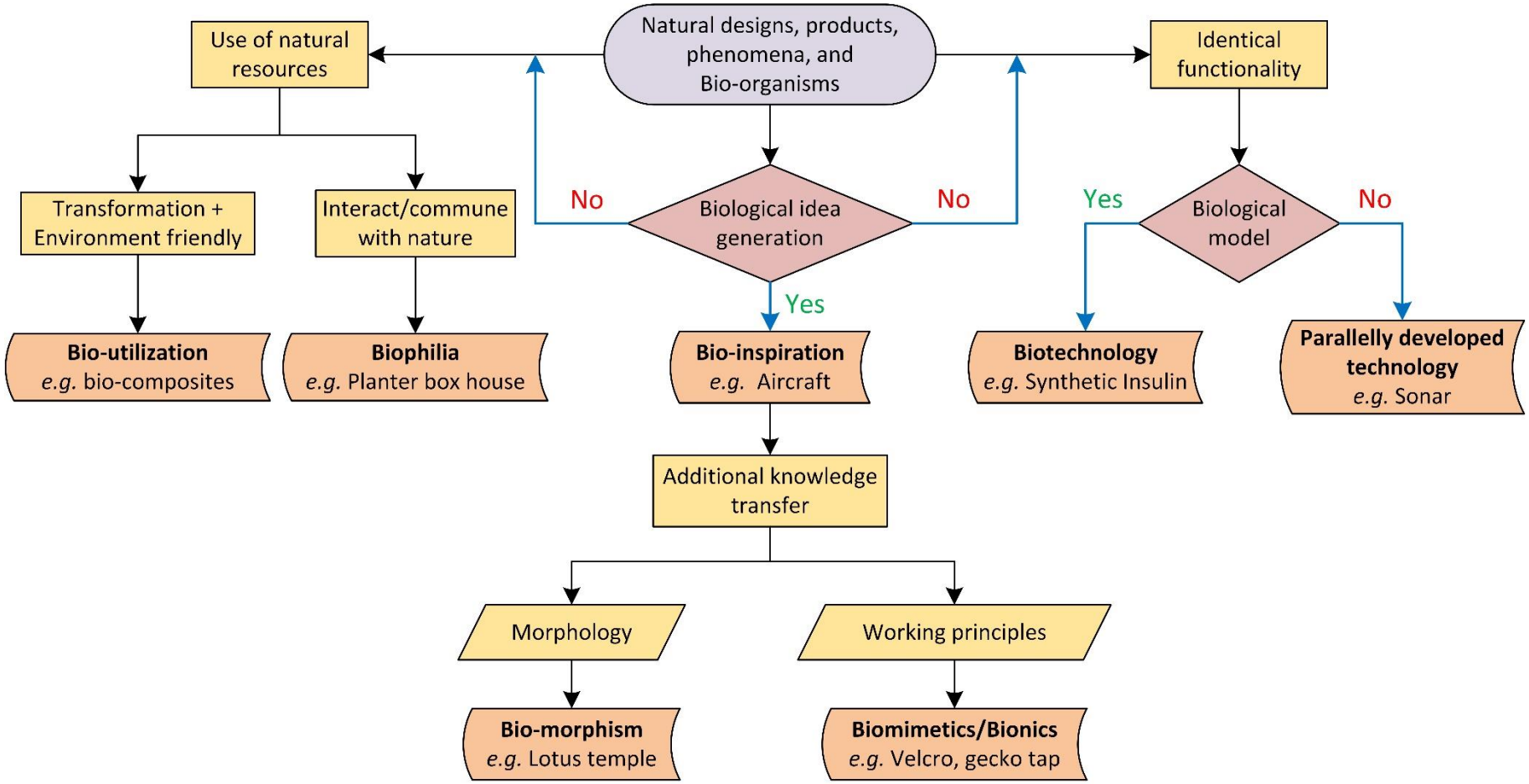

Figure 2.7 Decision tree to identify various types of nature-dereived research activities

Furthermore, another prevalent term 'biomimicry' encompasses bioinspiration, biomorphism, biomimetics along with an aspect of sustainability (Benyus, 2009). The characteristics such as energy efficiency, minimal use of materials, circular use of resources, self-sustenance, emission reduction, and others are identified as sustainability parameters (Speck et al., 2017). The remaining categories illustrated in Fig. 5 are defined presuming the absence of biological idea generation. Basic understanding of these terms is absolutely necessary to differentiate from 'bioinspiration' and its counterparts *viz.*, 'biomorphism' and 'biomimetics'. For further understating, the readers are referred to the definitions and explanations provided by Speck et al. (2017), Verbrugghe et al. (2023), and Blasiak et al. (2022).

The present review thesis describes various bioinspired activities with main attention only to the fluid dynamics in the context of VAWTs. All the activities (Fig. 6) are divided into three major classes, namely, the Savonius, Darrieus, and other rotor variants. Moreover, the bio-inspired techniques implemented in all the three rotor types are sorted in two main categories *viz.*, biomorphism and biomimetics. This is because of additional knowledge transfer happening in both categories, which additionally improves the knowledge of flow-physics and biological functionalities in return. Such improvements can lead to future possibilities of optimization since the influencing parameters and working principles are already known. Subsequently, all the bioinspired techniques/activities of the VAWTs are explained firstly through the perspective of the bio-organism or natural phenomenon. Thereafter, how the working principles from nature is carried over to the technical application in question. Lastly, the explanation on whether a given bio-inspired design belongs to 'biomorphism' or 'biomimetics', is provided for each of the bioinspired designs.

2.3.2 Logarithmic Spiral Blades

2.3.2.1 Pure Fibonacci spiral blades

In 2021, Blanco et al. (2021) proposed a Fibonacci spiral-shaped rotor blade for the Savonius rotor. The Fibonacci spiral is the approximation of the of the Golden spiral (r_{Φ}) that is actually the special case of the Logarithmic spiral (r_{log}) (Eq. 2.11). Conventionally, the logarithmic spiral is characterized by the growth factor (g) as per Eq. 2.11, which means the spiral radius (r) increases g times the original radius over every $\varphi = \pi/2$ (quarter arc) starting from any points on the spiral. For the Golden spiral, the value of g is equal to the Golden number (Φ) resulting into the expression of Eq. 2.12 (Marples and Williams, 2022). The value of the Φ is as per Eq. 2.13. Considering the growth characteristic of the Golden spiral, the Fibonacci spiral had been developed by setting the radii magnitude of each consecutive quarter arcs equal to the numbers

of the Fibonacci series (Eq. 2.14). In this series, higher the values of the series members, closer the ratio of the consecutive numbers to the Φ.

$$r_{\log} = ae^{k\varphi} = ae^{\left(\frac{2\ln g}{\pi}\right)\varphi} \tag{2.11}$$

where, r = spiral radius, g = growth factor and φ = spiral angle

$$r_{\Phi} = ae^{\left(\frac{2\ln \Phi}{\pi}\right)\varphi} \tag{2.12}$$

$$\Phi = \frac{1+\sqrt{5}}{2} \approx 1.618 \tag{2.13}$$

Fibonacci series: 1, 1, 2, 3, 5, 8, 13, 21, 34, 55, 98, ... (2.14)

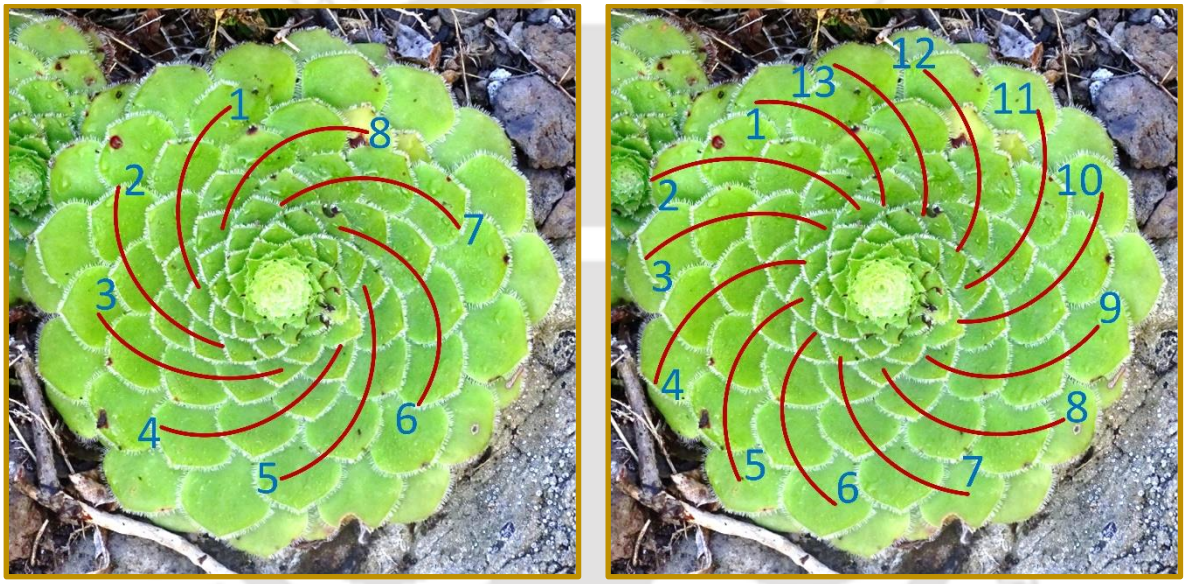

(a) 8 right-handed spiral **(b)** 13 left-handed spiral

Figure 2.8 Occurance of consecutive Fibonacci numbers in parastichies of Saucer plant (*Aeonium tabuliforme*) (Berg, 2021)

The motivation behind the proposal of the Golden spiral blade is because of the wide-spread appearance of the Φ in various natural as well as inanimate phenomena ranging from galactic to atomic scale, *e.g.*, variable stars, planetary orbits, Penrose tiling and quasicrystals, atomic bond lengths, and parastichies in phyllotaxis (arrangement of leaves on stem), Fibonacci series and others (Marples and Williams, 2022). The most intrigued example of the Φ's presence in form of Fibonacci series, is parastichies of Saucer plant (*Aeonium tabuliforme*) as shown in Fig. 2.8. The total of 8 right-handed spirals and 13 right-handed spirals are the consecutive numbers of Fibonacci series (Eq. 2.14), whose ratio is approximately equal to Φ. This is observed without any exceptions in the parastichies of Saucer plant, pine cone, conifer cone, spiral aloe, and others. However, it is important to clarify that very famous natural occurrence

of spiral such as sea-shell, hurricanes, and cyclones considered by Blanco Damota et al., (2022); Blanco et al. (2021); Damota et al. (2022) as Golden spiral, are actually the examples of the logarithmic spirals, not the Golden spiral (Hammer, 2016).

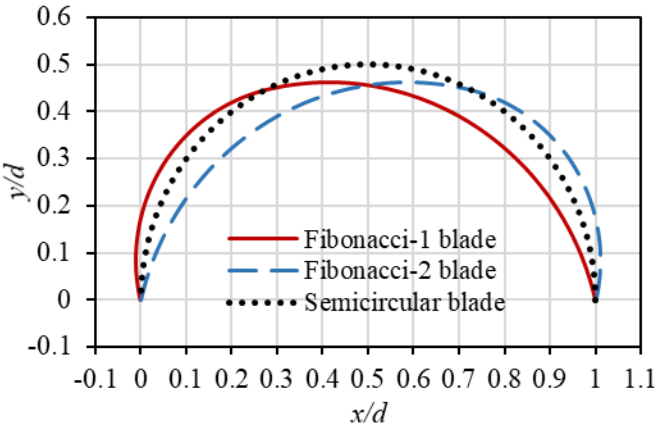

Figure 2.9 Pure Fibonacci spiral blades

The basic design of the Fibonacci spiral blade is made of two circular arcs having their radii equal to 34 and 55 mm, *i.e.*, two consecutive terms of the Fibonacci series (Eq. 2.14) (Blanco et al., 2021). Two more blade designs are iterated from this basic design, *viz.*, Fibonacci-1 and Fibonacci-2 blades (Fig. 2.9). The former one possesses the smaller radial arc (r = 34 mm) towards the rotor tip while the larger (r = 55 mm) towards the center of the rotor. On the other hand, the arrangement of the radial arcs is reversed for the Fibonacci-2 blade. In other words, the Fibonacci-1 blade has higher curvature towards the tip as compared to the Fibonacci-2 blade. The rotors with Fibonacci-1 and Fibonacci-2 blades are tested experimentally and numerically in comparison with the semicircular bladed rotor. The overall dimensions of all the rotors are set same as $D \approx 195$ mm, $H \approx 200$ mm, and $e/d \approx 0.03$. It is observed that Fibonacci-1 blade performs better than the semicircular blade, while the Fibonacci-2 blade performs inferior to the semicircular blade. Experimentally, there is an improvement of $C_{P,\,Opt}$ by 17.6% is observed in Fibonacci-1 blade as compared to the semicircular blade. The vortex attached downstream of the advancing blade's tip is found responsible behind the performance improvement in Fibonacci-2.

In 2022, Blanco Damota et al. (2022) conducted optimization study of the Fibonacci-1 bladed rotor with the help of numerical simulations (Damota et al., 2022) and surrogate models trained by artificial neural network (ANN). The optimum designs obtained in both the studies are provided in Table 2.2. In the first study, different values of any one design variable are tested numerically while maintaining remaining design variables constant to exhaustively search for

the optimum design value. In the second study, an ANN with *AR*, *e*/*d*, and *s*/*d* as the input parameters and C_P as output parameter, is trained utilizing simulated dataset. The optimum design obtained by ANN surrogate model shows an improvement of $C_{P,\,Opt}$ of Fibonacci-1 bladed rotor by 32.4% as compared to the semicircular bladed rotor.

Table 2.2 Optimization of Fibonacci-1 bladed rotor

Sr. No.	Investigators	Year	Design variables				
			n_b	*AR*	*e*/*d*	*s*/*d*	δ
1	Damota et al. (2022)	2022	2	7	0.15	0	180º
2	Blanco Damota et al. (2022)	2022	2	7.5	0.1125	0	112º

It is essential to clarify that the Fibonacci blade design is only a nature-inspired bio-morphic design. Since the working principle of the Φ pertaining to the natural phenomena is not observed being transferred to the flow physics of the Savonius rotor. Nevertheless, the Fibonacci bladed rotor has demonstrated the performance improvement as compared to the conventional semicircular bladed rotor.

2.3.2.2 Nautilus Blade

Inspired by the intriguing spiral shaped calcareous shell of the marine animal 'Nautilus' (Fig. 2.10), Tian (2017) designed and patented a VAT named as Nautilus wind rotor. Similarly, (Gao et al., 2020) implemented the same blade shape into the design of the Savonius rotor. The blade shape is designed similar to the spiral shape of the Nautilus shell. Nautilus belongs to the *Cephalopoda* class (consists of octopus, cuttlefish, squids, and others) having its body enclosed in the body-cavity (Fig. 2.11) of the outer calcareous shell and the tentacles extended out of the shell for locomotion (H. C. B. Grzimek, 2003). The locomotion is done by jet propulsion mode with the help of tentacles and the hood (Jacob, 2001). The internal structure of the shell is comprised of older body chambers separated by the septa, although interconnected by the siphuncle. The logarithmic spiral formation (Fig. 2.11) of the nautilus and other sea-shells is the result of having a tendency of new body mass most adjacent to the older shell part, which is not possible for more simpler linear growth (Hammer, 2016). Moreover, the linear growth would be prone to the stability issue due to mass imbalance. Further, the growth of the body surface towards the center is higher than that of the outer body surface, resulting into the logarithmic spiral shape. The occurrence of the logarithmic spiral shape is therefore fundamentally due to structural and stability reasons, and not due to hydrodynamic aspect. The nautilus avoids sinking and maintains buoyancy by filling up the older chambers with bodily gases through siphuncle. It is important to note that the same bluff structure of the nautilus

shell that is essential for maintaining buoyancy and safety, is also prone to the pressure drag at higher moving speeds (Jacob, 2001).

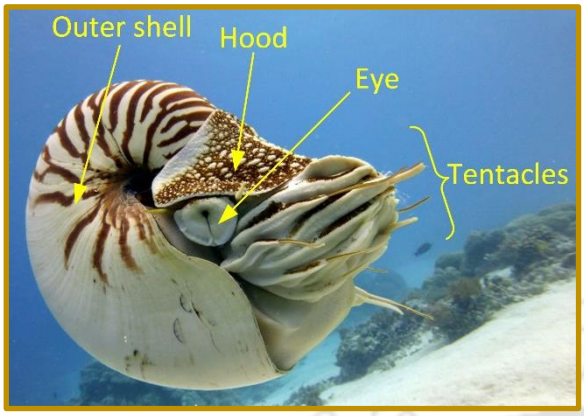

Figure 2.10 Palau Nautilus (*Nautilus belauensis*) (Squires, 2013)

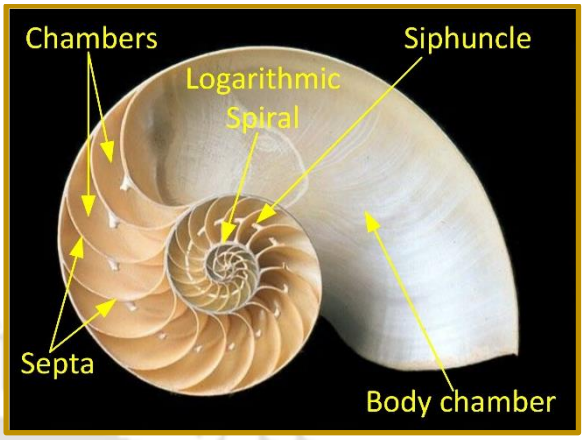

Figure 2.11 Planar cross-section of Pearly Nautilus (*Nautilus pompilius*) (Gall, 2023)

The logarithmic spiral (as per Eq. 2.11) governing the nautilus shape has growth factor (g) in the range of 1.261 to 1.348 (mean = 1.310) for almost all the species of the Nautili, except for Crusty Nautilus (*Allonautilus scrobiculatus*) having g = 1.341 to 1.372 (mean = 1.356) (Bartlett, 2019). In case of the nautilus blade, the image digitization conducted by the present authors reveals $g \approx 1.14$ to 1.33 and this almost resembles the g values of the Nautili. However, it is to be clarified that the exact dimension or curve profile of the nautilus blade is not provided in the patent (Tian, 2017) as well as subsequent publication (Gao et al., 2020). With this design background, the dimensions of the nautilus blade are plotted in Fig. 2.12.

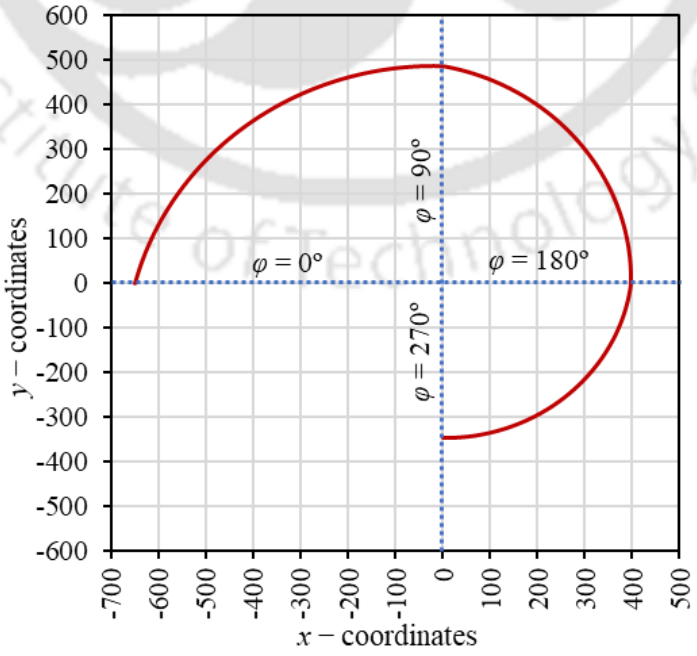

Figure 2.12 Dimensions of the Nautilus blade (in mm)

Using the dimensions provided in Fig. 2.12, (Gao et al., 2020) designed three different rotors having two, three and four-bladed Savonius rotors. The blades are spanned up to φ = 270º, 180º, and 130º for the two. three, and four bladed rotors. The resulting rotors having D = 1.3 m and H = 1 m are illustrated in Fig. 2.13. The 3D numerical results by ANSYS CFX simulated at U = 6 m/s and $\lambda \approx 5.4$ show that the three bladed rotor produces the highest torque (≈ 5.09 N·m) followed by the four (≈ 4.91 N·m) and two-bladed rotors (≈ 4.53 N·m). However, the torque fluctuation is the lowest in case of the four-bladed rotor trailed by three and two-bladed rotors. As the torque produced by the four-bladed rotor is almost equal to that of the three-bladed rotor besides the advantage of the lowest torque fluctuation in the former, a parametric study was conducted to find the optimum span of φ for four-bladed rotor. It is found that the optimum nautilus blade should be spanned over φ = 135º for the four-bladed rotor to gain a maximum torque (≈ 5.04 N·m) that is almost equivalent to the highest performing three-bladed rotor.

Moreover, the four-bladed rotor having two and three stages are also assessed. The phase angle (rotational dilation between subsequent rotor stages) is set as 45º and 30º for the two and three-staged rotors. The numerical finding indicates that the three-staged rotor displays the lowest fluctuation as compared to single and two-staged rotors.

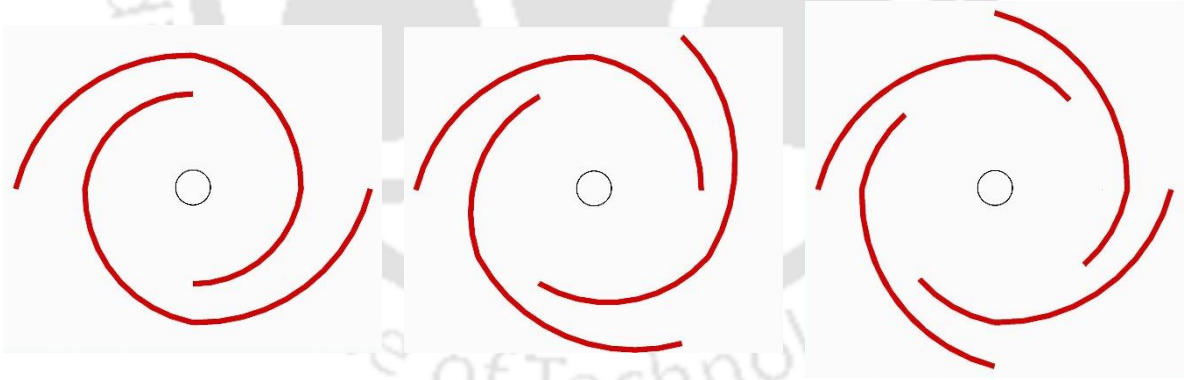

(a) Two-bladed rotor **(b)** Three-bladed rotor **(c)** Four-bladed rotor

Figure 2.13 Nautilus balded Savonius rotor

It is to be mentioned that the flow does not pass through the internal cavity of the nautilus shell as per the hydrodynamics and locomotion of the nautilus. On the other hand, the flow passes through the internal overlap region of the nautilus-bladed Savonius rotor. Moreover, the rotor does not have closed shell type blade like the nautilus shell. Therefore, the present nautilus blade design for the Savonius rotor is an example of the biomorphic design rather than the actual biomimicry.

2.3.2.3 Pseudo-Fibonacci blade

Another variant of the Fibonacci blade is introduced by Ashwindran et al. (2021) in 2021. As shown in Fig. 2.14, the Pseudo-Fibonacci blade is made of two parts, namely, the primary circular arc towards the blade tip and an elongated arm having very low curvature (almost straight arm). In this blade, the Golden ratio Φ manifests by the ratio of the *d/2* (radius of semicircular blade shown in Fig. 2.14) to the radius of the primary circular arc of the blade. The primary circular arc is spanned up to $\pi/2$ and then it is connected to the rotor center through the secondary straight arm. It may be noted that the blade profile does not possess any Fibonacci spiral shape, unlike the Fibonacci-1 and -2 blades. The 2D numerical simulation results indicate an increment of performance by 7.2% for Pseudo-Fibonacci bladed rotor ($D \approx$ 0.9 m) at λ = 0.59 and U = 8 m/s, as compared to the semicircular bladed rotor. The lower C_{Pr} distribution at the downstream of the advancing blade is the reason behind the performance improvement. Along with the introduction of the Pseudo-Fibonacci blade, Ashwindran et al. (2021) also conjectured the presence of irrational number $\sqrt{2}$ with the Φ inside the geometric construction of the Fibonacci-spiral. Similar to the Fibonacci blades, the Pseudo-Fibonacci blade is also considered as the biomorphic design due to the similar reason elaborated in Section 2.3.2.1.

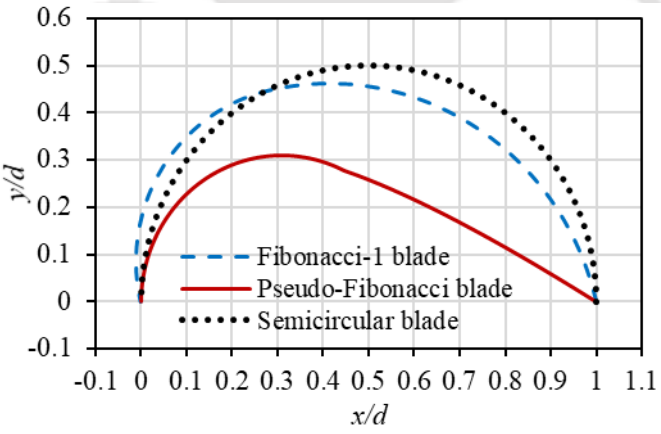

Figure 2.14 Fibonacci blades in comparison with semicircular blade

2.3.3 Fish Shaped Blade

The majority of the Savonius rotor blades are usually in the form of thin sheets. However, this conventional trend has been challenged by Tartuferi et al. (2015) by introducing thick high cambered airfoil-shaped rotor blades. Airfoil profiles such as SR3345 (33% camber value placed at 45% of the chord line) and SR5050 (50% camber value placed at 50% of the chord line) were developed to design the Savonius rotor. Numerical results show that that the SR3345 performs better than semicircular blade for the $\lambda < \lambda_{Opt}$. On the other hand, the SR5050

demonstrates performance improvement for the range of $\lambda > \lambda_{Opt}$. The reason behind the performance improvement in airfoil shaped blade is found to be the strengthening of low-pressure region behind the advancing blade.

Figure 2.15 Twin Koi fish rotating in circle (Hashem and Zhu, 2021)

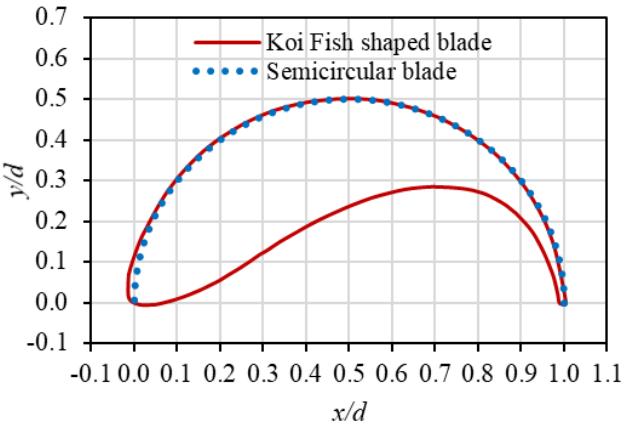

Figure 2.16 Koi fish shaped blade (Hashem and Zhu, 2021)

2.3.3.1 Koi Fish Shaped Blade

As the airfoil shaped blade resembles the slender body of the fish, Hashem and Zhu (2021) introduced a novel blade shape in 2021, inspired from the body of Koi carp fish (Fig. 2.15), which is the mutant of the Amur Carp fish (*Cyprinus rubrofuscus*) having white, red, and blue color patches on its body (B. Grzimek, 2003). As shown in Fig. 2.15, the Koi fish are observed circulating tightly in the pairs while cruising in the straight direction (Hashem and Zhu, 2021). This behavior resembles the rotation of the Savonius rotor operating in the water. This similarity led to the proposal of Koi fish shaped blades for hydrokinetic Savonius rotor as shown in Fig. 2.16. The shape of the upper arc of the Koi fish blade is found to be similar to the semicircular blade. The numerical simulation results show that the Fish shaped blade ($e/d \approx 0.36$, $s/d \approx 0$) performs better than the semicircular blade ($e/d \approx 0.36$, $s/d \approx 0$) with 9.4% increment in $C_{P,\,Opt}$ at $\lambda \approx 1$ and $Re \approx 1.13 \times 10^5$ ($U = 0.8$ m/s). Having observed the potential of the fish shaped blade, Hashem and Zhu (2021) also opted for design optimization implementing the evolution strategy (ES) technique on the radial basis function (RBF) surrogate model having e and s as input variables and C_P as output variable. The surrogate model was trained by the numerical simulation dataset by varying e/d in the range of 0.32 to 0.4, and s in the range of -0.032 to 0.032. As a result, the Fish shaped blade having $e/d \approx 0.332$ and $s/d \approx 0.009$ is found to be optimum showing $C_{P,\,Opt}$ 17.6% higher than the base variant of the Fish shaped blade at $\lambda \approx 1$ and $Re \approx 1.13 \times 10^5$ ($U = 0.8$ m/s). The flatter upstream surface of the advancing fish shaped blade enhances the overlap flow strengthening the pressure

recovery region of the returning blade. As a result, the overall rotor performance of the rotor improves with the implementation of the fish shaped blades.

2.3.3.2 Sand-eel Shaped Blade

Similarly, Hashem et al. (2022) introduced the sand-eel inspired fish shaped blade. Sand-eel also known as sand-lances belonging to *Ammodytidae* family (Fig. 2.17), is small, slender eel-like fish that is found in the shallow water bodies with sandy substrate (B. Grzimek, 2003). Using the body shape of the sand eel and applying additional camber to the body, a new blade shape is proposed that is quite similar to the one inspired from Koi carp fish as discussed in Section 2.3.2.1. The proposed blade shape is shown (Fig. 2.18) along with the parametrization in the form of normalized maximum camber (f_{max}/d) and maximum camber location (X_{max}/d) calculated from the blade tip. Moreover, the maximum thickness of the blade is kept 20% of f_{max} to maintain geometric shape of the blade.

Figure 2.17 Pacific sand-eel (*Ammodytes personatus*) (Johnson, 2022)

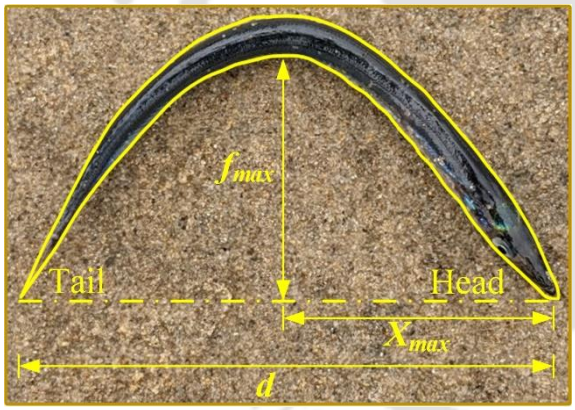

Figure 2.18 Parametrization of cambered Pacific sand-eel (Idgreen, 2021)

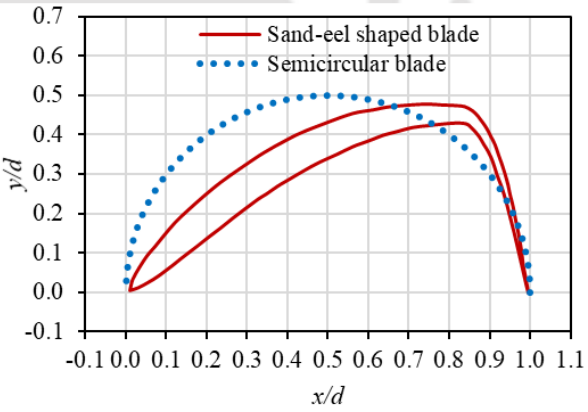

Figure 2.19 Sand-eel shaped blade (Hashem et al., 2022)

As a first step, two blades having head shape of the fish oriented towards the rotor center and away from it, are evaluated numerically by STAR-CCM+ 2021.3 software. The results show that the former blade design performs better than the latter. Parametric study is then conducted by numerically testing 54 variants of this blade by varying the parameters manually, *viz*, f_{max}/d and X_{max}/d. As a result, the optimum configuration of $f_{max}/d \approx 0.4$ and $X_{max}/d \approx 0.8$ is found to improve $C_{P,\,Opt}$ by 8.3% as compared to semicircular bladed rotor (Fig. 2.19) at $Re \approx 2.23 \times 10^5$ and $\lambda = 0.8$. The reason behind the performance improvement is the higher and lower C_{Pr} induced at concave and convex sides of the advancing blade, respectively.

Instead of using exhaustive search method for finding the optimum blade design adopted by Hashem et al. (2022), (Abdelghafar et al., 2023) used an evolutionary algorithm to find the optimum blade design. For the optimization, C_P evaluated at λ = 0.8 and U = 9 m/s (designed condition) was considered as the objective function with f_{max}/d and X_{max}/d as design variables controlling the curvature of the blades. It is important to note that a constant d = 0.184 m, maximum blade thickness = 0.2 f_{max}, and LE radius = 0.2d were set while designing the blades. The choices of f_{max}/d and X_{max}/d were constrained in the range of 0.2d-0.6d and 0.1d-0.9d, respectively. The optimization procedure was conducted by combining iSIGHT optimization platform with STAR-CCM+ software for numerical simulations. A total of 128 variants of the blade were evaluated numerically during the optimization, and as a result, a blade having f_{max}/d = 0.301 and X_{max}/d = 0.739 was found optimum showing C_P = 0.249 at λ = 0.8. The C_P of this optimum bladed rotor was 9.21% higher than the semicircular bladed rotor with identical dimensions. However, the $C_{P,\,Opt}$ = 0.255 was demonstrated by the optimum design at λ_{Opt} = 1, which is 10.58% higher than its counterpart. The optimum blade did not only improve the $C_{P,\,Opt}$ but it enhanced the C_P almost over the entire range of λ. The C_P for both the blades was found increasing steadily up to λ < 0.8. Above λ < 0.8 and hitting the λ_{Opt} condition, the performance trend for semicircular blade directly plunged whereas it remained high for optimum blade design over 0.8 < λ < 1.4.

Based on the observation of the blade variants developed through evolutionary generations, it is found that C_P is highly influenced by X_{max} as compared to f_{max}. Most importantly, the overall optimization procedure concluded that a location of maximum camber (X_{max}) in vicinity of the LE is beneficial in terms of high performance of the rotor. The optimum blade design strengthens the low C_{Pr} region at the convex side of the advancing blade, especially towards the tip, in comparison to the semicircular blade. This enhances net positive torque experienced by the blade besides facilitating large moment arm. The optimum blade was successful in improving the positive torque produced by the advancing blade, however, it also increased the negative torque contributed by the returning blade. Nevertheless, the net torque produced was positive and that was still higher than the semicircular bladed rotor.

2.3.3.3 Other fish-shaped Blades

Li et al. (2016) and Niu et al. (2018) proposed a fish-shaped blade as shown in Fig. 2.20. The source of this blade shape was not specified in the papers. However, the mathematical expressions for the suction side and pressure side airfoil edges are Eqs. 2.15 (Fourier fitting)

and 2.16 (polynomial fitting), respectively. Compared to other fish shaped blades, the present blade is less cambered. As the high curvature is present posterior to the airfoil, the front half of the rotor is considered as lift-based rotor and the rear half is considered as the drag-based rotor. Moreover, the curved portion of the airfoil can guide the fluid flow towards the leading edge of the following rotor blades, which improves the torque and power of the rotor. The pressure difference induced on the blades due to their fish-shape generates torque of the rotor. Traditionally, the lift-based and drag-based rotors are prone to lower starting torque and lower rotational speeds, respectively. These drawbacks can be overcome by this fish-shape bladed rotor.

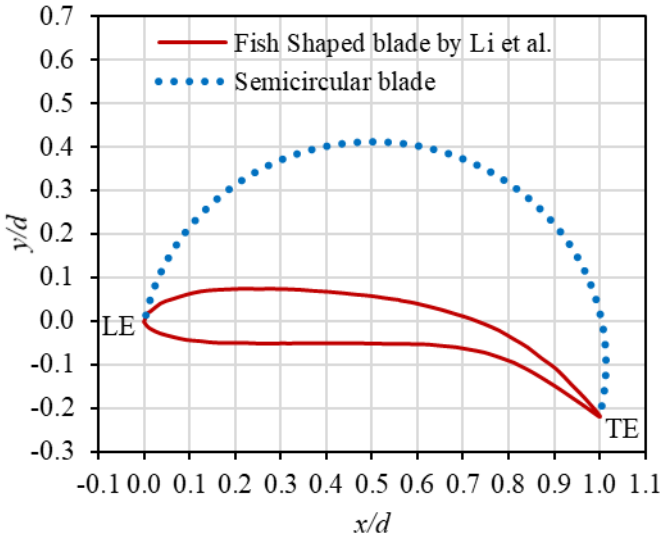

Figure 2.20 Fish-shaped blade proposed by (Li et al., 2016) and (Niu et al., 2018)

$$f(x)_{\text{Suction}} = 48.51 - 54.53\cos(1.571x) - 56.82\sin(1.571x) - 1.339\cos(3.142x) + 40.82\sin(3.142x) + 8.975\cos(4.713x) - 8.37\sin(4.713x) - 1.619\cos(6.284x) - 0.05546\sin(6.284x) \quad (2.15)$$

$$f(x)_{\text{Pressure}} = 13.22x^7 - 51.08x^6 + 79.58x^5 - 65.14x^4 + 30x^3 - 7.95x^2 + 1.135x + 0.007948 \quad (2.16)$$

The proposed rotor comprised of three blades had $D = H = 0.5$ m, $c = 0.275$ m, and the setting angle (Ψ) = 40° (Fig. 2.21). Unlike the conventional design of the Savonius rotor, the TE of the blade is quite away from the axis of rotation forming an inner circle denoted by D_{in}. Li et al. (2016) and (Niu et al., 2018) named the new rotor design as 'Fish-bionic wind wheel'. Li et al. (2016) conducted numerical analysis of the rotor to study the influence of setting angle (Ψ) on the rotor performance. The operating range was $U = 9$ m/s to 13 m/s. The values of Ψ starting from 36° to 42° were tested and concluded that the optimum value is $\Psi = 37°$. The overall C_T was found increasing with setting angle, however, it decreases with further increase of Ψ. From

the numerical pressure distribution, it is observed that the surface pressure at blade head remains relatively higher providing necessary starting torque to the rotating rotor. Niu et al. (2018) used an identical rotor design to assess its performance from wind tunnel experiments. The operating range was set as U = 7 m/s to 13 m/s. The $C_{P,\,Opt}$ of the rotor was found increasing for U = 7 m/s to 9 m/s covering the maximum $C_{P.\,Opt} \approx 0.51$. Thereafter, the C_P decreased with further increase of U. However, the performance characteristics of the rotor with respect to λ was not addressed in the thesis.

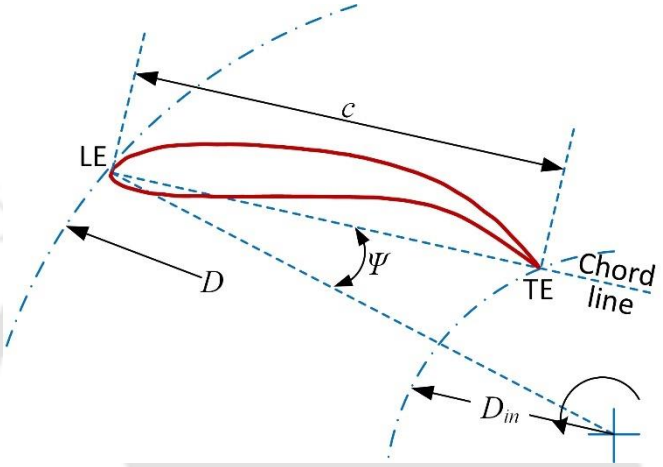

Figure 2.21 Rotor design proposed by (Li et al., 2016) and (Niu et al., 2018)

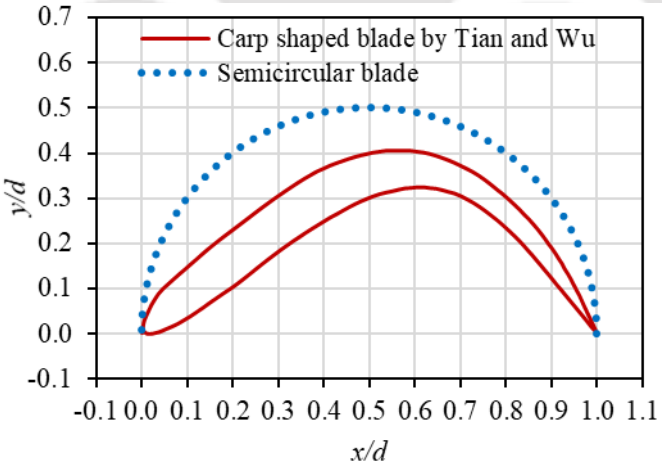

Figure 2.22 Fish-shaped blade proposed by (Tian and Wu, 2020)

Inspired from the body shape of a carp fish, Tian and Wu (2020) proposed a new blade shape as shown in Fig. 2.22. A novel rotor design in the form of anti-glare device to be installed at freeway was introduced (Tian and Wu, 2020). The overall dimensions of the rotor were: D = 0.3 m and H = 0.9 m. The rotor was investigated both numerically and experimentally over a range of U = 5 m/s to 25 m/s. However, the work (Tian and Wu, 2020) lacked in useful insights such as overall performance characteristics (C_P vs. λ) and flow physics.

Both the cases of the fish shaped blades, be it a Koi-carp shaped or a sand-eel shaped blades, are considered as the biomorphic blade designs since the proposal is made only based on the metaphoric resemblance of the fish shape with that of the airfoil shaped blades. There is no extension of actual working principle from fish shape to the rotor.

2.3.4 Fish-ridged Blade

The hydrodynamic shape of the fish is a result of long-term evolution to enhance survival and locomotion. In 2013, Song et al. (2013) proposed a new blade design inspired from the shape of the fish-ridge illustrated in Fig. 2.23 using an example of Blue Devil Damselfish (*Chrysiptera taupou*). The fish-ridge is defined as the dorsal shape of the fish body starting from head through dorsal fin, peduncle to the caudal fin. The original blade shape reported by Song et al. (2013) is similar to the Fish-ridged blade-1 as plotted in Fig. 2.24. The rotor having three Fish-ridged blade-1 with $D \approx H \approx 700$ mm, was then tested both experimentally and numerically. The rotor demonstrated $C_{P,\,Opt}$ of 20% at $U \approx 12.38$ m/s. From the numerical parametric optimization, the Fish-ridged blade-2 was found to produce $C_{P,\,Opt}$ of 24% at $U \approx$ 12.38 m/s. However, it is important to note that the novel rotor was not evaluated in comparison with the conventional semicircular bladed rotor. It means, whether or not the fish-ridged blade performs better than the semicircular blade, is not known.

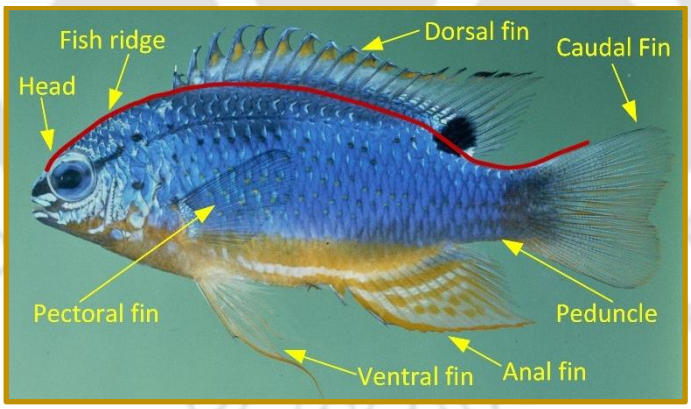

Figure 2.23 Illustration of fish-ridge on Blue Devil Damselfish (*Chrysiptera taupou*) (Randall, 1974)

The above mentioned research gap is addressed by Ma et al. (2017). In this study, rotors having semicircular blade ($n_b = 2$) and Fish-ridged blade-1 ($n_b = 2$) with $D \approx 700$ mm, are assessed numerically at $U = 8$ m/s. The 2D simulation results show that the Fish-ridged profile-1 is inferior to the semicircular blade. To overcome this drawback, a new Fish-ridged profile-3 (Fig. 2.24) is developed that demonstrates $C_{P,\,Opt} \approx 23\%$, almost equal to that of the semicircular blade. However, improvement in C_P is observed up to $\lambda \approx 0.7$, and thereafter, the C_P trend is

reversed for semicircular blade and Fish-ridged blade-3. Further, 12% increment in $C_{P.\,Opt}$ in Fish-ridged blade-3 is obtained as compared to the original Fish-ridged blade-1.

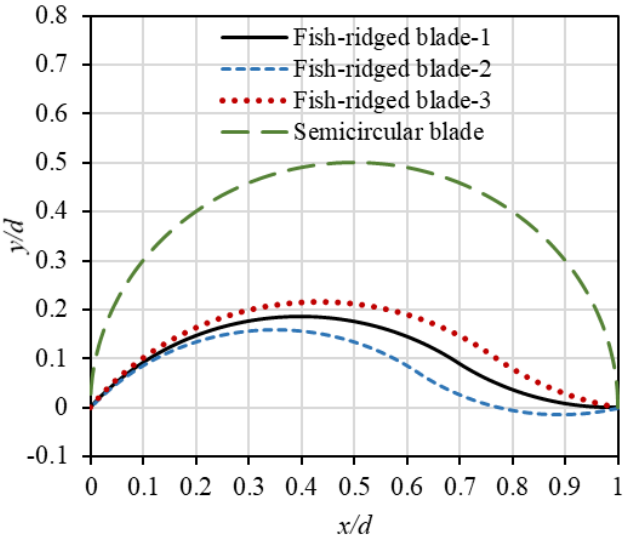

Figure 2.24 Fish-ridged shaped blade (Ma et al., 2017; Song et al., 2013)

Although the Fish-ridged blade shows a decent improvement in power characteristic, the question of how the fish-ridge blade implements fish-bionic concepts to enhance the torque mechanism of the rotor, is yet to be addressed. This Fish-ridged blade can be considered as the biomorphic blade design.

2.3.5 Barnacle Inspired Blade Surface

All of the above-mentioned examples of the bio-inspired designs address only the overall shape and curvature of the rotor blade. Alternatively, Ashwindran et al. (2022) implemented surface patterns inspired from the marine organism called 'Barnacles', over the rotor blades for the anticipated improvement in the rotor performance. The Barnacles are basically the crustaceans having permanent outer calcareous shell-like structure (especially in *Thoracica* infra-class) enclosing their bodies (H. C. B. Grzimek, 2003). They are usually mounted on the surface with their *cirri* extended out from carapace to capture the planktonic organism flowing in the marine currents (Fig. 2.25). When they capture the planktonic particles, they shrink back inside the outer shell, and then repeat the process again. The barnacles can mount on the surface of both living and non-living bodies, *e.g.*, floating logs, bottom of the ships, wooden pilings, bottles, corals, sea anemones, lobsters, crabs, jellyfish, fishes and other marine mammals (Fig. 2.26). It is reported that the undesirable establishment of the barnacle colonies (barnacle fouling) over submerged ship surfaces, tidal rotors, hydrofoils and locomoting marine organisms, deteriorates their performance due to induced drag. At moderate to high *Re*, the mature barnacle

(5-15 mm in diameter and height) increases pressure drag over the surface due to the flow separation. This also affect the performance of the Darrieus hydro-rotor as per the results reported in Stringer and Polagye (2020). However, this drag inducing characteristic might be useful for the torque enhancement of the Savonius rotor since it is primarily a drag-based rotor. With this attribute of barnacles in focus, Ashwindran et al. (2022) added barnacle shaped protrusions over the Pseudo-Fibonacci blade. However, the exact dimensions and distribution pattern of the barnacle shaped protrusions are not provided in the paper. Although the barnacles have shown drag enhancing trait, the numerical results of anticipated barnacle-inspired blade design perform inferior to that of the normal blade. This suggests further attention on the different design parameters such as *Re*, dimensions of barnacle shaped protrusions, density and distribution patterns and others.

The barnacle inspired surface of the blade can be considered as a bio-mimetic design, not the bio-morphic design, since the actual phenomenon of the drag enhancement is tried to implement in the blade design of the drag-based rotor. However, this attempt is unsuccessful in improving the rotor performance.

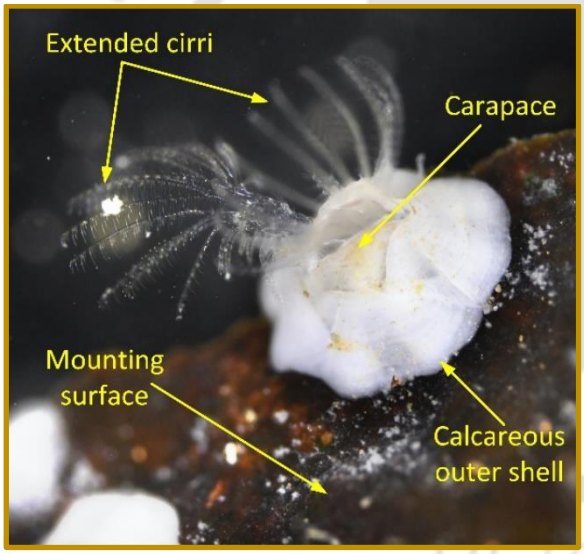

Figure 2.25 Illustration of Beaked Barnacle (*Austrominius modestus*) (Blogman, 2021)

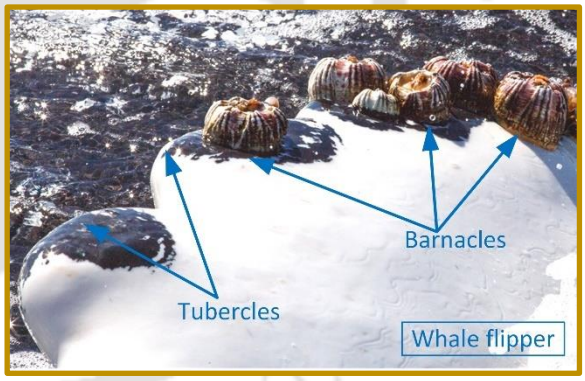

Figure 2.26 Whale Barnacle (*Coronula diadema*) mounted on the tubercles of Humpback whale's flipper (Lane, 2016)

2.4 Use of Soft Computing Techniques

In realm of Savonius rotor, Mohammadi et al. (2018) used experimental data documented by Kamoji et al. (2009) to train the ANN for performance prediction of Savonius rotor. The input variables used in the training are aspect ratio, overlap ratio, gap ratio, λ, blade twist, Reynolds numbers and existence of central shaft; while the output variable is the C_P. In addition to the

training neural network, genetic algorithm (GA) was also used to optimize the approximated function in order to find out optimum input variables. However, the study was focussed only on single type of blade shape and with limited numbers of rotor design variables. In the similar investigation carried out by Sargolzaei and Kianifar (2009), six different types of rotors were tested experimentally to gather data for ANN. Among the six types of rotors, one was with Bach type of blades while the others were of semicircular blades with different overlap ratios. It is important to note that the individual neural networks were trained for each rotor, instead of using cumulative data of all rotors for training a single ANN. Storti et al. (2019) discussed the optimization problem combining computational fluid dynamics (CFD) simulation, ANN training and genetic algorithm to find optimum design of the deflector plate for eight-bladed Savonius rotor. Debnath and Das (2010) used ANN only for the function approximation problem but not for the optimization problem. The input variables *viz.* overlap ratio, λ and angular velocity of three-bladed Savonius rotor were used and the C_P was used as output variable to train the network. The quality of approximation provided by trained ANN was discussed. Thus, it can be concluded that the ANN in Savonius rotor has either been used for optimization purpose with CFD attachments or used as only the function approximation tool to formulate the hidden unknown theoretical expressions.

2.5 Research Gaps and Present Objectives

In view of the literature survey presented in Sections 2.2.4 and 2.3, blade designs of the Savonius rotor can be identified as the most promising aspect to improve the rotor performance. Comparatively recent proposals of bioinspired blades seem very promising to work on. Therefore, the important research gaps in this direction are identified. In case of using traditional aerodynamic shapes, the core idea has been to use available streamlined bodies and take the advantage of their low drag characteristics. Such bodies are widespread in the field of aerodynamics since majority of the traditional aerodynamic problems deal with the reduction of the profile drag of the shape. Further, in the context of finding the superior blade shape, the majority of research articles available in the literature have provided *posteriori* flow physics analysis to explain the performance improvement and to complement the experimental observations. However, such a *priori* analysis of the flow structure and blade design approach are not yet available. This knowledge is desirable to provide the necessary prerequisites to enhance the performance of the novel blade shape or infer the performance based on the blade shape without any actual experimentation.

In order to address this niche, the present thesis is focused on proposing prerequisite flow conditions such that the novel blades developed implementing the recommended flow conditions can ensure the anticipated performance improvement. Therefore, the suitable bio-organisms or biological phenomena are explored in this thesis that obeys the proposed flow conditions. In the present work, the appropriate biological phenomena found are: (a) feeding mechanism of the seapen, (b) corrugations of the dragonfly wings. Additionally, in the context of various bioinspired design approaches defined in Section 2.3.1, almost all of the bioinspired blades of the Savonius rotor are the biomorphic designs. Nonetheless, it is recommended to prefer biomimetic design approach over the biomorphic design approach. The reason is that the biomimetic approach can help in gaining thorough understanding of the working principles and flow physics of the rotor and allied bio-organism. Such merits are not evident in the case of biomorphism since it revolves around superficial imitation of the external form of the bio-organism. Thus, the present thesis has adopted the biomimetic design approach for the blade development instead of the biomorphic approach embraced till date. The newly proposed blade designs are fabricated and then tested in wind tunnel to assess their power and starting torque characteristics. CFD (computational fluid dynamics) simulations using *Ansys Fluent* software have been carried out to know whether or not the proposed flow conditions are manifested successfully.

As mentioned in Section 2.4, the ANN training in case of only one type of the blade profile with few of the design variables (less than five variables) has been already reported in the literature. Considering this, another goal is set that is focused on formulating an ANN based surrogate model to predict the performance of the Savonius rotor. The novelty is that the combined data of the different blade shapes has been used to train ANN for the application of function approximation task, which has not been considered yet. Moreover, the number of input variables are also higher than the previous attempts. The experimental data reported in the literature have been used to train the models. The aim of this work is to check whether or not the unknown torque generating mechanisms pertaining to various blade shapes can be modelled by ANN. Parallelly, a GEP based surrogate model is developed which can formulate relationship among input and output variables in the traditional form of the equations, unlike ANN model that approximates a given function in the form of weights and biases. Thereafter, the GSM is merged with the ANN to predict $C_{P,\ Opt}$ and λ_{Opt} of a given rotor design. Furthermore, a novel data partitioning method is proposed while training the ANN. As the trained ANN maps input-output variables in form of weights and biases, which is not quite

intuitive to understand the influence of each and every design parameter on $C_{P,\,Opt}$. Thereby, parametric study is conducted besides developing a graphical user interface (GUI) based on the trained ANN model for predicting $C_{P,\,Opt}$.

2.6 Concluding Remarks

Based on the literature review presented in this chapter, several key conclusions can be drawn pertaining to the augmentation technique and current research trend in the field of Savonius wind turbine. Augmentation techniques of Group-I and Group-II improve the rotor performance but cannot sustain the distinct attribute of the Savonius rotor, *i.e.*, direction independence. On the other hands, augmentation techniques of Group-III can maintain the direction independence, however, they are unsuccessful in the performance improvement. Performance enhancement by implementing Group-IV augmentation techniques have been proved quite effective. The design recommendations reported regarding the design parameters of Group-IV are very important for developing overall designs of the rotors used in the present work. Among various techniques of Group-IV, the blade shape designing with the concepts of bioinspiration have become very popular nowadays. Majority of the bioinspired designs introduced for the Savonius rotor are the biomorphic designs, and not the biomimetic designs. Therefore, it is recommended to be focused on the biomimetic blade design of the Savonius rotor emphasizing more on the knowledge transfer between bio-organism and the blade design.

Along with that, implementation of soft computing techniques combined with conventional experimental and numerical approaches have become prevalent in Savonius rotor design. The main focus of such investigations are found to be the performance prediction and blade shape optimization.

Chapter – 3

Experimental and Numerical Setups

Chapter Layout:

Overview

In this chapter, experimental and numerical setups are discussed. Wind tunnel setup together with various measuring instruments and their relative configurations are described with the help of illustrations. The findings of the error analysis and blockage corrections of the wind tunnel setup are presented in this chapter to establish reliability in the present experimental setup. The second half of this chapter is focused on the numerical computational setup developed for the present research work. Different evaluation rubrics of the numerical setup such as size of the numerical domains, boundary conditions, mesh structures, solver specifications, independence tests, grid convergence, validation and others are discussed in this chapter. Both the experimental and numerical setups are used in the research investigations of the newly developed blades covered in the subsequent chapters.

3.1 Experimental Setup

3.1.1 Wind Tunnel Setup

The experiments are conducted in an open circuit sub-sonic wind tunnel having a closed test-section with dimension of 600 mm × 600 mm × 2000 mm (Fig. 3.1). The facility is situated at the wind tunnel laboratory of IIT Guwahati and it is manufactured by Sunshine Measurement Private Ltd.-Bangalore. Axial flow fan with the diameter of 1.3 m is capable of generating the maximum of U = 50 m/s wind velocity inside the test section. The overall contraction ratio of the wind tunnel is 9:1. The test models of the Savonius rotors are tested in this wind tunnel with deep-groove ball bearing mountings.

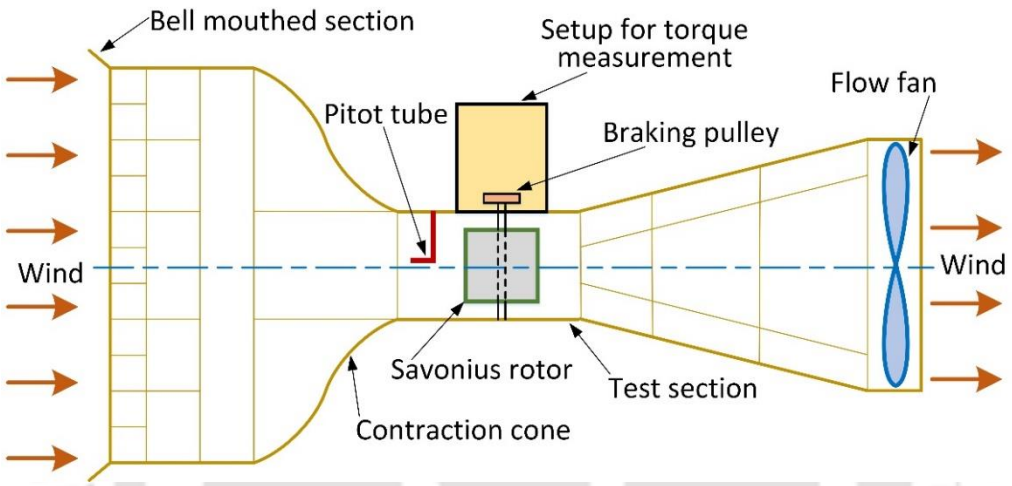

Figure 3.1 Schematic of the wind tunnel setup

The free stream velocity U is measured by a Pitot-tube together with electronic manometer (± 0.3% accuracy) without mounting the rotor in the test-section. The pitot-tube is mounted approximately 1500 mm (≈ 6D) away from the rotor center. Mechanical rope-brake type dynamometer (Fig. 3.2) with braking pully having diameter of 67 mm (D_P) is used to measure the torque produced by rotating rotors. The spring balances used in the dynamometer are having accuracy of ± 0.2%. In the dynamometer, one end of the rope is connected with the spring balance and another end is tied with the weight through the set of braking, tight-side, and slack-side pulleys. The rotations in RPM (rotations per minute) are measured by a proximity sensor having ± 0.5% accuracy.

The setup for measuring the static torque (T_S) experienced by the rotors is illustrated in Fig. 3.3. In this setup, one end of the rope is fixed on the brake pulley and another is attached to a wing-nut screw via an electric spring balance. The electric spring balance is used to avoid elongation of the spring as observed in the conventional spring balances. Further, the rope is

wounded on the brake pulley in such a way that the continuous rotation of the rotor is hindered. The θ of the rotor is changed with the help of wing-nut and screw. The movement of the wing-nut and screw facilitates the change in rope's length that enables corresponding rotary advancement of the rotor in its direction of rotation, resulting into the change of θ. The exact value of θ of the rotor is ensured with the help of an angular dial. This methodology has been successfully implemented by Tabassum and Probert (1987) and Rathod et al. (2019) to measure the static torque of the Savonius rotors.

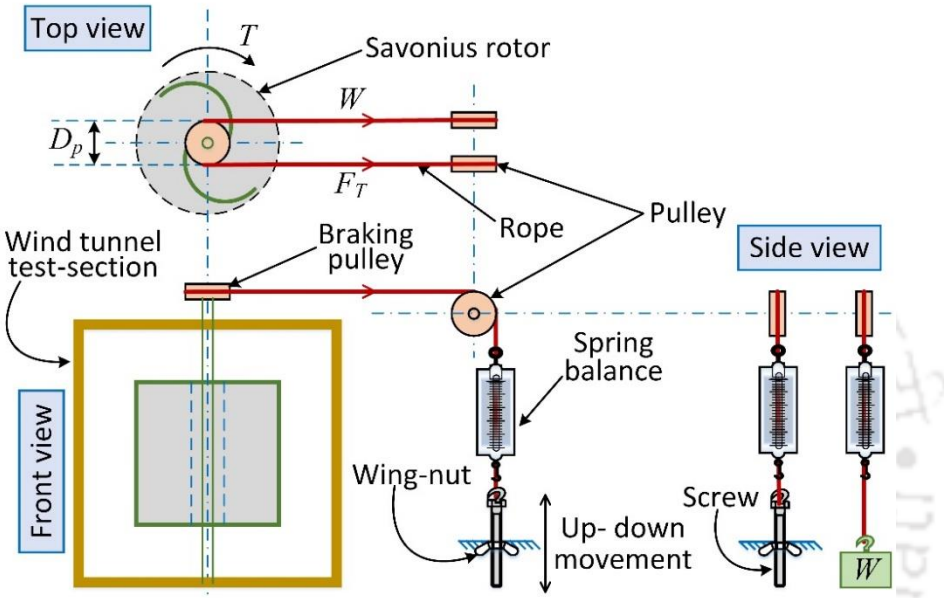

Figure 3.2 Schematic of the Dynamometer setup

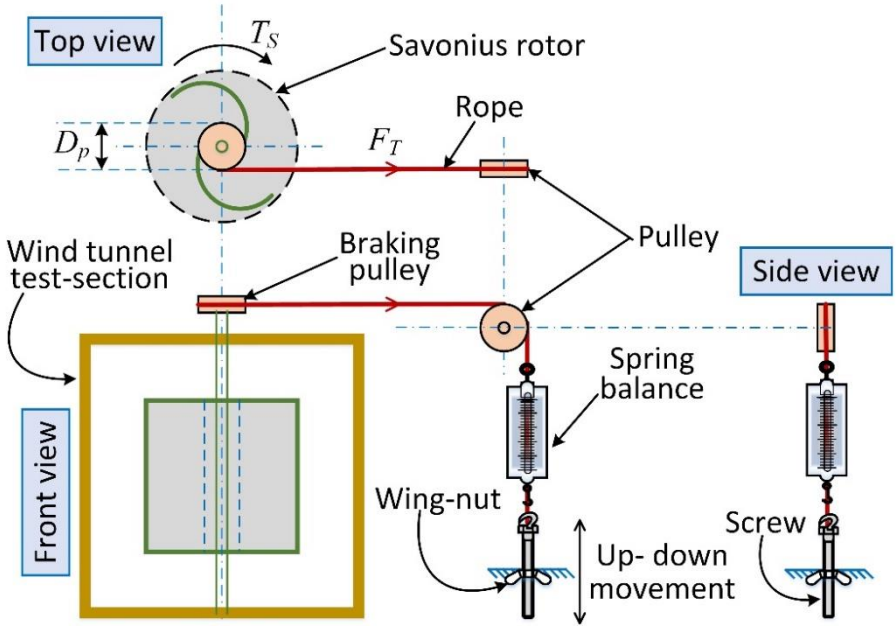

Figure 3.3 Schematic of static torque measurement setup

The parts in the actual rotor model assemblies are showcased in Fig. 3.4. The rotor models have either the sea-pen blade (discussed thoroughly in Section 4.4) or the semicircular blade. The difference between both the blade profiles are quite evident from Fig. 3.4. The curvature to the blades is provided by bending the galvanized sheet metal. The blades are then attached to the shaft through a pair of annular mounting sleeves. Thereafter, the end plates are mounted on top and bottom of both blades with the help of a pair of end plate couplers. The details dimensions of all the rotor parts are provided in Section 4.4.

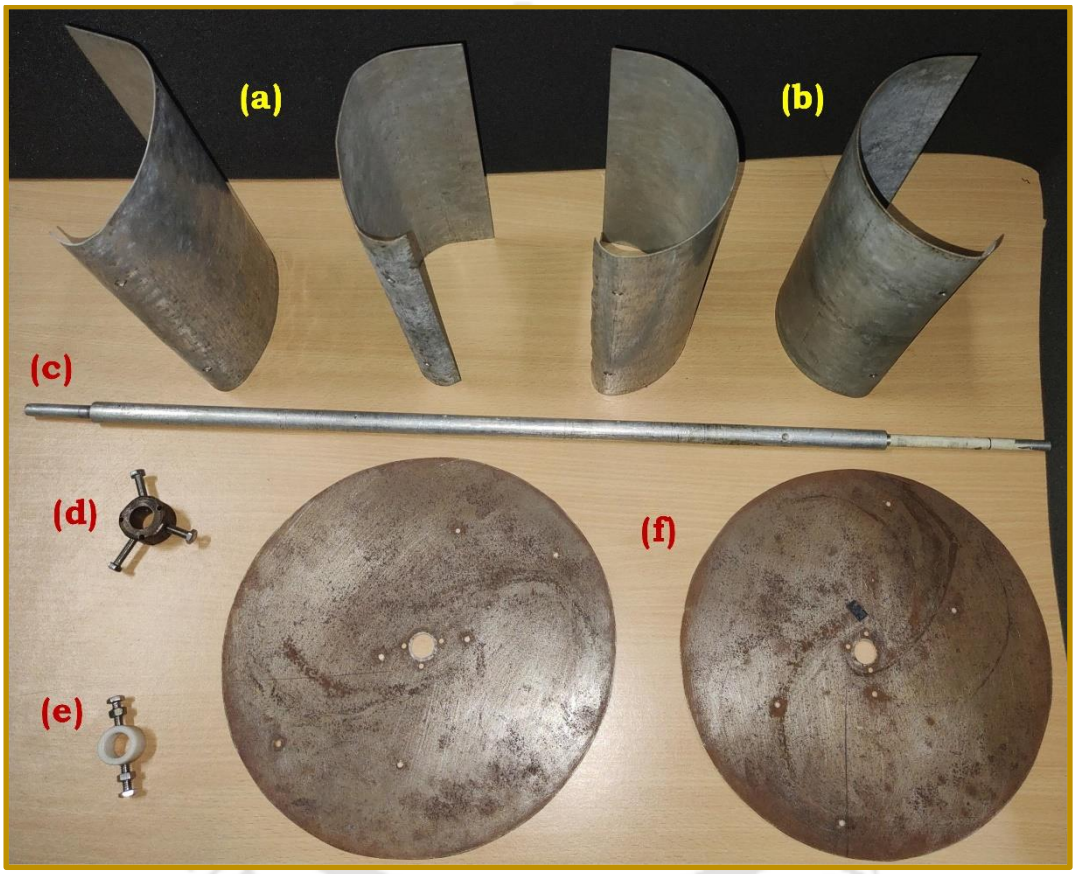

Figure 3.4 Parts of rotor model assembly **(a)** Sea-pen blades **(b)** Semicircular blades **(c)** Rotor shaft **(d)** End plate coupler **(e)** Annular mounting sleeve **(f)** End plates

The undercuts provided at each end of the shaft help them to be inserted in the deep-groove ball bearings mounted on the top and bottom surfaces of the wind tunnel test section as shown in Fig. 3.5(a). The brake pulley illustrated in Fig. 3.2 is mounted on a longer undercut protruding outside of the test section. Figures 3.5(b) and 3.5(c) are the real images of rope-brake dynamometer adjacent to the wind tunnel test section and proximity sensor, respectively. A small magnet is mounted on the periphery of rotating brake pully. The magnet rotates, the sensor experiences change in the rate of magnetic flux that indirectly provides the rotational speed of the rotor models.

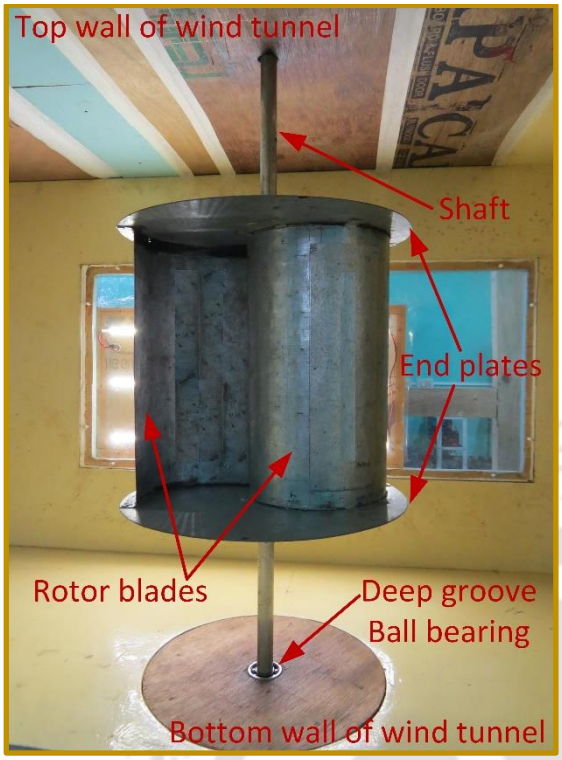

(a) A rotor model mounted inside wind tunnel test section

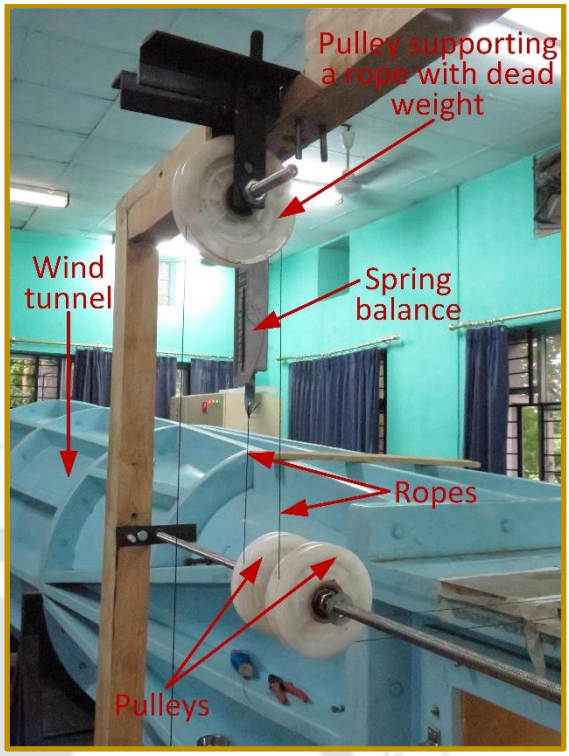

(b) Pulley configuration of rope-brake dynamometer

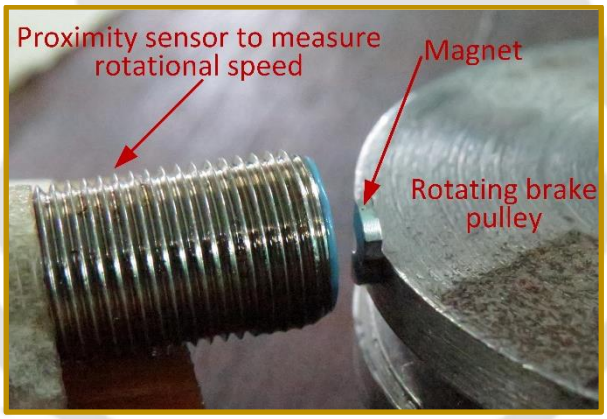

(c) A proximity sensor to measure the rotational speed

Figure 3.5 Images of actual experimental setup

3.1.2 Measurement Procedure

During experimentation, the rotor is allowed to rotate up to no load condition, and thereafter, gradual weight/load (W) is applied to the dynamometer and the resulting spring balance reading (F_T) along with RPM (N) are recorded (Fig. 3.2). This procedure is followed multiple times to gather multiple datasets of the same rotor for the error analysis (Section 3.1.3). Using values of W, F_T and D_P, the torque (T) produced by the rotor is calculated with the help of Eq. 3.1. The value of N is utilized to calculate λ (Eq. 2.8) at a given loading condition. The torque, T, is then used to calculate other dimensionless indices such as C_T and C_P as expressed in Eqs. 2.6

and 2.7. The C_P vs. λ characteristic is considered to compare the performance of the rotor designs.

$$T = \left(W - F_T\right) \times \frac{D_P}{2} \times 9.81 \tag{3.1}$$

For the starting torque characteristics of the rotors, tension force (F_T) measured by electric spring is used to calculate the static torque (T_S) corresponding to θ as per Eq. 3.2. With the help of T_S, C_{ST} is calculated with the help of Eq. 2.9. The different θ values are set by the wing-nut and screw arrangement (Fig. 3.3) discussed in Section 3.1.1. This methodology of calculation is repeated at every interval of $\theta = 10^o$, starting from $\theta = 0^o$ to 180^o. Beyond 180^o, all the values are repeated as the returning blade becomes advancing blade and *vice versa*. The free stream velocity U is set by controlling the rotational speed of the wind tunnel fan, and measured by the Pitot-tube together with electronic manometer illustrated in Fig. 3.1.

$$T_S = \frac{1}{2} D_P F_T \tag{3.2}$$

It is important to note that the C_T and C_P can be estimated with the help of C_{Pr} and C_{LT} as per the torque mechanism explained in Section 2.1. However, this methodology is quite complicated experimentally, therefore, the approach of torque measurement using mechanical dynamometer setup has been adopted in the present investigations.

3.1.3 Error Analysis

The experimental uncertainty analysis is carried out by the method of error propagation considering the accuracy values of different measuring instruments provided in Section 3.1.1. Using Eqs. (3.3) and (3.4) (Moffat, 1988), the estimated fractional uncertainty for λ and C_P are ± 0.58% and ± 0.85%, respectively.

$$\left(\frac{\partial \lambda}{\lambda}\right) = \sqrt{\left(\frac{\partial U}{U}\right)^2 + \left(\frac{\partial N}{N}\right)^2} \tag{3.3}$$

$$\left(\frac{\partial C_P}{C_P}\right) = \sqrt{\left(2\frac{\partial U}{U}\right)^2 + \left(\frac{\partial \lambda}{\lambda}\right)^2 + \left(\frac{\partial T}{T}\right)^2} \tag{3.4}$$

Alternatively, by repeating the experiments and measurement procedure (Section 3.1.2) at least 6 to 7 times, the standard deviation of sample is calculated. The standard error of means is then estimated using student's *t* test within 95% confidence level. For instance, the mean values of

C_P along with standard error of means in the form of error bars are presented in Fig. 3.6 for the sea-pen bladed and the semicircular bladed rotors, without the end plates at $Re = 1.2 \times 10^5$. In this case, the maximum length of the error bar obtained is ±0.37%, which is lower enough compared to theoretically estimated values through Eqs. 3.3 and 3.4. It is observed from Fig. 3.4 that the performance difference between both the rotors is sufficient enough since their error bars are not overlapping. Therefore, the estimated mean values of C_P for the sample can be considered to compare the power characteristics of two different rotors. This approach is implemented in the current research work to present the experimental data of rotor performance.

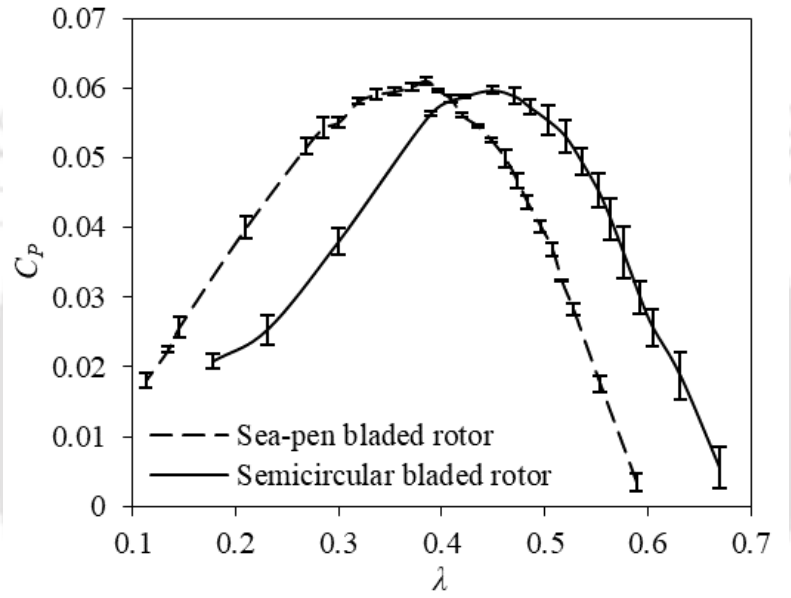

Figure 3.6 Mean C_P with error bars at $Re = 1.2 \times 10^5$

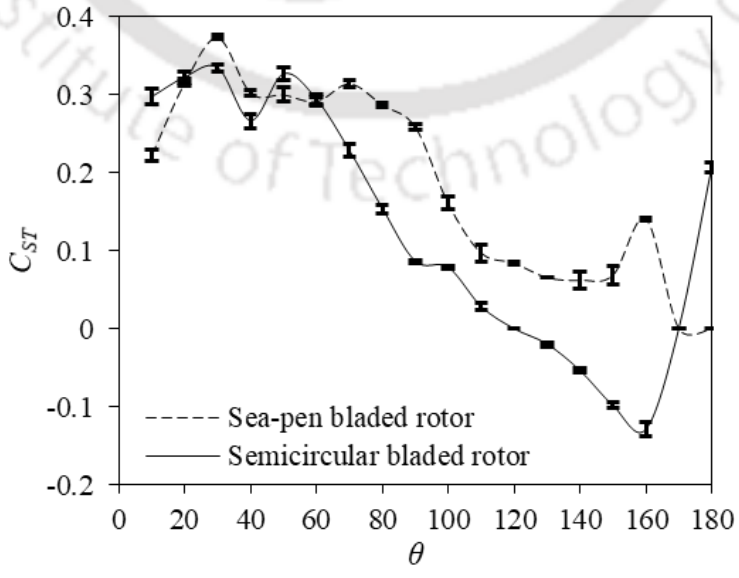

Figure 3.7 Mean C_{ST} with error bars at $Re = 1.2 \times 10^5$

Similarly, for starting torque characteristics, the experiments and measurement procedures (Section 3.1.2) at each θ are repeated multiple times to estimate the standard deviation and mean of the sample. The standard error of means within 95% confidence level is then estimated. As an example, the mean values of C_{ST} corresponding to θ besides the standard error of means in the form of error bars are plotted in Fig. 3.7 for $Re = 1.2 \times 10^5$. It can be observed that the error bars of C_{ST} trends corresponding to sea-pen and semicircular blades are not overlapping. Therefore, the average values of C_{ST} can be considered to compare and differentiate the C_{ST} characteristics of the rotors. This approach is adopted to present the experimental C_{ST} results in this thesis.

3.1.4 Blockage Correction

To assess the effect of blockage on the Savonius rotor performance, the blockage correction approaches such as *Pope* and *Harper*, and *Maskell* methods are usually implemented (Ross and Altman, 2011; Siram et al., 2022). Recently, Ross and Polagye (2020) reviewed different blockage correction techniques and suggested that the *Maskell* method should be implemented in case of bluff bodies like the Savonius rotor since the other blockage correction techniques based on the axial momentum theory are not capable in this case. Therefore, both the aforementioned blockage correction techniques are utilized for the present study. The blockage correction calculations for *Pope* and *Harper* method are executed using Eqs. 3.5 through 3.9. The corrected velocity (U_C) expressed in Eq. 3.7 is used to estimate corrected λ (Eq. 3.8) and corrected C_P (Eq. 3.8). This method diminishes the performance effectively.

$$\text{Blockage ratio} = \frac{A}{A_{wt}} \tag{3.5}$$

where, A and A_{wt} are the areas of rotor and wind tunnel test section, respectively.

$$\text{Correction factor } (\varepsilon_t) = \frac{1}{4}\text{Blockage ratio} \tag{3.6}$$

$$\text{Corrected velocity } (U_c) = U(1+\varepsilon_t) \tag{3.7}$$

$$\text{Corrected } \lambda = \left(\frac{U}{U_C}\right)\text{Uncorrected } \lambda \tag{3.8}$$

$$\text{Corrected } C_P = \left(\frac{U}{U_C}\right)^3 \text{Uncorrected } C_P \tag{3.9}$$

For implementing *Maskell* blockage correction method, the velocity correction correlations corresponding to different values of the blockage ratios are usually used (Alexander and

Holownia, 1978). For the present case, the appropriate velocity correction expressed in Eq. 3.10 is used to estimate the corrected rotor performance.

$$\text{Corrected velocity } (U_c) \approx 1.2U \tag{3.10}$$

The blockage corrected values of C_P at $Re = 1.2 \times 10^5$ for sea-pen blade along with uncorrected values are plotted in Fig. 3.8. It can be observed that the highest drop in C_P values is in the case of blockage correction by *Maskell* method followed by the *Pope* and *Harper* method. Whether or not the blockage correction is applied to the power characteristic, the relative performance trend between the sea-pen and the semicircular bladed rotors remains unchanged.

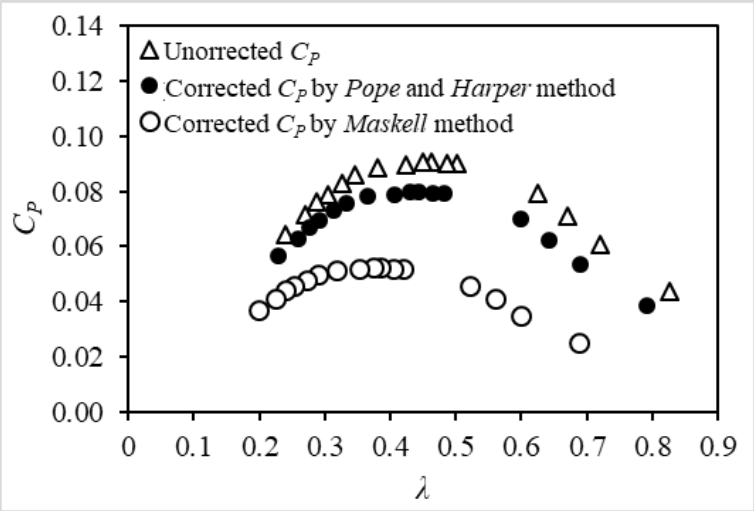

Figure 3.8 Blockage corrected values of C_P for sea-pen bladed rotor at $Re = 1.2 \times 10^5$

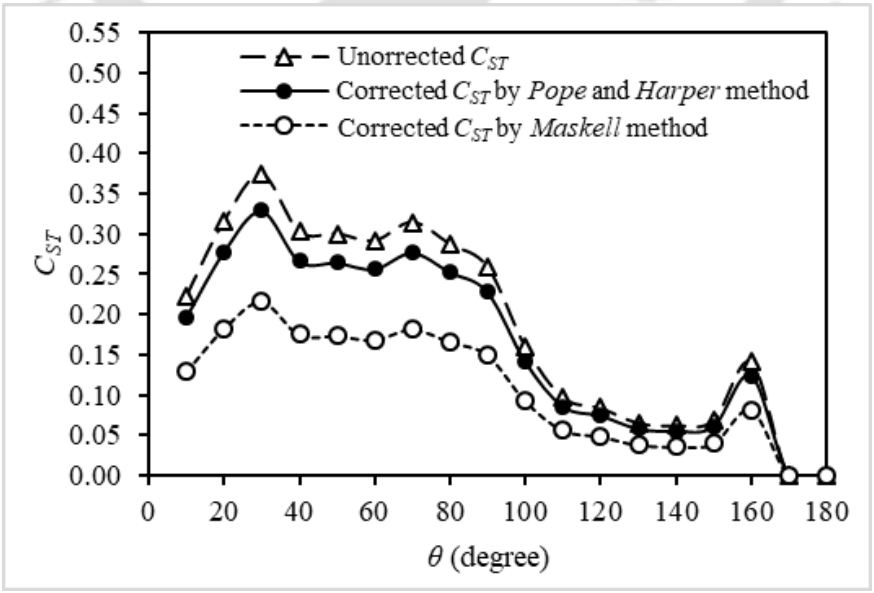

Figure 3.9 Blockage corrected values of C_{ST} for sea-pen bladed rotor at $Re = 1.2 \times 10^5$

A similar methodology can be also implemented in case of C_{ST} vs. θ characteristics. However, the corrected values of C_{ST} are calculated by Eq. 3.11. The blockage corrected values of C_{ST} at $Re = 1.2 \times 10^5$ for sea-pen blade along with uncorrected values are plotted in Fig. 3.9. Identical to the C_P, the highest drop in C_{ST} values is in the case of blockage correction by *Maskell* method followed by the *Pope* and *Harper* method.

$$\text{Corrected } C_{ST} = \left(\frac{U}{U_C}\right)^2 \text{Uncorrected } C_{ST} \tag{3.11}$$

3.2 Numerical Setup

The computational investigation is primarily carried out to know how the alteration in the fluid flow structure caused by blade design modification improve the rotor performance. In addition to that, performance comparison (C_P vs. λ) between novel sea-pen and semicircular bladed rotors can be carried out to get an estimation before conducting actual experiments. In order to know how the novel blade shape improves the performance, the computational values of C_{Pr} over blade surfaces are required to calculate C_{LT}. This procedure is expensive in terms of experimental setup and investigation. Therefore, it is essential to form computational setup.

The cross-section of the blades remains consistent throughout the height of the rotor, therefore, the 2D planer simulations based on finite volume method are performed to investigate the rotor performance numerically in commercial software *Ansys Fluent* (Ansys, 2021). Such 2D simulations usually overestimate the rotor performance as compared to that of 3D (three dimensional) simulations due to ignorance of the height, however, the former one is computationally less expensive and less time consuming (Roy and Saha, 2013a). Such overestimation of the rotor performance in the 2D simulation as compared to experimental values has been observed not only in the *Ansys Fluent* but also in other programming tools and in-house codes developed for different wind turbine models (Bangga et al., 2020; Franchina et al., 2019; Satrio et al., 2018). Quantitatively, Bangga et al. (2020) showed that the FLUENT and CFD TAU code overestimate the C_P values of HAWT up to 1.5 to 2 times as compared to the experimental values, even though 3D numerical domain is used. Similarly, Satrio et al. (2018) reviewed various findings on this aspects and documented the approximate overestimation of 70 % to 220 %, besides reporting overestimation of 70 % in C_P based on their own numerical findings. Moreover, it was recommended that such simulations can still be considered to evaluate relative performance trend of different turbines despite the overestimations.

Further, these simulations are widely considered since they can provide the insight of underlying phenomenon and also provide the precise trend for the Savonius rotors (Rathod et al., 2019; Roy and Saha, 2013a). Considering these advantageous traits, the 2D simulations have been carried out in the present investigation. The rotor designs presented in Sections 4.4 and 5.2 are used to construct the computational domains. The values of C_T and values of different fluid parameters such as C_{Pr} and C_{LT} are the outcomes of the present computational study.

3.2.1 Computational Domain and Boundary Conditions

The overall 2D computational domain is split into two parts *viz.* rotating circular domain and surrounding stationary rectangular domain as shown in Fig. 3.10. The rotating mesh domain is located slightly off to left side of the rectangular mesh domain in order to grant more mesh area to downstream wake of the rotor. A 2D pressure-based solver of *FLUENT* is used to simulate the present transient problem. The $k-\omega$ SST (shear stress transport) model is chosen because of its capability of solving unsteady fluid flow problems (Alom et al., 2021; Bangga et al., 2020; Edwards et al., 2012). This turbulence model utilizes the combination of original $k-\omega$ and $k-\varepsilon$ turbulence models for viscous laminar boundary layer region and turbulent boundary layer or wake regions, respectively.

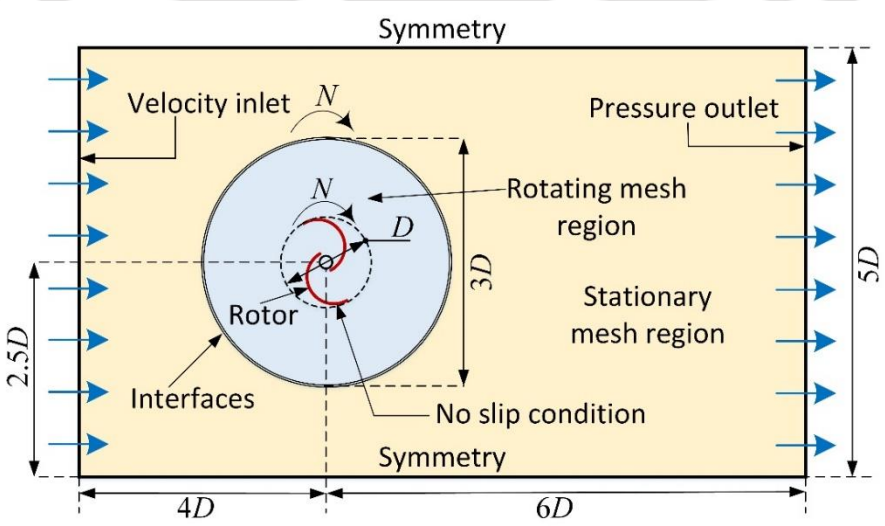

Figure 3.10 2D computational domain and boundary conditions

The second-order scheme is used to solve the discretized spatial terms in the governing equations. Similarly, the discretized temporal terms are solved by second-order fully implicit scheme. The residual criterion for the discretized terms is set as 10^{-3} for the simulations. In order to couple the pressure and velocity terms, the SIMPLE (semi-implicit method for pressure-linked equations) algorithm is preferred, which provides a better solution stability.

The suitable boundary conditions are then assigned to different domain boundaries as depicted in Fig. 3.10. The inlet boundary condition is set as constant velocity magnitude with its direction oriented perpendicular to the inlet boundary, and having turbulence intensity of 1% . The outlet boundary condition is chosen as pressure-based outlet with pressure value equated with atmospheric pressure. No slip boundary condition is provided on the walls of rotor and shaft. Rotating motion criteria is provided to the rotor, shaft and rotating circular mesh zone with values equal to N corresponding to given λ. The symmetry boundary condition is set on top and bottom edges of rectangular zone to impose the zero normal velocity gradient.

To finalize the dimensions of rotating and stationary mesh zones, the domain independence test is conducted (Lua et al., 2018; Satrio et al., 2018; Sun and Bhushan, 2012). As shown in Fig. 3.11, multiple mesh domain sizes are tested computationally at Re = 1.06 × 10^5 and λ = 0.6, and their C_T values are compared. The notation of the overall domain dimensions (e.g., *1D x 3D x 6D*) is in the form of 'diameter of rotating mesh region × width of stationary mesh region × length of stationary mesh region'. When the overall domain size is increased from *3D* × *5D* × *10D* to 5*D* × *7D* × *14D*, the change observed in the values of C_T is merely +0.37%. Therefore, the domain size *3D* × *5D* × *10D* is found appropriate in terms of its negligible dependence on increased size of the domain and computational cost. This methodology of domain independence test has been implemented in past studies (Lua et al., 2018; Satrio et al., 2018; Sun and Bhushan, 2012).

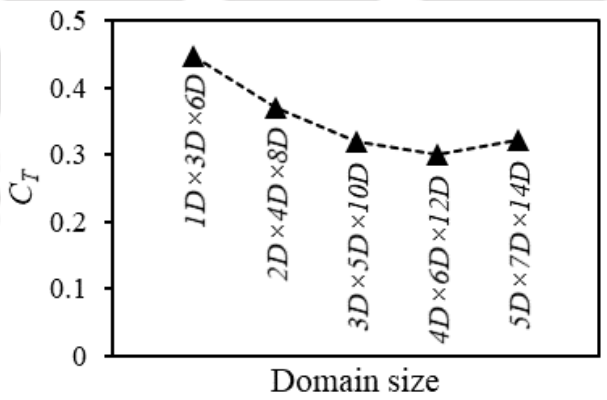

Figure 3.11 Domain independence test for semicircular blade at Re = 1.06 × 10^5 and λ = 0.6

3.2.2 Meshing

Both the mesh regions, *viz.*, rotating and stationary, possess an unstructured triangular mesh. Such mesh structure is capable of discretizing complex geometries, implementing hybrid mesh, mesh refinement and adaptation wherever necessary in the domain (Versteeg and Malalasekra,

2009). The sliding mesh technique is incorporated to facilitate the rotation of the rotor. Mesh interface is set between the outer and inner peripheries of the rotating and stationary mesh domains, respectively (Fig. 3.12a). In order to capture the boundary layer flow on blade surfaces and to calculate the surface dependent quantities effectively, inflation layers are formed as shown in Fig. 3.12(b). A thickness of the first layer of inflation is set as 4×10^{-5} m in such a way that the y^+ value can be maintained below unity (Sharma and Sharma, 2016), which is ≈ 0.976 for the present case. The total of 15 inflation layers with 20% growth rate are sufficient to cover the entire boundary layer-based velocity gradient over the blade surface.

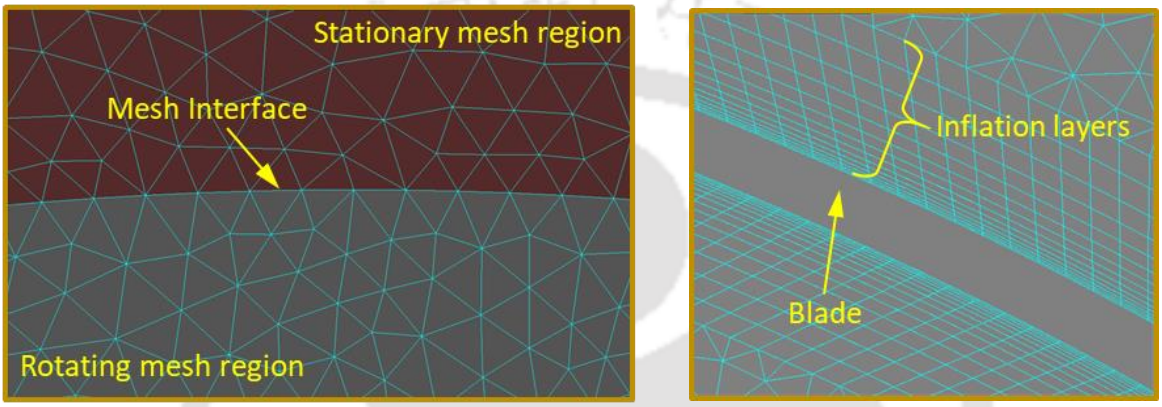

(a) Mesh interfacee **(b)** Inflation layers

Figure 3.12 Special mesh features of 2D mesh domain

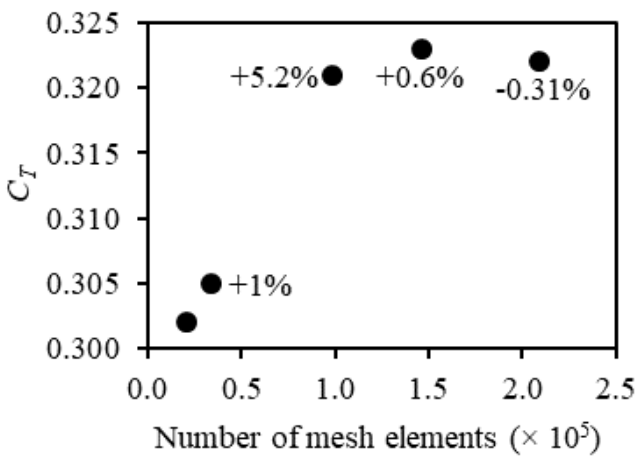

Figure 3.13 Grid independence test for semicircular bladed rotor at $Re = 1.06 \times 10^5$, $\lambda = 0.6$

Furthermore, the grid independence test is carried out to check the variability of simulated C_T on the number of grid elements. At some point, no significant change in C_T is observed even if the meshing is made finer. Such mesh structure is selected from mesh independence trend (Fig. 3.13) corresponding to semicircular bladed rotor for flow of $Re = 1.06 \times 10^5$ and non-

dimensional rotational speed of $\lambda = 0.6$. As per the figure, increment and decrement gained in value of C_T of any successive mesh size with respect to that of preceding one is shown in form of percentage. The percentage change in the values of C_T for mesh elements $\approx 1 \times 10^5$ and above with respect to the preceding mesh sizes, are minimal as labelled in the plot of Fig. 3.13. Based on this, a suitable mesh size is selected for the simulations and its quality is presented in Table 3.1. The present approach of grid independence test has been widely implemented in archieved literature of diverse scintific domains (Chu, 2016; Lua et al., 2018; Mohammadi et al., 2018; Roy and Ducoin, 2016).

Table 3.1 Mesh details for rotating and stationary mesh regions

Quality aspect	Rotating region	Stationary region	Overall region
Number of elements	58172	87702	145874
Maximum node length	3×10^{-3} m	10^{-3} m	–
Aspect ratio			
Minimum	1.001	1.0002	1.0002
Maximum	26.63	2.29	26.63
Average	2.59	1.18	2.05
Skewness			
Minimum	4.69×10^{-8}	7.18×10^{-8}	7.17×10^{-8}
Maximum	0.91	0.52	0.91
Average	9.94×10^{-2}	4.94×10^{-2}	8.01×10^{-2}
Orthogonal quality			
Average	0.95	0.96	0.96
Element quality			
Average	0.90	0.96	0.94
Growth rate on inflation layers	1.2	–	–

3.2.3 Grid Convergence

After conducting the mesh refinement and mesh independence tests (Section 3.2.2), it is essential to perform the grid convergence test for discretization error estimation. Thereby, the Richardson's extrapolation method is implemented for the present problem. The procedure suggested by Celik et al. (2008) in the form of a brief note published in the *ASME Journal of Fluids Engineering*, is followed.

Table 3.2 Specifications of grids at $Re = 1.06 \times 10^5$ and $\lambda = 0.6$

Mesh i	Number of elements	Number of nodes	h_i (mm)	$RF_{(i+1)(i)} = \frac{h_{i+1}}{h_i}$	$f_i = C_T$	$GCI_{(i+1)(i)}$
1	209562	108547	$h_1 = 3.861$	–	$f_1 = 0.322$	–
2	65977	36537	$h_2 = 6.882$	$RF_{21} = 1.782$	$f_2 = 0.314$	$GCI_{21} = 0.062$
3	20584	13644	$h_3 = 12.121$	$RF_{32} = 1.793$	$f_3 = 0.302$	$GCI_{32} = 0.095$

As the Richardson's extrapolation method deals with three mesh structures/grids (very fine, fine, and coarse), the same (Table 3.2) are selected from all the grids generated during the grid independence test (Fig. 3.11). As the unstructured grid type is preferred for the present numerical domain, the representative mesh sizes (h) for each grid are calculated using Eq. 3.12 (Celik et al., 2008) and listed in Table 3.2. Thereafter, the mesh refinement factor (RF) is calculated for each consecutive pair of coarse and fine grids. It is usually recommended that $RF > 1.3$ should be obeyed for the selected triad of grids based on empirical consideration (Celik et al., 2008). In the present case, the condition is fulfilled since the values of $RF_{21} \approx RF_{32} \approx RF \approx 1.78$. It is important to clarify that an extra simulation (with elements 65977) was performed in order to set $RF \approx 1.78$, as the former set of the grids (Fig. 3.11) was prone to $RF < 1.3$. This also helps to eliminate an abrupt transition of mesh elements in the range of 0.5×10^5 to 1×10^5.

$$h_i = \left[\frac{1}{N}\sum_{j=1}^{N}\left(\Delta A_j\right)\right]^{1/2} \approx \frac{\text{Total area of numerical domain}}{N} \tag{3.12}$$

where N = total number of mesh cells, ΔA_j = area of the j^{th} cell, and h_i = representative cell size of i^{th} mesh structure

Using the uniform value of $RF \approx 1.78$ over the grid triad (Table 3.2), the apparent order of convergence (O_c) can be calculated using Eq. 3.13 (Celik et al., 2008; Eça and Hoekstra, 2014; Roache, 1994; Slater, 2011). As a result, the $O_c \approx 0.703$ is obtained that is under the acceptable empirical range of $0.5 \leq O_c < 2$, corresponding to the theoretical second-order method (Eça and Hoekstra, 2014). Therefore, the value of $O_c \approx 0.703$ is acceptable for the present case. Moreover, the estimated value of $R_d \approx 0.667$ (discriminating ratio) obeys the correlation of $0 < R_d < 1$ (Eça and Hoekstra, 2014). Therefore, both the values of O_c and R_d undoubtedly indicate the monotonic convergence in the grid set.

$$O_c = \ln\left(\frac{f_3 - f_2}{f_2 - f_1}\right) \Big/ \ln(RF) = \ln\left(\frac{1}{R_d}\right) \Big/ \ln(RF) \tag{3.13}$$

Where, the values of f_1, f_2, and f_3 are provided in Table 3.2

Considering the values of f_1, f_2, RF, and O_c, the exact numerical solution for $h \rightarrow 0$ (tends to) can be estimated using Eq. 3.14 (Roache, 1994; Slater, 2011). The estimated value of $f_{h \rightarrow 0}$ is equal to 0.338 for the current set of grids. Thereafter, the grid convergence index (GCI) between two consecutive grids is calculated by Eq. 3.15. Since three grids are used to carry out the convergence test, the value for the factor of safety equals to 1.25 is selected (Roache, 1994;

Slater, 2011). The calculated values for GCI_{21} and GCI_{32} are listed in Table 3.2. Using the estimated values of GCI_{21} and GCI_{32}, whether or not the asymptotic range of convergence is achieved by the present grid triad, can be checked with the help of Eq. 3.16. The result obtained by Eq. 3.16 is 1.025, which is approximately equal to the unity, it can be said that the numerical solution is well within the asymptotic range of convergence.

$$f_{h\to 0} = f_1 + \left(\frac{f_1 - f_2}{RF^{O_c} - 1}\right) \tag{3.14}$$

$$GCI_{(i+1)(i)} = \left(1.25\left|\frac{f_{i+1} - f_i}{f_i}\right|\right) \Big/ \left(RF^{O_c} - 1\right) \tag{3.15}$$

$$\frac{GCI_{32}}{RF^{O_c} GCI_{21}} \approx 1 \tag{3.16}$$

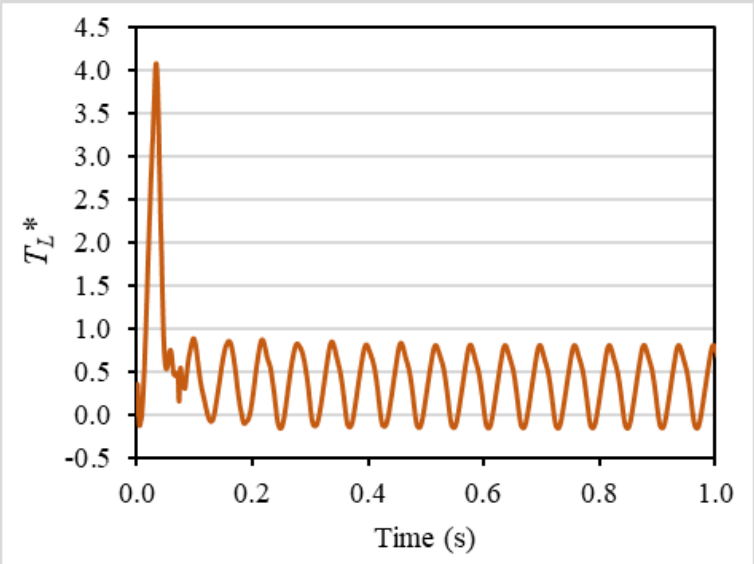

Figure 3.14 Variation of T_L* with time for sea-pen bladed rotor at Re = 1.06 × 10^5, λ = 0.934

Based on the results obtained, the exact value of C_T ($f_{h\to 0}$) is estimated to be 0.338 with an error band of 0.062 (value of GCI_{21}). To support this, the authors conducted a numerical simulation with mesh elements ≈ 456888 (approx. four times the mesh elements of the selected mesh structure as per Table 3.1). The value of C_T is obtained to be 0.336, which resembles the extrapolated value and does not show a significant deviation from the numerical results reported in the manuscript.

3.2.4 Validation

For the current transient problem, a time step is set in such a way that the rotor advances 1° per time step (Bangga et al., 2020). Sufficient number of time steps are ensured to reach the quasi-

steady solution of T_L*. For example, the variation of T_L* with respect to time for more than 10 revolutions of the sea-pen bladed rotor at Re = 1.06 × 10^5 and λ = 0.934 (Fig. 3.14) clearly shows the attainment of quasi-steady state. The time-averaged quantity of this variation of T_L^* gives value of overall C_T for the rotor.

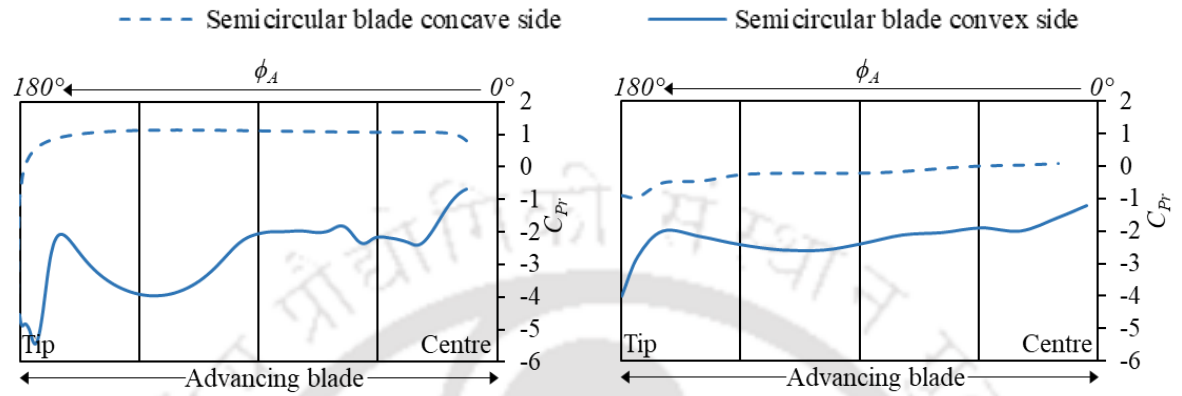

(a) Present simulation data **(b)** Reported experiment data (Fujisawa and Gotoh, 1994)

Figure 3.15 C_{Pr} distribution on advancing semicircular blade at θ = 45°, Re = 1.2 × 10^5 and $\lambda \approx \lambda_{Opt}$

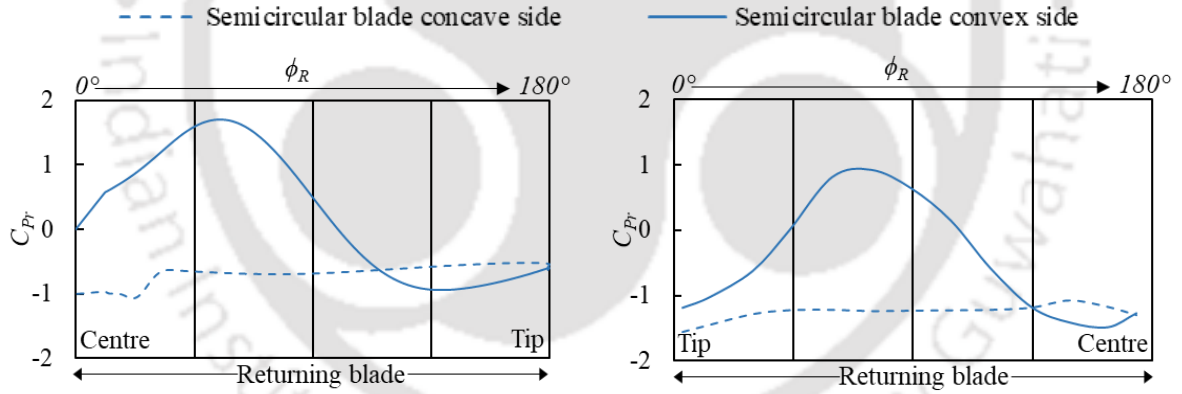

(a) Present simulation data **(b)** Reported experiment data (Fujisawa and Gotoh, 1994)

Figure 3.16 C_{Pr} distribution on returning semicircular blade at θ = 45°, Re = 1.2 × 10^5 and $\lambda \approx \lambda_{Opt}$

The present simulation setup is validated with the experimental findings of (Fujisawa and Gotoh, 1994). As C_{LT} and C_P are the derived quantities of C_{Pr} (Section 2.1), this validation is done in terms of C_{Pr} trends as shown in Figs. 3.15 and 3.16. The similarities observed between the simulated and experimental C_{Pr} trends are, (i) very low C_{Pr} at the tip of convex side advancing blade, (ii) very high C_{Pr} over $\phi_R \approx 45° - 90°$ of the returning blade convex side, (iii) almost consistent values of the C_{Pr} over concave side of both the advancing and the returning

blades, and others. Such validation process was followed in earlier studies (Rathod et al., 2019; Talukdar et al., 2022). Thus, the present numerical setup can be considered reliable for the extraction of the numerical fluid parameters.

3.3 Concluding Remarks

In this chapter, the experimental and numerical setups are elucidated and evaluated. It is important to note that the development, fabrication and the dimensions of the rotor models are not discussed in this chapter. This is because the bioinspired blade shape extractions and ensuing blade designs would require an adequate explanation of allied bioinspired phenomenon. Thereby, they are included individually in the next Chapters 4 and 5 rather than including in the present chapter.

Error analyses have shown that the error-bars representing the standard error of means of the experiments are not overlapping for both the C_P vs λ as well as C_{ST} vs θ trends. Therefore, the experimental setup can be considered reliable for the data collection. Likewise, the domain independence test, mesh independence test, and grid convergence test indicate that the selected mesh formation is dependable for the numerical solutions. The important recommendations reported in the literature are incorporated to develop the present numerical setup besides ensuring the reliability of the same.

Chapter – 4

Evolving a Novel Bioinspired Blade Shape Inspired From Orange Sea-Pen

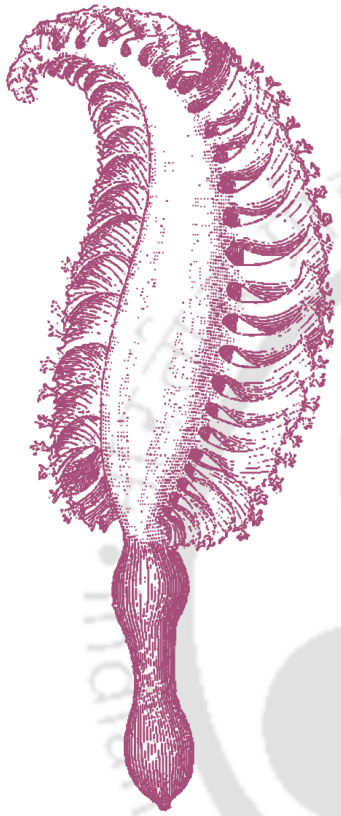

Chapter Layout:

Overview

This chapter documents the development of novel Savonius rotor blade inspired from the soft coral species named the Orange sea-pen (Ptilosarcus gurneyi). The chapter starts with comparative analysis between the Savonius rotors and autorotors in the context of their flow physics and torque mechanisms. As an outcome, principal flow conditions are deduced that can ensure the performance improvement if obeyed properly. The analogy is then established in the chapter between the proposed principal flow conditions and the feeding mechanism of the sea-pen. The experimental evaluation of the novel sea-pen bladed rotor is then reported in comparison with the conventional semicircular bladed rotor. Analysis of numerical findings is elucidated to check whether or not the principal flow conditions are fulfilled.

4.1 Background

As briefly mentioned in Section 2.5, the majority of research articles that deal with finding the optimum blade shape, have provided *posteriori* flow physics analysis to explain the performance improvement and to complement the experimental observations. However, such a *priori* analysis of the flow structure and blade design approach are not yet available. This knowledge is desirable to provide the necessary prerequisites to enhance the performance of the novel blade shape or infer the performance based on the blade shape without any actual experimentation. In order to address this niche, this chapter is begun with carrying out a concise literature review on the flow physics of the rotating Savonius rotor, and then, if possible, search for analogous phenomenon that deals with prevalent force and torque generating mechanisms. Some of these phenomena are, for example, autorotation, propulsion by flapping foils (Anderson et al., 1998; Arfaoui et al., 2021), flag fluttering, vortex induced vibrations, and others (Hans J Lugt, 1983). One common attribute in these phenomena is that the force experienced by the body (thrust or drag) is due to the acceleration-deceleration of the body together with simultaneous vortex generation with its subsequent shedding. Similarly, the rotating Savonius rotor can be considered as the accelerating-decelerating body, since each *dl* length of blade changes its orientation with respect to free stream fluid flow. Another important point is that the Savonius rotor is mainly a drag-based rotor, and accordingly, it is rather logical to emphasize on drag force maximization strategies (for advancing blade) than the traditional drag minimization strategies (for returning blade). Such strategies are widely adopted by natural organisms as compared to man-made aerodynamic architectures (Vogel, 1994).

With this in background, the chapter is commenced with the search of a suitable analogy for the torque mechanism of the Savonius rotor with that of other well established and studied flow phenomena. Based on the insight gained through this analogy, it is aimed to derive principal flow conditions which can help either to improve or to infer the rotor performance based on blade shape in *priori*. Thereafter, attempts are made to explore suitable bio-inspired techniques that follow the aforementioned principal conditions and can display promising indications of performance improvement

4.2 Savonius and Analogous Rotors

4.2.1 Flow Physics of the Savonius Rotor

The literature on the flow physics of the Savonius rotor is rather scanty as compared to experimental and numerical performance evaluation study. In this context, *Fujisawa et al.*

explained the torque mechanism of the Savonius rotor with the help of C_{LT} and C_{Pr} by investigating flow structure around the rotating rotor experimentally (Fujisawa, 1992; N. Fujisawa and Gotoh, 1992; Modi and Fernando, 1989). The flow field around the rotor is divided into three major regions (Fig. 4.1) *viz.*, stagnation regions at upstream of the advancing and returning blades, Coănda flow region and pressure recovery region. They remain more or less consistent for the entire rotation of the rotor, but especially more prominent over the range of $\theta = 0° - 45°$. In the Coănda flow region, the fluid flow follows the curvature of the advancing blade being deviated towards the pressure recovery region at the downstream of the returning blade. As θ increases above 45°, the nascent vortices which are originated due to flow separation, remain attached and then they detach beyond $\theta = 135°$ in the form of developed tip vortices as shown in Fig. 4.1. The sense of rotation is clockwise and counter-clockwise for vortices shed from the advancing and returning blades, respectively (Dobrev and Massouh, 2011). It is very important to note that the overlap length (e) and the gap length (s) also influence Coănda and pressure recovery regions at a miniscule level.

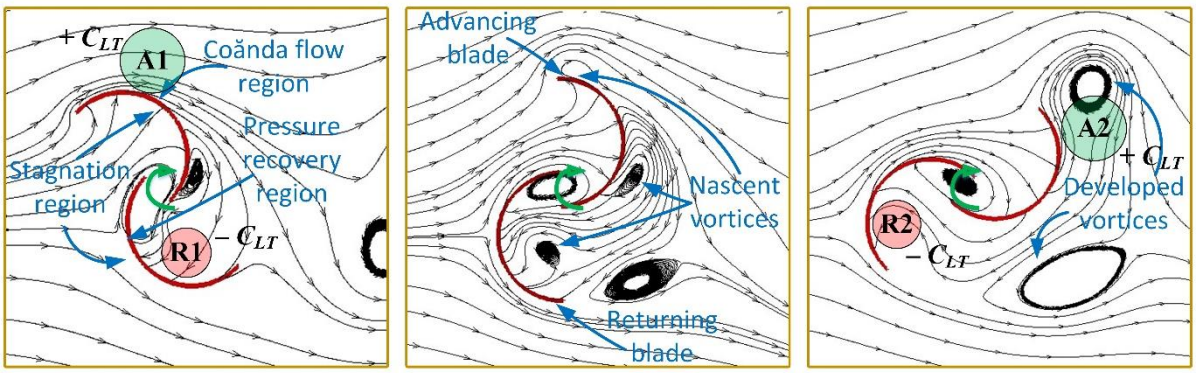

Figure 4.1 Flow field of rotating semicircular bladed Savomius rotor

The flow regions mentioned above actually govern the distribution pattern of C_{Pr} and C_{LT} over the blade surfaces. The stagnation regions at the upstream sides of both the blades generate high C_{Pr} values. On the other hand, the Coănda flow region creates areas (denoted by A1-A2 in Fig. 4.1) at downstream of the advancing blade dominated by much lower C_{Pr} values. Similarly, the areas R1-R2 with low C_{Pr} are created at downstream of the returning blade. All these regions, as illustrated in Fig. 4.1, are observed to be consistently present in the range of $\theta = 45° - 135°$. It has been observed that the low-pressure regions (A1-A2) remain more stronger than the regions R1-R2, especially towards tip of the advancing blade (Fujisawa, 1992; Fujisawa and Gotoh, 1994; Rathod et al., 2019). As a result, the magnitude of positive C_{LT} distributed on the advancing blade becomes higher than that of negative C_{LT} on the returning

blade, thereby initiating the rotational motion. In summary, it can be stated that the low C_{Pr} region (A1-A2) at downstream of the advancing blade is the key factor behind the torque mechanism of the rotor.

Whenever the performance increment or decrement is obtained in a modified or in a novel blade shape as compared to that of a semicircular blade, a significant change of C_{LT} distribution (either improvement or deterioration) at A1-A2 regions is observed. On the other hand, such changes at R1-R2 regions are insignificant. This portrays the significance of low C_{Pr} regions (A1-A2) at low θ values and attached vortices at high θ values in the process of rotor torque enhancement (Rathod et al., 2019; Roy and Ducoin, 2016; Talukdar et al., 2022). Based on the aforementioned discussion on flow physics, it can be opined that the dynamics of the Savonius rotor seems quite similar to the 'Autorotation' phenomenon, as reviewed in Section 4.2.2.

4.2.2 Flow Physics of the Autorotors

Historically, the origin of the Savonius rotor is often linked with the phenomenon of autorotation (Iversen, 1979). It is defined as the continuous rotation of the bodies in a parallel flow without any supply of external energy. The Savonius rotor is classified under 'pseudo-autorotation' phenomenon since its geometrical shape (concave and convex blades) naturally facilitates rotation as soon as it is released unlike in pure autorotation (*e.g.* rotation of flat plate or thin elliptical cylinder) which requires an initial impulse (H J Lugt, 1983).

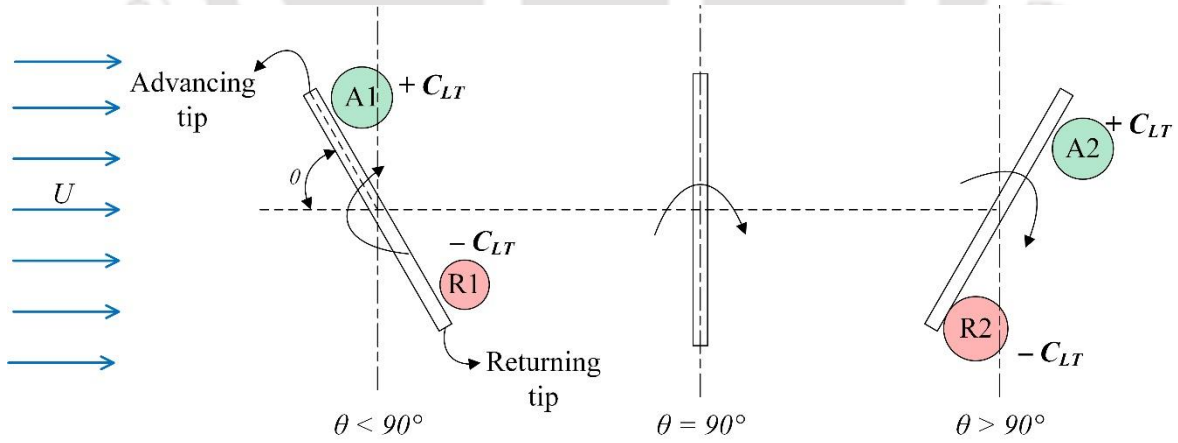

Figure 4.2 Flow field of autorotating flat plate

It is important to mention that the inertia is a very important factor for pure autorotation because of similarity in the shapes of the advancing and the returning edges/blades. On the other hand, it can be neglected for pseudo-autorotation (such as the Savonius rotor) since its advancing and returning blades possess two distinct drag shapes, namely, the concave and convex shapes,

respectively. Once the autorotation is started, the torque or power can be extracted from pure autorotors (*e.g.* autorotating flat plates, elliptical cylinders, airfoils and others) as well as from pseudo-autorotors (*e.g.* Savonius rotor) (Fernandes and Rostami, 2015; Smith, 1971).

According to Riabouchinsky (1935), in order to successfully autorotate a flat plate (Fig. 4.2), the low C_{Pr} region (A1) at $\theta < 90°$ position should be stronger than R2 at $\theta > 90°$. This condition is very essential for pure autorotation since the advancing and the returning edges/tips have identical shapes, however, not so essential for the pseudo-autorotation (like Savonius rotor) because of dissimilar advancing and returning blade shapes. Further, the low C_{Pr} regions (A1-A2) should always be stronger than their respective counterparts (R1-R2) at every θ position, maintaining the magnitudes of positive ΣC_{LT} at the advancing edge higher than that of negative ΣC_{LT} at the returning blade. Since the autorotating flat plate possesses sharp edges, the flow over the advancing edge cannot remain attached for a long duration and hence the low C_{Pr} regions (A1-A2, R1-R2) at lower θ values are transformed into the attached vortices as θ increases gradually during the rotation. Corroborating observations are also reported and explained numerically for the autorotation of very thin elliptical cylinder (approximately a flat plate) (Lugt, 1980; Lugt and Ohring, 1977). It states that the crucial condition for the sustenance of the autorotation is the presence of strong attached vortex behind the advancing edge (analogous to A1-A2 of Fig. 4.2) during $\theta = 45° – 135°$ and earlier along with negligible vortex effect behind the returning edge. It is necessary to clarify that the aforementioned study was carried out at $Re = 200$, however, it has been reported that these observations and conditions can be extended for very high values of Re in the order of 10^4 (Iversen, 1979; Smith, 1971). In order to strengthen the attached vortices behind the advancing blade, the implementation of sharp edges is advisable according to Lugt (1980); Lugt and Ohring (1977) since it enhances the detachment of vorticity layer/tongue which then rolls up into the vortex (Lugt, 1980; Riabouchinsky, 1935). If the curvature at the tip is high, the attached vortex (low C_{Pr} region) behind the advancing blade becomes stronger. Thus, it indicates that the blade/edge shape can influence the low C_{Pr} region and the attached vortex behind the advancing blade.

4.2.3 Analogy Between the Savonius rotor and the Autorotor

The discussion on the flow physics of the Savonius rotor and autorotation (Sections 4.2.1 and 4.2.2) display striking similarities in terms of low C_{Pr} regions (A1-A2) at the downstream of the advancing blade/edge. Although this comparison between them is carried out only qualitatively. From the above discussion, two principal conditions in context of the Savonius rotor can be elicited as follows:

(1) The strength of low C_{Pr} region (A1-A2) and the attached vortex at downstream of the advancing blade is vital to sustain rotation.

(2) Blade shape and curvature can manipulate the strength of the low C_{Pr} region and attached vortex.

In order to improve the rotor performance, attributes of the condition-1 should be strengthened with the help of condition-2. Herein, the low C_{Pr} region together with stagnation region on the advancing blade enhances the drag force (strong wake) and the positive ΣC_{LT} distribution. This results into the deliberate increase in the drag force of the advancing blade, if the condition-2 is followed. As already mentioned at the end of the Section 4.1, the deliberate increase of drag can be found in the natural organisms, since the traditional aerodynamic problems are focused more on the drag reduction strategies.

Thence, an attempt has been made to study and review the field of bio-mechanisms which enhance the drag characteristics. The main focus is to find the natural organisms that possess the optimized drag enhancement qualities and follow the aforementioned two conditions. Based on such qualities, a novel Savonius rotor blade having performance superior to the conventional semicircular blade can be designed. This has led to delve deep into the field of marine organisms as discussed in the Section 4.3.

4.3 Bioinspired Drag Enhancement Techniques

Intentional use of high drag shapes is prevalent in the phenomenon known as 'Passive suspension feeding'. It is a particle capture mechanism adopted by sessile suspenser feeders such as gorgonian sea-fans (order: *Alcyonacea*), sea-pens (order: *Pennatulacea*) and many other octacorals and hexacorals (sub-phylum: *Anthozoa*) (Kumar, 2018). These passive suspension feeders, grounded on sea-floor (benthic), capture and then feed on suspended planktic organisms which are flowing with sea currents. The passive feeders rely on external currents to bring the suspended food particles in proximity instead of actively producing flow by themselves (Riisgård and Larsen, 2010). The small filters or tentacle like appendages (called the 'polyps') on such feeders catch food particles flowing through or in the vicinity of their bodies. Researchers attempted to explain the passive suspension feeding mechanism through a point of view of 'Aerosol filtration theory' that deals with the interaction between food particles and filters (Rubenstein and Koehl, 1977). It is noticed that whenever downstream vortices are induced at leeward/downstream surface of suspension feeder's entire body, the rate of particle capturing is improved (Shimeta and Jumars, 1991). In addition to that, the low C_{Pr}

created by the downstream vortices and stagnation at the upstream result into drag-inducing pressure drop across feeder's body, which drive the water current through the filter (Best, 1988). This is not only applicable at a scale of feeder's whole body but also for small filters/appendages/tentacles located on the surface of these feeders.

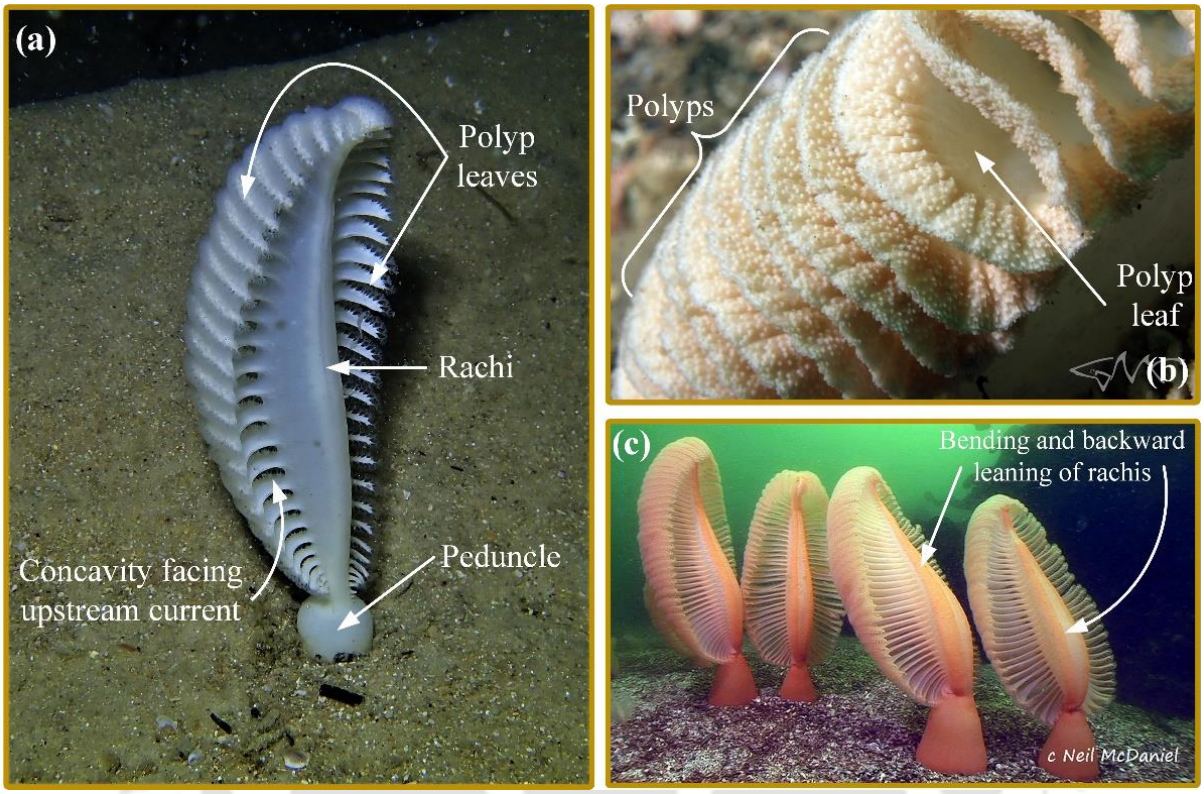

(a) The Great sea-pen (*Sarcoptilus grandis*) (Crossley, 2021) **(b)** Enlarged view of polyp leaves (Great sea-pen – *Sarcoptilus grandis*) (Strazzari, 2021) **(c)** Bending and leaning of rachis (Orange sea-pen – *Ptilosarcus gurneyi*) (McDaniel, 2006)

Figure 4.3 Morphology of a sea-pen

Food particles which cannot be captured at the upstream stagnation side are then entrapped inside circulation of downstream vortex and recaptured by polyps situated on downstream surface of the feeders. This results into a higher particle retention efficiency of the feeder. Such type of particle capturing and feeding mechanism is defined as 'vortex induced wake feeding', which bears a resemblance with the principal condition – (1) (Shimeta and Jumars, 1991). But the formation of downstream vortices is function of *Re* as expected, with characteristic dimension as the body width. The particle capture technique of 'vortex induced wake feeding' is exploited by many species of passive suspension feeders by deliberately orientating their polyps or appendages towards the downstream of their whole body to strengthen particle entrapment in vortices (Koehl, 1977; Leversee, 1976). Moreover, the feeders align their bodies perpendicular to the current direction in order to maximize particle capturing area and enhance

the vortex formation (Wainwright and Dillon, 1969). Interestingly, the bodies of the feeders also possess different body shapes/morphologies which are optimized for particle entrapment and suitable for given flow conditions or water currents as a result of evolutionary process. For example, the flat shaped bodies are found for the feeders belonging to habitats where oscillatory and tidal currents are widespread. Under the condition of persistent unidirectional water flow/currents, the bodies of such feeders develop curvature and align themselves such that its concavity faces upstream (Warner, 1977).

Such upstream facing concavities in the body shapes are most prominent in the leaves of sea-pens of family *Pennantulidae* (order: *Pennatulacea*) as shown in Fig. 4.3(a) (Best, 1988; Vogel, 1994). Based on initial examination of the shape, it looks very intriguing that the shape of concavity is not purely semicircular, but it is having high curvature at the tips/edges and low curvature in the central portion. The evolutionary process over a course of time might have equipped them with this type of shape in order to survive in the constant water currents and to capture food particles, again indirectly emphasizing on the principal condition – (2). A morphology of Sea-pens (family *Pennantulidae*) as shown in Fig. 4.3(a) consists of Rachis (a central support structure), Peduncle (anchored to sea-floor) and polyp leaves (leaf shaped arms protruding from rachis) (Williams, 2011). The filter elements or particle capturing appendages having small tentacles known as polyps (also called gastrozooids), are mainly congregated at downstream convex surface of sea-pen body spanning from edge to the rachis as shown in Fig. 4.3(b). This indicates that the polyps are taking advantage of 'vortex induced wake feeding' in downstream low C_{Pr} region, obeying the principal conditions – (1) and (2). During foraging, the concave leaves try to cover the area as much as possible to effectively capture food particles, and consequently, increasing the drag. Still the leaves try to maintain their concave shape by bending the rachis or slightly leaning backward to mitigate very high drag imposed by the flow as shown in Fig. 4.3(c). Thence, the shape of sea-pens' leaves (especially shape at convex side) seem to fulfil two principal conditions making it a potential candidate for a novel modified blade shape towards which the present investigation is aimed at.

One major difference emerged from the above discussion is that the aforementioned principal conditions are applicable only to rotating bodies, while the chosen sea-pen shape as a potential candidate, belongs to non-rotating quasi-static conditions. The conventional Savonius rotor is made up of two half-cylindrical blade shapes facing their concavity opposite to each other. In quasi-static flow condition with $Re = 10^4$–10^6, the values of C_D of the half-cylindrical blade shape are 2.3 and 1.2 with its concavity facing upstream and downstream, respectively (Horner,

1965). Nevertheless, it was deduced that the actual rotation of the Savonius rotor is possible due to aforementioned difference of C_D values. The same logic can be extended toward the implementation of bio-inspired blade design of the Savonius rotor. Comparably, the dragonfly wing is usually adapted to flapping motion and has an unsteady aerodynamics. Nevertheless, the researchers have attempted to study the lift characteristics of airfoil inspired from dragonfly wing in quasi-static conditions without applying the flapping motion to it (Sun and Bhushan, 2012). Influenced by this practice, the authors have checked the possibility of performance improvement in the bio-inspired blade shape (sea-pen leaf shape), although the sea-pen is adapted to the quasi-static flow conditions.

As a summary of Sections 4.2 and 4.3, the analogy between the Savonius rotor and the pure autorotation is established qualitatively and then two principal conditions are derived. Next, a suitable shape is explored by reviewing the biological organisms which obey the principal conditions. As a result, the shape of sea-pen leaf is found to be suitable for the present objective.

4.4 Bioinspired Blade Shape Development and Rotor Designs

Firstly, it is required to extract the shape and dimensions of the sea-pen leaf from the organism. The sea-pen species are found in variety of sizes, shapes and sea current velocities (Tudu et al., 2018). Among them, species such as Orange sea-pen (*Ptilosarcus gurneyi*) is one of the largest species that is well defined and studied morphologically. The orange sea-pen grows upto the length of 0.8 m with fully inflated polyp leaves extendeing upto 0.4-0.5 m above the benthic surface (Best, 1988; Shimek, 2011). The Sea-pens are usually found in habitats where velocity of water currents is in the range of 0.11 to 0.26 m/s. The same velocity range has been used by Best (1988) to study the passive suspension feeding and its influencing factors for orange sea-pen. Based on these dimensions and current velocities, the *Re* number lies in the range of 10^5–10^6 for larger sized sea-pens. For smaller sea-pens, the range falls into 10^2–10^4. It is important to clarify that these *Re* values are based on chracteristic length taken as length of rachis or width of sea-pen body, however, at a scale of individual small filter appendages or polyps, the *Re* values are in order of 10. By considering this, the size of the Savonius rotor should be such that its *Re* should fall in the aforementined range of higher values, thereby ensuring the similar regime of fluid flow. Moreover, similar design criteria are applicable for the Savonius hydrokinetic and wind turbines, making the calculated *Re* values reliable. Keeping this in mind, the *D* of the rotors is set at 0.25 m with U = 5, 6, 7 and 8 m/s, so that *Re* ranges from 0.7×10^5 to 1.2×10^5.

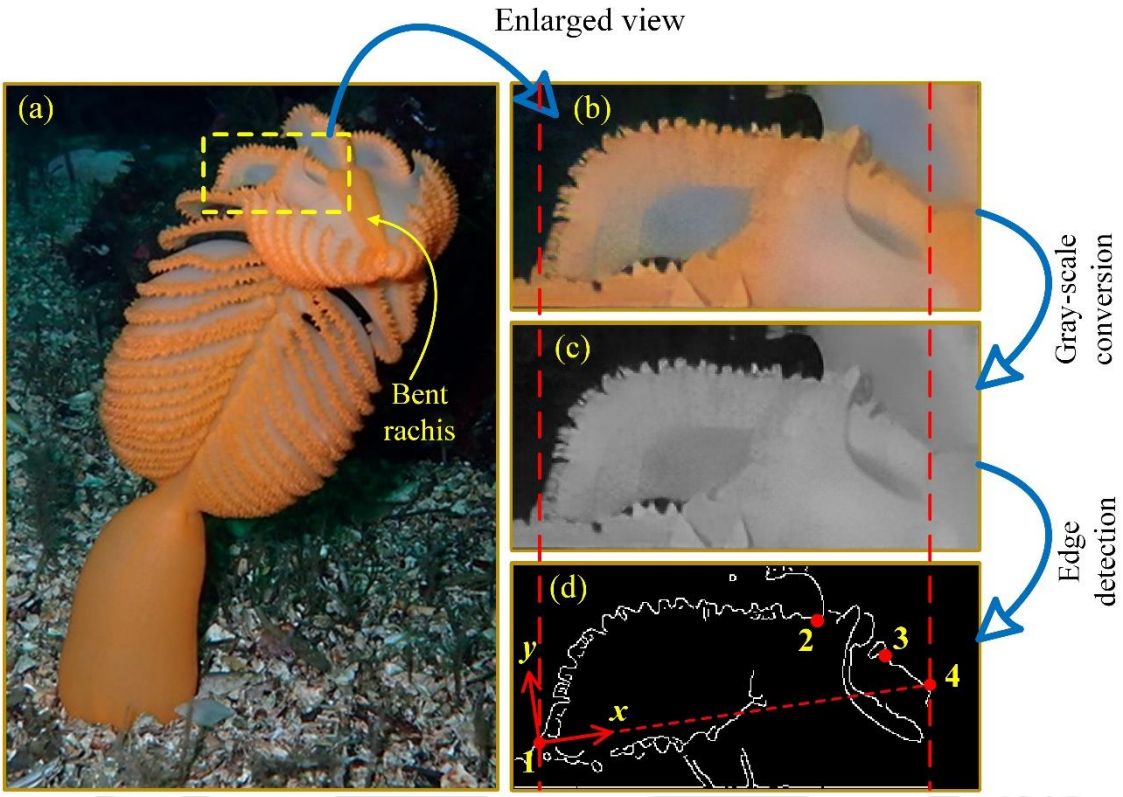

(a) Orange sea-pen (*Ptilosarcus gurneyi*) with bent rachis (Kathleen, 2020) **(b)** Planer enlarged view of polyp leaf **(c)** Gray scale image **(d)** Extracted edges of polyps and leaves with coordinate axes

Figure 4.4 Image processing and shape extraction process

As a next step, the shape of the sea-pen leaf is extracted from the photograph of orange sea-pen. Whenever the sea-pen is disturbed, it withdraws and contracts beneath the surface by deflating water from polyp leaves and rachis (Chimienti et al., 2018). The contracted sea-pen sometimes becomes three time smaller than the extended size. Hence it is not possible to measure the dimension and shape of the leaf, physically. Thus, the approximate planer view of leaf is obtained from an image (Fig. 4.4a) from *iNaturalist* (a citizen science platform), which is tagged as research grade material and catalogued in *GBIF* (global biodiversity information facility) (Kathleen, 2020). Such approach of extracting shape of bio-organism from image was adopted in many research articles. For example, shape extraction from the seed of Camphor tree (*Dryobalanops aromatica*) for the blade design of HAWT (Chu, 2016); and the shape extraction from the tubercles of Humpback whale (*Megaptera nouaeangliae*) to design leading edge of novel airfoil (Fish and Battle, 1995). Further, it is important to clarify that the shape tracing from an image of polyp leaf may not be accurate, still it can provide some degree of insight into its aerodynamics/hydrodynamics. For example, most of the reported investigations on hydrodynamic performance of humpback whale's flippers approximate scalloping pattern

of the tubercles as sinusoidal in nature instead of adopting exact contour of flipper, still it provides in depth insight into the performance improvement (Fish and Battle, 1995; Post et al., 2018; Skillen et al., 2015).

Thereafter, necessary image processing is carried out in *MATLAB 2021a* (*MATLAB Version (R2021a)*, 2021) in order to extract downstream edge of the polyp leaf (Fig. 4.4b). Firstly, the image is converted into gray-scale image, then its contrast is improved and the noise is reduced (Fig. 4.4c). The 'Canny edge detection' method with threshold value of 0.2 is implemented to detect the edge features by exploiting gray jump of the pixels at edges (Fig. 4.4d). The aspect ratios of the images are not changed during image processing. This method is often implemented in the field of bio-mimetics. As for example, Wang et al. (2020) implemented similar image processing method to extract shape of box-fish (*Ostracion cubicus*). On extracted edges, the outer-inner tips of the blade are marked as point 1 and 4, respectively, setting a straight distance between them equal to chord length of blade (d). The outer shape of the polyp leaf is visible in the form of periphery traced by points 1,2,3 and 4. The value of d is set as 0.125 m, equal to half of D. The 2D cartesian coordinate system is affixed to point 1 with x-axis coinciding the chord. The coordinates at the tips of each polyps are then extracted by digitizing (Fig. 4.4d), in order to trace the curve. Since the present investigation is aimed towards the performance of sea-pen blade, the resulting corrugated shape due to polyps is not considered. The set of xy-coordinates are then curve fitted with polynomial (R^2 = 0.9988) as expressed by Eq. 4.1. It is important to note that the overlapped edges of leaves cannot be detected *i.e.* edges between points 2 to 3 for the selected leaf, however, the polynomial fitting can approximately interpolate in this region. Hence the sea-pen blade represented by Eq. 4.1 is fabricated.

$$y = -3.3011x^6 + 13.935x^5 - 25.279x^4 + 23.802x^3 - 12.483x^2 + 3.3307x - 0.0068 \quad \text{where, } 0 < x < 1 \tag{4.1}$$

Once the xy-coordinates of the sea-pen curve are estimated, it can also be scaled up or down as per the need of rotor fabrication. A sea-pen curve is compared with other reported blade shapes *e.g.* Bach, arc-elliptical and semicircular, in Fig. 4.5 with 1:1 scale (Rathod et al., 2019; Roy and Saha, 2015). It is observed that the curvature of the sea-pen blade falls in between Bach type and arc-elliptical blades. The dimensions of both the sea-pen and semicircular bladed rotors are shown in Fig. 4.6. In order to accommodate a shaft (15 mm diameter) and an annular mounting sleeve (25 mm diameter), the d of both the blades are scaled up to 1.1 resulting into

137 mm, however, the overall shape, D and other dimensions are kept unchanged. This results into e = 25 mm ($e/d \approx 0.18$) as shown in Fig. 4.6. The D_O is set as 1.1 times D, which is equal to 275 mm diameter. The end plates are made in such a way that they can be removed whenever necessary. The turbine blades and end-plates are fabricated using 1.4 mm thick galvanized iron sheet. The height (H) of the rotors is fixed to 250 mm, maintaining the aspect ratio (H/D) equal to unity. It is important to clarify that the actual 3D shape of the sea-pen is not considered here to design the blade, instead the aforementioned 2D shape of the sea-pen leaf is extruded up to H = 250 mm with end plates attached to both the ends. Since the present study is focused primarily on examining the possibility of performance improvement of blade design based on the extracted 2D shape.

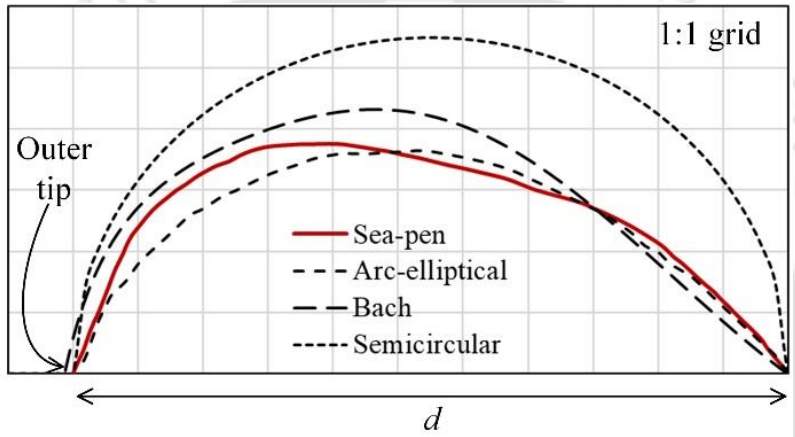

Figure 4.5 Comparison of sea-pen blade with other blades

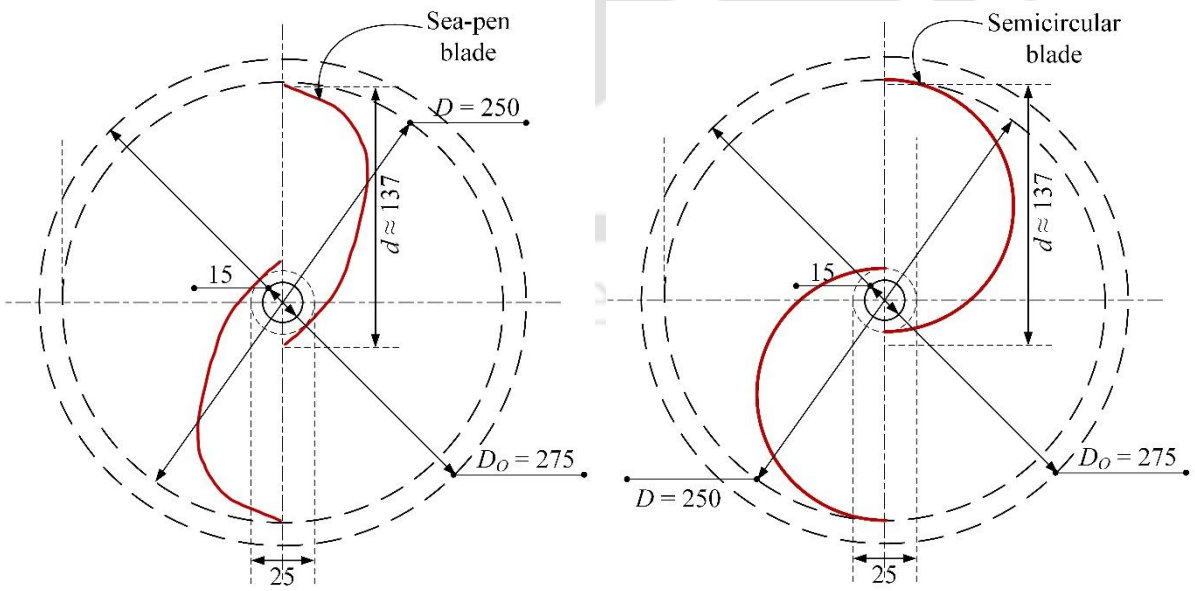

(a) Sea-pen bladed rotor **(b)** Semicircular bladed rotor

Figure 4.6 Dimensions of the rotors (in mm)

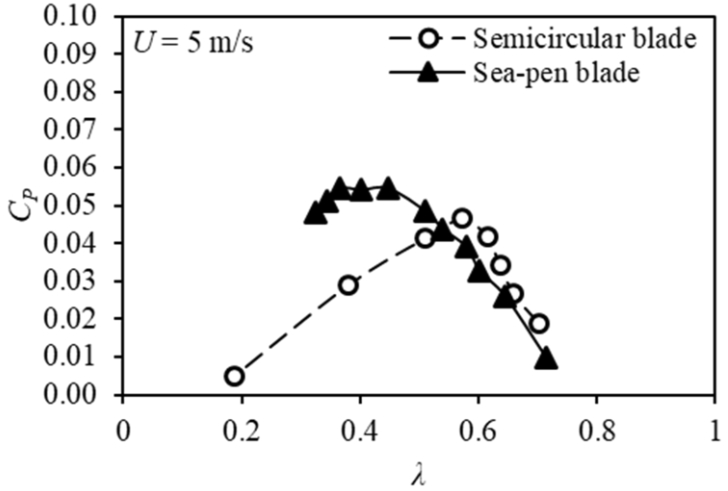

(a) $Re = 0.77 \times 10^5$

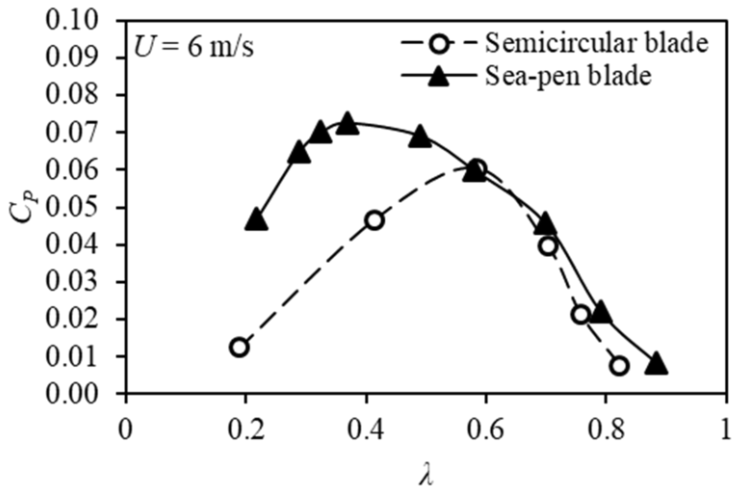

(b) $Re = 0.92 \times 10^5$

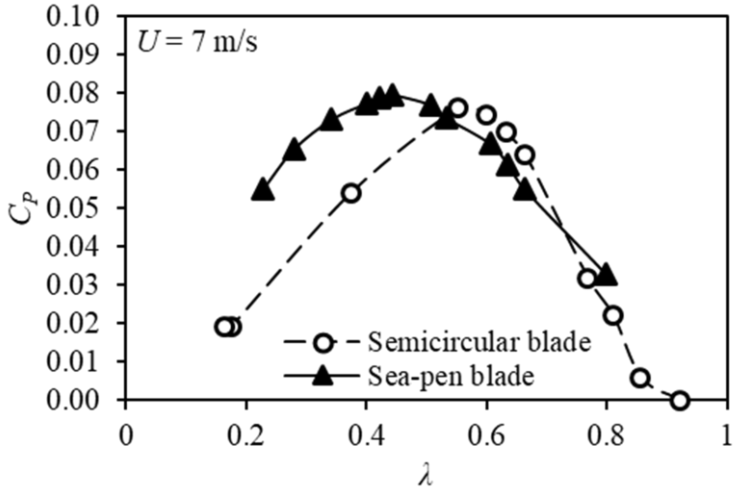

(c) $Re = 1.06 \times 10^5$

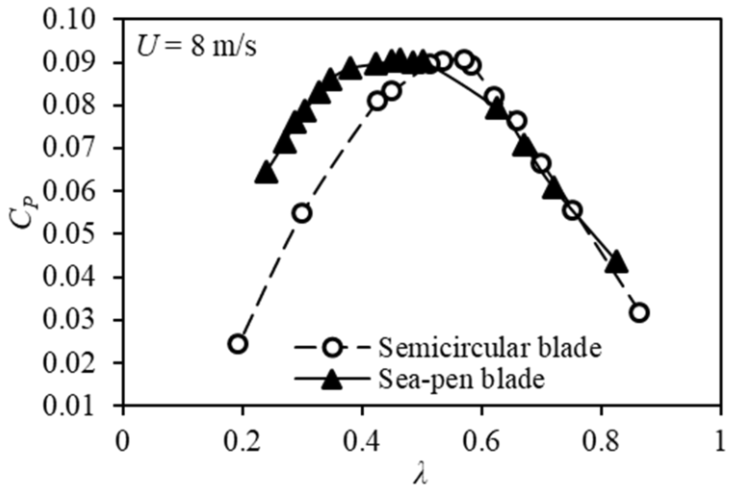

(d) $Re = 1.2 \times 10^5$

Figure 4.7 Experimental power characteristics of the sea-pen and the semicircular bladed rotors at different *Re* values

4.5 Results and Discussion

4.5.1 Load Characteristics of the Blades with End Plates

Initially wind tunnel experiments are carried out to assess the performance of the sea-pen bladed and semicircular bladed rotors. The performance trend in the form of C_P vs. λ curves for both the rotors with end plates at $Re = 0.77 \times 10^5$, 0.92×10^5, 1.06×10^5 and 1.2×10^5 is presented in Fig. 4.7. The performance characteristic curves usually show bell-shape that is consistent with different *Re* numbers and blade shapes as shown in Fig. 4.7.

Herein, C_P values are low at small λ values, thereafter, these values gradually increase and then drop with further increase of λ. It is evident from Fig. 4.7 that the sea-pen bladed rotor shows performance improvement as compared to semicircular bladed rotor, however, it is limited to λ values less than λ_{Opt} of the semicircular bladed rotor for each *Re* number. For lower *Re* numbers, increment of $C_{P,\,Opt}$ for sea-pen bladed rotor is also observed as compared to the semicircular bladed rotor as presented in Figs. 4.7(a) and (b). Quantitatively, an improvement of 17% and 21% in $C_{P,\,Opt}$ is attained for the sea-pen bladed rotor as compared to the semicircular bladed rotor at $Re = 0.77 \times 10^5$ and 0.92×10^5, respectively. On the other hand, no substantial difference of $C_{P,\,Opt}$ is observed among the rotors at $Re = 1.06 \times 10^5$ and 1.2×10^5. In all cases, λ_{Opt} of the sea-pen bladed rotor is observed to be shifted towards the left side of power characteristic curve as compared to that of the semicircular bladed rotor. In other words, the optimum performance of the sea-pen bladed rotor is achieved at lower λ values than those of the semicircular bladed rotor. At λ values higher than λ_{Opt} of the semicircular bladed rotor, the performance trend of the semicircular bladed rotor is slightly higher as compared to the sea-pen bladed rotor forming a intersection between C_P vs λ curves at an approximate location of λ_{Opt} of the semicircular bladed rotor.

Table 4.1 Optimum performance of rotors

Operating conditions		Types of blades			
		Sea-pen blade		Semicircular blade	
U (m/s)	*Re*	λ_{Opt}	$C_{P,\,Opt}$	λ_{Opt}	$C_{P,\,Opt}$
5	0.77×10^5	0.40	0.054	0.57	0.046
6	0.92×10^5	0.37	0.073	0.58	0.060
7	1.06×10^5	0.44	0.079	0.55	0.076
8	1.2×10^5	0.46	0.090	0.57	0.090

During experimentation, it is observed that the rotational speed of the semicircular bladed rotor drops drastically after attainment of the $C_{P,\,Opt}$, while relatively stable performance and rotating

motion is demonstrated by the sea-pen bladed rotor. This indicates that the sea-pen bladed rotor is more stable in the experimentally tested range of λ values as compared to its counterpart. Overall, the $C_{P,\,Opt}$ of both the rotors increases with U (hence the Re), however no such significant change in λ_{Opt} is observed. These values of each rotor for different U and Re in form of $C_{P,\,Opt}$ and respective λ_{Opt}, are tabulated in Table 4.1. The performance of the newly developed sea-pen bladed rotor is found to be favorable in the lower half of the λ values, and thus it is superior to the semicircular bladed rotor in this lower range. Further, it can be stated that the starting torque produced by the sea-pen bladed rotor would be higher than that of the semicircular bladed rotor under similar operating conditions.

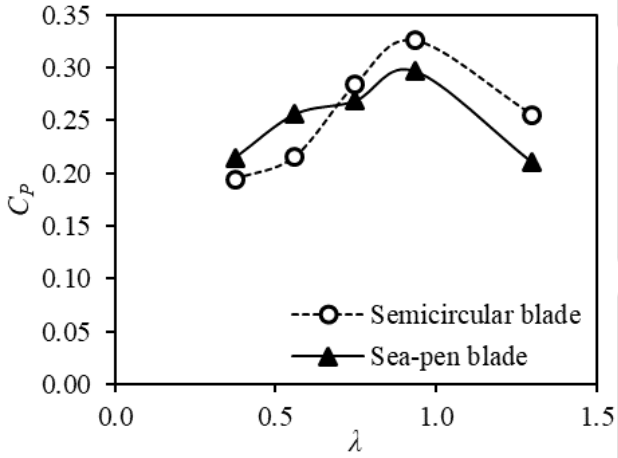

Figure 4.8 Numerical power characteristics of the rotors at $Re = 1.06 \times 10^5$

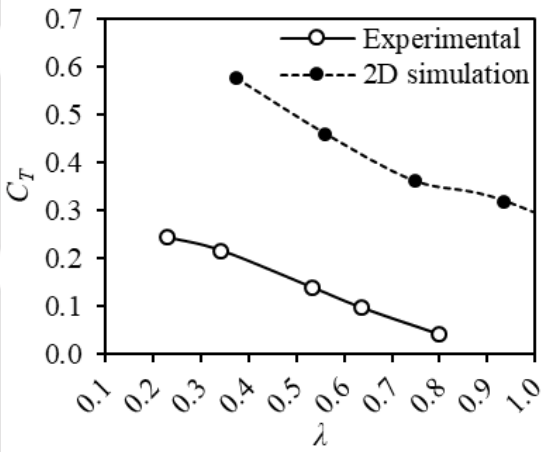

Figure 4.9 Validation for the Sea-pen bladed rotor at $Re = 1.06 \times 10^5$

The performance trend similar to the experimental one is also obtained by numerical simulations as shown in Fig. 4.8 for $Re = 1.06 \times 10^5$. The sea-pen bladed rotor shows a higher performance as compared to the semicircular bladed rotor in the left half of λ range and *vice-versa* for the remaining half of the λ range. As observed experimentally, the numerical power characteristics of both the rotors also intersect each other near to the $C_{P,\,Opt}$ of the semicircular bladed rotor. However, the actual values of numerical C_P are over-estimated as compared to experimental C_P. This is demonstrated in Fig. 4.9 in terms of experimental and numerical C_T for sea-pen blade at $Re = 1.06 \times 10^5$. Overestimation of such magnitudes has also been reported in the literature in the context of 2D simulation with SST $k - \omega$ model (Bangga et al., 2020; Franchina et al., 2019; Satrio et al., 2018). The reason behind this is the negligence of the height of the rotor in the 2D simulations. Still the simulations are capable of modelling the almost linear C_T vs λ characteristic, resembling the experimental one. Although the values are overestimated, the relative trend of performance for both the rotors remains unchanged.

Therefore, the numerical solutions are used for flow physics analysis while actual values of performance are considered from experimental results (Bangga et al., 2020; Rathod et al., 2019; Satrio et al., 2018). By considering this, the following discussion is dedicated to find the reason behind the performance improvement and to check whether the principal conditions established in Section 4.2.3 are fulfilled by the sea-pen blade or not.

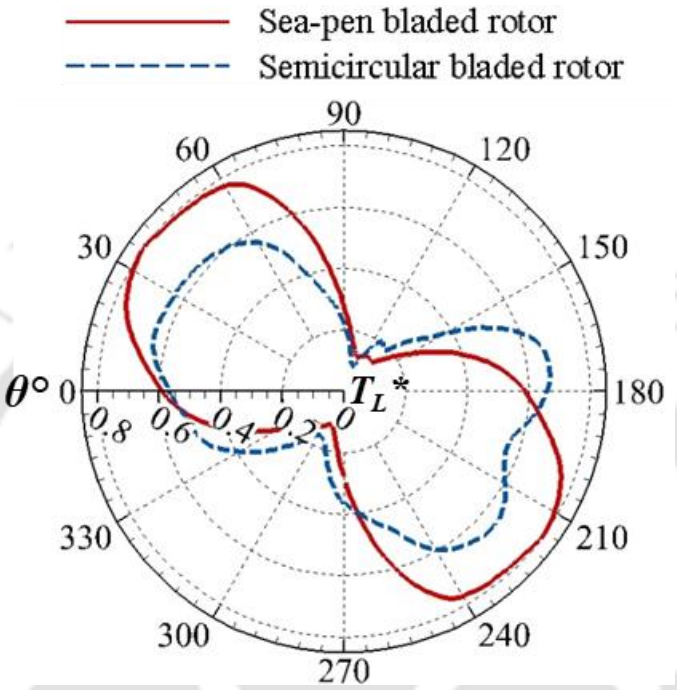

Figure 4.10 Comparison of numerical T_L* at Re = 1.06 × 10^5 and λ = 0.5

As mentioned earlier, C_T at a given λ is the time average of different instantaneous T_L* values corresponding to θ over a complete rotation. Using the results of simulations, at Re = 1.06 × 10^5 and λ = 0.5, the T_L* values for both the blades are calculated and compared in Fig. 4.10. At this λ, the sea-pen bladed rotor performs better than the semicircular bladed rotor. It can be observed that T_L* of the sea-pen bladed rotor is higher than that of the semicircular bladed rotor over almost the entire range of θ. Among them, the largest difference of T_L* between two rotors is observed at θ = 30° – 60°. Therefore, the improvement in T_L* for the sea-pen bladed rotor is investigated at θ = 45° and then the conclusions drawn from this investigation are extended to other θ values. As the T_L* is depended on C_{LT} (Eq. 2.5), it is important to study the distribution of the C_{LT} over both the rotors at θ = 45° as shown in Fig. 4.11. Using C_{Pr} values extracted from numerical solution, the values of C_{LT} are calculated as per the methodology and equations provided in Section 2.1. Figure 4.11 depicts the distribution curves of C_{LT} for the advancing and the returning blades of both the rotor types. The area bounded between C_{LT} curves of the advancing blades is denoted as A_1. Similarly, the area denoted as R_1 is bounded between C_{LT}

curves of the returning blades. Usually, the area bounded by advancing blade's C_{LT} distribution curve remains larger than that of the returning blade, resulting into the net positive torque of both the rotors. In comparison with semicircular blade, it is found that the increment of $+C_{LT}$ (marked as A_1 region) in sea-pen blade is observed towards the tip of the advancing blade for ϕ_A = 90° – 180°. While, the increment in $-C_{LT}$ (marked as R_1 region) is observed only around mid-chord (ϕ_R = 90°). In remaining regions, neither substantial increment nor decrement of C_{LT} is observed. The calculated area (numerical integration) of the bounded regions such as A_1 and R_1 are 23.71 and 6.14 units, respectively. It clearly demonstrates the performance improvement of the sea-pen bladed rotor as compared to the semicircular bladed rotor. This explanation can also be extended to θ value other than θ = 45°. Thus, the performance improvement of sea-pen bladed rotor is due to high $+C_{LT}$ values concentrated at the advancing blade over mid chord to the blade tip. Moreover, the changes observed at the returning blade is not significant.

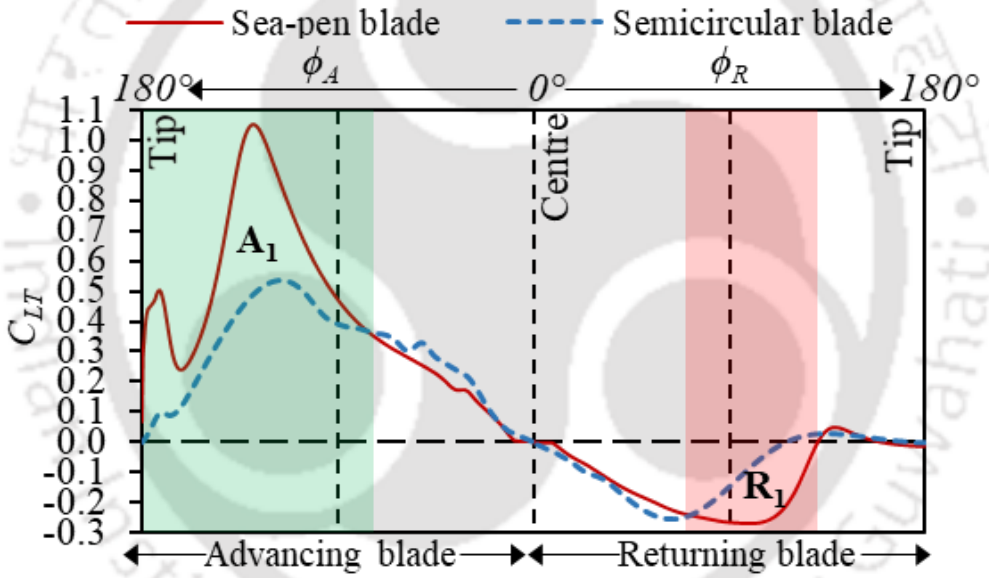

Figure 4.11 Comparison of numerical C_{LT} at Re = 1.06 × 10^5 and λ = 0.5

This can be explained further from distribution of C_{Pr} over the concave and convex sides of the advancing blades of both the rotors as shown in Fig. 4.12. It is important to clarify that the overall C_{Pr} trends over both the advancing and returning sides of the semicircular blade are similar to the reported experimental data (Fujisawa and Gotoh, 1994). Such similarities are also observed in many computational studies incorporating simulations of the semicircular bladed rotor (Rathod et al., 2019; Talukdar et al., 2022). As shown in Fig. 4.12, the trend of C_{Pr} on concave sides of both the shapes are almost identical. Therefore, the values of ΔC_{Pr} is mainly dependent only on C_{Pr} of convex side. On the other hand, the values of C_{Pr} over the convex

side are lower for sea-pen blade than semicircular blade for ϕ_A = 120° – 180°. This indicates an enhancement of very low C_{Pr} region at tip of the advancing blade, but towards downstream convex side, due to novel shape of sea-pen blade, which clearly fulfils principal condition (1) mentioned in Section 4.2.3. Moreover, the minor enhancement of low C_{Pr} is also found around ϕ_A = 45°. Only difference lies with them is that the former one is located at larger moment arm of blade surface, while the latter one is located towards center of rotor which provides a smaller moment arm. Hence, a higher C_{LT} is concentrated towards the tip of the advancing blade in the form of region A_1. Thus, it can be concluded that the novel shape of sea-pen blade is successful in satisfying the two principal conditions mentioned in Section 4.2.3 and shows a superior performance to that of the conventional semicircular shape in the lower operating range of λ.

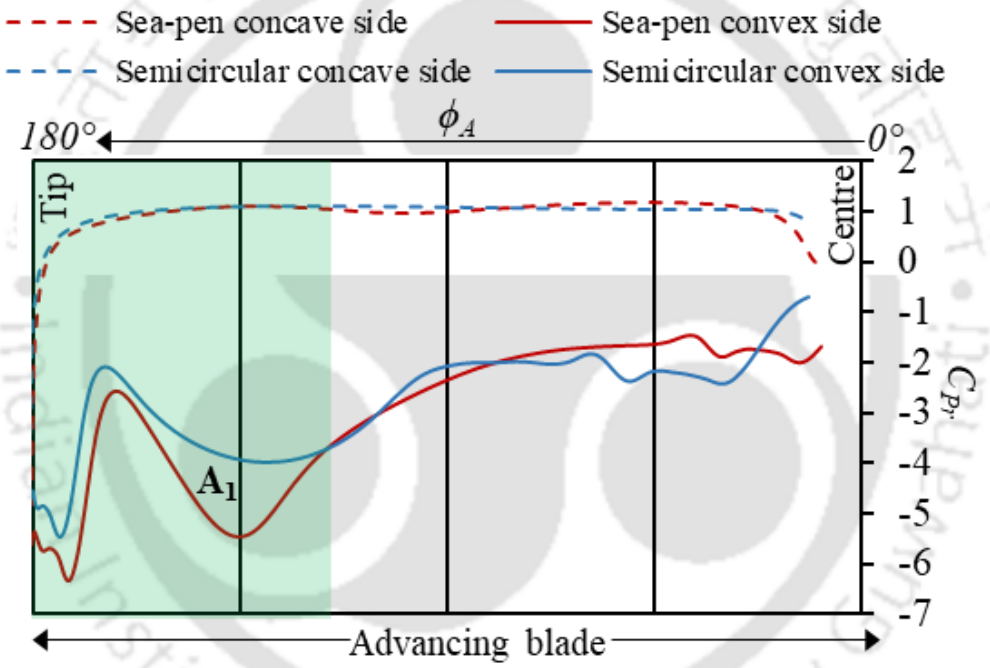

Figure 4.12 Comparison of numerical C_{Pr} at Re = 1.06 × 10^5 and λ = 0.5

As the λ increases from λ_{Opt}, the strength of the stagnation region on advancing blade decreases while low C_{Pr} region/vortex remains attached for the extended period (Fujisawa, 1992). As the rotational speed of the rotor increases, the relative tangential velocity at the tip of advancing blade decreases as compared to the same at the tip of returning blade (opposite direction). This causes a very high stagnation zone and hence a high drag on the returning blade. This can be the reason behind the performance deterioration of the sea-pen bladed rotor after λ_{Opt}. Similar type of trend has also been observed in other types of blade. For example, performance of the Bach type rotor is inferior to that of the semicircular bladed rotor beyond λ_{Opt} (Alom and Saha, 2019a). Similarly, Ushiyama et al. (1986) also observed the performance drop in Bach type

rotor in comparison with the semicircular bladed rotor for $\lambda > 0.6$. Such behavior is also documented by Tartuferi et al. (2015) in their novel airfoil shaped blades for $\lambda > 0.6$. Even if the present novel sea-pen bladed rotor is not able to improve the performance in the entire operating range of λ, it is successful in improving the performance below λ_{Opt} and in fulfilling two principal conditions.

4.5.2 Load Characteristics of the Blades without End Plates

Both types of the rotors are also experimented without the end plates at $Re = 0.77 \times 10^5$, 0.92×10^5, 1.06×10^5 and 1.2×10^5. For example, the experimental performance characteristic is plotted for the sea-pen bladed rotor without and with the end plates at $Re = 1.2 \times 10^5$ (Fig. 4.13). The performance improvement of the Savonius rotor with the implementation of end plates is a thoroughly studied topic in the literature (Alom and Saha, 2018a; Roy and Saha, 2013b). Such improvement is also observed for the sea-pen and semicircular bladed rotors in current study.

Based on the close examination of sea-pen morphology presented in Fig. 4.3(a) and 4.3(c), it is clearly visible that the concavity of leaves is also present at top and bottom tips of rachis. The reason behind this can be the retention of stagnant fluid at upstream of the sea-pen without leaking it from the top, which is quite identical to the working principle of end plates. Therefore, the physiology of the sea-pen also suggests the possibility of performance improvement if the end plates are implemented to block the leakage of the stagnant fluid.

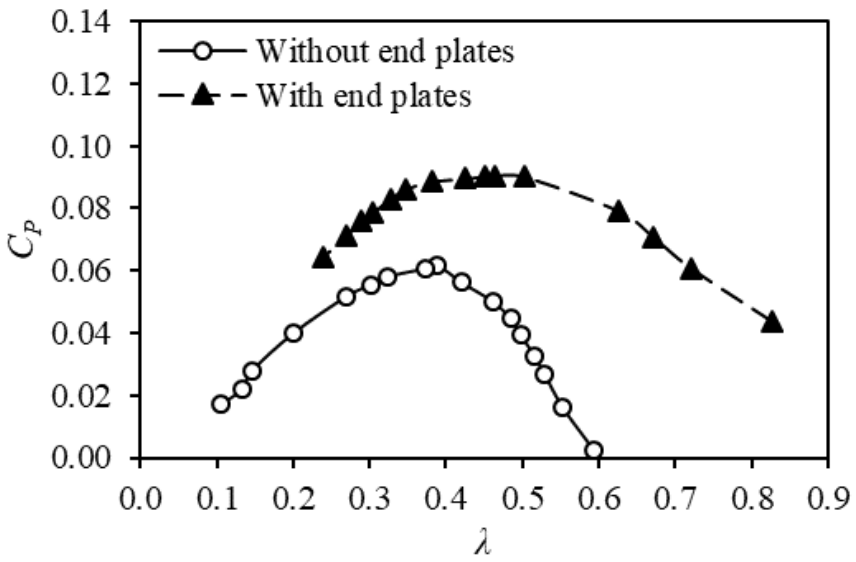

Figure 4.13 Comparison between the sea-pen bladed rotors with and without the end plates at $Re = 1.2 \times 10^5$

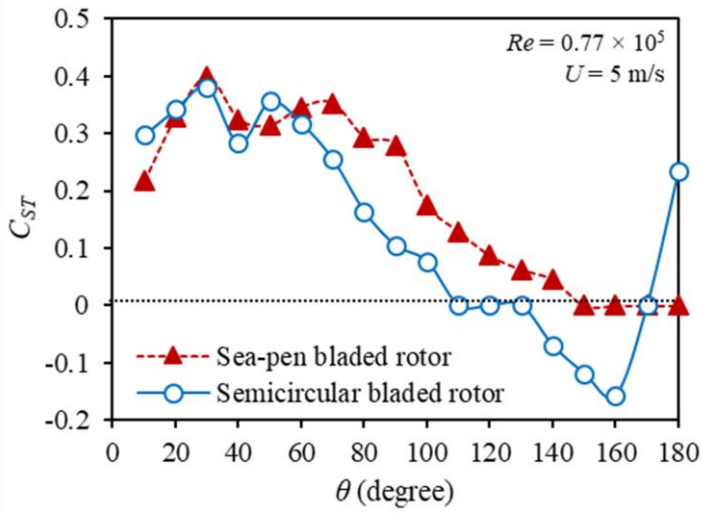

(a) Re = 0.77 × 10^5

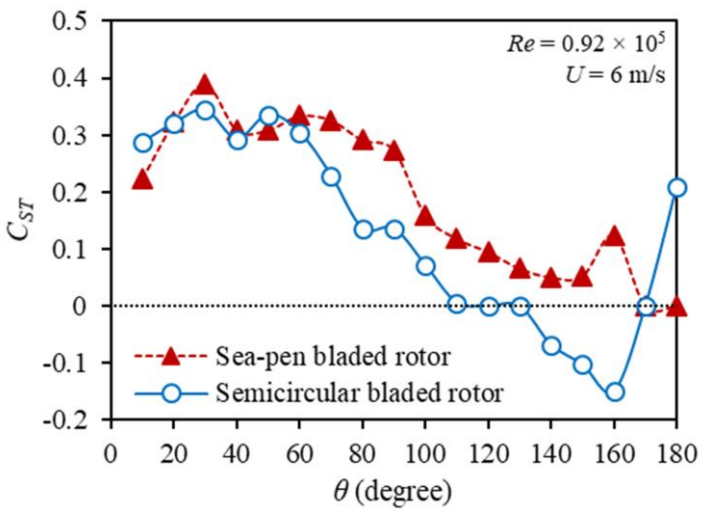

(b) Re = 0.92 × 10^5

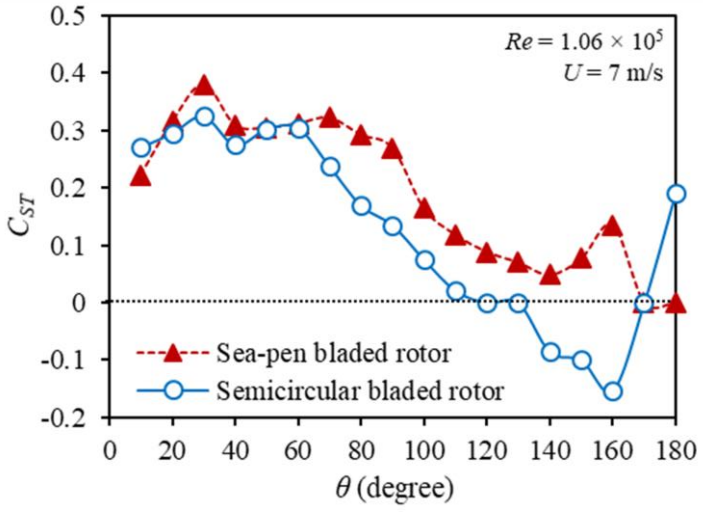

(c) Re = 1.06 × 10^5

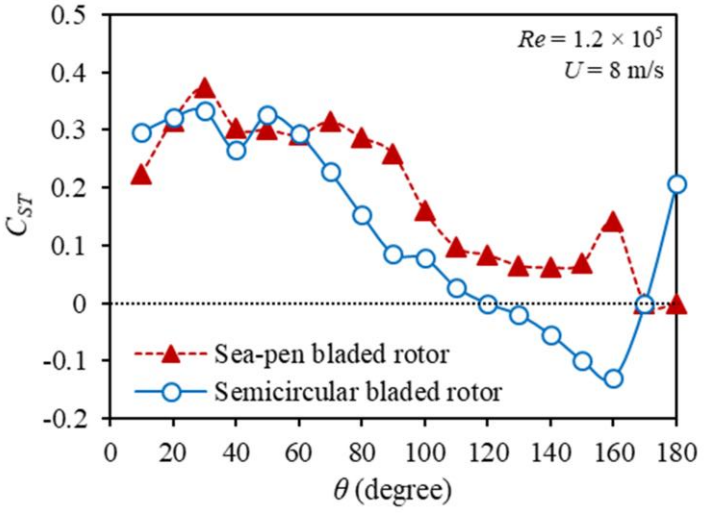

(d) Re = 1.2 × 10^5

Figure 4.14 Experimental static torque characteristics of the sea-pen and the semicircular bladed rotors at different Re values

4.5.3 Starting Torque Characteristics

Wind tunnel experiments are carried out to assess the static torque of a developed sea-pen bladed rotor. Experiments are also conducted with a semicircular bladed rotor to have a direct comparison. The static torque characteristics in the form of C_{ST} vs. θ curves for both the rotors at $Re = 0.77 \times 10^5$, 0.92×10^5, 1.06×10^5, and 1.2×10^5 are presented in Fig. 4.14. These operating ranges are similar to those adopted for evaluating rotary load characteristic. In both the rotors, the maximum values of C_{ST} are observed at $\theta = 20^o$ to 60^o (approximately) preceded by an increasing trend for $\theta < 20^o$. Thereafter, the steady decrease of C_{ST} is observed up to $\theta \approx 170^o$. This trend is repeated for the remaining half rotation of the rotors, *i.e.*, $\theta = 180^o$ to 360^o. Similar trend and magnitudes of the C_{ST} are observed by Fujisawa (1992) at $Re \approx 1.5 \times 10^5$. This supports and validates the present observations.

There is no substantial change of C_{ST} values with respect to *Re*. However, the power coefficient (C_P) of both the rotors in rotating condition is observed being dependent on *Re*. For both the rotors, maximum value of $C_{ST} \approx 0.38$ is gained close to $\theta = 30^o$ that is almost consistent for all the four values of *Re*. Further, the maximum values of C_{ST} in this region is almost same for both the rotors, without any substantial increase or decrease. For all the *Re* values, the semicircular bladed rotor shows positive C_{ST} for $\theta = 0^o$ to 130^o, and thereafter, negative C_{ST} for $\theta = 130^o$ to 170^o. This is also observed in the sea-pen bladed rotor, however, the negative C_{ST} region (for $\theta = 130^o$ to 170^o) of semicircular bladed rotor is absent and is replaced by positive C_{ST} values in the sea-pen bladed rotor. Therefore, at any θ, the sea-pen bladed rotor is able to gain enough starting torque for the commencement of rotation. However, this is not applicable for the semicircular bladed rotor, especially in the range of $\theta = 130^o$ to 170^o, because of the presence of negative C_{ST}. In this range, the semicircular bladed rotor advances subtly in the negative direction (as per sign convention of Fig. 2.1b), but it again experiences a positive C_{ST} that makes the rotor to advance in positive direction. As a result, oscillation of the rotor is observed in the vicinity of $\theta \approx 130^o$ and 170^o. Such oscillations are not observed for the sea-pen bladed rotor due to the presence of positive C_{ST} throughout the θ.

The reason behind the lack of negative C_{ST} for sea-pen blade in $\theta = 130^o$ to 170^o is due to the strengthening of higher pressure at pressure recovery region (located at downstream concave side of the returning blade) proposed by Fujisawa (1992), and Fujisawa and Gotoh (1994). This region remains influential during rotating and stationary conditions of the rotor. The bluffness semicircular bladed rotor is higher than the sea-pen bladed rotor even around $\theta = 0^o$ and 180^o.

At θ = 130º to 170º, the returning blades of both rotors remain at upstream, while the advancing blades remain at downstream. As the sea-pen bladed is relatively slenderer than its counterpart, the former does not create severe flow separation as compared to the latter at downstream of the returning blade. Consequently, the pressure recovery is higher for sea-pen blade than the semicircular blade. Therefore, the negative torque produced by the returning blade reduces in case of sea-pen blade as compared to semicircular blade, and hence the overall negative C_{ST} also reduces. This effect and similar C_{ST} distribution are also observed by Roy and Saha (2015) for Bach type, modified Bach type, and Benesh type blades. As the sea-pen blade is similar to these blades (slender blades compared to semicircular blades) as per Fig. 4.5, similar C_{ST} distribution can be expected. Overall, the role of overlap region on the pressure recovery region (Fujisawa, 1992; Fujisawa and Gotoh, 1994) seems identical to the influence of slender blade shape.

Comparatively, the sea-pen bladed rotor induces a higher C_{ST} than the semicircular bladed rotor in the range of θ = 60º to 170º. This is found to be consistent in the tested range of *Re*. The highest value difference between the C_{ST} trends of both the rotors is observed at $\theta \approx$ 160º. This clearly indicates the superiority of the sea-pen bladed rotor as compared to semicircular bladed rotor in terms of C_{ST}. Moreover, the increment of C_{ST} for sea-pen bladed rotor is observed, especially, where the semicircular bladed rotor produces low and negative values of C_{ST}. In other words, the sea-pen bladed rotor can produce higher starting torque in the range of θ in which the conventional semicircular bladed rotor is prone to be non-rotatable. It is to be noted that the sea-pen also orients its concave body at 90º with the incoming sea-current to maximize its feeding capability by enhancing the strength of the attached vortices at downstream, *i.e.*, strengthening the vortex induced wake feeding mechanism (Shimeta and Jumars, 1991). Similarly, the rotor having sea-pen inspired blade shape also tends to induce higher C_{ST} nearby θ = 90º than the semicircular blade shape. This again supports the extension of the working principal of sea-pen's feeding mechanism to the torque inducing mechanism of the sea-pen bladed rotor, as mentioned at the end of Section 4.3.

It is reported for rotation rotors that the blade shape of the sea-pen blade strengthens the low-pressure region at the convex side of the rotating advancing blade as compared to the conventional semicircular blade. This region also remains present in the stationary condition, although not being able to attach for a long time unlike in the rotating condition. This results into a moderately higher torque producing capability of rotating rotor as compared to the

stationary rotor (Fujisawa and Gotoh, 1994). It can therefore be deduced that the reason behind the performance improvement due to implementation of sea-pen inspired blade for rotating condition is also applicable for the stationary condition.

4.6 Concluding Remarks

The preliminary results from the experimental and numerical investigations show that the novel blade shape inspired from the leaf of the Orange sea-pen (*Ptilosarcus gurneyi*) possesses the potential to perform superiorly to the conventional semicircular blade. By exploiting the analogy between the working principles of the Savonius rotor and autorotation, two principal conditions are derived for the purpose of performance improvement, *viz.*, (a) Importance of attached low pressure region/vortex behind advancing edge/blade, (b) Principal condition-1 can be attenuated by the shape of the advancing tip/edge. Both of these conditions are fulfilled by the novel sea-pen blade according to findings of the present study. Other findings obtained by testing all the rotors at U = 5 m/s to 8 m/s are as follow:

- The sea-pen blade performs better than the semicircular blade at $\lambda < \lambda_{Opt}$ and *vice-versa* for $\lambda > \lambda_{Opt}$ for each *Re* numbers studied.
- For low *Re* numbers such as $Re = 0.77 \times 10^5$ and 0.92×10^5, the $C_{P,\,Opt}$ of the sea-pen blade is higher than that of the semicircular blade.
- For higher *Re* numbers such as $Re = 1.06 \times 10^5$ and 1.2×10^5, no significant difference in $C_{P,\,Opt}$ of both the blades is observed.
- The relative experimental trends are also supported by the 2D numerical solution.
- The performance improvement of the sea-pen blade is mainly because of high $+C_{LT}$ and low C_{Pr} values concentrated towards the tip of the advancing blade.
- The sea-pen blade with the end plate performs better than without the end plates.
- The approximate peripheral lengths of the fabricated sea-pen and semicircular blades are 180 mm and 238 mm, respectively, clearly indicates that the less amount of sheet metal is required to fabricate the sea-pen blade as compared to the semicircular blade.
- In the context of starting torque characteristics, the sea-pen bladed rotor is superior to the semicircular bladed rotor
- The increment of C_{ST} in the sea-pen bladed rotor as compared to semicircular bladed rotor is observed in the range of θ = 60º to 170º, with highest enhancement at θ = 160º.

- The negative C_{ST} region present in the semicircular bladed rotor in the range of $\theta = 130^{o}$ to 170^{o}, is completely absent in case of the sea-pen bladed rotor.
- The maximum value of $C_{ST} \approx 0.38$ is obtained at $\theta = 30^{o}$, which is applicable for both the rotors.
- The implementation of the sea-pen inspired blade does not improve the maximum C_{ST} but it enhances the starting torque characteristics at particular θ values, where the conventional rotor is inferior to generate the necessary starting torque.

Based on the aforementioned conclusions drawn, it can be concluded that the sea-pen bladed rotor is superior to the conventional semicircular bladed rotor in both static as well as rotary conditions.

Chapter – 5

Development of Corrugated Blades Inspired from Dragonfly Wings

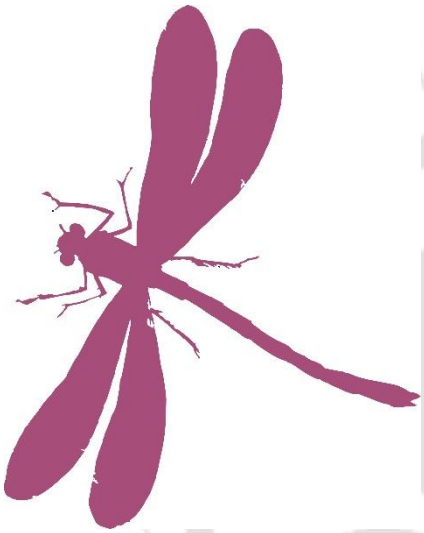

Chapter Layout:

Overview

In continuation to Chapter 4, this chapter further exploits the principal flow conditions with the implementation of the corrugation on the rotor blades inspired from the dragonfly wings. The chapter is initiated with the role of the peaks and valleys found on the corrugated wings of the dragonfly on the lift enhancement. The procedure of the extraction of design dimensions from the cross-section of the pleated dragonfly wing is then explained followed by the multiple design iterations of the corrugated blades for the Savonius rotor. The model rotors are then tested numerically. The reasons behind the performance improvement in the corrugated blades are then discussed besides analysing on how the flow conditions actually have been exploited by the corrugation.

5.1 Background

By following the principal flow conditions discussed in Section 4.2.3, the novel sea-pen inspired blade shape has been successfully developed that gives a superior performance as compared to the conventional semicircular blade. To progress further in this direction, the objectives of this chapter is set to search for another suitable bio-inspired phenomenon that can effectively exploit the principal conditions.

Figure 5.1 Cross-section of dragonfly forewing (Abd El-Latief et al., 2021; Okamoto et al., 1996)

At the initial glance, the corrugated blades, inspired from the bio-organisms such as dragonfly, seem to be suitable for the purpose mentioned. The corrugated blades as shown in Fig. 5.1 resembles a pleated flat plate along its chord-wise direction. This type of wing is found in insect species such as dragonflies, damselflies, and the locusts. The corrugated structure is known to provide the necessary stiffness against the span-wise bending of the airfoil or the insect-wing (Murphy and Hu, 2010). However, it is also reported that the corrugated blade provides a higher lift as compared to the conventional airfoil. It is interesting to note that the corrugated wings are evolved for the flapping flight, still these wings provide a higher lift in the stationary condition (Hui and Tamai, 2008; Levy and Seifert, 2009). There are many hypotheses proposed by researchers explaining the lift enhancement of the corrugated airfoil. One of the intuitive explanations is that the flow passing over the corrugated airfoil would be trapped inside the valleys. As a result, the flow becomes stagnant and rotates slowly inside the valleys making the corrugated airfoil functioning as a streamlined airfoil (Murphy and Hu, 2010). Kesel (2000) suggested that the low pressure (with negative C_{Pr}) induced due to trapped vortices at the valleys of the corrugated airfoil towards the suction side contributes to the increase in the lift. At higher angle of attacks, the unsteady vortex structures produced at the leading edge are also prone to be trapped in the valleys of the corrugated blades and can maintain high lift coefficients up to $Re \approx 10^5$ (Murphy and Hu, 2010). Further, it is reported that the effect of the corrugation on the lift characteristic is insensitive to the change of Re and can be observed over a wide range of $Re = 0.58 \times 10^5$ to 1.25×10^5 (Murphy and Hu, 2010). If these characteristics

of the vortex entrapment and hence strengthening low C_{Pr} distribution through the corrugation is combined with the principal condition-1 of the Savonius rotor; it can be hypothesized that the vortices induced at the low-pressure region A1 (Fig. 4.1) of the rotor can be trapped, and as a result, the strength of low C_{Pr} region (A1) can be enhanced thereby improving the overall rotor performance. In other words, it is aimed to implement the corrugated blades in the design of the Savonius rotor and assess its performance in comparison with the rotor having conventional (non-corrugated) semicircular blades. Moreover, till date, the corrugation has not been introduced yet in the blade design of the Savonius rotor.

It is important to point out that the concept of corrugation is originally developed from the flapping wings. The bodies with the periodic movements such as oscillation, flapping, heaving and others are considered as an accelerating-decelerating bodies (Hans J Lugt, 1983). Such bodies leave behind the periodic vortex shedding pattern either in drag or in thrust inducing configurations. Similarly, the rotation of the Savonius rotor also produces periodic vortex shedding. This rotating body can also be considered as the accelerating-decelerating body since every parts of the rotating body changes their directions continuously. Considering these similarities, it is anticipated that the concept of corrugation, originally found in the flapping wings, can be carried over to the rotating Savonius rotor.

In this section, the flow physics of the Savonius rotor and the working principle of the corrugation on the airfoil are elaborated. Thereafter, how the corrugation along with the principal condition-1 would help to improve the rotor performance is explained. Based on this, the corrugated rotor blades are designed and presented in Section 5.2.

5.2 Design of the Corrugated Blades

To design the corrugated semicircular blade, the insights gained from the corrugated airfoil design provided in Fig. 3 are implemented. This corrugated blade profile used in the present study is taken from one of the profiles provided by Kesel (Fig. 5.1). This profile belongs to the mid-span of the forewing of the dragonfly (*Aeshna cyanea*) (Abd El-Latief et al., 2021; Kesel, 2000; Okamoto et al., 1996; Vargas and Mittal, 2004). As shown in Fig. 5.2, the maximum depth of valleys in corrugation is approximately 5% of the total chord length (l_c) of the corrugated airfoil. The major corrugation angle (α) formed by the line segments forming the valley or the peak of the corrugation are approximately equal to 100º. Such corrugation is spanned approximately over 37% of chord length (l_c) starting from the leading edge (LE).

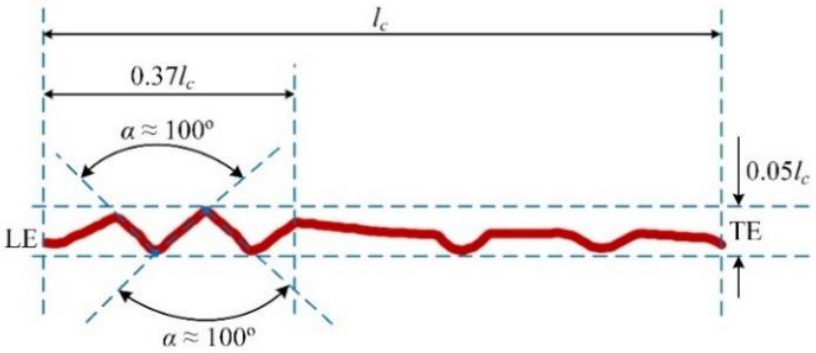

Figure 5.2 Extracted dimensions from the corrugated blade of Fig. 5.1 (Kesel, 2000; Vargas and Mittal, 2004)

The abovementioned specifications are considered to design the corrugated profiles of the Savonius rotor, *viz.*, Profile-1 and Profile-2, as shown in Fig. 5.3(a) and 5.3(b), respectively. It is important to note that the rudimentary shape of both the corrugated profiles is the conventional semicircular shape (Fig. 5.3c). As shown in Fig. 5.3(a), the corrugation is applied to approximately 37% of the total periphery (*i.e.*, $\phi \approx 0^o$ to 67^o starting from blade tips) of the half-circular blade similar to that of the corrugated airfoil. However, the corrugation is not implemented exactly from tip of the blade in order to maintain the projected length of the profile (≈ 137.5 mm) to be constant. Resembling the corrugated airfoil, the depth of the corrugation (from peak to the valley) is set as 10 mm that is approximately 5% of the peripheral length of the blade. The corrugation angle ($\alpha = 60^o$) is maintained throughout the corrugation of the Profile-1. Because of geometric constraints faced during the computer aided design (CAD) modelling of Profile-1, the initial line segment of the corrugation is slanted 15^o with the vertical direction. This ensures the uniformity of α value throughout the corrugation of Profile-1. Further, implementation of $\alpha = 100^o$ in Profile-1 is not possible due to the abovementioned geometric constraints because of the curvature involved in the semicircular blade profile.

Another corrugated profile design *viz.*, Profile-2 is created that is completely distinct from Profile-1 in terms of α, depth of corrugation, location and spread of the corrugation. Despite having the Profile-1, the necessity of synthesizing Profile-2 is addressed in Section 5.3.1 based on their performance evaluation. Unlike Profile-1, the corrugation on Profile-2 is spread over $\phi \approx 45^o$ to 90^o (from the tips), approximately. Further, the peaks of the corrugation exist only towards the lower side of the profile's circular outline, having the thickness of 5 mm. In the entire corrugation of Profile-2, $\alpha = 90^o$ is set uniformly. In this region of the blade, maintaining $\alpha = 60^o$ creates the geometric incompatibility in the CAD modeler due to curvature present in the semicircular profile. Therefore, $\alpha = 90^o$ is selected which is also in the proximity to $\alpha = 100^o$ of corrugated airfoil.

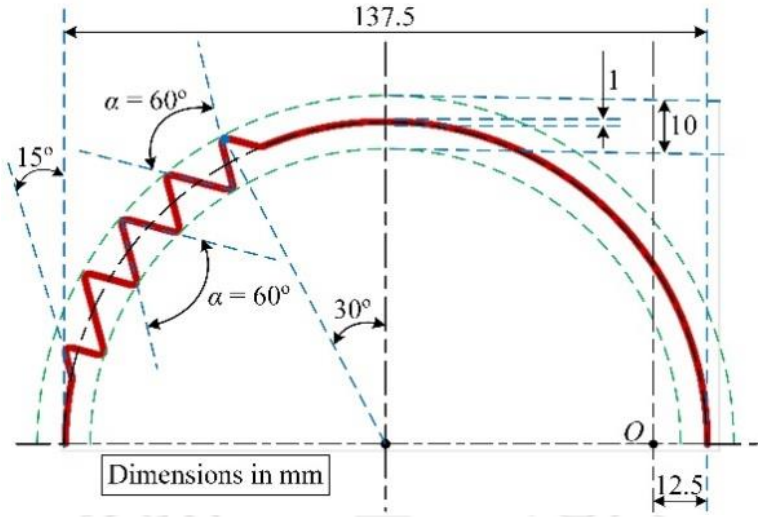

(a) Design of Profile-1

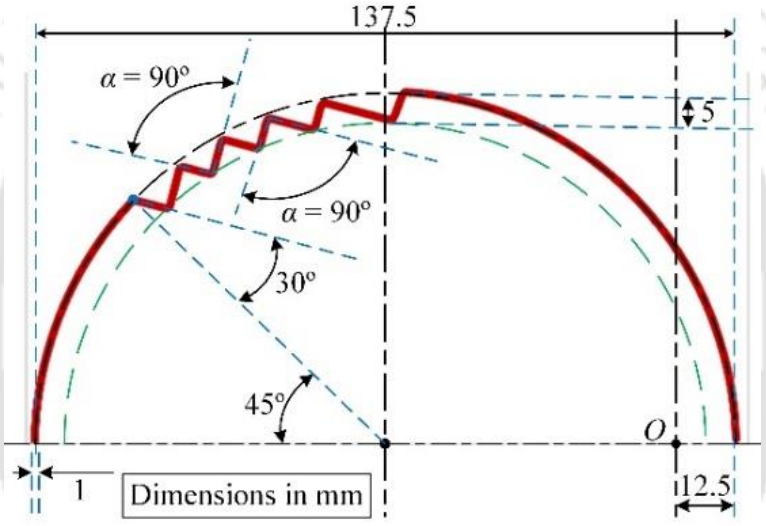

(b) Design of Profile-2

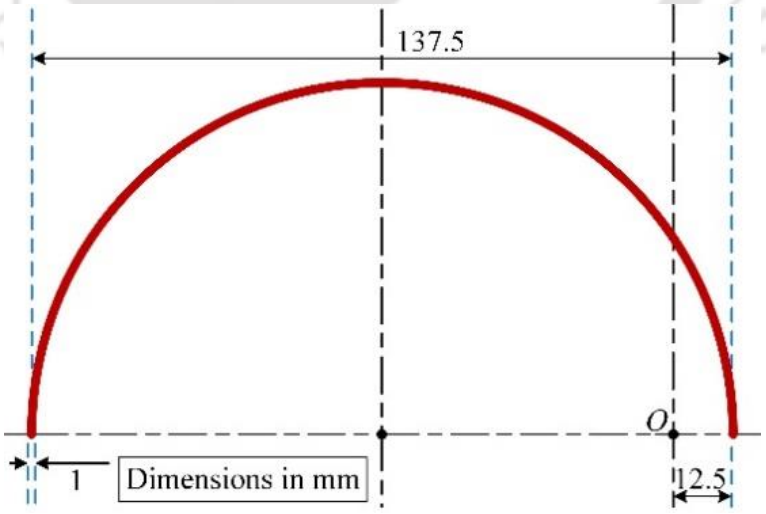

(c) Design of non-corrugated semicircular profile

Figure 5.3 Design of blade profiles for the numerical simulations

By comparing both the blade profiles, it can be noted that the corrugation on Profile-1 directly influences the region A1 (Fig. 4.1) and hence the principal condition-1. This is because of the location and spread of corrugation towards the tip of profiles. On the other hand, the corrugation on Profile-2 is located far from the blade tip without directly disturbing the low-pressure region A1 and the corresponding principal condition-1. The insights gained from the flow physics (Section 4.2) of the Savonius rotor are considered while designing both the profiles. The overall design of three individual rotors having blades made of Profile-1, Profile-2 and semicircular profile is identical. The overall diameter (D) of all three rotors is maintained at 250 mm. Further, the radius of the rudimentary semicircular profile is set at 68.75 mm. The overlap distance (e) of 25 mm is applied in the rotor design. The thickness of the profile is equal to 1 mm in the numerical setup. It is important to note that small radius (1 mm to 2 mm) is applied at the apices of peaks and valleys of the corrugation to eliminate the sharpness in the numerical model. The rotor height is set at 250 mm and the same is also specified as reference value in the *ANSYS FLUENT* software (Ansys, 2021).

5.3 Results and Discussion

In this section, numerically estimated performances of Profile-1, Profile-2 and non-corrugated conventional semicircular profile are discussed. The reason behind the performance improvement is also addressed in terms of fluid variables such as T_L^*, C_T, C_{LT} and C_{Pr}.

5.3.1 Numerical Load Characteristics of Blades

Numerical simulations are carried out to assess the performance of rotors having semicircular profile and the newly proposed corrugated profiles *viz.,* Profile-1 and Profile-2. The numerical simulations for these rotor blade designs are conducted using the computational domain narrated in Chapter 3. The performance trends in the form of C_T vs. λ curves for different blade profiles are compared in Fig. 5.4 at $Re = 1.06 \times 10^5$. The C_T vs. λ curve is usually found being linear with decreasing value of C_T as λ increases. As the present work addresses only the preliminary examination of the corrugated blades, the numerical simulations are conducted only for limited Re numbers.

Herein, C_T values are very large at small values of λ for all the profile and then gradually decreases with increase in λ. It is evident from Fig. 5.4 that the C_T values of Profile-1 is lower than that of the non-corrugated semicircular profile, therefore, no improvement is obtained. On the other hand, the Profile-2 shows higher values of C_T as compared to the non-corrugated

profile for lower values of λ (Fig. 5.4). As λ is increased further, this particular trend reverses, and thus, the non-corrugated profile provides slightly higher or almost equal values of C_T as compared to Profile-2. At $\lambda \approx 0.55$, the value of C_T for Profile-2 is almost 8% higher than the non-corrugated profile that is highest among the increments obtained at other lower values of λ. However, it is important to note that almost similar values of $C_{P,\,Opt} \approx 29\%$ at $\lambda \approx 0.75$ is obtained for both Profile-2 and non-corrugated profile. This means the corrugation in Profile-2 improves the C_T at low λ without disturbing the optimum rotor performance. Further, the operating condition of $\lambda \approx 0.55$ is chosen to investigate the C_T improvement due to corrugation in terms of C_{Pr} and C_{LT} as discussed in Section 5.3.2.

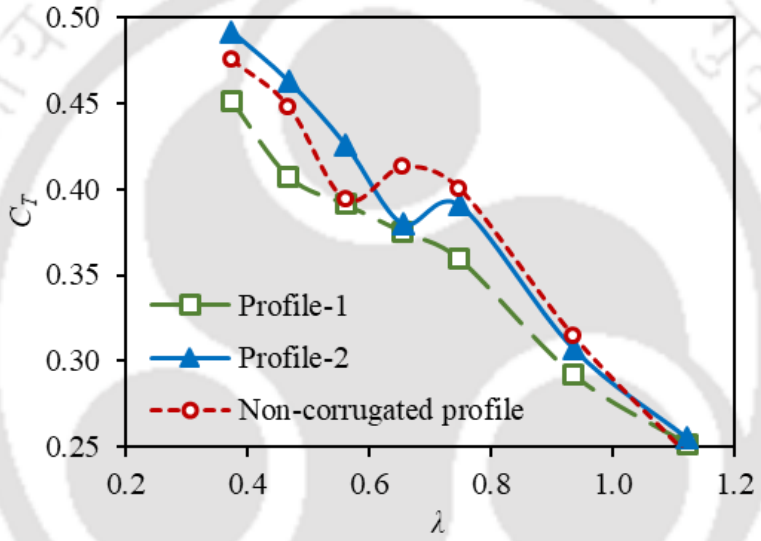

Figure 5.4 Numrical torque characteristics of tested profiles at Re = 1.06 × 10^5

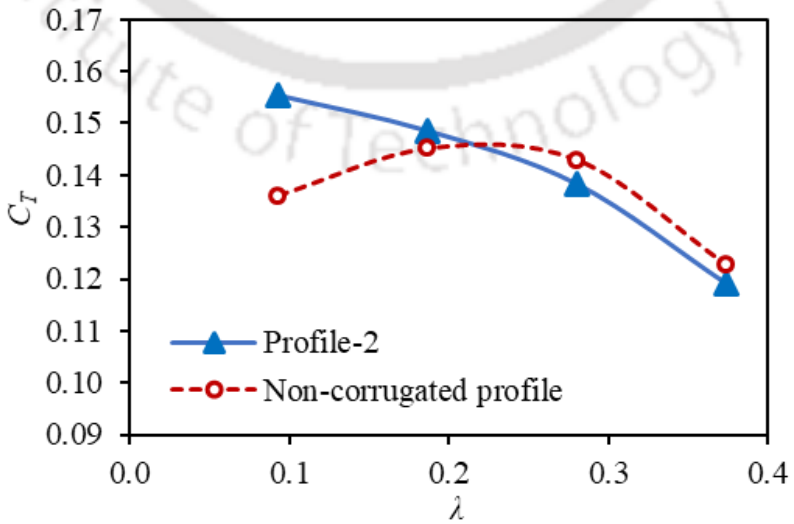

Figure 5.5 Numrical torque characteristics of tested profiles at Re = 0.77 × 10^5

Based on the numerical C_T values, it can be stated that the corrugation located at the tip of Profile-1 directly disturbs the principal condition-1, and hence, it becomes unsuccessful in enhancing the performance. Further, the peaks of the corrugation protruded above the semicircular midline seem to perturb the useful low C_{Pr} region (A1) (Fig. 4.1) and the principal condition-1. This is deduced based on the findings of multiple simulations carried out by the present authors while addressing different design combinations of corrugation besides Profile-1 and Profile-2. In order to mitigate this problem, Profile-2 is synthesized in such a way that it lacks the protruded peaks of the corrugation and is located away from the profile tip. As a result, the Profile-2 provided an improved performance than the other corrugated profiles that are not included in this work. In this chapter, the results of Profile-1, Profile-2 and non-corrugated semicircular profile have only been presented. Further, it has become clear that the Profile-2 performs better than the other two blade profiles, and therefore, the Profile-2 and the semicircular profile without corrugation will be addressed as corrugated and non-corrugated profiles, respectively, in Section 5.3.2. These corrugated (Profile-2) and non-corrugated profiles are also tested at $Re = 0.77 \times 10^5$ that is an operating condition at low wind velocity of $U = 4$ m/s (Fig. 5.5). As reported in the literature, the performance trends of the Savonius rotor remain uniform and consistent with Re, except at higher values of C_T obtained with the increase of Re. As shown in Fig. 5.5, the relative trend of C_T between the corrugated and the non-corrugated blades is similar to that of Fig. 5.4 for $Re = 1.06 \times 10^5$.

5.3.2 Physics Behind the Performance Improvement

To understand the improvement of C_T due to corrugation implemented in the semicircular profile, the simulated T_L^* distributions of corrugated (Profile-2) and non-corrugated profiles are plotted in Fig. 5.6 for $\theta = 0^o$ to 180^o at $\lambda = 0.55$ and $Re = 1.06 \times 10^5$. The reason is that the value of the C_T for a given value of λ is a time averaged value of the instantaneous T_L^* values corresponding to different θ values over a complete rotation. Further, the particular values of θ can be investigated at which the corrugation is effective since the orientation of the corrugated part of the profile changes with respect to the wind direction in a rotation.

In Fig. 5.6, the limited range of $\theta = 0^o$ to 180^o is depicted since the values are repetitive in nature for remaining half cycle of the rotation. The improvement of T_L^* (dimensionless local torque) is observed more or less in the entire range of θ, except for small range of $\theta \approx 10^o$ to 30^o. Instead of explaining improvement of T_L^* at each θ, one particular value of θ is picked up as a representative. The explanation of T_L^* improvement at the representative θ can then be

carried over to other values of θ. For the present case, such a chosen representative value is $\theta = 0^o$ since the corrugation on the profile is oriented parallel to the incoming wind direction, similar to the corrugated airfoil. Moreover, the corrugated profile performs better than the non-corrugated profile at the same value of θ. Therefore, the subsequent discussion presented in the form of C_{Pr} and C_{LT} is based on $\theta = 0^o$.

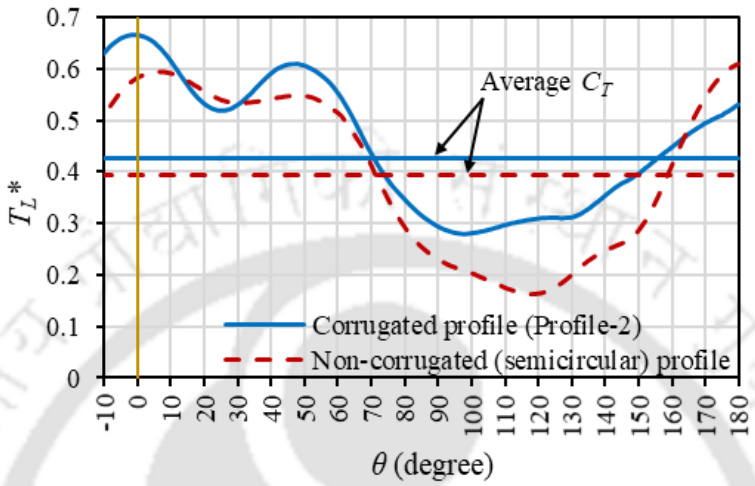

Figure 5.6 Comparison of numerical T_L* at Re = 1.06 × 10^5 and λ = 0.55

As explained in Section 5.1, the corrugation enhances the low C_{Pr} region inside the valleys that improves the lift characteristics of the airfoil in return. To check whether or not the corrugation applied is successful, the C_{Pr} distributions of both the profiles are presented in Fig. 5.7 for $\theta = 0^o$ at operating condition of λ = 0.55 and Re = 1.06 × 10^5. It can be clearly seen that the corrugation influences more on the convex side of both the profiles than the concave sides in terms of C_{Pr}. In the convex side of the advancing profile, the corrugation causes step-wise distribution of the C_{Pr} over $\phi_A \approx 90^o$ to 135^o (region A_1), that is absent in the non-corrugated profile as per Fig. 5.7(a). This stepwise distribution of C_{Pr} is also observed in the returning profile over $\phi_R \approx 90^o$ to 135^o (region R_1 in Fig. 5.7b), however, this is less prominent than the advancing profile. This type of C_{Pr} distribution is absent in the concave sides of both the advancing and returning corrugated profile (Profile-2) since the local flow here is not parallel to the corrugation. At the advancing profile (Fig. 5.7a), slightly lower values of the C_{Pr} are observed as compared to that of the non-corrugated profile throughout the range of ϕ_A. On the other hand, this trend of C_{Pr} for the convex side is altered in the returning profile.

Based on the overall C_{Pr} distribution as shown in Fig. 5.7, the most prominent influence of corrugation on the C_{Pr} is observed in the region of R_1 of returning profile over $\phi_R \approx 90^o$ to 150^o and above. In this region of returning side, the difference of the C_{Pr} values in between the concave and convex sides is more prominent and higher in the corrugated profile than the non-corrugated profile.

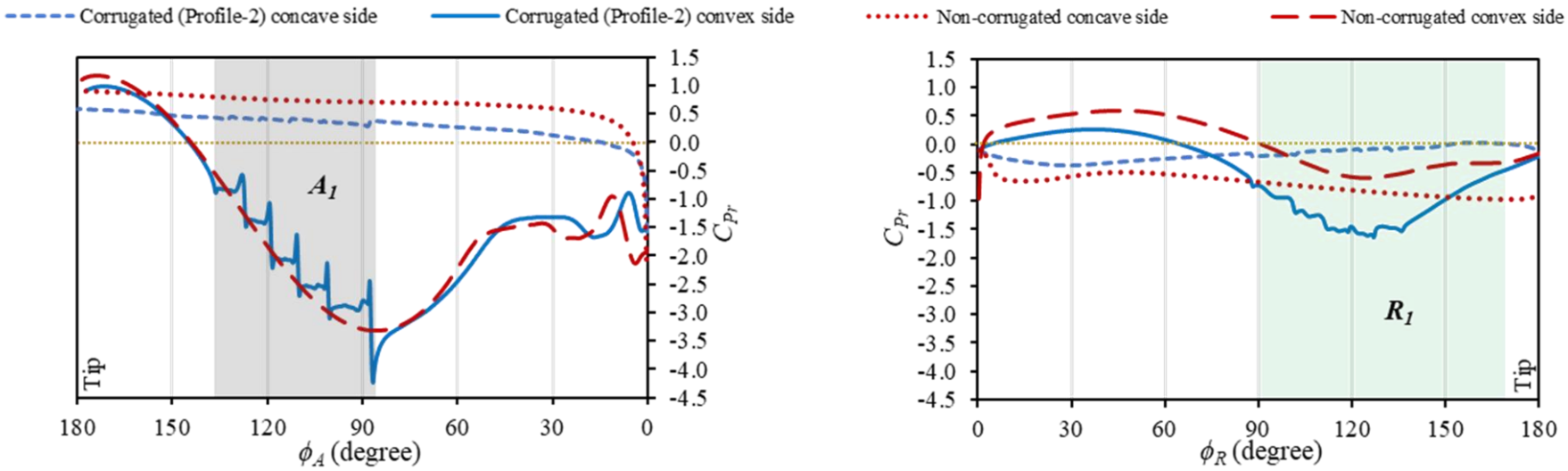

(a) Advancing blade **(b)** Returning blade

Figure 5.7 Comparison of numerical C_{Pr} at Re = 1.06 × 10^5 and λ = 0.55

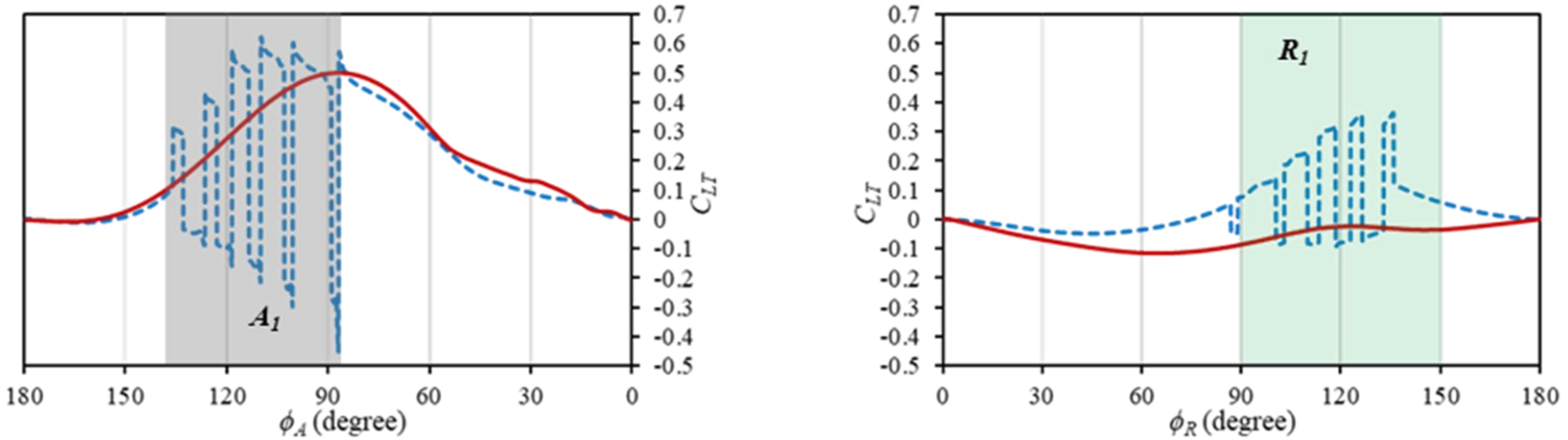

(c) Advancing blade **(d)** Returning blade

Figure 5.8 Comparison of numerical C_{LT} at Re = 1.06 × 10^5 and λ = 0.55

This is mainly because of the low C_{Pr} region created inside the valleys of the corrugation at the convex side. It is important to clarify that the corrugation of advancing profile is under the influence of stagnation as it is in direct contact with the upstream flow due to the curvature of the circular profile for $\phi_A > 90^o$. On the other hand, the corrugation on returning profile is not in the influence of the stagnant flow as the upstream flow is already perturbed by the advancing profile. The corrugation thus becomes more effective in maintaining a low C_{Pr} at the returning profile rather than the advancing profile. Based on these C_{Pr} distribution trends, it can be deduced that the corrugation is successful in capturing low C_{Pr} in its valleys for both the profiles, however, more prominently in the returning profile. It is not sufficient to investigate only the C_{Pr} distribution over the profile surfaces, instead the study of C_{LT} distribution together with the C_{Pr} distribution is essential to find how much this strengthened low C_{Pr} over corrugation actually contributes in useful positive C_{LT}. Having considered this point, the C_{LT} distribution at both the advancing and returning sides of corrugated as well as non-corrugated profiles are explained in the next paragraph.

With the help of numerical C_{Pr} values, the C_{LT} values are calculated by implementing mathematical procedure narrated in Section 1. Such numerically found trends of C_{LT} for the advancing and the returning profiles without and with the corrugations are presented in Fig. 5.8. The operating conditions for the results presented in Fig. 5.8 were $\theta = 0^o$, $\lambda = 0.55$, and $Re = 1.06 \times 10^5$, similar to those of C_{Pr} trends in Fig. 5.7. The area bounded by the C_{LT} curve of the advancing profile is higher than that of the returning profile, resulting into the net positive torque experienced by the rotor that is crucial for the continuation of the rotary motion. In comparison to the non-corrugated profile, the sudden increase and drop of C_{LT} is observed in the corrugated profile due to changes in the slope of *dl* forming the valleys as compared to the original circular shape of the profile. These regions are highlighted as A_1 (Fig. 5.8a) and R_1 (Fig. 5.8b) for advancing and returning profiles, respectively. The drop in the values of C_{LT} would also results into the negative values.

The above behavior of the C_{LT} trend can be explained with the help of Fig. 5.9 that illustrates the force diagram acting on the corrugated profile (Fig. 5.9a) and the corrugated airfoil (Fig. 13b). This corrugated airfoil having only one valley is adapted from Fig. 5.2. Two points *'a'* and *'b'* are considered being located on two different blade segments forming a valley. In case of the rotor blade profile, both of these line segments have completely different slopes with respect to each other and the original circular arc segment (in the absence of corrugation). As

a result of the pressure distribution over the line segments, two force vectors F_a and F_b are acting on the points a and b, respectively. The force components and their respective moment arms with respect to the rotor's rotational axis (O) are also provided in Fig. 5.9. Due to the change in the slopes of the line segments forming the valley, the largest force components $F_{a,y}$ and $F_{b,x}$ induce positive and negative torques, respectively, with respect to O. This results into the sudden drop of the C_{LT} with respect to ϕ as observed in the region A_1 and R_1. If the other force components, *viz.*, $F_{a,x}$ and $F_{b,y}$ are trivial in terms of magnitude, then in that case, the overall values of the moments M_a and M_b become positive and negative, entirely. This can be clearly observed in the region A_1 of Fig. 5.8.

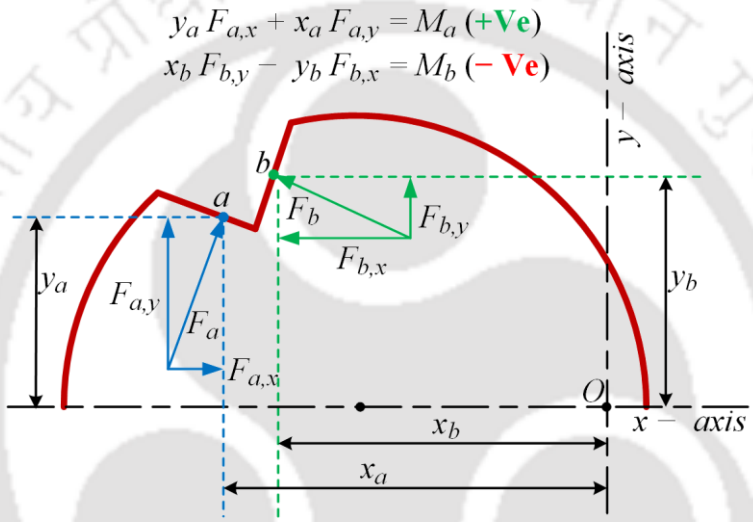

(a) Force acting on the rotor blade profile

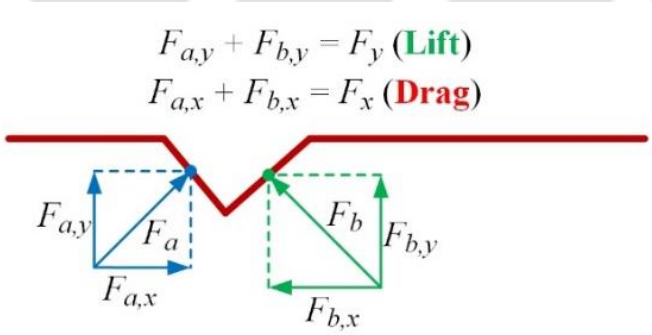

(b) Force acting on the corrugated blade

Figure 5.9 Illustration of froce diagram

On the other hand, this type of observation has not been reported for the airfoil since the lift force is given an importance rather than the torque acting on the surface. Moreover, the points a and b located on the airfoil have small y moment arm, generating a minimal torque by the drag forces ($F_{a,x}$ and $F_{b,x}$) in the horizontal direction. However, the moment arms for the lift forces ($F_{a,y}$ and $F_{b,y}$) are comparatively larger but their senses of torque are identical unlike the

case of rotor profile. The rise and drop of C_{LT} is thus observed in the blade profile, which is absent in the corrugated airfoil that is subjected to lift force.

For the advancing profile, the corrugation increases the positive C_{LT} over $\phi_A \approx 90^o$ to 135^o as compared to non-corrugated blade design, while parallelly introducing the negative C_{LT} limited for very small strips of ϕ_A (region A_1) (Fig. 5.8a) in-between the strips having increased positive C_{LT}. This limits the increase of positive C_{LT} due to corrugation on the advancing profile. For the returning profile, the corrugation transforms the negative C_{LT} distribution over almost entire range of the ϕ_R into the intermittent distribution positive and negative C_{LT} for $\phi_R \approx 90^o$ to 150^o. However, the area bounded by the positive C_{LT} is larger than that of the negative C_{LT} resulting into the net positive torque experienced by the corrugated profile. Moreover, the decrement in the magnitude of the negative C_{LT} is also observed outside the region R_1 (Fig. 5.8b), *i.e.*, the corrugation also influences C_{LT} distribution on the non-corrugated portion of the returning profile. This type of changes in C_{LT} distribution is absent in the case of the corrugated advancing profile. It is to be noted that the substantial change of C_{LT} trend occurs only in the highlighted regions A_1 and R_1.

Qualitatively, the area bounded by the C_{LT} curves (Fig. 5.8a) for the advancing corrugated and non-corrugated profiles are approximately 29.9 and 37.5, respectively. This clearly shows that the corrugation diminishes the total positive C_{LT} contributed by the advancing profile. For the returning profile, the areas bounded by the C_{LT} curves (Fig. 5.8b) with and without corrugation are 5.24 and -10.07 (negative sign is due to negative C_{LT}), respectively. These values clearly indicate that the corrugation fully transforms the C_{LT} from completely being negative to the positive. The net values of C_{LT} bounded area (combining both the advancing and the returning profiles) are 35.14 and 27.43, respectively, for the cases with and without corrugation. This shows that the corrugation directly increases the total local torque experienced by the rotor for the present case of $\theta = 0^o$.

As observed in Section 5.3.1, the advantageous traits of the corrugation are only limited to the lower values of λ. With the increase in λ, the strength of the stagnation region on the advancing profile decreases while that of the returning profile increases. This is due to very high and very low relative velocity (with respect to incoming wind velocity) of the returning and advancing profiles, respectively. The higher strength of the stagnation region at the returning profile would deteriorate the effectiveness of the corrugation on the returning profile in terms of producing low C_{Pr} and hence the high positive C_{LT}. Similar type of C_T trend with respect to λ has been

also observed in Bach type (Ushiyama et al., 1986), airfoil type (Tartuferi et al., 2015), and fish ridge type (Ma et al., 2017) blades. Even if the introduction of corrugation to the blade profile is not improving C_T over the entire range of λ, it is still successful in lower λ values and inducing lower C_{Pr} region resembling that of the adapted corrugated airfoil inside the valleys. Thus, the present numerical analysis of the corrugated profile has shown promising results as compared to the non-corrugated profile and can be a potential candidate for the blade design of future Savonius wind rotors.

5.4 Concluding Remarks

Numerical investigation of this chapter demonstrates that the novel corrugated profile inspired by the dragonfly wings has the potential to perform superiorly over the non-corrugated profile. By exploiting the principal flow conditions (Section 5.2.3) using corrugation, the performance of the rotor profiles can be improved. Besides, the location of the corrugation is a key factor in improving the blade design and hence the rotor performance. In the present investigation, the corrugation away from the tip of the corrugated profile (Profile-2) is found to be beneficial rather than being located on the profile tip (Profile-1). However, the higher torque is obtained at low λ values in case of Profile-2. The parameters C_{Pr} and C_{LT} are then evaluated to find the performance improvement of Profile-2. This is to understand whether or not the corrugation in blade profile works similarly to that of the corrugated airfoil by strengthening the lower C_{Pr} distribution.

The numerical results reveal the potential of corrugation in enhancing the low C_{Pr} region on the convex sides, especially for the returning profile. This enhancement is found to be ineffective in the C_{LT} contribution as the length segments forming the valleys of the corrugation produce the intermittent negative C_{LT} values simultaneously with positive C_{LT} values. Thus, the increase of positive C_{LT} is very much limited and is found mostly distributed towards the returning profile. It can be stated that the performance of the corrugated blades needs to be checked experimentally to support the numerical findings of the present investigation. Further, the parametric study consisting the influence of different parameters such as depth of corrugation and corrugation angle on the rotor performance can also be conducted.

Chapter – 6

Development of Surrogate Models for Performance Prediction

Chapter Layout:

Overview

This chapter documents the development of the surrogate models based on the soft computing techniques such as artificial neural network (ANN) and genetic expression programming (GEP). The reasons why the ANN and GEP have been chosen for the present case are covered in this chapter. A model function is hypothesized establishing relationships among the input variables (design and operating rotor parameters) and output variable (rotor performance). The detailed training procedures are then documented in this chapter. Detailed topology of the ANN and the GEP models are narrated. The discussion on evaluation of the trained surrogate models is provided in the form of regression plots, error histograms, training parameters and others. This chapter ends with the discussion on the efficacy of each surrogate model in comparison to each other.

6.1 Background

Based on the objectives set in Sections 1.5 and 2.5, the present chapter is focused on the development of the surrogate models to predict C_P using soft computing techniques. For the C_P estimation of based on input values of design and operating parameters, an empirical model was developed by Kamoji et al. (2009), however, this model incorporated only a limited number of input design variables. To tackle this inadequacy of the empirical approach, researchers opted for different soft computing models, that can approximate a function of C_P having multiple design parameters as input variables by exploiting documented experimental data. One of such techniques is the ANN that is quite capable and convenient for the purpose of function approximation and modelling hidden phenomenon comprising the multiple input and output variables (Hornik et al., 1989). As reported, this function approximation capability of ANN is widely utilized in different technical domains, *e.g.*, estimation of diesel engine performance and its emission products using plant-oil based fuel (Kshirsagar and Anand, 2017), shear strength of concrete slabs (Tran and Kim, 2021), effects of different design parameters on cold-formed steel members (Pala and Caglar, 2007), parametric study of electric field enhanced ultrafiltration (Sarkar et al., 2009), prediction of flow force and flow rated acting on hydraulic valves with design dimensions as input (Cao et al., 2004), estimation of thermal error on feed axis of machine tool using temperature values as input parameter (Li et al., 2020) and others.

Moreover, for the function approximation problems, many other techniques such as splines, multivariate adaptive regression splines (MARS), classification and regression trees (CART), support vector machines (SVM), adaptive neuro-fuzzy inference system (ANFIS) and others are also prevalent (Dhar et al., 2010). For example, Alizamir et al. (2020) predicted the solar radiation using 6 different function approximation techniques including MARS, CART, ANN and ANFIS. The ANN is found to have performed best when the relationship between the input and the output variables are highly non-linear as compared to other techniques. As reported, the MARS is also capable of handling both linearity and non-linearity of the variables, however, it is prone to overfitting. Similar outcomes are also observed for SVM and CART. In the study, it was reported that the ANN performed slightly better than the other mentioned techniques. Szul et al. (2020) approximated a model for heat energy of buildings by implementing different techniques and stated that the ANN provided lowest error as compared to other techniques like MARS, CART and SVM. Similarly, Ahmadi et al. (2019) developed a model to estimate the dynamic viscosity of silver/water nano-fluid and demonstrated a better

performance of ANN in comparison to MARS and other regression techniques in terms of error minimization. Similar trend was also observed during the performance prediction of hot mix asphalt pavements carried out by (Kirbaş and Karaşahin, 2016). In some of the reported studies, no significant superiority of the ANN was observed in comparison to the aforementioned techniques (Alizamir et al., 2020; Wu et al., 2021), however, the performance demonstrated by the same was not degrading. In view of the above observations and merits of ANN technique, it can be considered as a prospective candidate for its implementation as a function approximation tool for the performance estimation of the Savonius rotor.

However, it is important to note that the function approximation provided by ANN is not in the form of traditional mathematical expressions. This is made possible by comparatively latest technique named 'Genetic Expression Programming (GEP)' which is based on evolutionary algorithm. Due to robustness and effectiveness of this technique, it is being substantially used in different problems *i.e.* symbolic regression problem (function approximation), classification problem, real parameter optimization problem, combinatorial optimization problem and others (Zhong et al., 2017). The examples undermentioned in this paraphrase illustrate capability of GEP for its use as an optimization and function approximation tool in wide range of research fields. In the field of rock mechanics, Ozbek et al. (2013) formulated mathematical expression of estimating uniaxial strength of different rocks by using weight, water absorption, porosity etc. as independent variables. Li et al. (2018) used GEP to construct a mathematical expression of ordinary differential equation for collected experimental data. Murad et al. (2020) approximated strength of reinforced concrete joints using experimentally collected data of concrete compressive strength and joint dimensions as independent variables. In field of meteorological science, Yassin et al. (2016) developed function approximation of evapotranspiration (evaporation and transpiration) of water from ground surface to atmosphere in arid region by ANN and GEP models and compared them. A similar comparison study of ANN and GEP was carried out by Martí et al. (2013) to estimate water quality parameters in irrigation. The GEP has also been implemented in the field of renewable energy. For example, Sadeghi et al. (2020) used GEP to estimate thermal performance of evacuated tube solar collectors trained by numerically simulated data. Thus, GEP is a potential candidate as an optimization and function approximation tool. However, the implementation of GEP as either function approximation or optimization has not been done in the field of wind turbines.

It is highly desirable to consider these techniques to predict different performance parameters of Savonius rotor from the known governing variables. Having established this formulation, it

is very useful to design a Savonius rotor and its installation in a geographical location. Details of current objectives in this regard, are mentioned in Section 6.2.

6.2 Goal of Using ANN and GEP in the Savonius Wind Rotors

6.2.1 Goal of ANN

The ANN is a wide field that covers mathematics, neurology, computer science and engineering, statistics, data processing and others. As mentioned earlier, the ANN training in case of only one type of the blade profile with few of the design variables (less than five variables) has been reported in the literature. Considering this, a new goal is defined and accordingly a brief literature review of ANN is presented herein. The novelty of the current investigation is that the combined data of the different blade shapes has been used to train ANN for the application of function approximation task, which has not been yet considered. The aim of this work is to check whether or not the unknown governing flow physics and torque generation is similar for all types of blade profiles and shapes of Savonius rotor.

Based on the studies reported till date, a novel normalized/standardized design representation method applicable to all types of blade profiles/shapes is proposed. The proposed influencing design parameters are depicted in Fig. 6.1(a). The typical multi-staged (n_s = 3 and 2) rotors is shown in Fig. 6.1(b); while the number of blades (n_b = 3 and 2) in a rotor is depicted in Fig. 6.1(c). Now, based on the available data, the performance of the Savonius rotor can be expressed by Eq. 6.1 that consists of 13 input variables. Out of these 13 input variables, the variables like D, p, q, θ_1, θ_2, e, s, D_o and U are depicted in Figs. 6.1(a) through (c), while the variables *viz.* H, A_{wt} and U are illustrated in Fig. 6.1(d). The reason behind the selection of these input variables is explained and elaborated in the following section.

The selection of appropriate numerical values of the variables (p/q, θ_1, and θ_2) that influence the blade shape is discussed as a hypothesis proposed in Table 6.1. The physical/natural phenomenon by which the 13 independent variables (Eq. 6.1) influences the single dependent variable namely the Savonius rotor performance in terms of C_P is unknown. Still the hidden mechanism of the unknown natural phenomenon is tried to be formulated by collecting the experimental input and output data. This type of study in the realm of machine learning is known as the inverse problem (Masters, 1993). The inverse problem in this study is basically a high dimensional nonlinear function approximation and multiple regression problem (Masters, 1993). There are many other techniques like splines, additive models, hinging hyperplanes, MARS (multivariate adaptive regression spline), and CART (classification and

regression tree) to address the problem of multidimensional nonlinear function approximation, but ANN is proved to be consistent and efficient among the aforementioned techniques (Dhar et al., 2010). It is therefore decided to use ANN techniques to address the present problem.

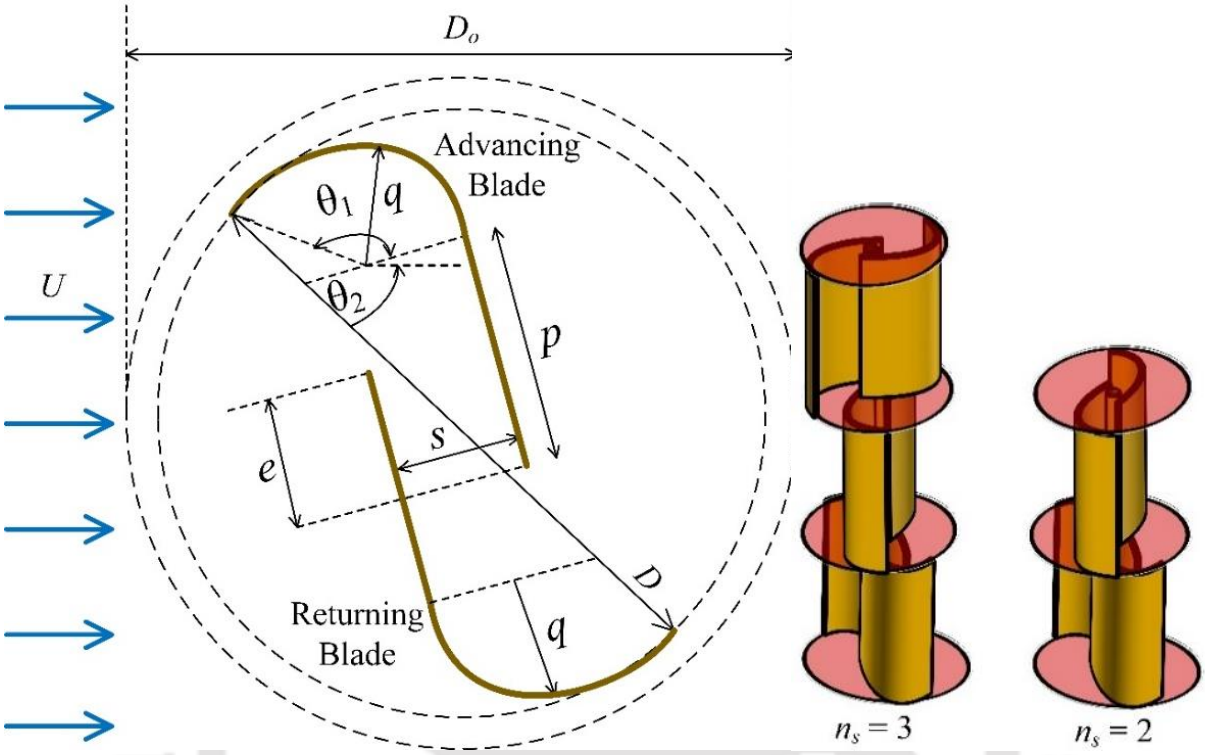

(a) Cross section of two bladed rotor

(b) Depiction of 3- and 2-staged rotors

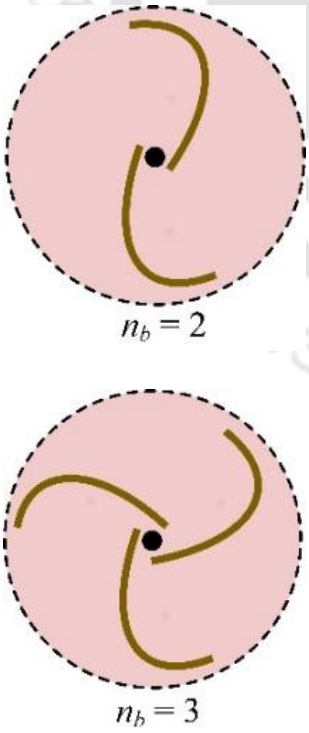

(c) Depiction of 3- and 2-bladed rotors

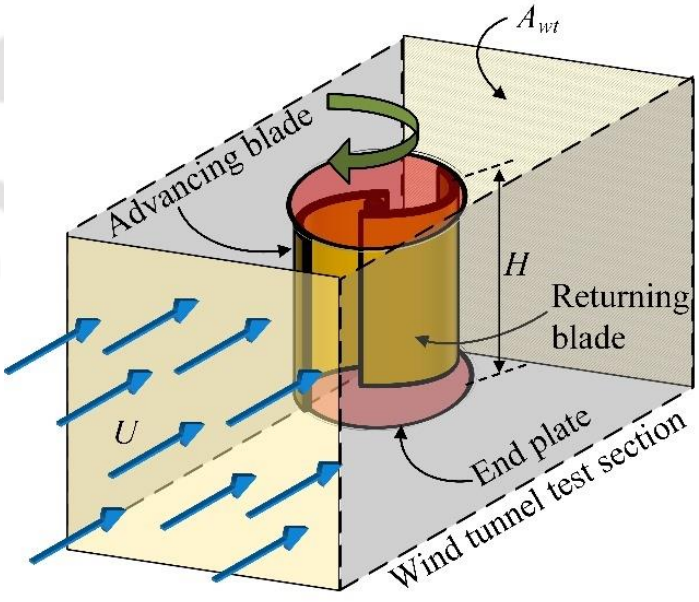

(d) Savonius rotor inside the wind tunnel

Figure 6.1 The novel normalized/standardized design representation

$$C_P = f\left(D, H, A_{wt}, \frac{p}{q}, \theta_2, \theta_1, n_S, n_B, e, s, D_0, U, \lambda\right) \tag{6.1}$$

Table 6.1 Hypothesis and goal formulated for ANN of Savonius rotor

Hypothesis	New set of input variables are defined to formulate the shape of the blades *i.e.* p/q, θ_1, θ_2 as depicted in the Fig. 6.1(a). Using these proposed variables, the different blade shape can be expressed as below; 1. For semicircular blade, $p = 0$ because there is no straight blade part. The curvature of the blade is on both sides of the blade's centre, and hence, $\theta_1 = \theta_2 = 90^\circ$. 2. For Bach type blade, p is not equal to zero but there is a finite value, which gives finite value of p/q. The blade curvature is formed only on the single side of the curvature centre and another side is straight. Therefore, $\theta_2 = 0$ and θ_1 is any finite value. 3. The value of proposed variables for Benesh type blade would be similar to that of Bach type blade, except the nonzero value of θ_2. This method will bring uniformity among the data points of all the three blades and can simultaneously be used to train the network.
Goal	Implementing the Hypothesis, the goal of this study is to formulate Eq. 6.1 using ANN with supervised learning techniques. Using the experimental data in wind tunnel for all the aforementioned three types of blades, an attempt is made to train the neural network. If the attempt is successful, it can be concluded that the flow physics and governing mathematical function (Eq. 6.1) to estimate rotor performance for each of the above blades are similar.

In this chapter, the training of the neural network is performed using *MATLAB R2020b* software. The subsequent sections deal with the basic introduction and working principle of neural networks, data selection and modifications implemented on it, determining the topology of the ANN with sufficient literature review and discussion of the results obtained. Out of several popular types of ANN architectures, the suitable type to formulate Eq. 6.1, is discussed in Section 6.4 with proper reasoning. In Section 6.7, various questions that are essential to be answered before determining the neural network topology *i.e.* optimum number of hidden neurons, learning algorithms, activation functions, weights and biases initialization algorithms, are reviewed from the available research.

6.2.2 Goal of GEP

The goal of GEP is similar to the goal of ANN presented in Section 6.2.1. The only difference is that the GEP facilitates the possibility of finding function approximation in a more tradition mathematical way (for example, $y = f(x)$ – an analytical function) which is not possible for ANN. The role of Eq. 6.1 and hypothesis presented in Table 6.1 is consistent for both GEP as well as the ANN.

6.3 Explanation on Choice of Variables for Function Approximation

The essence of this section is extracted from the literature review on Savonius rotor flow physics and experimental design optimization. The total local torque is the summation of the local torque produced by each and every infinitesimal length of both the advancing and the returning blade surfaces. This local torque produced is the function of the pressure difference between its convex and concave sides and its moment arm created with respect to the rotor centre. Out of both, the former one is governed by the blade shape and the later one is by the length of the blade, or in other words, the rotor diameter (D). It is also reported that the change in D while maintaining constant projected area of the rotor causes a change in the rotor performance. Hence, D is chosen as one of the independent input variables as it directly influences the torque generation. The blockage of the rotor, which is defined as the ratio of the rotor's projected area ($D \times H$) to the wind tunnel's test section area (A_{wt}) also influences the rotor performance. Since this study consists the available experimental wind tunnel data, the A_{wt} and the rotor height (H) should be included as the independent variables. Further, it is not required to include rotor's projected area separately, because it is merely the multiplication of the independent variables D and H.

It is understood that the pressure difference between convex and concave sides of the blade is one of the influencing factors of the local torque (Fujisawa and Gotoh, 1994). The value of this pressure difference varies over the surfaces of both the rotor blades during rotation. In addition to that, the distribution of this pressure difference is not identical for both the advancing and returning blades because of their dissimilar relative velocities with respect to free stream velocity in terms of their magnitude and direction. This pressure distribution on the blade surface changes with the blades shape that influences the torque generated, and hence, the rotor C_P. Thus, the variables narrating the blade shapes *i.e.* p/q, θ_1, and θ_2 (hypothesis-1) need to be included into the list of the input variables. These three input variables are depicted in Fig.

6.1(a), where p and q represent the straightness and the curvature part of the blade. The distribution and spread of the curvature are defined by the variables θ_1 and θ_2.

In two-bladed Savonius rotor, one blade works as advancing blade, while the other as returning blade. This role of blades can be manipulated in three and multiple-bladed rotors, which can alter the pressure distribution on blade surface and hence the torque generation. Thus, the numbers of blades in a stage (n_s) needs be included in the set of independent variables. It is known that the total local torque is the function of the rotor angle, and hence, the rotational motion of the rotor which gives a periodic repetition of the total local torque value. As the total local torque value is non-uniform and periodic over the time scale, the net torque (T) generated by the rotor is expressed as the mathematical average value of total local torque distribution over a cycle. This calculated average torque value is sufficient to compare the performance of two different rotors, theoretically. However, a large Savonius rotor gives fluctuating torque which can affect the structural strength of the rotor and its assembly. Moreover, a single-stage rotor has a lower value of starting torque at lower rotor angles, and this sometimes makes a single-stage rotor to have non-self-starting characteristics. To mitigate these issues, the researchers have implemented a design of multi-staging (number of stages = n_s) with each stage having the phase angle difference equal to $180°/n_s$. Thus, n_s has proven its eligibility to be included in the set of the input variables.

The pressure distribution on the concave and the convex surfaces of both the advancing-returning blades is a result of different types of flow patterns *i.e.* the Coănda flow over the convex side of advancing blade, pressure recovery flow on the concave side of returning blade leaking through the gap (s) as well as overlap length ϵ and stagnation flow towards the upstream side of both the blades. Out of these flows, the Coănda flow and the stagnation regions depend on the blade shapes. On the other hand, the pressure recovery flow on the concave side of returning blade depends on the combination of the gap (s) and overlap (e) lengths. Many researchers have tried to investigate the mechanism of the pressure recovery flow and have found interesting insights into the flow physics of the rotating rotor. Due to stagnation point created on the concave side of the advancing blade, some part of the upstream flow is forced to move through the overlap and the gap region which impinges on the concave side of the returning blade creating a high-pressure region. This high-pressure region diminishes the effect of high drag force of the stagnation region at the returning convex surface, this results into the net decrement of the negative rotor torque, thereby improving the rotor performance. This phenomenon has also been observed experimentally by the researchers (Fujisawa, 1992). Since

the e and s influence the torque generation actively, both the variables are necessarily to be included in the list of the input variables.

Since the stagnation points are present on the blade surfaces towards the upstream flow side, the fluid tends to pass from the stagnation region through the top and bottom surfaces of the rotor (perpendicular to the rotor axis) causing deterioration of the rotor performance. In order to capture this high-pressure fluid of stagnation region, researchers have implemented the end plates with D_O diameter and observed the improvement of rotor performance. Thus, the diameter of end plates (D_O) has proven its candidature as an independent input variable.

In wind tunnel testing, it is found that the performance of Savonius rotor depends on the free stream velocity (U) due to the blockage effect. As the rotor is placed inside the wind tunnel test section, the minor increment in U can be observed due to the change in effective test sectional area of the tunnel, and this results into the variation of rotor performance (Pope and J. J. Harper, 1966; Ross and Altman, 2011). Additionally, it is very common that the flow conditions in experiments is defined using the Reynolds number (Eq. 2.10) but in this case D has already been selected as input variable and hence the remaining variable U should be selected as input variable. However, as the working fluid is air, the density (ρ) and dynamic viscosity (μ) of air have been ignored because of their low variability over temperature in the incompressible flow regime under consideration. These facts indicate the suitability of U as the input variable. The last one remaining in the list of the independent input variables is the λ expressed by Eq. 2.8, and this depends on both the D and U. Though the policy of taking only the independent variable without any other mathematical manipulation and inter-variable relationship is implemented, λ is chosen as the input variable whose only independent part is ω. The reason behind selecting λ as an input variable is that the power characteristic of any rotor is prevalently represented by C_P and λ. Like λ, the C_P (as expressed in Eq. 2.7) is one and only dependent output variable, that contains an independent part as torque in form of torque coefficient (C_T). Thus, the power characteristic curve of C_P versus λ of the rotor is governed by the 13 input variables as mentioned.

6.4 ANN Architecture

The idea of using the neural network structures was first introduced by Warren S. McCulloch and Walter H. Pitts in the year 1943 (McCulloch and Pitts, 1943). Based on this nonlinear modelling of neuron, Frank Rosenblatt proposed the perceptron model for supervised learning method (Rosenblatt, 1957). The artificial neuron used in the neural networks mainly consists

of the synapses, summing point, activation function and a bias as shown in Fig. 6.2. The synapses, which are also known as the weights, are basically a connecting links between the input signals and summation junction. The task of the synapses is to multiply input signal with constant mathematical value and generate a modified signal. Then the multiple input signals multiplied by different synaptic weight values are summed at the summation junction. In other words, the summation junction establishes a linear combination using the input signals and respective synaptic weights. The output of the summation might create a very large amplitude of the output signal because of the linear combination and summation of modified input signals of different values. Therefore, a characteristic activation function should be used to limit the amplitude of the output signal from the summation junction. In addition to the activation functions, the bias is used to increase or decrease the value of the output signal from the summation junctions.

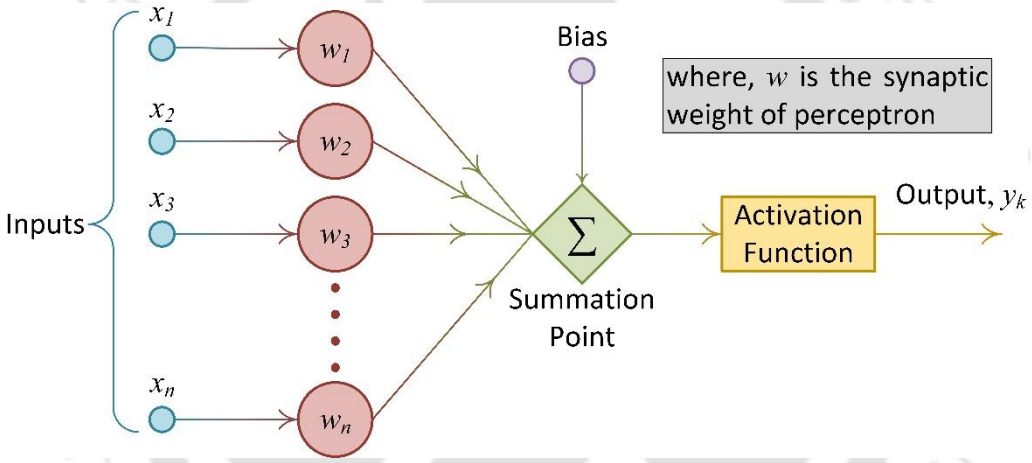

Figure 6.2 Structure of artificial perceptron

In practical use, the neural network with multiple perceptrons are used similar to the one shown in Fig. 6.3. These perceptrons can be interconnected using different neural network architectures *i.e.* single layer feed-forward networks, multi-layer feed forward networks, recurrent networks, and bridged networks. Out of these architectures, the multi-layer perceptron (MLP) is widely used for different problems like fitting, multivariable regression, pattern classification, and time series analysis (Haykin, 2009). It has been proven that the MLP has a property to be a general function approximator (Trenn, 2008). Further, MLP with back propagation algorithm can be used as nonlinear multivariable input-output mapping which is well suited for the proposed problem (Haykin, 2009). The MLP architecture consists of output layer, input layer and one or more hidden layers in between. The number of hidden layers is decided based on problem type, number of input-output nodes, approximation capability and many other factors. However, the universal approximation theorem proves that the single

hidden layer is sufficient for MLP to get uniform approximation for given function (Haykin, 2009; Hornik et al., 1989). In addition to that, for multivariable regression and function approximation problems, the single hidden layer is believed to be sufficient and usage of excessive number of hidden layers causes increment in false/local minima and unstable gradient (Masters, 1993). Therefore, in the present study, a fully connected MLP with single hidden layer has been implemented.

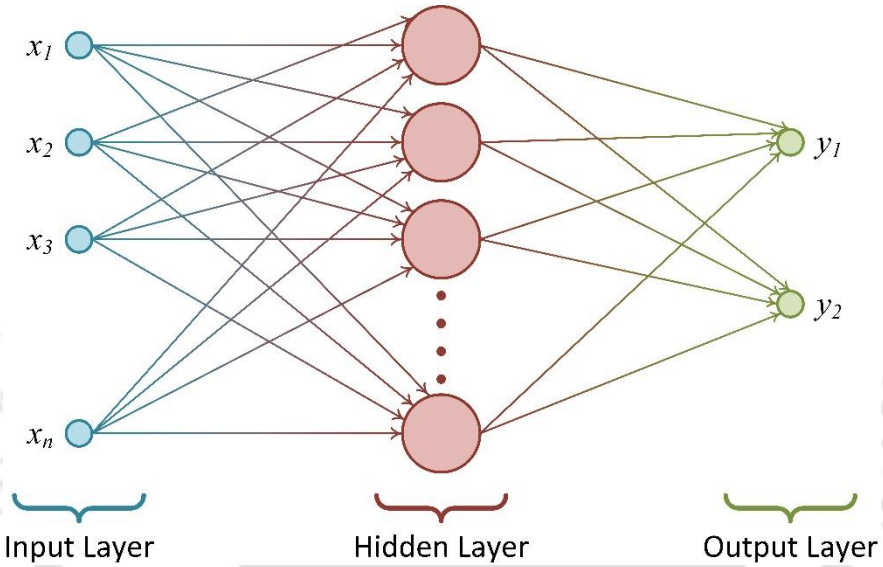

Figure 6.3 Single hidden layer MLP neural network

The architecture of single hidden layer fully connected MLP network is illustrated in Fig. 6.3**.** This architecture consists three layers *viz.* input, hidden and output layers. The input layer gives the input signals that is fed to the perceptrons of the hidden layer by the synapses. The MLP is fully connected, and hence, all the input signals are connected via synapses to each and every hidden neurons/perceptrons. The synaptic connections between the hidden layer and the output layer are similarly constructed as the connections between input and hidden layers.

Once the neural network topology is decided, the synaptic weights are decided by neural network learning. The popular method for neural network learning is back propagation algorithm. This algorithm is a combination of two phases *i.e.* forward and backward phases. In forward phase, the guessed synaptic weights are used with propagating input signals towards the output to generate the output signals. In backward phase, the calculated output signal is compared to the desired response for error estimation, and then, the synaptic weights are adjusted to minimize this error. There are many algorithms for adjusting the synaptic weights and to minimize the error. The choice of these algorithms is based on the size of neural network, the type of data and the type of problem.

6.5 GEP Architecture

John Holland invented the genetic algorithm (GA) in 1975 by blending the biological phenomenon like genetics and evolution theory into the computer system for optimization problem solving (Holland, 1992). The conventional techniques for optimization or finding minima-maxima problem are based on gradient descent method, which is a calculus based traditional approach. This technique opts for 'the best' solution among the set of the solutions. However, it fails sometimes to give the global optimum, instead it provides a local optimum solution. In contrary to this, the nature does not opt for 'the best', rather 'a better' than the 'available good solutions'. In order to execute this, the nature uses some distinctive mechanisms which are scientifically theorized as the concept of 'Evolution' and 'Survival of the fittest'. Therefore, the philosophy behind the optimization through the genetic algorithm is the 'constant improvement' and not the 'best result' (Goldberg, 1988). Researchers have suggested that the main advantage of the genetic algorithm is its robustness (ability to solve wide range of problems) compared to traditional techniques due to the qualities *viz.* direct use of coding, search from a population, blindness to auxiliary information, randomized operators (Goldberg, 1988). For the multimodal problem (a problem having multiple maxima and minima), global maxima or minima can be obtained by genetic algorithm very easily and efficiently. However, the process of getting to the maxima and minima is very fast in case of the traditional conjugate gradient method. In the traditional technique, the method of travelling from one point to another point is used in order to reach the maxima/minima, while the set of probable solution points are used simultaneously to get successive better set of probable solutions in the technique of GA. In other words, GA works with the coding of the parameter set, and not with the individual parameters themselves. This displays that the GA searches for a population of points and not for a single point.

In GA, the mathematical values are represented as the string of 0 and 1 having finite length, which is called a 'Chromosome'. The population of these chromosomes is called as a 'generation'. For the selection of the chromosomes for population, GA uses stochastic transition rules rather than the deterministic rules. These chromosomes are manipulated through the generations using the fitness functions, which is quite different than the calculus-based methods which are depended on first and second derivatives. The fitness function is nothing but a proxy of the concept of 'survival of fittest' in GAs. In function fitting problem the fitness function is defined by such a way that the maximum fitness value is obtained as the error tends to zero. The manipulation of the chromosomes is carried out using different

techniques, whose working principles are similar to that of natural evolutionary process *i.e.* mutation, crossover, transposition, inversion, recombination etc. The rate of these manipulations is defined by means of mathematical values in genetic algorithms. The aforementioned procedure is illustrated in Fig. 6.4.

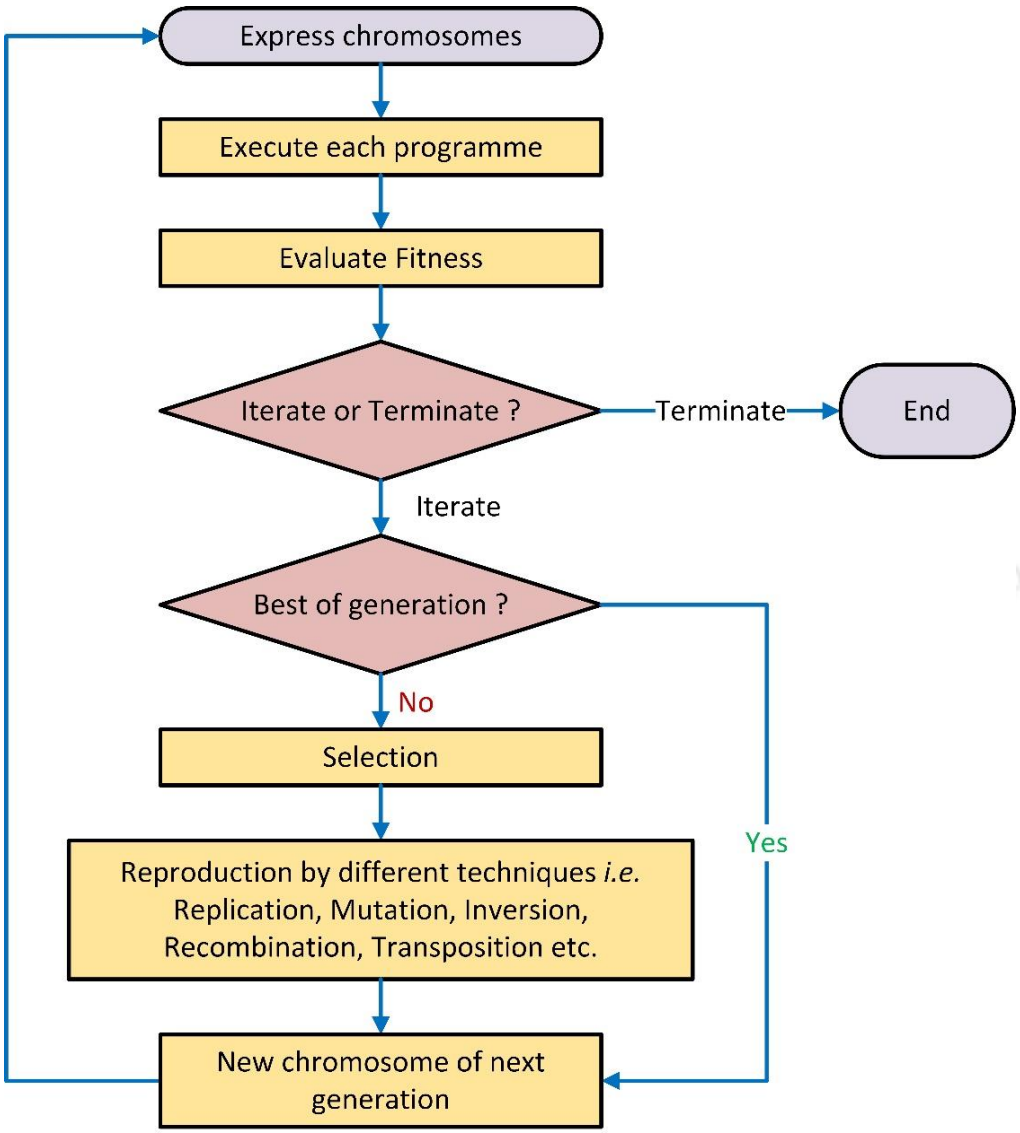

Figure 6.4 Flow chart of genetic algorithm

The chromosome of GA works both as the genotype (gene sequence) and phonotype (visible attributes of gene sequence). Therefore, the change to chromosome (genotype) displays the change of corresponding mathematical value (phenotype) in GA. The attributes like binary structural unit, dual nature (genotype-phenotype), simple language and fixed length of chromosomes cause limited functional use of GA. This limitation of fixed length chromosome/solution is addressed with the help of Genetic Programming (GP) invented by Cramer in 1985. The syntax of GP includes more versatile alphabets instead of using 0 and 1

by facilitating a richer way of representation. The chromosome in the GP is expressed in the form of 'Parse tree' and configured by LISP (List processing) programming language (Ferreira, 2005). The Parse tree is configured such a way that it represents a mathematical equation or expression. The working principle of chromosome manipulation of GP is done by changing and substituting the Parse tree branches. However, this sometimes leads to structural impossibility or syntactic errors. The provision in the GP algorithm has to be made to search for the syntactically erroneous structure in the successive generations of chromosomes, exhaustively. This sometimes makes the GP inefficient.

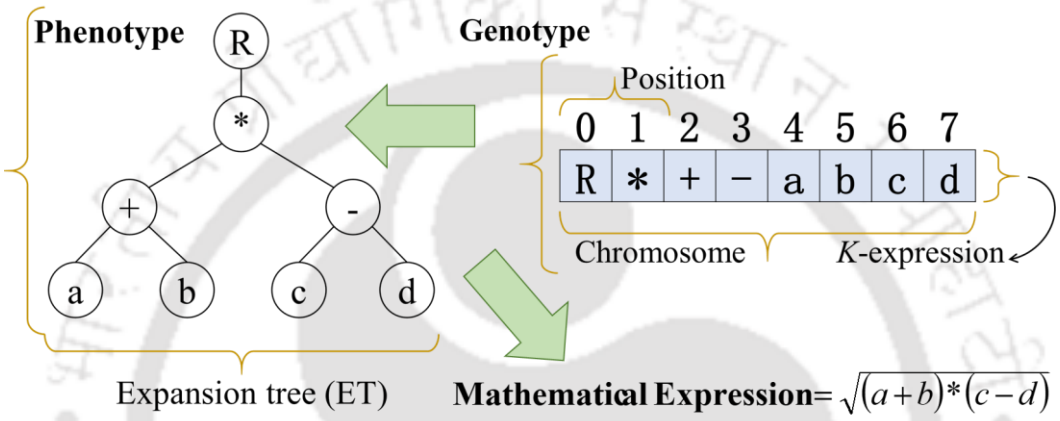

Figure 6.5 Syntax of GEP programming

The mentioned limitation of GP is eliminated by another technique named 'Genetic Expression Programming' (GEP) invented by Cândida Ferreira in 1999 (Ferreira, 2005). The syntax rules used in GEP are such that the chromosomes always generate syntactically valid structure after reproduction. In GEP technique, the chromosome works as genotype as well as the phenotype in the form of *K*-expression and expansion tree (ET), respectively. As an example, both the genotype and phenotype representations of a chromosome with their actual mathematical expression are depicted in Fig. 6.5. The genotype chromosome is a fixed length string containing variables (terminals) and mathematical operators. The *K*-expression of this genotype chromosome is then structured as ET with the help of '*Karva'* programming language. The ET is then read from top to bottom and left to right in order to extract the mathematical expression. However, it is important to note that the ET can also be read as the mathematical expression, neural networks or sophisticated decision tree as per the problem specifications. The length of chromosome remains constant during the reproductive manipulations; however, the length and branch configuration of ET are prone to the changes which in turn changes the mathematical expression. The change in mathematical expression is

then evaluated by the fitness function using available data points belonging to the case of function approximation problem. It is important to note that GEP uses the original genetic algorithm for problem solving with modified chromosome structure. Based on these advantages of GEP, it is advisable to implement it for solving undertaken function approximation problem instead of its predecessors. In this chapter, the software named *GeneXProTools 5.0* is used to construct and solve GEP topology.

6.6 Data Selection, Extraction and Processing in ANN

From the published literature, the wind tunnel experimental data of Savonius wind rotor have been collected in Table 6.2 and have been considered for ANN training.

Table 6.2 List of research papers used for ANN data extraction

Investigators	Types of blades	Variables
Fujisawa and Gotoh (1994)	Semicircular	e
Hayashi et al. (2005)	Semicircular	D, H, n_s, U
Kamoji et al. (2008)	Semicircular	D, H, n_s, U
Kamoji et al. (2009)	Bach type	D, H, e, p/q, θ_1, θ_2, U
Khan (1978)	Semicircular and Bach type	e
Modi and Fernando (1989)	Bach type	D, H, p/q, θ_1, θ_2
Modi et al. (1984)	Bach type blade	D, H, p/q
Roy and Saha (2015)	Semicircular, Bach and Benesh type	U
Sheldahl et al. (1978)	Semicircular	n_b
Ushiyama et al. (1986)	Semicircular	D, H, e, s, D_o

In literature, the dimensions of the rotor are often expressed in terms of ratios *i.e. AR*, *OR*, *GR*, and such others. In contrary to this fact, the current research uses absolute value of turbine dimensions in order to eliminate inter-variable functional relationship except the shape factor. However, the dimensions like p and q can also be expressed using the value of p/q and rotor diameter D with mathematical calculations. The p/q is defined as the shape factor of the blade, that determines whether the shape is semicircular, Bach or Benesh type. Moreover, '*e'* can also be used to differentiate the Benesh type blade and the Bach type blade as the former one has the higher 'e' value as compared to the later one. The D is defined as the distance between the peripheral points of the blades as shown in Fig. 6.1(a). For the multistage rotors, the total rotor height has been considered, and not the individual stage height. Instead of taking the blockage factor, the wind tunnel area (A_{wt}) and the rotor area (indirectly represented by the D and H) are used as the independent variables in order to take consideration of the blockage effect. The effect of the shaft diameter has not been included in this study. The free stream velocity selected

as one of the independent variables was measured in wind tunnel without placing the rotor. As the different blockage correction methods are used in different research works (Pope and J. J. Harper, 1966; Ross and Altman, 2011), all the power characteristics data have been converted into the non-corrected power characteristics for ANN training in order to bring uniformity in the dataset. The blockage characteristic will be addressed by ANN's relationship generating capability between multiple variables. The rotor without the end plates are taken as $D_o = 0$.

To make the data compatible with the neural network configuration, especially for the activation function, the value of the all individual variables is mapped in the range of [-1, 1] and then normalized using Eq. 6.2 and data provided in Table 6.2. Table 6.3 compiles the maximum and minimum values of all the variables with units.

$$x_{norm} = \frac{x_{tar} - x_{\min}}{x_{\max} - x_{\min}} \tag{6.2}$$

Table 6.3 Minimum maximum bounds of variables

Sr. No.	Variable	Max Value (x_{max})	Min Value (x_{min})
1	D	1.007 m	0.0966 m
2	H	1 m	0.12931 m
3	A_{wt}	28.89 m^2	0.16 m^2
4	p/q	4.3733	0
5	θ_1	150°	90°
6	θ_2	90°	0°
7	n_s	3	1
8	n_b	3	2
9	e	0.2 m	0 m
10	s	0.03535 m	0 m
11	D_0	1.3393 m	0 m
12	U	18 m/s	0 m/s
13	λ	1.913	0
14	C_p	0.516	0

The batch type supervised learning method is used to this type of data and problem. The total data are divided into three sets *viz.*, training, validation and test sets. The training set is used to determine the synaptic weights of the neural network during its training. The validation set is not directly used in training but it is used for the stopping criteria to validate the neural network. The test set is neither used to train the network nor to validate, but it is used to evaluate the network accuracy. The literature suggests that the total training data should be divided in three parts as 70%, 15% and 15% for training, validation and testing purpose, respectively (Bagheri et al., 2019). However, this is not compulsory and the data in current study have been divided

into 80%-10%-10%. The size of the training data also influences the generalization characteristics of the neural network. The estimated size of the training data can be determined using the thumb rule expressed in Eq. 6.3 (Haykin, 2009);

$$\text{Size of training data set } (N) = \text{Order of } \left(\frac{\text{Total number of free parameters}}{\text{Fraction of errors permitted on test data}} \right) \tag{6.3}$$

The neural network in this study has 13 input independent variables and would require 5 to 25 number of hidden neurons which gives the total number of free parameters (synaptic weights and biases) in the range of the 65 (13×5) to 455 (13×35). If the $1/10^{th}$ fractional error is allowed to the test data, the given thumb rule suggests at least 650 to 4550 input data points. The current data set contains approximately 1500 data points, and this is quite sufficient for the neural network training purpose. The data extracted for ANN is used to train the GEP. However, some of the input variables are adjusted accordingly to fit it into the GEP, which is discussed in Section 6.9.2.

6.7 Topology of MLP

6.7.1 Number of Hidden Neurons

The important step towards establishing neural network topology is to decide the number of hidden neurons (n_h) in hidden layer. Many studies reported provide empirical relationships to decide the number of hidden neurons based on number of input variables, number of output variables, degree of approximation, generalization quality, and training time (Sheela and Deepa, 2013). One such study is the mathematical analysis done by Trenn (2008). In the present study, the number of hidden neurons (n_h) in single hidden layer are determined based on approximation order (n) and number of input neurons (n_i) using Eq. 6.4 (Trenn, 2008).

$$n_h \geq \frac{\binom{n+n_i}{n_i}}{n_i+2}, \quad \text{if the condition } \binom{n+n_i}{n_i} \leq (n_i+2)\left(n_i+1+2\sqrt{n_i}\right) \text{is satisfied;}$$
$$n_h \geq \left\{ 2\sqrt{\binom{n+n_i}{n_i}+2(n_i+1)} \right\} - \{n_i+3\} \tag{6.4}$$

Table 6.4 Number of hidden neurons by different methods

n_i	n	n_h calculated by different method		
		Trenn (2008)	Li et al. (1995)	Shibata and Ikeda (2009)
13	2	>7	4.62	3.6
13	3	>37	-	3.6

From Eq. 6.4, one can get different values of n_h by using different combinations of n_i and n. Eq. 6.1 contains 13 input variables, and therefore, the problem undertaken has n_i = 13, and this is fixed. Table 6.4 shows the value of n_h for approximation order (n) 2 and 3. Literature also shows that the second and higher order approximation for neural networks perform better than the first order approximation (Li et al., 1995). Though the higher number of the hidden neurons improves approximation order and performs better, it deteriorates the generalization characteristics of the neural network (Hunter et al., 2012; Wilamowski and Irwin, 2011). Therefore, there should be an upper bound to the number of the hidden neurons. Moreover, this method considers the approximation order but it does not consider the number of output variables (n_o), which is the limitation of this method.

Li et al. have also suggested a rather simple empirical relationship as Eq. 6.5 to find n_h for n = 2, although in that study the network was used for time-series analysis (Li et al., 1995). This method has similar disadvantage as that of Eq. 6.4.

$$n_h = \frac{\sqrt{1+8n_i}-1}{2} \tag{6.5}$$

There are several empirical relations which relates both the number of input and output nodes to determine number of hidden nodes, instead of using approximation order (Masters, 1993; Shibata and Ikeda, 2009). One of these relations is presented as Eq. 6.6.

$$n_h = \sqrt{n_i n_o} \tag{6.6}$$

Based on these empirical relationships, the lower bound and upper bound on number of hidden neurons are found to be 5 and 37 for n = 2 and n = 3, respectively. Further to pinpoint the exact optimal number of hidden neurons (n_h), The exhaustive search methods are widely used by researchers (Roma et al., 2017). The exhaustive search method to determine optimum n_h laid between lower-upper bounds (Table 6.5) is discussed in Subsection 6.9.1.1.

6.7.2 Choice of Learning Algorithm

After determining the number of hidden layers and hidden neurons, the next step would be the selection of the appropriate learning algorithm. The choice of a particular learning algorithms depends on several factors *i.e.* size of neural network (small/medium/large), type of problem (approximation/classification/regression/etc.), learning time, accuracy and memory requirements. For this study, the number of the network elements (weights and biases) as mentioned before, are in the range of 65 to 325. Therefore, this neural network can be classified

as small to medium sized neural network based on *MATLAB guide* (Beale et al., 2010). To select the eligible learning algorithm, sufficient qualitative literature analysis has been carried out. Dhar *et al.* have carried out a detailed comparison and benchmarking among backpropagation learning algorithms *viz.* standard backpropagation, resilient backpropagation, conjugate gradient, Levenberg-Marquardt (LM), radial basis function, simulated annealing, neural fuzzy; for standard machine learning benchmarking problems *i.e. IRIS* problem, *XOR*, *N*-bit parity, two spiral problem, regression and approximation problems (Dhar et al., 2010). The study suggests the LM algorithm to be superior to other algorithms especially for function approximation and *IRIS* problem in terms of RMS error. *MATLAB guide* also illustrates the training of different approximation problems having different number of the network elements and concludes that the LM algorithm is best for small to medium sized networks, whereas the scaled conjugate gradient (SCG) method is best for large sized networks (Beale et al., 2010). Hagan and Menhaj (1994) also state that LM algorithm works efficiently for the neural networks consisting few hundred weights. Hunter et al. (2012) commented on the efficiency of LM algorithm among other 2^{nd} order algorithms. *Moller* theoretically studied the SCG algorithm and mentioned this algorithm to be very effective for the large-scale problem. This directs us to use LM algorithm to train the neural network in this study (Meiller, 1993). According to Wilamowski and Irwin (2011), LM algorithm is remarkably efficient and therefore should be strongly recommended for small to medium sized neural network function approximator and pattern classifier.

It has therefore been decided to use the LM algorithm to train the neural network. The LM algorithm is a second order, global search back propagation algorithm, which is a combination of both the Newton's method and gradient descent method (Haykin, 2009; Levenberg, 1944). The LM algorithm is designed to only support MLP architecture, batch learning approach and mean squared error loss functions that can be implemented by *MATLAB R2020b*.

6.7.3 Choice of Activation Functions

The activation function also referred as the squashing function or transfer function which limits the range of output values to some predefined limits. Theoretically, it has been proven that the single hidden layer MLP with simple sigmoid transfer function establishes the connections between input and output variables in the form of Fourier series sine transform (Menon et al., 1996). There are many types of activation functions such as standard sigmoid (logistic function), pure linear, hyperbolic tangent sigmoidal function (*tansig*), and hard activations functions. Out of these activation functions, the sigmoidal functions, especially standard (Eq.

6.7) and hyperbolic tangent sigmoidal function (Eq. 6.8) should be used for function approximation and multi-dimensional nonlinear mapping in order to ensure that the mapping function is differentiable (Bishop, 1998; Meiller, 1993). Though both the standard and hyperbolic tangent sigmoidal functions are desirable, the latter one is more advantageous because of its steeper derivative and its squashing ability in the range [-1, 1] (Rasamoelina et al., 2020). For approximation and multi-dimensional nonlinear mapping, it is effective to choose the hyperbolic tangent sigmoidal (Eq. 6.8) function and pure linear (Eq. 6.9) for the hidden layer and output layer, respectively (Bishop, 1998; Rasamoelina et al., 2020). It is also observed that the neural network with hyperbolic tangent activation functions at hidden layer converges faster than the standard logistic functions with minimum RMS error values (Meiller, 1993; Mohammadi et al., 2020). There are many experimental investigations in different scientific applications portraying best results using mentioned choice of activation functions (Bagheri et al., 2019; Mohammadi et al., 2020; Motamarri and Boccelli, 2012). However, the hyperbolic tangent sigmoidal function (*tansig*) (Eq. 6.8) is recommended in order to make the present neural network more efficient.

$$\text{Standard sigmoid function (logistic function): } \sigma(x) = \frac{1}{1+e^{-x}} \tag{6.7}$$

$$\text{Hyperbolic tangent sigmoid function (tansig) : } \tanh(x) = \frac{2}{1+e^{-2x}} - 1 \tag{6.8}$$

$$\text{Pure linear activation function : } purelin(x) = x \tag{6.9}$$

6.7.4 Random Number Generator

The convergence of MLP neural network depends on the initial value of the weights prior to the beginning of the network training. These initial values are generated using Mersenne-Twister pseudo random number generator in *MATLAB R2020b*, which is popularly used in machine learning applications (Matsumoto and Nishimura, 1998; Mohamad et al., 2010).

6.8 Topology of GEP

The chromosome of GEP is a member of the population in given generation. The chromosome contains either single gene (uni-genic chromosome) or multiple individual genes (multi-genic chromosome). In multi-genic system, the individual genes are interlinked mathematically with specified algebraic or Boolean operators. Figure 6.6 shows a multi-genic chromosome with two genes which are interlinked by algebraic summation function as the linking function. The

gene is made of two domains namely the head domain and the tail domain as shown in Fig. 6.6.

The head domain usually contains mathematical operators (*i.e.* +, -, *, /, Square Root-R etc.) and the terminals/variables (*i.e.* a, b, c, d, e). The tail domain is only made of terminals. The head domain is used to mould or encode the mathematical or Boolean function for the problem at hand, while the tail acts as a buffer between two successive genes in order to ensure the syntactically correct structure by providing enough terminals. These excessive terminals provided in the tail domain may or may not be used in the ET, for example, the syntactically correct 'Sub ET2' is built by {*, a, b} while the terminals and operators between position 3-8 remain unused which is unlike the 'Sub ET2'. There is no particular technique to decide the length of head, however, the number of functions {+, -, R, *, /} and number of terminals {a, b, c, d, e} shed light on deciding the length of head domain. For a given example shown in Fig. 6.6, the length of head domain is 4 (from position 0-3) and the tail domain is 5 (from position 4-8), resulting the length of gene as 9 (from 0 to 8). Based on the length of head, the length of the tail can be calculated using Eq. 6.10 (Ferreira, 2005).

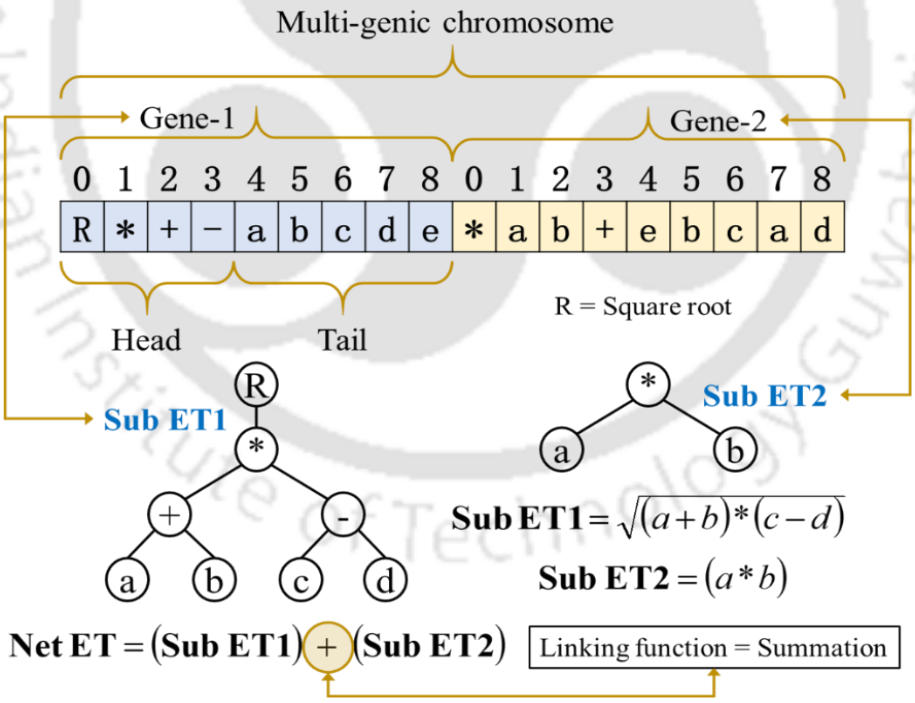

Figure 6.6 Topology of GEP chromosome

$$\text{Length of Tail} = \left[\left(\text{Length of Head}\right)\times\left(\text{Maximum Arity}-1\right)\right]+1 \qquad (6.10)$$

In Eq. 6.10, the 'Maximum Arity' is defined as the number of terminals/variables which can be linked by given mathematical function. For example, the function '+' links two terminals to

execute the mathematical operation of summation, resulting into Arity = 2. Similarly, the square root function 'R' results into Arity = 1. For every problem, the length of head is chosen *priori*. The summation of the head and tail length gives total length of a gene. All the genes in the multi-genic chromosome are equal in length.

According to the researchers, the multi-genic system is believed to be appropriate and efficient compared to uni-genic system for solving complex function approximation problems. Each gene in multi-genic systems is separated from another and is evolved independently. The genes are then expressed phenotypically in the form of individual 'Sub ETs' *viz.* Sub ET1 (belongs to gene-1) and Sub ET2 (belongs to gene-2). At last, the chromosome is fully expressed by linking the Sub ETs using linking functions *i.e.* summation, subtraction, multiplication, division, other Boolean operators etc. As an example, the Sub ETs are linked with summation function in Fig. 6.6. Considering this, the current GEP topology is constructed in the form of multi-genic system.

From literature review, it is found that the GEP-RNC (genetic expression programming with randomly generated numerical constants) is used for function approximation problem. This variant of GEP is similar to its predecessor but the gene contains different randomly generated numerical constants together with the terminals. Moreover, the library of these randomly generated numbers named as 'Dc' is placed adjacent to the tail domain of gene which is structurally independent to tail and head domain. The evolution of 'Dc' takes place similarly to the evolution of other part of gene. The number of numerical constants and their distribution range is decided *priori* based on experience. Thus, the GEP-RNC configuration is implemented in this study to solve the problem. The governing parameters of genetic algorithm are discussed in Subsection 6.9.2.

6.9 Results and discussion

As discussed in Section 6.6, the data presented in Table 6.2 is used for training, validation and testing for both ANN as well as GEP models. Random data partitioning is carried out independently for both the models. The data partition in terms of percentage is specified subsequently in Table 6.6 and Table 6.8 for ANN and GEP models, respectively. In both the models the experimental C_P values are considered as output and other remaining variables of Eq. 6.1 are considered as input variables. Thereafter, the ANN and GEP models are trained and results obtained are discussed in subsequent sections.

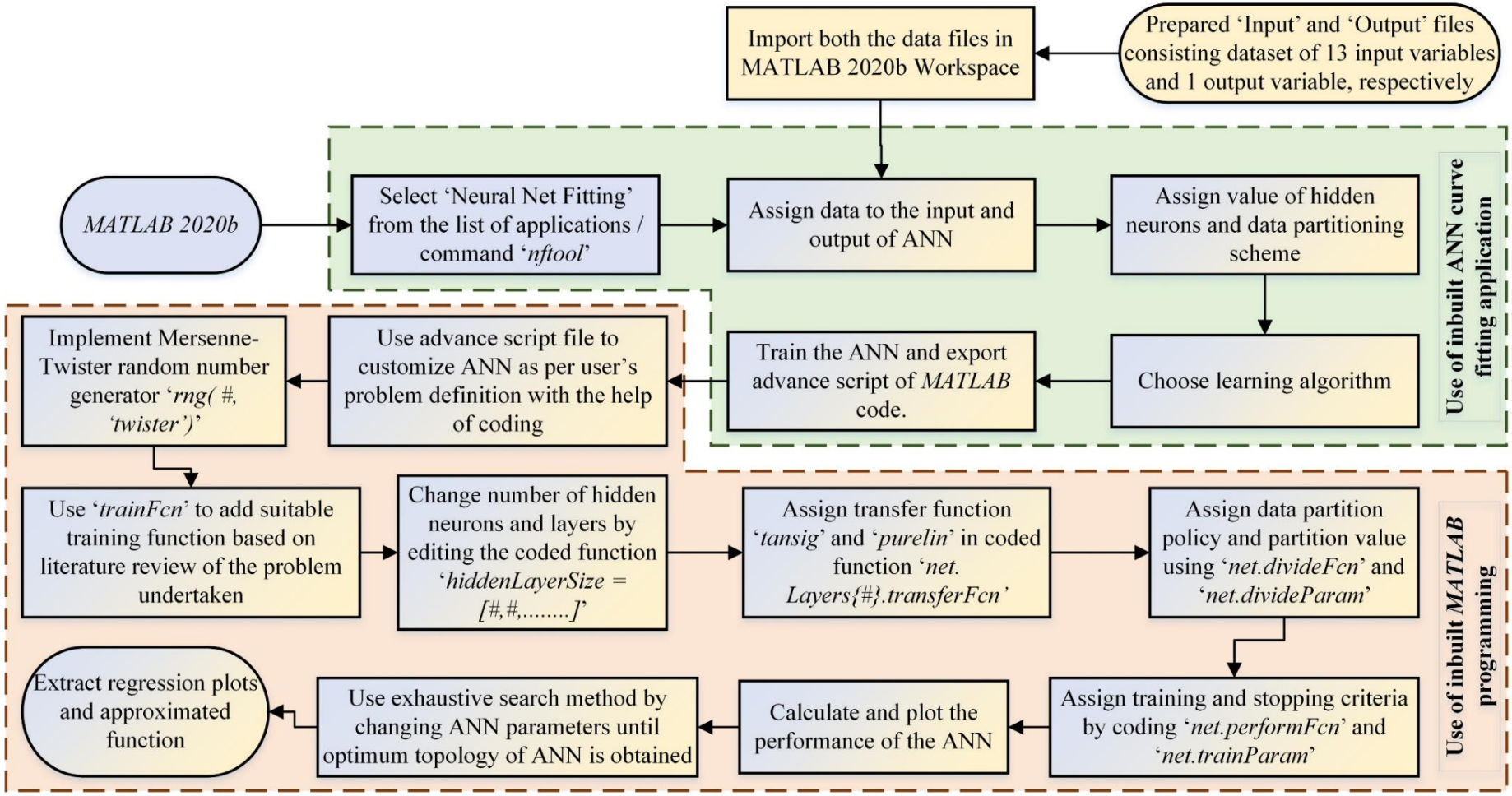

Figure 6.7 Procedure of ANN training using *MATLAB R2020b*

6.9.1 ANN model

In order to construct and train the ANN, the combination of both the inbuilt ANN curve fitting application of *MATLAB R2020b* and programming are adopted. The key steps of overall construction and training procedure of ANN is illustrated in the form of a flow chart (Fig. 6.7). The inbuilt ANN curve fitting application is very easy to use. However, the *MATLAB* programming is considered mainly to customize the tool for selection of wide range of transfer functions, data partitioning, weight initializations, learning algorithms.

The results obtained by following the procedure depicted in Fig. 6.7 are discussed in the subsequent Subsections 6.9.1.1 and 6.9.1.2.

6.9.1.1 Selecting Optimum Topology of ANN

It has been determined that the single hidden layer MLP neural network is to be used. Hence, the remaining task is to determine the optimum number of the hidden neurons. The lower and upper bound of the number of the hidden neurons are 7 and 37, respectively. For this purpose, neural network with different numbers of hidden neurons are evaluated using parameters *i.e.* network performance, correlation factor (R^2), relative error (ε). The expressions to calculate R^2 and ε are provided as Eqs. 6.11 and 6.12, respectively. The test data is used to calculate ε of the trained network using the mentioned equations. In Eq. 6.11, x_{mean} refers to the arithmetic mean value of the data and x_{norm} is calculated from Eq. 6.2.

$$R^2 = \frac{\sum_{1}^{N}\left(x_{norm} - x_{mean}\right)^2}{\sum_{1}^{N}\left(x_i - x_{mean}\right)^2} \tag{6.11}$$

$$\varepsilon = \frac{\sum_{1}^{n}\frac{\left|x_{tar} - x_{est}\right|}{\left|x_{est}\right|} \times 100}{n} \tag{6.12}$$

The value of R^2 lies between 0 and 1. When the value of R^2 tends to value 1, estimated value (x_{est}) and the target value (x_{tar}) of depended output variable (C_p) are highly correlated. This means that the neural network is fitting the actual experimental data properly. Therefore, it is necessary to train a neural network such that it would give a nearby unity value of R^2. As the network is trained, the gradient value gets lower and so the performance value decreases. The lower is the performance value, the higher is advantage of the neural network. Considering these three evaluation parameters, simulations have been carried out and the results are presented in Table 6.5.

Table 6.5 Performance of different ANN topologies

n_h	Performance on test data	R^2 on test data	ε % of test data
5	0.0022	0.7305	0.27
7	0.0014	0.8302	0.22
9	0.0058	0.9405	0.20
11	0.0019	0.7982	0.29
13	0.000432	0.9413	0.15
15	0.0013	0.8711	0.23
17	0.0014	0.8603	0.19
19	0.000639	0.9388	0.28
21	0.000533	0.9407	0.17
23	0.000455	0.9502	0.18
25	0.0013	0.8595	0.20
27	0.000343	0.9630	0.15
29	0.000706	0.9272	0.17
31	0.0011	0.8989	0.25
33	0.000383	0.9561	0.17
35	0.000255	0.9658	0.19

Table 6.6 Specification of optimum ANN topology

Parameters	Specification
Input	13
Output	1
Hidden layer of neural network	1
Number of neurons	27
Training/validation/Test Percentage	80%/10%/10%
Numbers of Epochs/Iterations	70
Back propagation algorithm	Levenberg-Marquardt
Mean Squared error	Range of 10^{-3}
Performance limit	Range of 10^{-4}
Number of the Validation check	20
Activation function for hidden layer	Tansigmoid (*tansig*)
Activation function for output layer	pure linear (*purelin*)

Table 6.5 shows that the value of ε is very low but the correlation between the estimated and the target test data value is lower for the neural network with lower number of the hidden neurons (5 to 17). Hence, it is decided to increase n_h and find better choice of the neural network. The increment in the value of R^2 is found with lower value of ε for the range of the hidden neuron numbers 17-29. In this range, the lowest value of ε (= 0.15%) has been obtained for n_h = 27, with R^2 = 0.9630 and the performance = 0.000343. These values of the parameters and number of the hidden layer neurons are found effective based on the number of different

input and output variables according to the literature in different scientific domain (Bagheri et al., 2019; Mohamad et al., 2010). If the number of hidden neurons is increased further from 27, the value of R^2 fluctuates around aforementioned optimum R^2, however, the ε also increases. This observation shows that the generalization characteristics of the neural network deteriorates and increases the error value ε, suggesting that 27 hidden neurons are optimum for the neural network. Finally, the operating parameters of the selected ANN are listed in Table 6.6.

6.9.1.2 Stopping Criteria for ANN Training

The operating parameters and neural network configurations are provided in Table 6.6. The stopping criteria of the training is set as the maximum fail of the validation checks. The performance of the neural network training is measured in terms of decrement in mean squared error (*MSE*) with each epoch. The formula for calculating the *MSE* is expressed in Eq. 6.12.

$$MSE = \frac{1}{N}\sum_{i=1}^{N}\left(x_{est} - x_{tar}\right)^2 \tag{6.12}$$

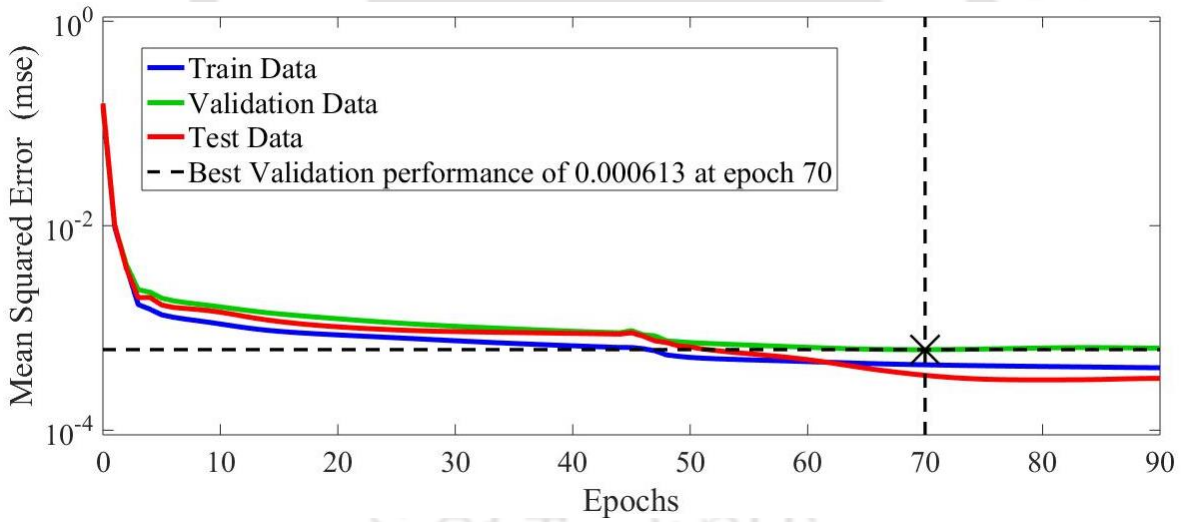

Figure 6.8 Performance curve of the neural network training

It is not possible to decrease the *MSE* continuously with each epoch for the infinite time. After getting minimum *MSE* in this training problem of the neural network, the learning process fails to decrease the *MSE* of the validation data continuously for 20 times (which is the set stopping criteria). Therefore, the 70th epoch is taken as the best epoch of the trained neural network. This method of stopping in the learning of the neural network is called as the early stopping method. The training above the 70th epoch can be denoted as the overtraining of the network. In Fig. 6.8, it is clearly visible at 70th epoch that the error in training data decreases with epoch, but on

contrary, the error in the validation data and especially the test data increases. This clearly shows that the overtraining is done after the best epoch. However, all the three curves are closely packed and this suggests that there is not any major error difference between testing, validation and the training phase. Thus, the selected network is the best for the data selected in the present study.

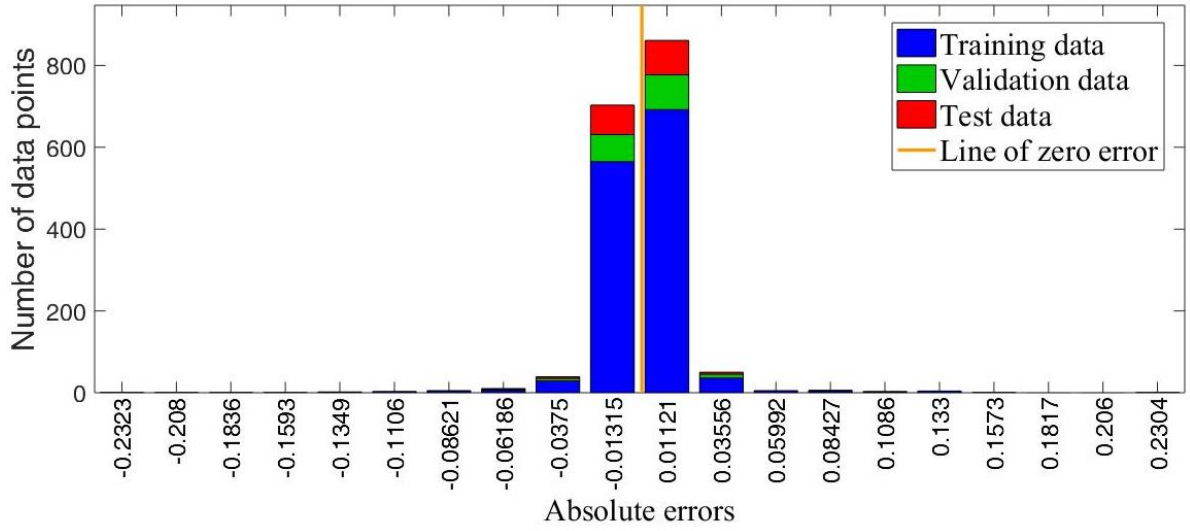

Figure 6.9 Error histogram of the trained neural network

The error histogram is presented in Fig. 6.9 in order to get qualitative and the quantitative idea of the error distribution. This histogram shows how many data points having near zero absolute errors out of total number of the data points. Figure 6.9 shows that the majority of the data points are distributed near zero absolute error line and it is consistent for all three data sets *i.e.* training, validation and testing. The expression of the absolute error is provided in Eq. 6.13.

$$\text{Absolute error} = x_{est} - x_{tar} \tag{6.13}$$

Figures 6.10 and 6.11 show the comparison between the estimated value of C_P by the trained neural network and the actual experimental (target) value of C_P for both the entire data set as well as test data test, respectively. It is important to note that the selected test data for Fig. 6.11 have not been used during the training. In addition to that, the random number generator has been used to randomly select the test data from the total compiled data in order to eliminate human bias and prejudice against particular dataset. Figures 6.10 and 6.11 suggest that the trained neural network is successfully predicting the performance of the rotor based on the prescribed set of input data for all of the three blades *i.e.* Semicircular, Bach and Benesh types.

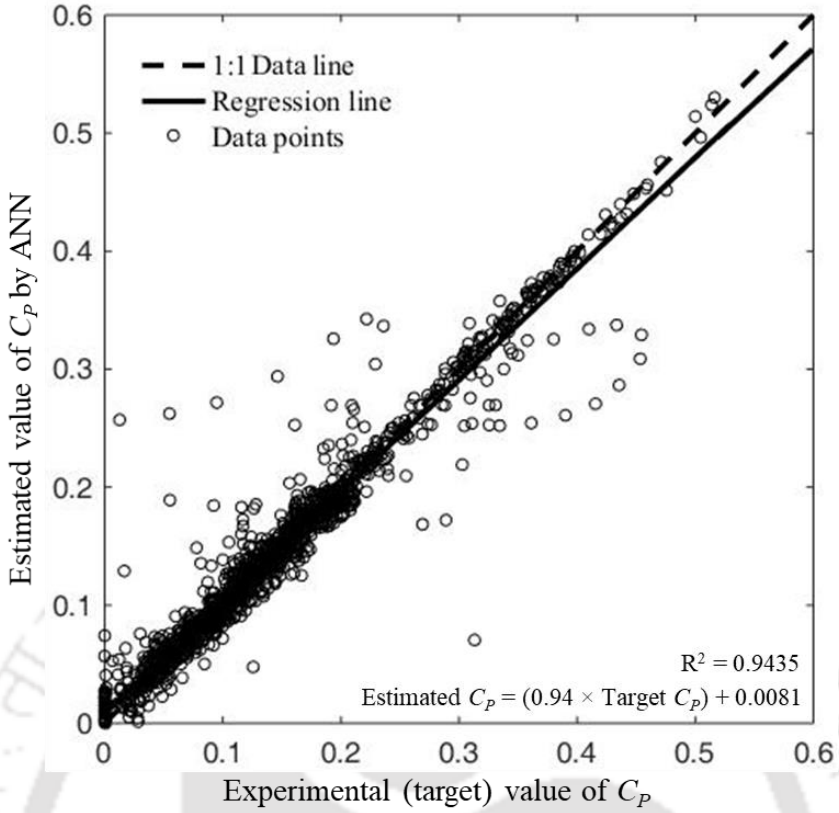

Figure 6.10 Estimated vs Experimental (target) C_P value of all data using ANN

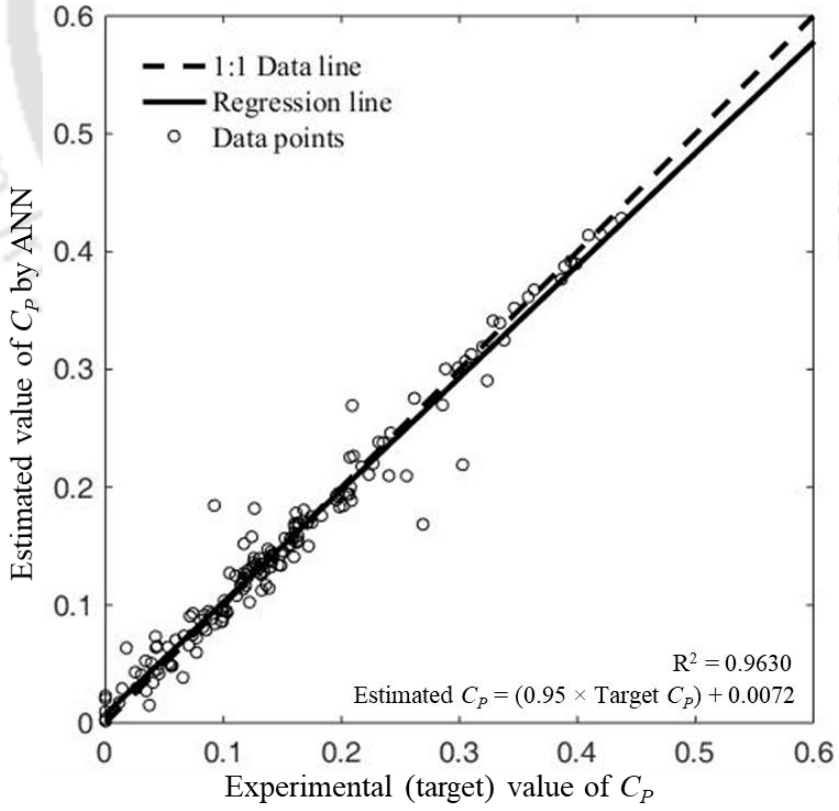

Figure 6.11 Estimated vs Experimental (target) C_P value of test data using ANN

6.9.2 GEP Model

Literature suggests that there are no 'thumb rules' for selecting the design and evolution parameters for GEP topology (Ferreira, 2005). Table 6.7 summarizes the specification of optimum GEP parameters which are based on the exhaustive search methodology. The data used in GEP is same as used in ANN. It has been found that the Bell-shaped curve obtained in characteristic C_P vs λ graph can be expressed as Eq. 6.14. The equation gives the hint that the C_P is approximately a polynomial of λ, which leads us to add the variables λ, λ^2 and λ^3 as terminals of GEP (Paraschivoiu, 2002). Out of the variables covered in Eq. 6.1, the variables namely the D, s, A_{wt} and D_o have weak influence over C_P as per the different trials done in GEP evolution. Thus, the mentioned variables are omitted in the final GEP model. However, the variable λ indirectly relates D to C_P. The trial tests also indicated that the variables $\theta_2 - \theta_1$ (in radian) and n_s / n_b are more effective in function approximation than the individuals. The list of variables/terminals used in the GEP is presented in Table 6.7.

$$C_P = f\left(\lambda \times (1-\lambda)\right) \tag{6.14}$$

Table 6.7 Variables and numerical constants used in GEP

Notation in ET	Expression/value
d0	H
d1	p/q
d2	$\theta_2 - \theta_1$
d3	n_s / n_b
d4	e
d5	U
d6	λ
d7	λ^2
d8	λ^3
c2	-1.9449446089053E-03
c5	-9.9450666829432E-03

The topology of optimum GEP is presented in Table 6.8. The mean absolute error (MAE) defined in Eq. 6.1 is chosen as fitness function for GEP evolution. The numerical value of evolution parameters *i.e.* mutation rate, recombination rate, transposition rate etc. are selected based on optimum configuration suggested in software *GeneXProTools 5.0*. (Table 6.8). It has been suggested that the mutation rate has most influence over the efficiency of evolution followed by transposition rate compared to other parameters (Deb and Agrawal, 2002). In addition to that, the mutation becomes more effective when the population size is very small

in the range of 30-100 (Ferreira, 2005). Therefore, the population size of 100 is selected. Larger size of the population also causes the expensive computational cost which is not recommended.

Table 6.8 Specification of GEP topology

Parameters	Specification
Number of chromosomes	100
Head size	13
Tail size	14
Dc size (for numerical constants)	14
Gene size	41
Number of genes	3
Linking function	Subtraction
Maximum Arity	2
Function set	+, -, *, /
Training / validation and Test Percentage	70% / 30%
Data normalization	Mapped in [0,1]
Fitness function	Mean absolute error (MAE)
Mutation rate	0.00138
IS transposition rate	0.00546
RIS transposition rate	0.00546
Inversion rate	0.00546
One-point recombination rate	0.00277
Two-point recombination rate	0.00277
Gene recombination rate	0.00277
Gene transposition	0.00277
All genetic operator rates for numerical constants	0.00206
Numerical constants	10 randomly generated floating type constant bounded between [-0.1,0.1]

The function approximation obtained by GEP is presented in Fig. 6.12 as phenotypical ETs. The chromosome is multi-genic type consisting 3 genes, hence 3 sub ETs are obtained which are linked with subtraction. The mathematical expression of each Sub-ET and resulting C_P expression are expressed in Eqs. 6.15 through 6.18. This function approximation is able to correlate the data with R^2 = 0.65 and R^2 = 0.61 for training data and validation data, respectively. The mean absolute error values calculated for training and validation data are 0.059 and 0.064, respectively. The selected numerical constants 'c2' and 'c5' in Eqs. 6.17 and 6.18 during the evolution of GEP are included in Table 6.7. These equations clearly show the polynomial structure made of λ and its coefficients made of other variables (*i.e.* H, p/q, $\theta_2 - \theta_1$, n_s / n_b, e, U) which clearly supports the Eq. 6.14. These coefficients of polynomial control the

shape of the C_P vs λ graph, means the variables *i.e.* H, p/q, $\theta_2 - \theta_1$, n_s / n_b, e, U indirectly control the graph shape.

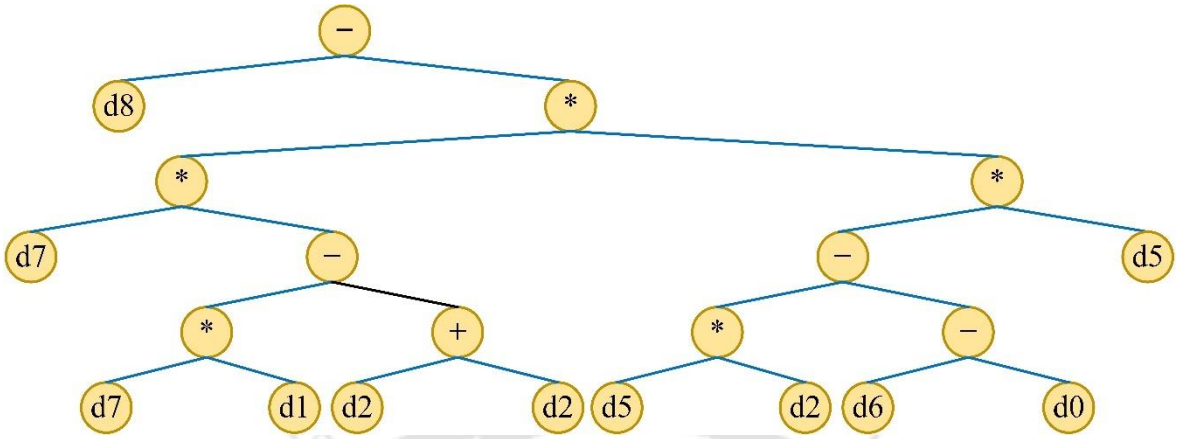

(a) Sub-ET1

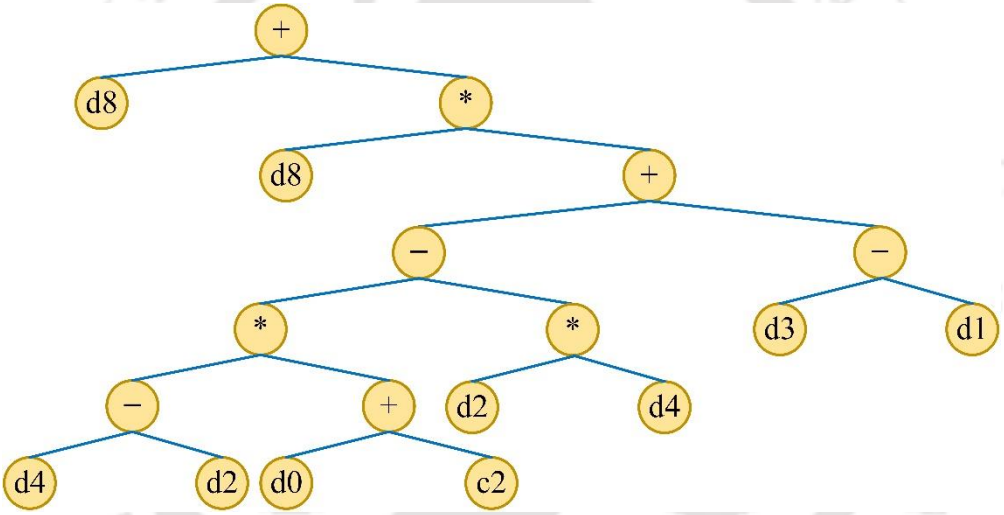

(b) Sub-ET2

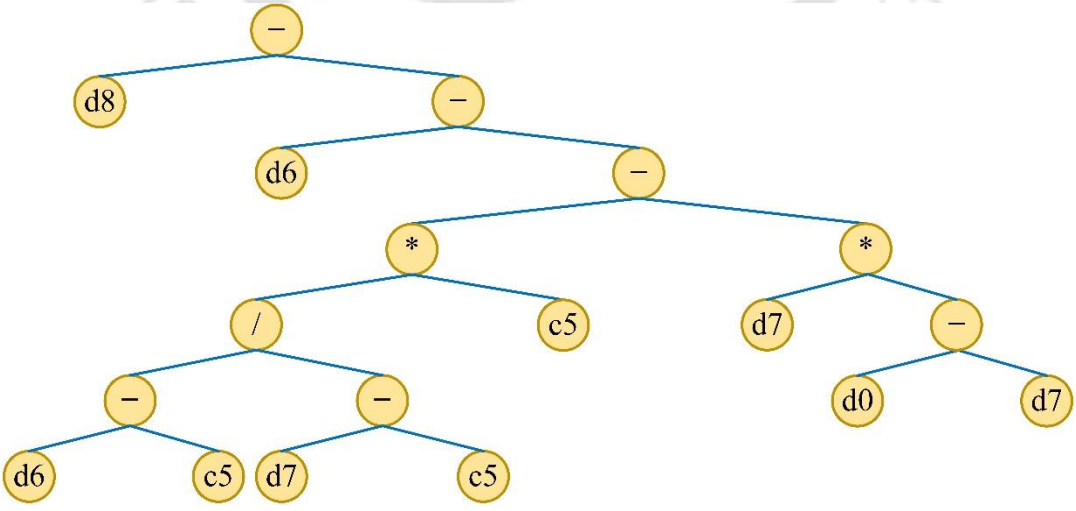

(c) Sub-ET3

Figure 6.12 An expansion tree representation of the soltion by GEP

$$C_P = (\text{Sub - ET1}) - (\text{Sub - ET2}) - (\text{Sub - ET3}) \tag{6.15}$$

$$\text{Sub - ET1} = \lambda^3 - \left[\left\{\lambda^2\left(\left(\frac{p}{q}\right)\lambda^2 - 2(\theta_2 - \theta_1)\right)\right\} \times \{U(U(\theta_2 - \theta_1) - (\lambda - H))\}\right] \tag{6.16}$$

$$\text{Sub - ET2} = \lambda^3 + \lambda^3\left[\left[\{(e - (\theta_2 - \theta_1)) \times (H + C_2)\} - ((\theta_2 - \theta_1)e)\right] + \left(\frac{n_s}{n_b} - \frac{p}{q}\right)\right] \tag{6.17}$$

$$\text{Sub - ET3} = \lambda^3 - \left[\lambda - \left\{\left(\frac{(\lambda - C_5)}{(\lambda^2 - C_5)} \times C_5\right) - \lambda^2\left(H - \lambda^2\right)\right\}\right] \tag{6.18}$$

Figures 6.13 and 6.14 show the comparison between the estimated value of C_P by the GEP model and the actual experimental (target) value of C_P for both the entire data set as well as test dataset. It is important to note that the selected test data for Fig. 6.14 have not been used during the training. In addition to that, the random number generator has been used to randomly select the test data from the total compiled data in order to eliminate human bias and prejudice against particular dataset.

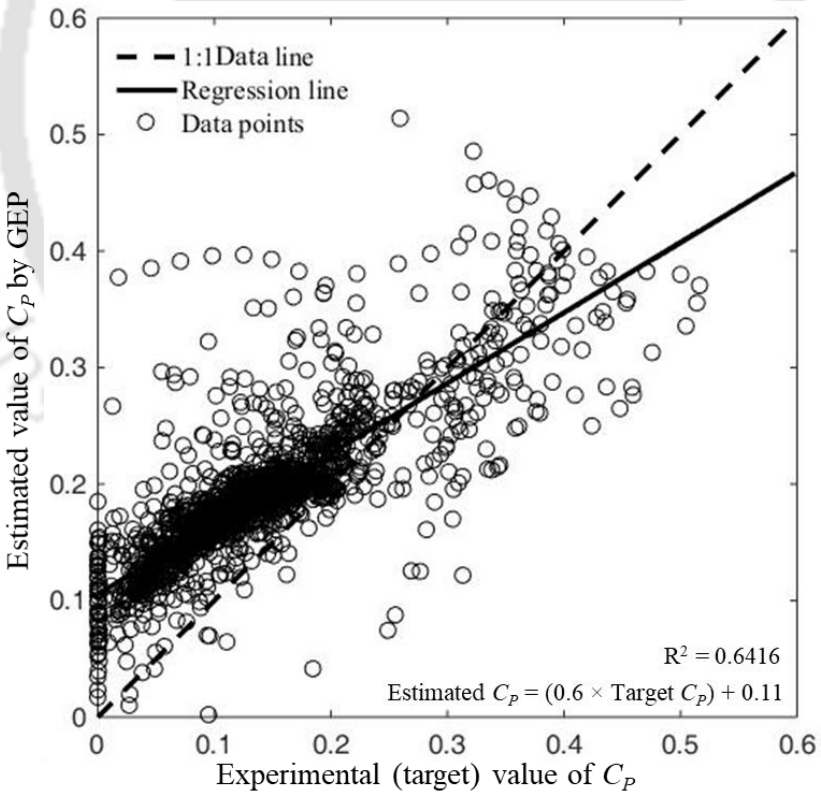

Figure 6.13 Estimated vs Experimental (target) C_P value of all data using GEP

Figures 6.13 and 6.14 suggest that the trained GEP model weakly predicts the performance of the rotor based on the prescribed set of input data for all of the three blades *i.e.* semicircular,

Bach and Benesh types. This is based on R^2 value lower than unity as compared to that of the ANN model. The reason behind the ANN predicting more accurately than the GEP is due to their different algorithmic structures. During the training process, a wide range of values can be assigned to the weights of the neurons due to their numeric nature. On the other hand, GEP has to be trained by permutations and combinations made of limited numbers of mathematical operations. Therefore, ANN can formulate the hidden equation that is close enough to the actual hidden equation, while the GEP cannot. Therefore, the ANN model can predict more accurately than the GEP model.

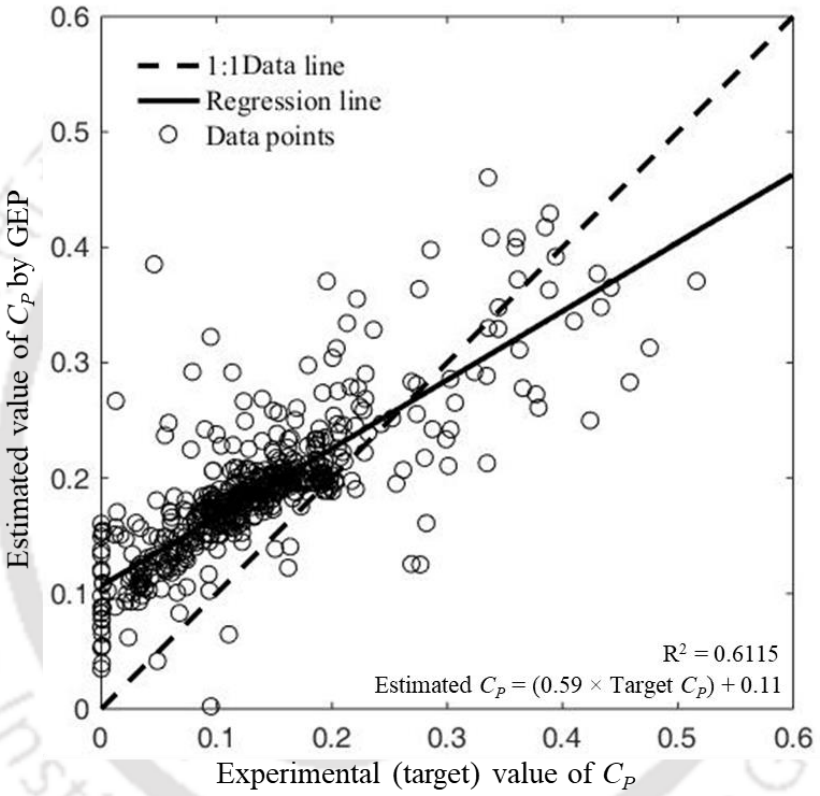

Figure 6.14 Estimated vs Experimental (target) C_P value of test data using GEP

6.10 Concluding Remarks

In this chapter, the application of ANN and GEP, have been applied in order to estimate the Savonius wind rotor's performance based on different independent design variables. The available experimental data on Savonius wind rotor have been used to train ANN and GEP. The input variables used in ANN and GEP architecture includes newly proposed design shape factors, number of blades and stages, gap and overlap lengths, height and diameter of the rotor, cross sectional area of wind tunnel where the experiments are carried out, free stream wind velocity, and tip speed ratio. Based on this, the unknown governing function constituted by the

aforementioned input variables is established using ANN and GEP to approximate/forecast the performance of the rotor as output.

The results show that the ANN and GEP fit the data with R^2 = 0.97 and R^2 = 0.65, respectively. However, latter one is inferior to former one in terms of fitting the data. Moreover, the GEP expression clearly shows the C_P vs λ as polynomial of λ. The accuracy of the fitting provided by the ANN is superior than the GEP. The results obtained by ANN and GEP confirm that proposed hypothesis of defining a new set of variables (*i.e.* p/q, θ_2, θ_1) to express any shape of the blade is logical to train the ANN and GEP. These trained networks can thus be used to predict the performance or 'C_P vs λ' graph of the Savonius wind rotor having any shape of the blade. These observations also shed the light on the fact that the governing working principle and governing multivariable equation behind all blade shapes are similar. As an assimilation, the distinctive feature of this study is that the newly defined shape factors facilitate to train both the ANN and GEP using experimental data of different blade types altogether, which is not opted before as per the best knowledge of the author.

Efforts are successfully made to use soft computing techniques like ANN and GEP for prediction of Savonius rotor performance. The geometric and flow-based variables are combined to make thirteen input variables for these techniques. Literature based data is successfully used to test and validate the architectures of ANN and GEP.

Chapter – 7

Prediction of Optimum Performance and Parametric Study

Chapter Layout:

Overview

In continuation to the Chapter 6, the trained ANN surrogate model is merged with the golden section method (GSM) to search the optimum performance ($C_{P,\,Opt}$) for a given rotor designs and operating conditions. Besides that, a new data partitioning strategy is also proposed and implemented for the ANN training in this chapter. How the GSM algorithm moulded to search for optimum rotor performance is then discussed. The trained ANN merged with the GSM is then evaluated in the form of regression plots and error histograms. The parametric study is then presented to check whether or not the surrogate model combined with the optimizer is capable of effectively modelling the influence of each design and operating parameters on the rotor performance. The programming of the surrogate model together with the optimizer is then transformed in the form of graphical user interface (GUI) so as to facilitate ease of operation and prediction when operated by the researchers. It is important to note that the new ANN training is provided in Appendix to avoid superfluous repetitions.

7.1 Background

While executing the function approximation of Eq. 6.1 in Chapter 6, it was found that all the input design and operating parameters, except λ, determine the overall bell-shaped performance curve (C_P vs λ). For example, line-1 and line-2 plotted into Fig. 7.1 belong to two different sets of parametric values corresponding to different rotor designs. For a given rotor design, different values of C_P can be obtained at different operating conditions as represented by λ. As the mechanical loading condition on the rotor changes, the rotational speed of the rotor gets altered, resulting into a change of λ values along with C_T and C_P. In short, design and operating variables of Eq. 6.1 determine the overall shape of bell-shaped performance curve (C_P vs λ), while the remaining input variable λ plots C_P at different operating conditions on the performance curve.

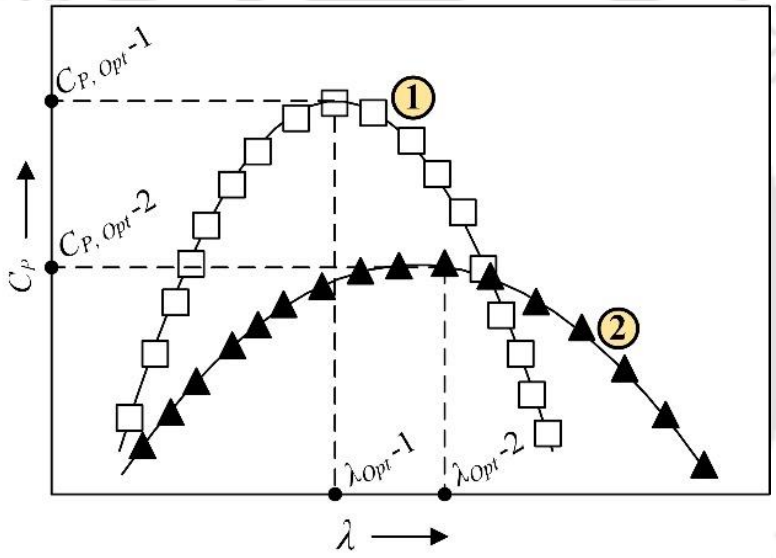

Figure 7.1 Typical C_P vs λ curves

Even though the trained ANN of Chapter 6 can predict the C_P, the most desired outcome of rotor is its optimum performance ($C_{P,Opt}$), since it is substantially used as the parameter for the comparison between two distinct rotors. The experimental prediction of this $C_{P,Opt}$ would involve many sets of experiments and still a range of λ would be arrived containing the expected $C_{P,Opt}$. Similarly, many computational simulations are required to arrive at such a range at the expense of large computational time. Alternatively, $C_{P,Opt}$ can roughly be speculated by providing different input values λ into the trained ANN model, but it is impractical and time consuming. In other words, Eq. 6.1 is successful in modelling the performance characteristics of the Savonius rotor, yet it lacks in providing the direct values of $C_{P,Opt}$ as output. However, as a solution, the trained ANN can be considered to replace the computational and experimental

tools if combined with the optimization technique for the current goal. Basically, the peak performance (λ_{Opt}, $C_{P,\,Opt}$) is a global maximum of the unimodal bell-shaped performance curve (C_P vs λ) of the Savonius rotor. This characteristic motivates the present investigators to combine the optimization technique with the trained ANN to estimate the (λ_{Opt}, $C_{P,\,Opt}$) of the Savonius rotor, directly. It is important to note that the ANN approximates a given function in form of weights and biases of neurons, and not in the form of traditional continuous function. Therefore, the numerical elimination technique of optimization like 'Golden Section Method' (GSM) is to be used to estimate (λ_{Opt}, $C_{P,\,Opt}$), rather than using a differential calculus based analytical optimization method (Das et al., 2019; Kheldoun et al., 2016; Yazıcı et al., 2021). There are many elimination techniques for optimization such as Dichotomous search, interval halving technique, Fibonacci method other than the GSM for unimodal single variable problem. For the present problem of finding (λ_{Opt}, $C_{P,\,Opt}$), all these methods are applicable since C_P becomes a univariate problem after assigning the remaining design and operating parameters for a given power characteristic curve (C_P vs. λ). Among them, the Fibonacci method provides the highest reduction ratio for interval pruning and hence requires the lesser numbers of iteration to arrive at the required accuracy among other methods (Balaji, 2021). However, different Fibonacci numbers from Fibonacci series are required as iteration progresses that requires a large number of different numbers to be stored for a longer iteration process. To eliminate this demerit of the Fibonacci method, the GSM method is chosen as it requires only a single constant value *viz.* golden ratio ($\phi \approx 0.618$) unlike the multiple Fibonacci numbers for pruning intervals. Moreover, for very large number of iteration (tends to infinity), the Fibonacci method acts as an asymptotic to the GSM method. The GSM thus possesses a high reduction ratio as well as simple operative procedure.

As a summary, the goal of the present work is to build and combine both ANN and GSM algorithms to estimate (λ_{Opt}, $C_{P,\,Opt}$) of the Savonius rotor, directly. The main objective of the present study is to predict the maximum power output of a designed Savonius rotor. It should be noted that, there exists no machine learning based methodology to predict the peak power of the designed Savonius rotor. The means to arrive at this intended destination is either by performing explicit numerical simulations or experimental investigations for a host of geometric parameters and these have already been reported (Akwa et al., 2012; Alom and Saha, 2018a; Roy and Saha, 2013b). This justifies the need to investigate for a methodology which can reduce the computational and/or experimental costs to propose the maximum power of the

rotor. Such methodology would be useful in the design phase of experiments/simulations for a given rotor design to narrow down the operating range of geometric parameters. Further, with the help of the proposed methodology, it is also possible to change the values of design parameters to improve the rotor performance. In the process of devising such a method, the training of ANN model is aimed as a prerequisite to exploit the documented experimental dataset. Both the ANN and GSM algorithms are formulated with the help of *MATLAB R2020b* software. As stated earlier, the trained ANN maps input-output variables in form of weights and biases of the neurons, which is not quite intuitive to understand the influence of each and every design parameter on $C_{P,\,Opt}$. In view of this, the parametric study is conducted in this chapter, besides developing a 'Graphical User Interface (GUI)' based on trained ANN model for predicting $C_{P,\,Opt}$.

7.2 New Data Partitioning Strategy

The function approximation using ANN model uses a batch type supervised learning method. The entire dataset thus has to be divided into three categories *viz.* training dataset, validation dataset and testing dataset. The training dataset is used to train the ANN model in order to determine the weights and biases of neurons. The validation dataset is not directly being used for the training purpose, rather being used for stopping the training process and validation. Lastly, the test dataset is reserved for evaluating the trained ANN as this dataset is not used for the training purpose, and hence, it can be considered as completely new dataset for the trained ANN.

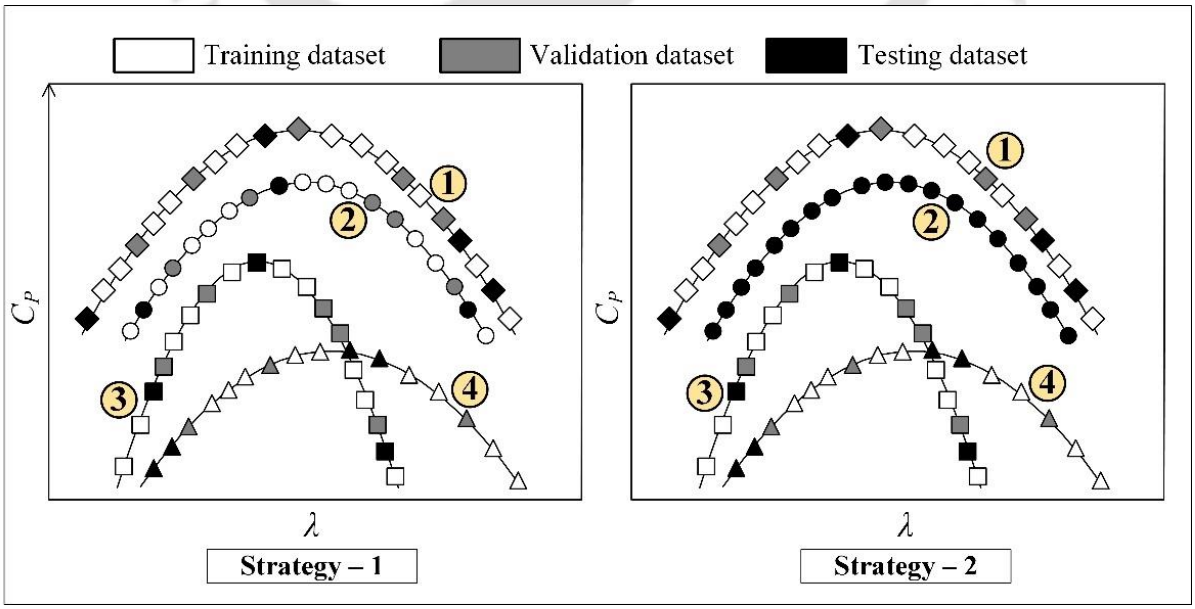

Figure 7.2 Comparison between data partitioning strategies

Generally, the random partitioning schemes are adopted for data-partitions as Strategy-1 in Fig. 7.2. In this strategy, there are always some data points corresponding to each and every performance curve (for example, data lines 1 to 4), which are included in the training dataset. This Strategy-1 has successfully been implemented by Mohammadi et al. (2018), Sargolzaei and Kianifar (2009), and Chapter-6 of the present thesis to train the ANN model for the Savonius rotor for small to large number of input variables. This strategy is proved to be successful in mapping the power characteristics of different rotor designs. However, the training data extracted by the Strategy-1 would contain multiple data instances which acquire identical values of the rotor design parameters (parameters mentioned in Eq. 6.1, except λ) with only difference in the values of λ. In order to diminish the influence of such data instances on the training dataset, a distinct and new approach named as Strategy-2 (illustrated in Fig. 7.2) is adopted in the present study. In this strategy, some of the entire C_P vs λ performance curves are randomly selected and included into the testing dataset, for instance, the data line 2 of Strategy-2. As mentioned earlier, the shapes of these data lines representing bell-shaped performance curves (C_P vs λ) are governed by the design variables of Eq. 6.1 except λ. The Strategy-2 is thus proposed in such a way that it can focus on this attribute. In other words, the strategy-2 can train an ANN model that can tackle any unfamiliar values of design parameters that are not a part of training dataset, previously. On the other hand, if the Strategy-1 is used, only the unfamiliar values of λ are encountered, and not the remaining rotor design parameters. Lastly, the partitioning is carried out in such a manner that approximately 60% input data instances are the part of training dataset and the remaining 20% – 20% instances are the part of validation and testing dataset. In majority of ANN training studies, almost similar partitioning is carried out in the approximate formation of 70% – 15% – 15% for training – validation – testing purposes, however, it is not mandatory.

7.3 Golden Search Algorithm to Estimate $C_{P,\,Opt}$

As discussed in last paraphrase of Section 7.1, the trained ANN model fails to provide the direct values of $C_{P,\,Opt}$, however, it provides values of C_P corresponding to a particular λ for a given rotor. In the performance curve (C_P vs λ) of any Savonius rotor, it can be observed that all the data points on the curve have same values of design parameters (*e.g. D, H, p/q,* θ_1, θ_2, n_s, *e, s, Do,* and *U*), but only λ varies. Still the values of λ remain bounded approximately between 0 to 2 for all the rotors. Hence the C_P vs λ curve corresponding to a given rotor design can be considered as $C_P = f(\lambda)$. Consequently, $C_{P,\,Opt}$ of that curve becomes the maxima of the function $C_P = f(\lambda)$. This suggests to combine a suitable maximum point searching technique

with the trained ANN model. It is important to specify that the function of C_P approximated by ANN is in the form of weight and biases, and not in conventional mathematical form. This motivates to use numerical elimination technique such as GSM for the present unimodal problem. This technique has successfully been implemented by a host of researchers into similar kind of problems (Das et al., 2019; Kheldoun et al., 2016; Yazıcı et al., 2021).

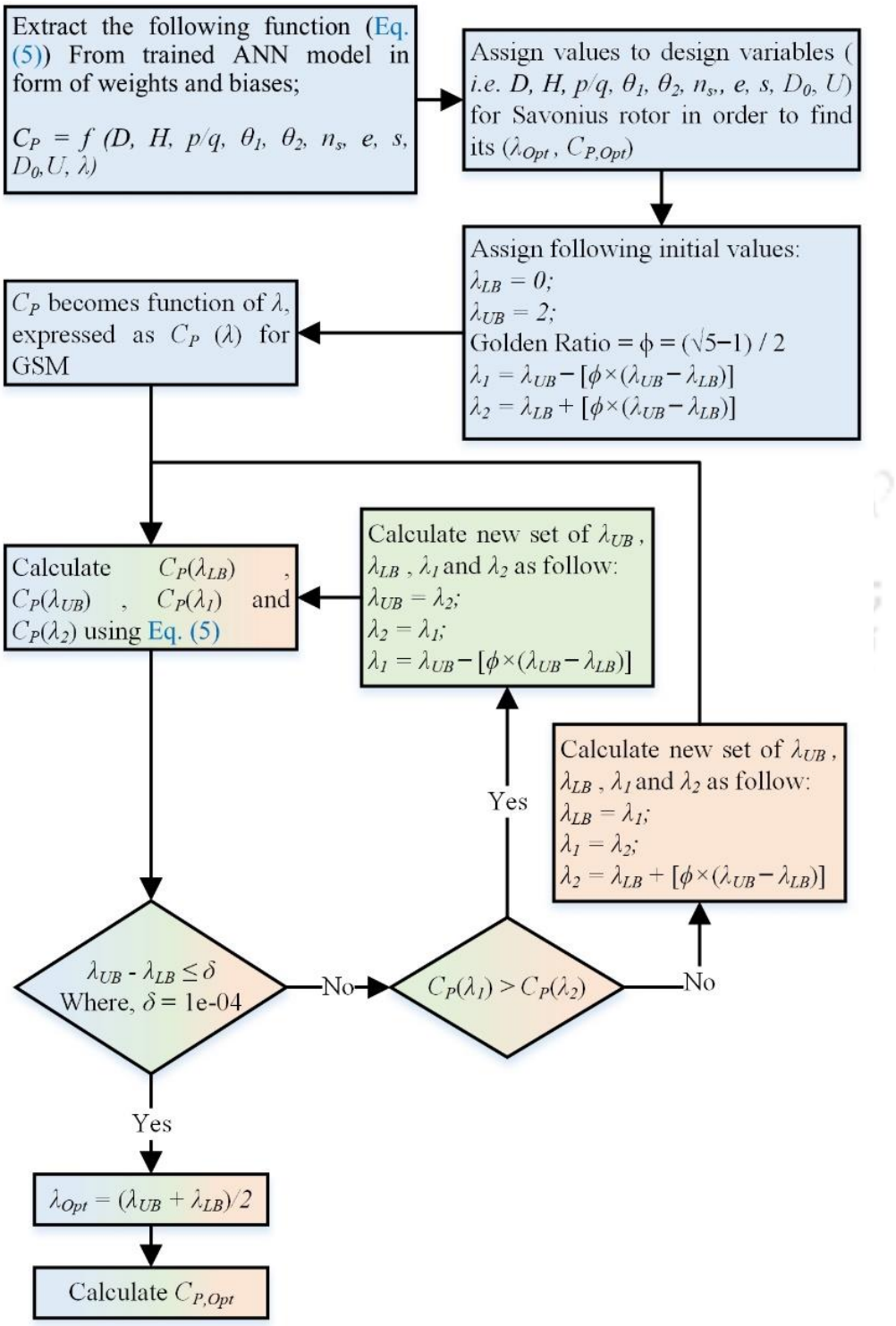

Figure 7.3 GSM algorithm

The GSM algorithm merged with the trained ANN model developed using *MATLAB R2020b* software is illustrated in Fig. 7.3. It shows that the GSM algorithm is moulded into finding the global maxima of a unimodal function $C_P = f(\lambda)$. In this algorithm, the upper and the lower bounds of λ are fixed as $\lambda_{UB} = 2$ and $\lambda_{LB} = 0$, respectively, since $(\lambda_{Opt}, C_{P,\,Opt})$ lies in-between. The value of Golden Ratio (ϕ) for the GSM is provided in the Fig. 7.3. Using ϕ, the initial values of intermediate λ_1 and λ_2 are calculated. Thereafter, values of $C_P(\lambda_{LB})$, $C_P(\lambda_{UB})$, $C_P(\lambda_1)$ and $C_P(\lambda_2)$ are calculated and compared. Depending upon the inequalities obtained between values of $C_P(\lambda_1)$ and $C_P(\lambda_2)$, the corresponding interval holding lower value of C_P is pruned. For example, if $C_P(\lambda_1) < C_P(\lambda_2)$, the interval $[\lambda_{LB}, \lambda_1)$ is pruned, else interval $(\lambda_2, \lambda_{UB}]$ is pruned. The values of λ_{LB}, λ_{UB}, λ_1, λ_2 are then updated and the aforementioned steps are repeated in a loop format until $\lambda_{UB} - \lambda_{LB} < 10^{-4}$ criterion is fulfilled. As a result, $\lambda_{LB} \approx \lambda_{UB} \approx \lambda_{Opt}$ and $C_{P,\,Opt}$ are obtained.

7.4 Results and Discussion

After partitioning the data (Sections 7.2), the ANN model is formulated and trained as per Appendix besides its evaluation and error analyses. Thereafter, in Section 7.4.1, implementation of GSM is described. The parametric study is then carried out and the graphical user interface is developed in the Sections 7.4.2 and 7.4.3, respectively.

7.4.1 Implementation of GSM Algorithm

As the optimum trained ANN model has the potential to predict the C_P, the GSM algorithm can be merged with it. Now this combined model is capable of estimating $C_{P,\,Opt}$ values of a given rotor, when the values of input design parameters are provided. Though the ANN model with minimum error of estimation is selected, some instances of test and overall datasets are still possessing high amount of error as observed previously. If more focus is given to $C_{P,\,Opt}$ values of the rotors rather than all the possible C_P values of C_P vs λ curve, errors manifested by the lesser important C_P values can be diminished, since $C_{P,\,Opt}$ values are more important. Therefore, a comparison is made between the estimated and the experimental values of $C_{P,\,Opt}$ for the entire dataset (compiled in Table A1) as shown in Fig. 7.4. It can be observed that the instances are conscentrated towards 1:1 line, which is quite promising with $R = 0.9789$. Additionally, the histogram (Fig. 7.5) is also showing the centrally weighted error distribution with majority of instances bounded in-between ± 0.009, equivalent to dissimilarities in third decimals points. Thus, ANN combined with GEP is capable of estimating $C_{P,\,Opt}$ values directly with minimum possible error. Using these $C_{P,\,Opt}$ values, a parametric study is carried out to examine the effects of different rotor parameters on its performance.

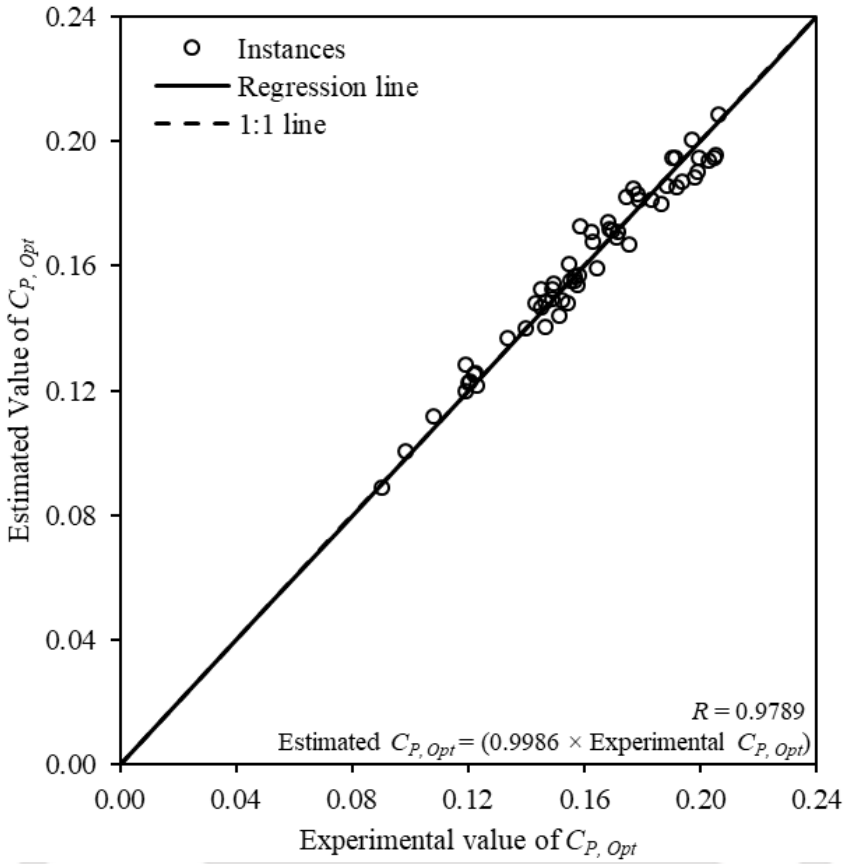

Figure 7.4 Estimated vs Experimental $C_{P, Opt}$ value of overall dataset using combined ANN and GSM

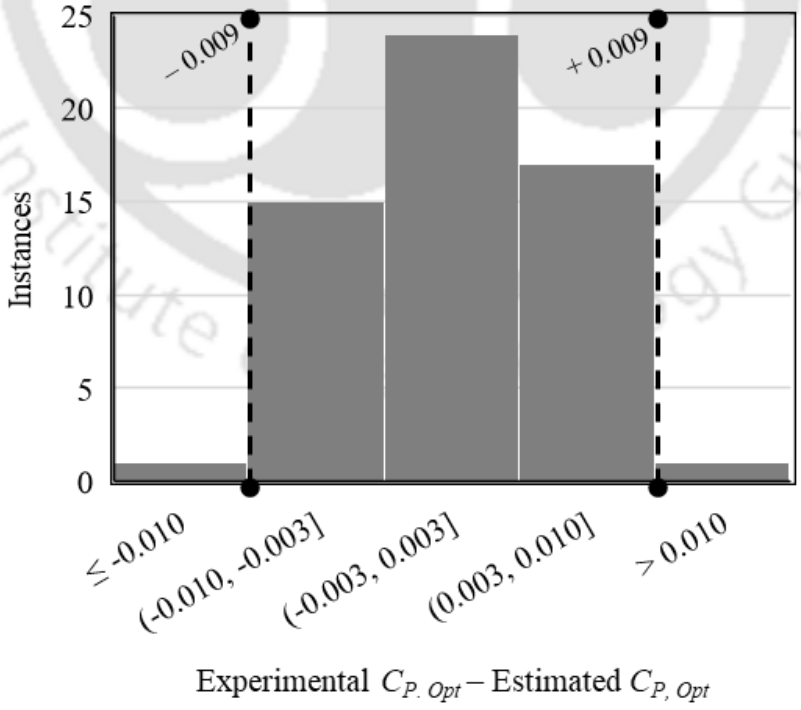

Figure 7.5 Error histogram for combined ANN and GSM

7.4.2 Parametric Study

In this section, dependency of $C_{P,\,Opt}$ on different parameters is studied by implementing the combination of aforementioned ANN and GSM algorithm. It is important to note that the ANN trained function approximation model can work in maximum-minimum bounds of parameters specified in Table A.1 of Appendix. However, the values in-between specified limits but outside of overall training dataset are considered and discussed in Subsections 7.4.2.1 through 7.4.2.5.

7.4.2.1 Effect of Free Stream Velocity (U)

Four rotor configurations of similar dimensions of $H \approx D \approx 0.22$ are selected to show the influence of U over $C_{P,\,Opt}$. As D remains the same for all the rotors, Re also remains the same at a given U value. The results presented in Fig. 7.6 consist of data series 1 to 3 belonging to semicircular blade ($p/q = 0$, $\theta_1 = 90°$ and $\theta_2 = 90°$) and data series 4 belonging to Bach type blade ($p/q = 0.2$, $\theta_1 = 124°$ and $\theta_2 = 0°$). Here, U is varied between 6 m/s to 12 m/s during the analysis while maintaining the values of remaining variables unchanged. It is evident that $C_{P,\,Opt}$ improves as U increases in the given range and this is supported by literature (Kamoji et al., 2008; Sheldahl et al., 1978). Increment of incoming fluid energy with U is the reason behind this improved performance. This trend is also consistent for all types of rotors such as single-staged rotor, multistage rotor, semicircular and Bach type rotors and others.

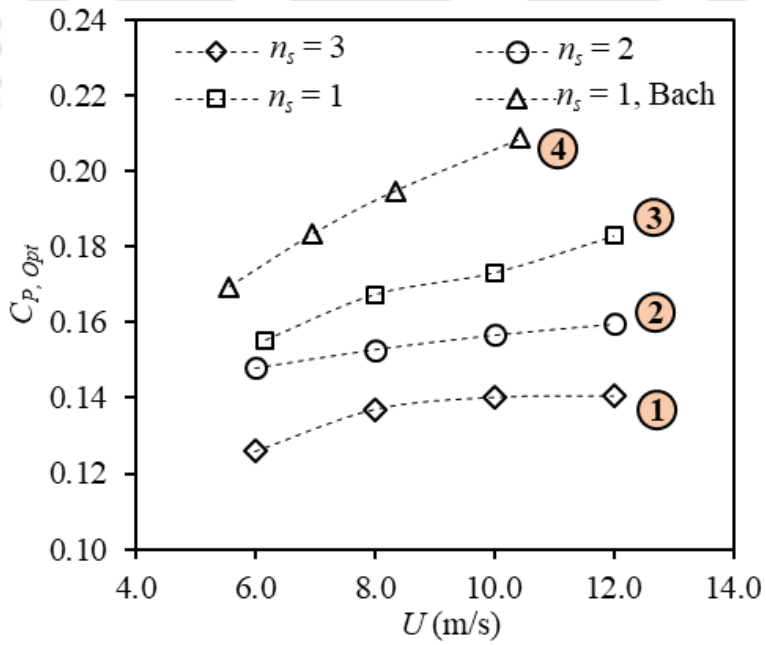

Figure 7.6 Effect of U on $C_{P,\,Opt}$

7.4.2.2 Effect of Number of Stages (n_s)

Figure 7.7 shows the variation of $C_{P,\,Opt}$ of rotors with respect to n_s at different U values. Herein, the size of the rotors is kept constant ($H \approx D \approx 0.22$), thereby maintaining the constant projected area and Re number for each rotor. But U is varied from 6 to 12 m/s in order to check whether or not the behaviour is consistent. Rotors selected for this purpose are of semicircular bladed (p/q = 0, θ_1 = 90° and θ_2 = 90°). Other design parameters are kept unchanged. It can be commented that the optimum performance of the multi-staged rotor is inferior to that of single-staged rotor. For each cases of U, the highest $C_{P,\,Opt}$ is demonstrated by n_s = 1, trailed by n_s = 2 and n_s = 3, respectively. The multi-staging facilitates a reduction in rotor torques, however, it fails to provide a superior performance based on the reported experimental results (Hayashi et al., 2005). The same is indicated by the trained ANN model in this paramentic study of n_s.

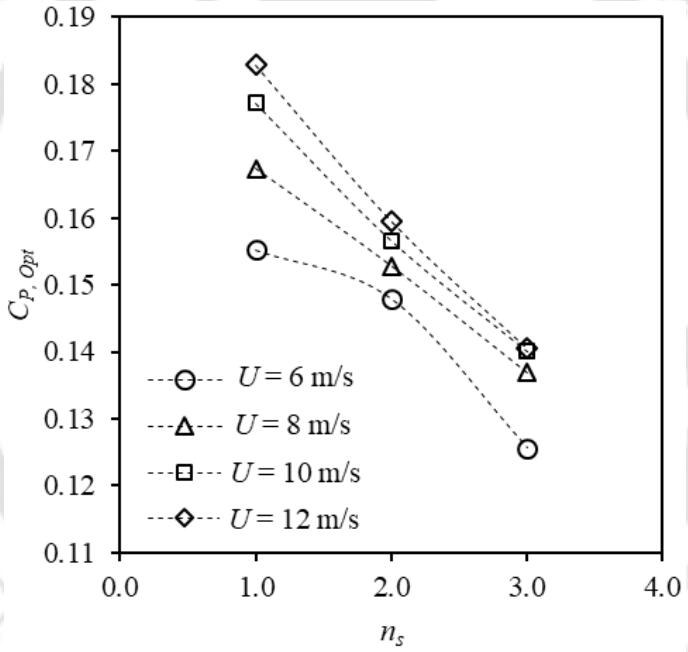

Figure 7.7 Effect of n_s on $C_{P,\,Opt}$

7.4.2.3 Effect of Gap Length (s)

Three designs of the Savonius rotor having $s \approx 0\%$, 10% and 16 % of D are tested in order to inspect the effect of s on the optimum rotor performance. However, in abscissa of Fig. 7.8, the s is presented in form of absolute values. All the designs possess identical values of $D \approx 0.22$ m and $H \approx 0.16$ m, so as to maintain the constant value of Re for all three rotors. These single-staged rotors possess Bach type blade (p/q = 0.2, θ_1 = 124° and θ_2 = 0°). The trends are examined for two different values of $U \approx 8.5$ and 10.5 m/s, without altering the values of the remaining parameters. In both the velocities, the performance decreases with an increase of s.

Experimental results reported in the past also support this observation. The reason behind this diminishing performance is believed to be an excessive gap flow that results into a weak pressure recovery region of the returning blade (Fujisawa, 1992; Nobuyuki Fujisawa and Gotoh, 1992). This justification can also be applicable to overlap length (e) of the rotor.

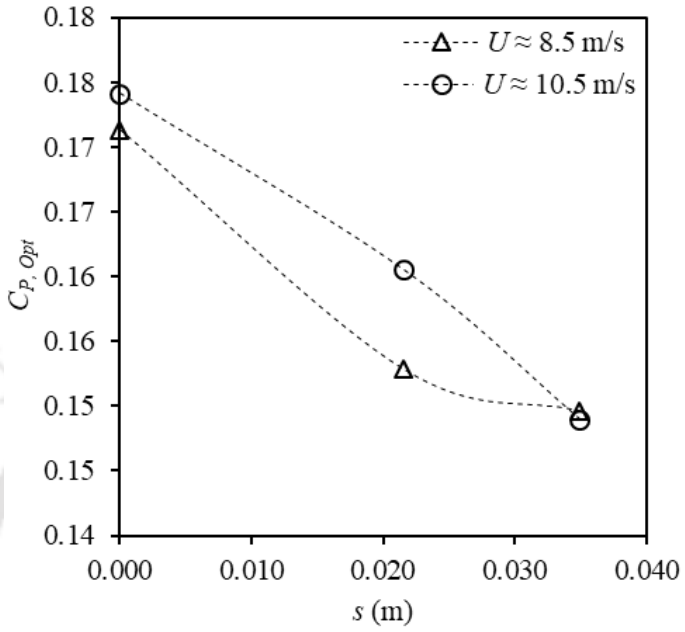

Figure 7.8 Effect of s on $C_{P,\,Opt}$

7.4.2.4 Effect of Blade Shape Parameters (p/q, θ_1 and θ_2)

Figure 7.9 shows the influence of blade shape factor (p/q) on $C_{P,\,Opt}$. The rotors used for this purpose possess $D \approx 0.2$ m, $H \approx 0.15$ m, $\theta_1 = 124°$, $\theta_2 = 0°$, $e = s = 0$ m and $D_o \approx 1.1D$. p/q = 0.2, 0.4 and 0.6 are tested in the merged ANN-GSM algorithm under operating condition of $U \approx 8.5$ and 10.5 m/s. The results indicate that the $p/q = 0.2$ provides the highest performance compared to others. This displays that monotonic increase in blade's straightness (p) while fixing the radius of curvature (q) leads to a lower performance (Kamoji et al., 2009). Not only that, to what extent q is spanned on blade shape (θ_1) also affects the performance. This can clearly be understood with help of Fig. 7.10, where $p/q = 0.2$ is fixed and different values of θ_1 are considered *viz.*, 110°, 124°, 135° and 150°. Other rotor dimensions and values of U are similar to those of the previous ones. The $C_{P,\,Opt}$ increases initially upto $\theta_1 = 124°$, and thereafter, it plunges down for the remaining higher values of θ_1. Higher value of θ_1 can be interpreted as a high spread of circular blade shape, and therefore, characteristics of the circular blade can be menifested in high θ_1 values. It is known that the Bach shape performs better than the semircular blade (Roy and Saha, 2015), and hence the Bach blade with high values of θ_1 performs poorly as compared to moderate θ_1.

By simultaneously using values of p/q, θ_1 and θ_2, the performance of semicircular and Bach type blades can also be compared. For example, consider Fig. 7.6 of Section 7.4.2.1, which contains data series 3 of semicircular blade (p/q = 0, θ_1 = 90° and θ_2 = 90°) and data series 4 of Bach type blade (p/q = 0.2, θ_1 = 124° and θ_2 = 0°). Other dimensions and operating conditions are identical. Figure 7.5 clearly demonstrates that the Bach type blade performs better than the semicircular blade obeying the documented experimental outcomes of literature.

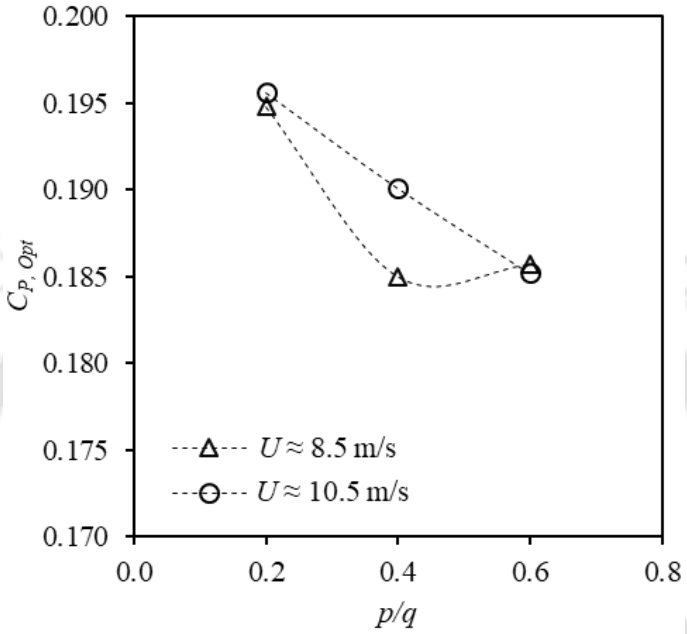

Figure 7.9 Effect of p/q on $C_{P,\,Opt}$

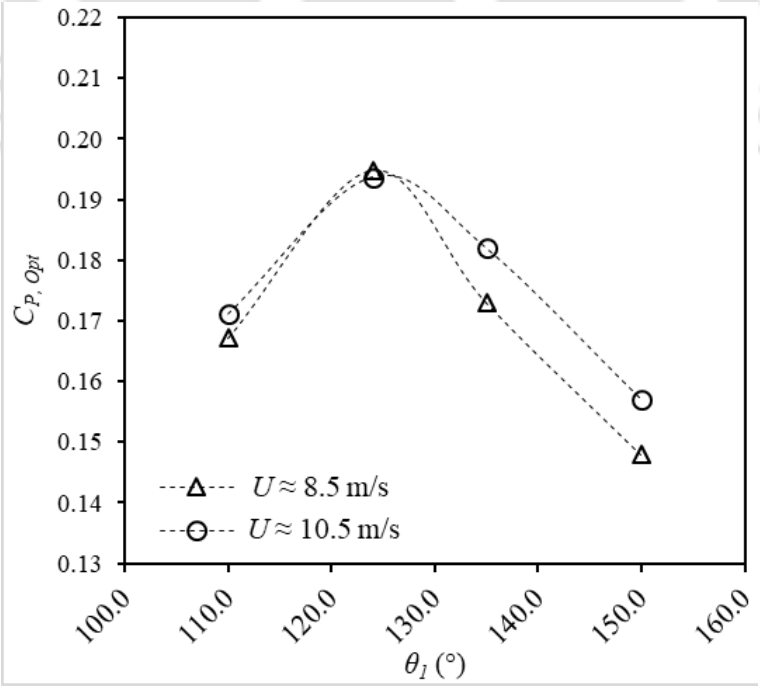

Figure 7.10 Effect of θ_1 on $C_{P,\,Opt}$

7.4.2.5 Effects of Remaining Design Parameters

The parameters such as H and D form the projected area of the rotor that directly control the conversion of incoming fluid energy. If the performance of rotor is estimated by varying H and keeping D constant, the Re remains unchanged but the projected area changes. Hence, the $C_{P,\ Opt}$ calculated for these cases should not be compared. Alternatively, if the prejected area is maintained constant by simultaneously changing D and H, Re also changes, and hence the comparison cannot be made here. Ushiyama et al. (1986) reported that the $C_{P,\ Opt}$ increases with increse of aspect ratio (= H/D) from 1 to 4, while maintaining the prejocted area (A) and U constant. On contrary to this, Kamoji et al. (2009) reported that the $C_{P,\ Opt}$ increases, become maximum and then decreses as H/D increases, while maintaining D constant.

Considering the results presented in Sections 7.4.2.1 through 7.4.2.5, it can be commented that the trained ANN model is successful in modelling the hidden performance mechanism of the Savonius rotor by intertwining multiple input and output variables. Moreover, the combined ANN and GSM algorithm can be used as the successful estimation tool of $C_{P,\ Opt}$ for the future design purposes.

7.4.3 Design of Interactive Graphical User Interface (GUI)

For the ease of utility, the trained ANN model along with GSM algorithm are configured with interactive GUI with the help of development platform of *MATLAB R2020b* software. Graphic structure of the GUI is shown in Fig. 7.11. It is very easy and intuitive to use unlike its programming counterpart. The interface demands to enter values of input parameters enlisted in pop-up window. For guidance, the graphical definitions of every parameters are also provided. Here, it is important to note that any input value of λ is not required since its upper-lower bounds (= 2 and 0, respectively) are specified in GSM algorithm. Thereafter, user is required to click on 'Start Estimation' button, which triggers background calculation in trained ANN + GSM algorithm and provides λ_{Opt} as well as $C_{P,\ Opt}$ at the output parameters tab.

7.5 Concluding Remarks

A novel data partitioning strategy is implemented, which has not been used in the reported ANN articles related to the Savonius rotor. The overall dataset is divided on the basis of 60% – 20% – 20% for training, validation and testing datasets, respectively. For finding $C_{P,\ Opt}$ directly, the GSM algorithm is successfully linked with the ANN model. The combination of ANN and GSM algorithms provided higher correlation of $R \approx 0.978$ between the experimental

and the predicted value of $C_{P,\,Opt}$. The errors of majority instances are found to be concentrated around zero error lines. Thence, the parametric study is conducted with the help of $C_{P,\,Opt}$ values to gain an insight into the influence created by different rotor parameters on performance. It is proved that the ANN has modelled the hidden performance mechanisms successfully. Lastly, the interactive GUI is developed to implement both the ANN and the GSM algorithms for future purposes.

The present approach can be applied to an individual wind-tunnel setup, for which the historical experimental data are available and the same can be utilized for developing a neural network model that can predict the performance of different rotor designs before conducting the actual experiments in the setup. In case of scarcity in the experimental dataset, the machine learning technique such as the generative adversarial network (GAN) can be implemented for predicting the optimum rotor performance.

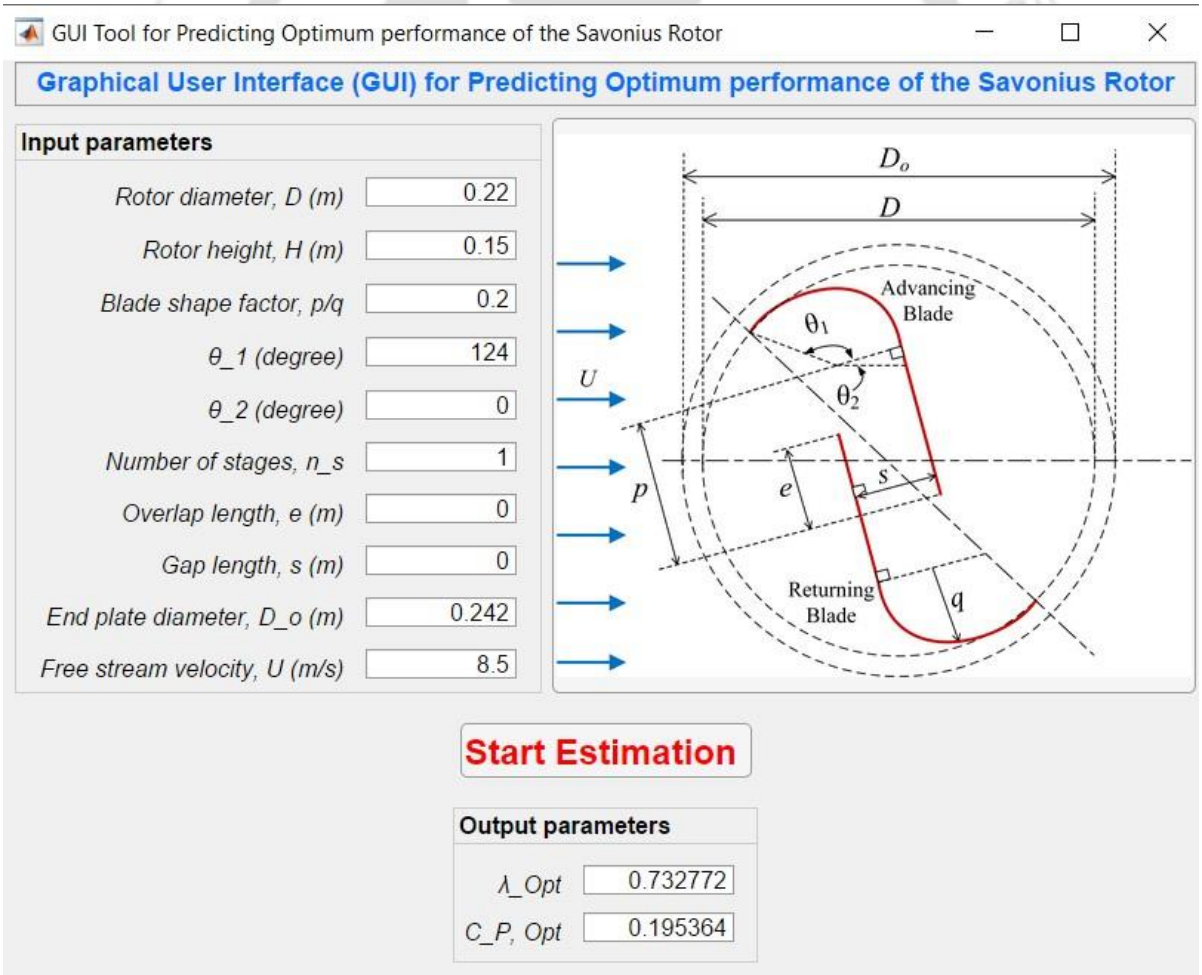

Figure 7.11 Interactive GUI for prediction of $C_{P,\,Opt}$

Chapter – 8

Conclusions and Future Scope

Chapter Layout:

Overview

The original contributions of the present research work and its novelty are highlighted in the starting of this chapter besides compiling the key findings of each research task presented in each of the chapters. Considering the present research work as a base, possible future scope is then outlined with proper reasoning. In order to address these upcoming opportunities, the author of this thesis conveyed a set of recommendations for aspiring researchers in this field with adequate guidelines, explanations, examples, and most importantly, the apparent challenges to be overcome.

8.1 Contribution of the Present Work

The Savonius rotor, being a variant of vertical axis wind turbine demonstrates several peculiarities such as potential for small-scale standalone energy conversion systems, adaptation for confined urban installations, capable of off-grid energy conversion, capable of self-starting at low wind speed, and low noise generation. Even though possessing such qualities, the performance of the Savonius rotors is inferior to other members of the VAWTs, and therefore, they have been constantly subjected to the performance enhancement by the research community in the form of augmentation techniques, design modifications, optimization, and novel blade designs. Among them, development of the bioinspired blade shapes has emerged as a recent trend for performance improvement.

In view of this, two novel bioinspired blade shapes have been developed as a part of the present work. The first bioinspired blade has been derived from the Orange sea-pen (*Ptilosarcus gurneyi*) by imitating its vortex induced feeding mechanism to strengthen the torque mechanism of the Savonius rotor. The principal flow conditions have been introduced for future development of the novel blades. It is very important to note that the sea-pen has not been introduced yet in the field of bioinspired designs until the present work. This is also applicable for the outlined principal flow conditions. After successfully developing the shape of the sea-pen blade, it has been subjected to experimental and numerical assessment. It has been found that the sea-pen blade can successfully outperform the conventional semicircular blade, not only in terms of rotating performance but also in the starting torque characteristics. Numerical findings also supported these observations and confirmed the compliance to the principal flow conditions besides the successful emulation of the vortex feeding mechanism. Further, the flow conditions have been further boosted and expanded by introducing the peaks and the valleys in the form of corrugation inspired from the pleated dragonfly wings. The numerical assessments have demonstrated its potential for the performance improvement. The corrugation had been already introduced in the literature for wing design, however, it is the first time the corrugation is introduced for the blade design of the Savonius rotor.

Furthermore, surrogate models have been formulated to predict the rotor performance using artificial neural network (ANN) and genetic expression programming (GEP). This work is the first attempt among the contemporary soft computing studies to incorporate large number of design and operating parameters as input variables of the surrogate models. Reported experimental data have been utilized to train the surrogate models. Additionally, golden section method (GSM) has been merged to the surrogate model to predict the optimum performance

of any given rotor designs. Moreover, a new data partitioning method has been proposed for the training of the ANN based surrogate model. As the final outcome, a graphical user interface has been developed using the trained surrogate model along with the optimization model to bring ease to the users while predicting the performance.

8.2 Future Scope of the Present Work

- The sea-pen blade fabricated possesses a uniform cross-sectional shape inspired from the polyp leaf profile of the orange sea-pen though the actual shape of the sea-pen (Fig. 4.3) shows signs of the curvature in the direction parallel to its rachis. Therefore, a new blade shapes can be synthesized by imitating the actual 3D shape of the entire sea-pen body instead of mimicking just a polyp leaf profile like in the present case. This additional rachis-wise curvature might replace the end plates in the context of blocking the leakage of stagnant fluid in the direction parallel to the rotor height.
- There are plethora of sea-pen species adapted to different flow conditions in the sea, which developed peculiar morphological differences in the polyp leaf shapes. Such diversity of the sea-pen should be explored to develop even superior blade shapes suitable for some unique operating conditions and other niches.
- Upon closely examining the outer edge of the polyp leaf (Fig. 4.3), small protrusions and dimples can be observed. Such surface patterns are ignored in the current design of the sea-pen blade for preliminary simplification. Nevertheless, the surface patterns can be implemented in the blade design to know whether or not it alters the performance in comparison with the smooth surfaced sea-pen blade.
- In the present thesis, only the 2D CFD simulations have been conducted. Researchers can conduct 3D CFD simulations for gaining more insights into the principal flow conditions and the modified torque mechanism of the sea-pen bladed rotors.
- Regarding the corrugated blades, a limited number of design iterations of the corrugated blades are tested numerically. Further parametric optimization and its experimental evaluation can be suggested as a future scope.
- Along with performance prediction of the rotors using surrogate modelling, blade design optimization can be carried out by merging the trained surrogate model with a suitable optimizer.
- Other than the present soft computing techniques, more trendy and modern techniques such as generative adversarial networks (GANs) can be used to develop a surrogate model.

8.3 Recommendations for the Aspiring Researchers

In view of the understandings gained based on the research work presented in this thesis, the author opines that there are four major methodologies, namely, bioinspiration approaches (Section 8.3.1), bioinspired design and optimization (Section 8.3.2), and choice of biomimetics over biomorphism (Section 8.3.3); which can be implemented to develop novel performance improving bioinspired blades for the Savonius rotors. These methodologies are elucidated with the help of appropriate examples of bioinspired designs covered in this thesis.

8.3.1 Bioinspiration Approaches

In the field of bioinspiration, there are mainly two approaches to develop bioinspired solutions *viz.* biology push approach (bottom-up approach) and technology pull approach (top-down approach) as delineated in Fig. 8.1. In the first approach, the process of technical development starts with the biological question raised by the observation of an intriguing bio/natural organism or phenomenon. For example, nautilus blade (Section 2.3.2.2), which was motivated by the peculiar shape of the creature, and not by the necessity of solving any technical fluid dynamic problem related to performance improvement.

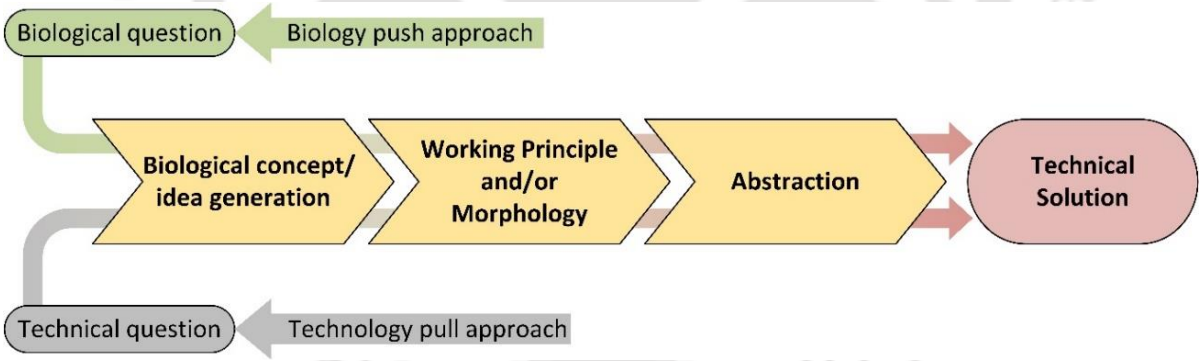

Figure 8.1 Flow-chart of bioinspiration combined with optimization

In the second approach, namely the technology pull approach, the technical development starts with the technical question posed by the actual technical problem. For solving the problem, search for the suitable bio/natural organism or phenomenon has to be conducted. For instance, the seapen inspired blade (Chapter 4). Here, the original issue was to improve the pressure distribution towards the blade tips, which was then taken care by finding a suitable bio-organism named seapen. In both the approaches, the aim destination however was to find a feasible bioinspired technical solution for the rotor (Fig. 8.1).

From the perspective of fluid dynamicists/engineers who are interested developing bioinspired rotor designs, the technology pull approach seems to be more suitable since the fluid dynamic issue or the research gap related to the flow physics of the turbines are already reported in the literature. Moreover, They are more familiar with this than in-depth knowledge of numerous bio-organisms. The Darrius and the Savonius turbines are thoroughly investigated turbine designs with decent performance. Their drawbacks are well-known and thereby the technology pull approach can be very useful to mitigate these drawbacks and to improve the performance further from the existing benchmark (if successful bioinspired design is developed). On the other hand, in the biology push approach, the likelihood of finding a bio-organism or natural phenomenon that can be suitably manifested in the novel turbine design is very erratic and exhaustive. In addition to this, there is no guarantee whether the performance of this novel design would be superior to the existing designs.

Thus, the authors of the present thesis recommend the technology pull approach as a more suitable and feasible option for developing bioinspired designs for already existing blade design or augmentation technique. In contrast, the biology push approach is recommended while synthesizing novel blade profile or augmentation technique, which are radically distinct from the prevalent designs.

8.3.2 Bioinspired Design and Optimization

Sometimes, instead of directly using biomorphic designs, optimization is conducted to find the optimum design capable of demonstrating the highest C_P. Traditionally, the parametric optimization is conducted through exhaustive search method by manually selecting the values of design variables. This is a time-consuming process. Alternatively, the same task can be carried out with the help of modern optimization algorithms as discussed below.

As depicted in Fig. 8.2, the prerequisite to the optimization process is to figure out the suitable set of the design parameters. For example, Sand-eel shaped blades for the Savonius rotor (Section 2.3.3.2), in which the suitable blade design parameters such as f_{max}/d and X_{max}/d are selected prior to optimization (Abdelghafar et al., 2023). Thereafter, design of experiment (DoE) task is carried out to generate various values of selected design parameters with specified constraints. DoE is generally led with the help of optimum Latin hypercube sampling. Different blade designs as per sample values of design parameters are then constructed along with corresponding numerical domain. Numerical simulations are then conducted for the prepared

set of the blade designs. These process stages are then linked with the optimization algorithm. Soft computing techniques such as neural networks, evolutionary algorithms, swarm intelligence and others can be chosen as an optimization algorithm. Until the C_P value reaches the global maxima, the optimization process is repeated continuously. If the convergence obtained, the values of the design parameters provided by the algorithm are the optimum. The optimum design is then subjected to wind tunnel experimentation, validation and detailed flow physics analysis. Another similar example of this approach is the design optimization of the Savonius rotor having *Koi*-fish shaped blade with gap ratio (*s/d*) and overlap ratio (*e/d*) as design parameters (Hashem and Zhu, 2021).

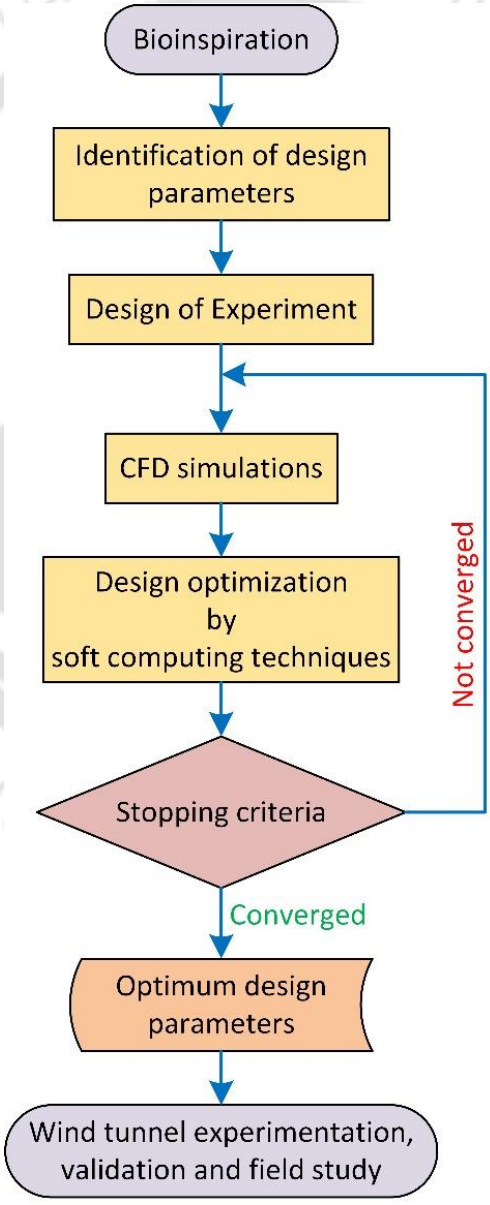

Figure 8.2 Flow-chart of bioinspiration combined with optimization

The only challenge faced in this approach is the appropriate choice of design parameters. The parameters which can significantly influence the rotor performance as well as its flow-physics, are considered as the suitable design parameters. Therefore, it is reasonable to opt for biomimetics rather than biomorphism since the former one, by its definition (Section 2.3.1), deals with in-depth study of working principles and flow physics related to rotor design and corresponding bio-organism.

8.3.3 Choice of Biomimetics over Biomorphism

As briefly mentioned in the last part of Section 8.3.2, the choice of biomimetic approach not only facilitates the appropriate selection of the design parameters but also help in gaining through understanding of working principles and flow physics of the turbines and allied bio-organism. The insight gained by this enriches the overall understanding of torque mechanism of the rotor, which is helpful to the research community for further performance improvement in future. Such merits are not evident in the case of biomorphism since it revolves around superficial imitation of the external form of the bio-organism. Thus, the authors of the present thesis would like to suggest pursuing biomimetic design approach rather than the biomorphic approach if possible.

References

Abd El-Latief, M. E., Elsayed, K., Abdelrahman, M. M., 2021. Parametric study of a corrugated airfoil in a forward flight at ultra-low Reynolds number. SN Appl. Sci. 3, 1-14. https://doi.org/10.1007/s42452-020-04105-y

Abdelghafar, I., Kerikous, E., Hoerner, S., Thévenin, D., 2023. Evolutionary optimization of a Savonius rotor with sandeel-inspired blades. Ocean Eng. 279, 114504. https://doi.org/10.1016/j.oceaneng.2023.114504

Abraham, J. P., Plourde, B. D., Mowry, G. S., Minkowycz, W. J., Sparrow, E. M., 2012. Summary of Savonius wind turbine development and future applications for small-scale power generation. J. Renew. Sustain. Energy 4, 042703. https://doi.org/10.1063/1.4747822

Ahmadi, M. H., Mohseni-Gharyehsafa, B., Farzaneh-Gord, M., Jilte, R. D., Kumar, R., Chau, K., 2019. Applicability of connectionist methods to predict dynamic viscosity of silver/water nanofluid by using ANN-MLP, MARS and MPR algorithms. Eng. Appl. Comput. Fluid Mech. 13, 220–228. https://doi.org/10.1080/19942060.2019.1571442

Akwa, J. V., Vielmo, H. A., Petry, A. P., 2012. A review on the performance of Savonius wind turbines. Renew. Sustain. Energy Rev. 16, 3054–3064. https://doi.org/10.1016/j.rser.2012.02.056

Alaimo, A., Esposito, A., Milazzo, A., Orlando, C., Trentacosti, F., 2013. Slotted blades Savonius wind turbine analysis by CFD. Energies 6, 6335–6351. https://doi.org/10.3390/en6126335

Alexander, A. J., Holownia, B. P., 1978. Wind tunnel tests on a Savonius rotor. J. Ind. Aerodyn. 3, 343–351. https://doi.org/10.1016/0167-6105(78)90037-5

Alizamir, M., Kim, S., Kisi, O., Zounemat-Kermani, M., 2020. A comparative study of several machine learning based non-linear regression methods in estimating solar radiation: Case studies of the USA and Turkey regions. Energy 197, 117239. https://doi.org/10.1016/j.energy.2020.117239

Alom, N., Saha, U. K., 2019a. Evolution and progress in the development of Savonius wind turbine rotor blade profiles and shapes. ASME J. Sol. Energy Eng. 141, 030801. https://doi.org/10.1115/1.4041848

Alom, N., Saha, U. K., 2019b. Drag and lift characteristics of a novel elliptical-bladed Savonius rotor with vent augmenters. ASME J. Sol. Energy Eng. 141, 051007. https://doi.org/10.1115/1.4043516

Alom, N., Saha, U. K., 2018a. Four decades of research into the augmentation techniques of Savonius wind turbine rotor. ASME J. Energy Resour. Technol. 140, 050801. https://doi.org/10.1115/1.4038785

Alom, N., Saha, U. K., 2018b. Performance evaluation of vent-augmented elliptical-bladed Savonius rotors by numerical simulation and wind tunnel experiments. Energy 152, 277–290. https://doi.org/10.1016/j.energy.2018.03.136

Alom, N., Saha, U. K., Dewan, A., 2021. In the quest of an appropriate turbulence model for analyzing the aerodynamics of a conventional Savonius (S-type) wind rotor. J. Renew. Sustain. Energy 13, 023313. https://doi.org/10.1063/5.0034362

Altan, B. D., Atilgan, M., Özdamar, A., 2008. An experimental study on improvement of a Savonius rotor performance with curtaining. Exp. Therm. Fluid Sci. 32, 1673–1678. https://doi.org/10.1016/j.expthermflusci.2008.06.006

Anderson, J. M., Streitlien, K., Barrett, D. S., Triantafyllou, M. S., 1998. Oscillating foils of high propulsive efficiency. J. Fluid Mech. 360, 41–72. https://doi.org/10.1017/S0022112097008392

Ansys, 2021. Ansys Fluent (2021 R1), Ansys Inc., Canonsburg, PA, USA.

Arfaoui, B., Bouzaher, M. T., Guerira, B., Bensaci, C. E., 2021. On the performance of swing arm flapping turbines. ASME J. Sol. Energy Eng. 143, 011013. https://doi.org/10.1115/1.4047954

Ashwindran, S. N., Azizuddin, A. A., Oumer, A. N., 2021. Study of √2 conjecture in the construction of drag induced wind turbine blade morphology. Evergr. Jt. J. Nov. Carbon Resour. Sci. Green Asia Strateg. 8, 574–585. https://doi.org/10.5109/4491649

Ashwindran, S. N., Azizuddin, A. A., Oumer, A. N., Idris, M. S., 2022. Alternative method of nature inspired geometrical design strategy for drag induced wind turbine blade morphology. Int. J. Automot. Mech. Eng. 19, 9759–9772. https://doi.org/10.15282/ijame.19.2.2022.11.0753

Bagheri, A., Nazari, A., Sanjayan, J., 2019. The use of machine learning in boron-based geopolymers : Function approximation of compressive strength by ANN and GP. Measurement 141, 241–249. https://doi.org/10.1016/j.measurement.2019.03.001

Balaji, C., 2021. Search methods, in: Thermal system design and optimization. Springer India, pp. 177–242. https://doi.org/10.1007/978-3-030-59046-8

Bangga, G., Dessoky, A., Wu, Z., Rogowski, K., Hansen, M. O. L., 2020. Accuracy and consistency of CFD and engineering models for simulating vertical axis wind turbine loads. Energy 206, 118087. https://doi.org/10.1016/j.energy.2020.118087

Bartlett, C., 2019. Nautilus spirals and the Meta-Golden ratio Chi. Nexus Netw. J. 21, 641-656. https://doi.org/10.1007/s00004-018-0419-3

Beale, M. H., Hagan, M. T., Demuth, H. B., 2010. Neural network toolbox TM 7 user ' s guide, 9th ed. The Mathworks, Inc., Massachusetts.

Benesh, A. H., 1996. Wind turbine with Savonius-type rotor. US5494407A. https://patentimages.storage.googleapis.com/d3/b3/c4/dba34e04362278/US5494407.pdf

Benyus, J. M., 2009. Biomimicry: Innovation inspired by nature, HarperCollins Publishers Inc., New York, USA.

Berg, C., 2021. Saucer plant-Aeonium tabuliforme (CC-BY) [WWW Document]. GBIF-Global Biodivers. Inf. Facil. https://doi.org/10.15468/dl.d6r78z

Best, B. A., 1988. Passive suspension feeding in a sea pen : Effects of ambient flow on volume flow rate and filtering efficiency. Biol. Bull. 175, 332–342. https://doi.org/10.2307/1541723

Bishop, C. M., 1998. Neural networks and their applications. Rev. Sci. Instrum. 65, 1803–1830. https://doi.org/10.1063/1.1144830

Blanco Damota, J., Rodríguez García, J. de D., Couce Casanova, A., Telmo Miranda, J., Caccia, C.G., Galdo, M. I. L., 2022. Optimization of a nature-inspired shape for a vertical axis wind turbine through a numerical model and an artificial neural network. Appl. Sci. 12, 8037. https://doi.org/10.3390/app12168037

Blanco, J., Rodriguez, J. de D., Couce, A., Lamas, M. I., 2021. Proposal of a nature-inspired shape for a vertical axis wind turbine and comparison of its performance with a semicircular blade profile. Appl. Sci. 11, 6198. https://doi.org/10.3390/app11136198

Blasiak, R., Jouffray, J. B., Amon, D. J., Moberg, F., Claudet, J., Søgaard Jørgensen, P., Pranindita, A., Wabnitz, C. C. C., Österblom, H., 2022. A forgotten element of the blue economy: marine biomimetics and inspiration from the deep sea. PNAS Nexus 1, 1–17. https://doi.org/10.1093/pnasnexus/pgac196

Blogman, 2021. Beaked barnacle-Austrominius modestus (CC-BY-NC) [WWW Document]. GBIF-Global Biodivers. Inf. Facil. https://doi.org/10.15468/dl.yxhr2q

Cao, M., Wang, K. W., Devries, L., Fujii, Y., Tobler, W. E., Pietron, G. M., Tibbls, T., McCallum, J., 2004. Steady state hydraulic valve fluid field estimator based on non-dimensional artificial neural network (NDANN). J. Comput. Inf. Sci. Eng. 4, 257–270. https://doi.org/10.1115/1.1765119

Celik, I. B., Ghia, U., Roache, P. J., Freitas, C. J., Coleman, H., Raad, P. E., 2008. Procedure for estimation and reporting of uncertainty due to discretization in CFD applications. ASME J. Fluids Eng. 130, 078001. https://doi.org/10.1115/1.2960953

Chan, C. M., Bai, H. L., He, D. Q., 2018. Blade shape optimization of the Savonius wind turbine using a genetic algorithm. Appl. Energy 213, 148–157. https://doi.org/10.1016/j.apenergy.2018.01.029

Chen, J., Jan, K., Zhang, L., Lu, L., Yang, H., 2012. Influence of phase-shift and overlap ratio on Savonius wind turbine's performance. ASME J. Sol. Energy Eng. 134, 011016. https://doi.org/10.1115/1.4004980

Chen, L., Chen, J., Zhang, Z., 2018. Review of the Savonius rotor's blade profile and its performance. J. Renew. Sustain. Energy 10, 013306. https://doi.org/10.1063/1.5012024

Chimienti, G., Angeletti, L., Mastrototaro, F., 2018. Withdrawal behaviour of the red sea pen Pennatula rubra (Cnidaria: Pennatulacea). Eur. Zool. J. 85, 64–70. https://doi.org/10.1080/24750263.2018.1438530

Chu, Y. J., 2016. A new biomimicry marine current turbine: Study of hydrodynamic performance and wake using software OpenFOAM. J. Hydrodyn. 28, 125–141. https://doi.org/10.1016/S1001-6058(16)60614-5

Crossley, M. J., 2021. Great sea-pen (Sarcoptilus grandis) (CC-BY-NC-SA) [WWW Document]. iNaturalist.org. https://doi.org/10.15468/dl.yvyd3g

Damota, J. B., García, J. de D.R., Casanova, A. C., Miranda, J. T., Caccia, C. G., Galdo, M. I. L., 2022. Analysis of a nature-inspired shape for a vertical axis wind turbine. Appl. Sci. 12, 7018. https://doi.org/10.3390/app12147018

Das, D., Desai, S., Kulkarni, V., Gadgil, H., 2019. Performance assessment of energy deposition based drag reduction technique for Earth and Mars flight conditions. Acta Astronaut. 159, 418–428. https://doi.org/10.1016/j.actaastro.2019.01.049

Deb, K., Agrawal, S., 2002. Unserstanding interaction among genetic algorithm paramters, in: Banzhaff, W., Reeves, C. (Eds.), Foundation of genetic algorithm. Morgan Kaufmann Publishers, Inc., San Francisco, California, pp. 265–286.

Debnath, B. K., Das, R., 2010. Prediction of performance coefficients of a three-bucket Savonius rotor using artificial neural network. J. Renew. Sustain. Energy 2, 1–11. https://doi.org/10.1063/1.3467510

Dhar, V. K., Tickoo, A. K., Koul, R., Dubey, B. P., 2010. Comparative performance of some popular artificial neural network algorithms on. Indian Acad. Sci. 74, 307–324. https://doi.org/10.1007/s12043-010-0029-4

Dobrev, I., Massouh, F., 2011. CFD and PIV investigation of unsteady flow through Savonius wind turbine. Energy Procedia 6, 711–720. https://doi.org/10.1016/j.egypro.2011.05.081

DTU, 2023. Wind Speed atlas of India [WWW Document]. Technol. Univ. Denmark. URL https://globalwindatlas.info/area/India

Eça, L., Hoekstra, M., 2014. A procedure for the estimation of the numerical uncertainty of CFD calculations based on grid refinement studies. J. Comput. Phys. 262, 104–130. https://doi.org/10.1016/j.jcp.2014.01.006

Edwards, J. M., Angelo Danao, L., Howell, R. J., 2012. Novel experimental power curve determination and computational methods for the performance analysis of vertical axis wind turbines. ASME J. Sol. Energy Eng. 134, 031008. https://doi.org/10.1115/1.4006196

El-Askary, W. A., Nasef, M. H., AbdEL-hamid, A. A., Gad, H. E., 2015. Harvesting wind energy for improving performance of Savonius rotor. J. Wind Eng. Ind. Aerodyn. 139, 8–15. https://doi.org/10.1016/j.jweia.2015.01.003

Emmanuel, B., Jun, W., 2011. Numerical study of a six-bladed Savonius wind turbine. ASME J. Sol. Energy Eng. 133, 044503. https://doi.org/10.1115/1.4004549

Fernandes, A. C., Rostami, A. B., 2015. Hydrokinetic energy harvesting by an innovative vertical axis current turbine. Renew. Energy 81, 694–706. https://doi.org/10.1016/j.renene.2015.03.084

Ferreira, C., 2005. Gene expression programming studies in computational intelligence, 2nd ed, Springer, Verlag.

Fish, F. E., Battle, J. M., 1995. Hydrodynamic design of the humpback whale flipper. J. Morphol. 225, 51–60. https://doi.org/10.1002/jmor.1052250105

Franchina, N., Persico, G., Savini, M., 2019. 2D-3D Computations of a vertical axis wind turbine flow field: Modelling issues and physical interpretations. Renew. Energy 136, 1170–1189. https://doi.org/10.1016/j.renene.2018.09.086

Fujisawa, N., 1992. On the torque mechanism of Savonius rotors. J. Wind Eng. Ind. Aerodyn. 40, 277–292. https://doi.org/10.1016/0167-6105(92)90380-S

Fujisawa, N., Gotoh, F., 1994. Experimental study on the aerodynamic performance of a Savonius rotor. ASME J. Sol. Energy Eng. 116, 148–152. https://doi.org/10.1115/1.2930074

Fujisawa, N., Gotoh, F., 1992. Visualization study of the flow in and around a Savonius rotor. Exp. Fluids 12, 407–412. https://doi.org/10.1007/BF00193888

Fujisawa, N., Gotoh, F., 1992. Pressure measurements and flow visualization study of a Savonius rotor. J. Wind Eng. Ind. Aerodyn. 39, 51–60. https://doi.org/10.1016/0167-6105(92)90532-F

Gall, L., 2023. Pearly nautilus- Nautilus pompilius [WWW Document]. GBIF-Global Biodivers. Inf. Facil. https://doi.org/10.15468/dl.6jcffk

Gao, M., Li, Z., Cheng, L., Zhang, W., 2020. Aerodynamic performance and wake effect of new type nautilus blade vertical axis wind turbine, in: 2020 5th International Conference on Power and Renewable Energy, ICPRE 2020. IEEE, Shanghai, China. September 12-14, pp. 577–581. https://doi.org/10.1109/ICPRE51194.2020.9233224

Goldberg, D., 1988. Genetic algorithms in optimization, search and machine learning, Addison Wesley Publishing Company Inc., Massachusetts.

Golecha, K., Eldho, T. I., Prabhu, S. V., 2011. Influence of the deflector plate on the performance of modified Savonius water turbine. Appl. Energy 88, 3207–3217. https://doi.org/10.1016/j.apenergy.2011.03.025

Grinspan, A. S., Saha, U. K., Mahanta, P., 2004. Experimental investigation of twisted bladed Savonius wind turbine rotor. Int. Energy J. 5, 1–9. http://www.rericjournal.ait.ac.th /index.php/reric/article/view/142/110

Grzimek, B., 2003. Grzimek's animal life encyclopedia: Fishes I-II, 2nd ed. MI: Gale Group, Farmington Hills, Canada.

Grzimek, H. C. B., 2003. Grzimek's animal life encyclopedia: Protostomes, Transactions of the American Microscopical Society. MI: Gale Group, Farmington Hills, Canada. https://doi.org/10.2307/3225015

GWEC, 2022. Global Wind Report 2022. Brussels, Belgium.

Hagan, M. T., Menhaj, M. B., 1994. Training feedforward networks with the Marquardt algorithm. IEEE Trans. Neural Networks 5, 2–6. https://doi.org/10.1109/72.329697

Hammer, Ø., 2016. The perfect shape-spiral stories. Copernicus Cham. https://doi.org/10.1007/978-3-319-47373-4

Hashem, I., Kerikous, E., Hoerner, S., Thévenin, D., 2022. Performance Investigation of a Savonius wind turbine with unconventional blade designs inspired by sand eels, in: Conference on Modelling Fluid Flow (CMFF'22), The 18th International Conference on Fluid Flow Technologies. Budapest, Hungary. August 30-September 2.

Hashem, I., Zhu, B., 2021. Metamodeling-based parametric optimization of a bio-inspired Savonius-type hydrokinetic turbine. Renew. Energy 180, 560–576. https://doi.org/10.1016/j.renene.2021.08.087

Hayashi, T., Li, Y., Hara, Y., 2005. Wind tunnel tests on a different phase three-stage Savonius rotor. JSME Int. J. Ser. B 48, 9–16. https://doi.org/10.1299/jsmeb.48.9

Haykin, S., 2009. Neural networks and learning machines, 3rd ed. Pearson Education Inc., New Jersey.

Holland, J. H., 1992. Adaptation in natural and artificial system, The MIT Press, Massachusetts Ave. Cambridge, MA. https://doi.org/10.1016/S0376-7361(07)53015-3

Horner, S. F., 1965. Pressure drag, in: Fluid-dynamic drag: Practical information on aerodynamic drag and hydrodynamic resistance. Horner Fluid Dynamics, Bakersfield, California, pp. 1–28. https://doi.org/10.1093/benz/9780199773787.article.b00088376

Hornik, K., Stinchcombe, M., White, H., 1989. Multilayer feedforward networks are universal approximators. Neural Networks 2, 359–356. https://doi.org/10.1016/0893-6080(89)90020-8

Hu, Y., Tong, Z., Wang, S., 2009. A new type of VAWT and blade optimization. IET Conf. Publ. 2009. https://doi.org/10.1049/cp.2009.1392

Hui, H., Tamai, M., 2008. Bioinspired corrugated airfoil at low Reynolds numbers. J. Aircr. 45, 2068–2077. https://doi.org/10.2514/1.37173

Hunter, D., Yu, H., Member, S., Pukish, M. S., Member, S., Kolbusz, J., Wilamowski, B. M., 2012. Selection of proper neural network sizes and architectures - A comparative study. IEEE Trans. Ind. Informatics 8, 228–240. https://doi.org/10.1109/TII.2012.2187914

Idgreen, 2021. Pacific sand lance-Ammodytes personatus (CC-BY-NC) [WWW Document]. GBIF-Global Biodivers. Inf. Facil. https://doi.org/10.15468/dl.9n3qx5

IEA, 2022. World energy outlook 2022, International Energy Agency (IEA).

IEA, 2021. India energy outlook 2021, India Energy Outlook 2021. https://doi.org/10.1787/ec2fd78d-en

Irabu, K., Roy, J. N., 2007. Characteristics of wind power on Savonius rotor using a guide-box tunnel. Exp. Therm. Fluid Sci. 32, 580–586. https://doi.org/10.1016/j.expthermflusci.2007.06.008

ISO, 2015. ISO 18458 2015-05 2015: Biomimetics-Terminology, concepts and methodology. Beuth, Berlin.

Iversen, J. D., 1979. Autorotating flat-plate wings: The effect of the moment of inertia, geometry and Reynolds number. J. Fluid Mech. 92, 327–348. https://doi.org/10.1017/S0022112079000641

Jacob, D. K., 2001. Buoyancy, hydrodynamics, and structure in chambered cephalopods, in: Briggs, D. E. G., Crowther, P. R. (Eds.), Palaeobiology II. pp. 397–401. https://doi.org/10.1002/9780470999295.ch94

Johnson, K. L., 2022. Pacific sand lance-Ammodytes personatus (CC-BY-NC) [WWW Document]. GBIF-Global Biodivers. Inf. Facil. https://doi.org/10.15468/dl.7jd2r3

Kamoji, M. A., Kedare, S. B., Prabhu, S. V., 2008. Experimental investigations on single stage, two stage and three stage conventional Savonius rotor. Int. J. Energy Res. 32, 877–895. https://doi.org/10.1002/er.1399

Kamoji, M. A., Kedare, S. B., Prabhu, S. V, 2009. Experimental investigations on single stage modified Savonius rotor. Appl. Energy 86, 1064–1073. https://doi.org/10.1016/j.apenergy.2008.09.019

Kathleen, R., 2020. Orange sea-pen (Ptilosarcus gurneyi) (CC-BY-NC) [WWW Document]. GBIF-the Glob. Biodivers. Inf. Facil. https://doi.org/10.15468/dl.redsde

Kesel, A. B., 2000. Aerodynamic characteristics of dragonfly wing sections compared with technical aerofoils. J. Exp. Biol. 203, 3125–3135. https://doi.org/10.1242/jeb.203.20.3125

Khan, M. H., 1978. Model and prototype performance characteristics of Savonius rotor windmill. Wind Eng. 2, 75–85. https://www.jstor.org/stable/43749106

Kheldoun, A., Bradai, R., Boukenoui, R., Mellit, A., 2016. A new golden section method-based maximum power point tracking algorithm for photovoltaic systems. Energy Convers. Manag. 111, 125–136. https://doi.org/10.1016/j.enconman.2015.12.039

Kirbaş, U., Karaşahin, M., 2016. Performance models for hot mix asphalt pavements in urban roads. Constr. Build. Mater. 116, 281–288. https://doi.org/10.1016/j.conbuildmat.2016.04.118

Koehl, M. A. R., 1977. Water flow and the morphology of zoanthid colonies, in: Proceedings,Third International Coral Reef Symposium. Rosensteil school of marine and atmospheric science, University of Miami, Miami, Florida. May, pp. 437–444.

Kshirsagar, C. M., Anand, R., 2017. Artificial neural network applied forecast on a parametric study of Calophyllum inophyllum methyl ester-diesel engine out responses. Appl. Energy 189, 555–567. https://doi.org/10.1016/j.apenergy.2016.12.045

Kumar, J. S. Y., 2018. Octacorals, in: Kailash, C., Raghunathan, C. (Eds.), Faunal diversity of biogeographic zones : Islands of India. Zoological Survey of India, Kolkata, India, pp. 73–80.

Lane, G., 2016. Whale barnacle-Coronula diadema (CC-BY-NC) [WWW Document]. GBIF-Global Biodivers. Inf. Facil. https://doi.org/10.15468/dl.42b2kq

Levenberg, K., 1944. A method for the solution of certain Non-linear problems in least squares. Q. Appl. Math. 2, 164–168. http://www.jstor.org/stable/43633451

Leversee, G. J., 1976. Flow and feeding in fan-shaped colonies of the Gorgonian coral , Leptogorgia. Biol. Bull. 151, 344–356. https://doi.org/10.2307/1540667

Levy, D. E., Seifert, A., 2009. Simplified dragonfly airfoil aerodynamics at Reynolds numbers below 8000. Phys. Fluids 21, 071901. https://doi.org/10.1063/1.3166867

Li, G., Ke, H., Li, C., Li, B., 2020. thermal error modeling of feed axis in machine tools using particle swarm optimization-based generalized regression neural network. J. Comput. Inf. Sci. Eng. 20, 021003. https://doi.org/10.1115/1.4045292

Li, G. S., Yang, Z. X., Song, L., Chen, Q., Li, Y. B., Chen, W., 2016. Effects of setting angle on performance of fish-bionic wind wheel. IOP Conf. Ser. Earth Environ. Sci. 40, 012016. https://doi.org/10.1088/1755-1315/40/1/012016

Li, J., Chow, T. W. S., Ying-Lin, Y., 1995. The estimation theory and optimization algorithm for the number of hidden units in the higher-order feed forward neural network, in: Proceedings of ICNN'95 - International Conference on Neural Networks. IEEE, Perth, WA, Australia. November 27-December 1, pp. 1229–1233. https://doi.org/10.1109/ICNN.1995.487330

Li, K., Chen, Y., Li, W., He, J., Xue, Y., 2018. Improved gene expression programming to solve the inverse problem for ordinary differential equations. Swarm Evol. Comput. 38, 231–239. https://doi.org/10.1016/j.swevo.2017.07.005

Li, Z., Gao, M., Cao, X., Cheng, L., Wang, X., An, G., Sun, H., 2022. Structural optimal design and power generation characteristics of a bionic type nautilus vertical axis wind turbine. J. Eng. 2022, 64–75. https://doi.org/10.1049/tje2.12095

Liang, T., Liu, X., Fan, P., Zhu, L., Bi, Y., Zhang, Y., 2020. Prediction of long-term creep life of 9Cr–1Mo–V–Nb steel using artificial neural network. Int. J. Press. Vessel. Pip. 179, 104014. https://doi.org/10.1016/j.ijpvp.2019.104014

Lua, K. B., Lu, H., Lim, T. T., 2018. Rotating elliptic cylinders in a uniform cross flow. J. Fluids Struct. 78, 36–51. https://doi.org/10.1016/j.jfluidstructs.2017.12.023

Lugt, H. J, 1983. Vortex flow in nature and technology, 1st ed. John Wiley & Sons, Inc., New York.

Lugt, H. J, 1983. Autorotation. Annu. Rev. Fluid Mech. 15, 123–147. https://doi.org/10.1146/annurev.fl.15.010183.001011

Lugt, H. .J., 1980. Autorotation of an elliptic cylinder about an axis perpendicular to the flow. J. Fluid Mech. 99, 817–840. https://doi.org/10.1017/S0022112080000924

Lugt, H. J., Ohring, S., 1977. Rotating elliptic cylinders in a viscous fluid at rest or in a parallel stream. J. Fluid Mech. 79, 127–156. https://doi.org/10.1017/S002211207700007X

Ma, C., Song, L., Zhang, M. Z., 2017. Performance study for a novel vertical axis wind turbine based on simulation analysis, in: Proceedings of the 14th International Conference on Networking, Sensing and Control, ICNSC 2017. IEEE, Calabria, Italy. May 16-18, pp. 549–554. https://doi.org/10.1109/ICNSC.2017.8000151

Mackay, D., 2009. Sustainable energy-without the hot air, 1st ed, UIT Cambridge Ltd. UIT Cambridge Ltd., Cambridge.

Manwell, J. F., Mcgovan, J. G., Rogers, A. L., 2009. Wind energy explained: Theory, design and applcation, Second edi. ed. John Wiley & Sons Ltd, United Kingdom.

Marples, C. R., Williams, P. M., 2022. The golden ratio in nature: A tour across length scales. Symmetry (Basel). 14, 1–20. https://doi.org/10.3390/sym14102059

Martí, P., Shiri, J., Duran-Ros, M., Arbat, G., de Cartagena, F. R., Puig-Bargués, J., 2013. Artificial neural networks vs. gene expression programming for estimating outlet dissolved oxygen in micro-irrigation sand filters fed with effluents. Comput. Electron. Agric. 99, 176–185. https://doi.org/10.1016/j.compag.2013.08.016

Masters, T., 1993. Practical neural network recipes in C++. Academic Press Inc., San Diego, California.

MATLAB Version (R2021a), 2021. The MathWorks Inc., Natick, Massachusetts, USA.

Matsumoto, M., Nishimura, T., 1998. Mersenne Twister: A 623-dimensionally equidistributed uniform pseudo-random number generator. ACM Trans. Model. Comput. Simul. 8, 3–30. https://doi.org/10.1145/272991.272995

McCulloch, W. S., Pitts, W. H., 1943. A logical calculus of the ideas immanent in nervous activity. Bull. Math. Biophys. 5, 115–133. https://doi.org/10.1007/BF02478259

McDaniel, N., 2006. Orange sea-pen (Ptilosarcus gurneyi) (CC-BY-NC) [WWW Document]. GBIF-the Glob. Biodivers. Inf. Facil. https://doi.org/10.15468/dl.6uufte

Meiller, M. F., 1993. A scaled conjugate gradient algorithm for fast supervised learning. Neural Networks 6, 525–533. https://doi.org/10.1016/S0893-6080(05)80056-5

Menon, A., Mehrotra, K., Mohan, C. K., Ranka, S., 1996. Characterization of a class of sigmoid functions with applications to neural networks, Neural Networks 9, 819–835. https://doi.org/10.1016/0893-6080(95)00107-7

MNRE, 2023. Annual Report 2022-23. Delhi, india.

Modi, V. J., Fernando, M. S. U. K., 1989. On the performance of the Savonius wind turbine. ASME J. Sol. Energy Eng. 111, 71–81. https://doi.org/10.1115/1.3268289

Modi, V. J., Roth, N. J., Fernando, M. S. U. K., 1984. Optimum-configuration studies and prototype design of a wind-energy-operated irrigation system. J. Wind Eng. Ind. Aerodyn. 16, 85–96. https://doi.org/10.1016/0167-6105(84)90050-3

Moffat, R. J., 1988. Describing the uncertainties in experimental results. Exp. Therm. Fluid Sci. 1, 3–17. https://doi.org/10.1016/0894-1777(88)90043-X

Mohamad, N., Zaini, F., Johari, A., Yassin, I., Zabidi, A., 2010. Comparison between Levenberg-Marquardt and scaled conjugate gradient training algorithms for breast cancer diagnosis using MLP, in: 6th International Colloquium on Signal Processing & Applications (CSPA). IEEE, Malacca, Malaysia. May 21-23, pp. 162–168. https://doi.org/10.1109/cspa.2010.5545325

Mohamed, M. H., Janiga, G., Pap, E., Thévenin, D., 2011. Optimal blade shape of a modified Savonius turbine using an obstacle shielding the returning blade. Energy Convers. Manag. 52, 236–242. https://doi.org/10.1016/j.enconman.2010.06.070

Mohammadi, F., Bina, B., Karimi, H., Rahimi, S., Yavari, Z., 2020. Modeling and sensitivity analysis of the Alkylphenols removal via moving bed biofilm reactor using artificial neural networks: Comparison of Levenberg Marquardt and particle swarm optimization training algorithms. Biochem. Eng. J. 161, 107685. https://doi.org/10.1016/j.bej.2020.107685

Mohammadi, M., Lakestani, M., Mohamed, M. H., 2018. Intelligent parameter optimization of Savonius rotor using artificial neural network and genetic algorithm. Energy 143, 56–68. https://doi.org/10.1016/j.energy.2017.10.121

Mojola, O. O., 1985. On The Aerodynamic design of the Savonius windmill rotor. J. Wind Eng. Ind. Aerodyn. 21, 223–231. https://doi.org/10.1016/0167-6105(85)90005-4

Motamarri, S., Boccelli, D. L., 2012. Development of a neural-based forecasting tool to classify recreational water quality using fecal indicator organisms. Water Res. 46, 4508–4520. https://doi.org/10.1016/j.watres.2012.05.023

Murad, Y. Z., Hunifat, R., AL-Bodour, W., 2020. Interior reinforced concrete beam-to-column joints subjected to cyclic loading: Shear strength prediction using gene expression programming. Case Stud. Constr. Mater. 13, e00432. https://doi.org/10.1016/j.cscm.2020.e00432

Murphy, J. T., Hu, H., 2010. An experimental study of a bio-inspired corrugated airfoil for micro air vehicle applications. Exp. Fluids 49, 531–546. https://doi.org/10.1007/s00348-010-0826-z

Niu, W. Q., Li, M., Yang, Z. X., Liu, C., 2018. Wind speed influence analysis on performance of fish-bionic wind wheel, in: Int. Conf. Adv. Mechatron. Syst. ICAMechS 2018. Zhengzhou, China. August 30-September 2, pp. 46–51. https://doi.org/10.1109/ICAMechS.2018.8507095

Ogawa, T., 1986. The effect of a deflector plate and rotor end plates on performance of Savonius type wind turbine. Bull. JSME 29, 2115–2121. https://doi.org/10.1299/jsme1958.29.2115

Okamoto, M., Yasuda, K., Azuma, A., 1996. Aerodynamic characteristics of the wings and body of a dragonfly. J. Exp. Biol. 199, 281–294. https://doi.org/10.1242/jeb.199.2.281

Ozbek, A., Unsal, M., Dikec, A., 2013. Estimating uniaxial compressive strength of rocks using genetic expression programming. J. Rock Mech. Geotech. Eng. 5, 325–329. https://doi.org/10.1016/j.jrmge.2013.05.006

Pala, M., Caglar, N., 2007. A parametric study for distortional buckling stress on cold-formed steel using a neural network. J. Constr. Steel Res. 63, 686–691. https://doi.org/10.1016/j.jcsr.2006.07.005

Paraschivoiu, I., 2002. Wind turbine design: With emphasis on Darrieus concept, 1st ed, Polytechnic International Press. Montréal, QC Canada.

Plourde, B. D., Abraham, J. P., Mowry, G. S., Minkowycz, W. J., 2012. Simulations of three-dimensional vertical-axis turbines for communications applications. Wind Eng. 36, 443–453. https://doi.org/10.1260/0309-524X.36.4.443

Pope, A., J. J. Harper, 1966. Low speed wind tunnel testing. John Wiley & Sons Ltd., New York.

Post, M. L., Decker, R., Sapell, A. R., Hart, J. S., 2018. Effect of bio-inspired sinusoidal leading-edges on wings. Aerosp. Sci. Technol. 81, 128–140. https://doi.org/10.1016/j.ast.2018.07.043

Ramadan, A., Yousef, K., Said, M., Mohamed, M. H., 2018. Shape optimization and experimental validation of a drag vertical axis wind turbine. Energy 151, 839–853. https://doi.org/10.1016/j.energy.2018.03.117

Randall, J. E., 1974. Blue devil damselfish- Chrysiptera taupou [WWW Document]. GBIF-Global Biodivers. Inf. Facil. https://doi.org/10.15468/dl.sdx9tz

Rasamoelina, D. A., Adjailia, F., Sincak, P., 2020. A Review of activation function for artificial neural network, in: SAMI 2020 IEEE 18th World Symposium on Applied Machine Intelligence and Informatics. Herl'any, Slovakia. January 23–25, pp. 281–286. https://ieeexplore.ieee.org/stamp/stamp.jsp?arnumber=9108717

Rathod, U. H., Talukdar, P. K., Kulkarni, V., Saha, U. K., 2019. Effect of capped vents on torque distribution of a semicircular-bladed Savonius wind rotor. ASME J. Energy Resour. Technol. 141, 101201. https://doi.org/10.1115/1.4043791

Reupke, P., Probert, S. D., 1991. Slatted-blade Savonius wind-rotors. Appl. Energy 40, 65–75. https://doi.org/10.1016/0306-2619(91)90051-X

Riabouchinsky, D. P., 1935. Thirty years of theoretical and experimental research in fluid mechanics. J. R. Aeronaut. Soc. 39, 282–348. https://doi.org/10.1017/s0368393100112039

Riisgård, H. U., Larsen, P. S., 2010. Particle capture mechanisms in suspension-feeding invertebrates. Mar. Ecol. Prog. Ser. 418, 255–293. https://doi.org/10.3354/meps08755

Roache, P. J., 1994. Perspective: A method for uniform reporting of grid refinement studies. ASME J. Fluids Eng. Eng. 116, 405–413. https://doi.org/10.1115/1.2910291

Roma, L., Bieniek, J., Komarnicki, P., Marcin, D., Detyna, J., 2017. Estimation of operational parameters of the counter-rotating wind turbine with artificial neural networks. Arch. Civ. Mech. Eng. 17, 1019–1028. https://doi.org/10.1016/j.acme.2017.04.010

Rosenblatt, F., 1957. The perceptron - A perceiving and recognizing automaton, Report No. 85-460-1. Buffalo, New York.

Ross, H., Polagye, B., 2020. An experimental assessment of analytical blockage corrections for turbines. Renew. Energy 152, 1328–1341. https://doi.org/10.1016/j.renene.2020.01.135

Ross, I., Altman, A., 2011. Wind tunnel blockage corrections: Review and application to Savonius vertical-axis wind turbines. J. Wind Eng. Ind. Aerodyn. 99, 523–538. https://doi.org/10.1016/j.jweia.2011.02.002

Roy, S., Ducoin, A., 2016. Unsteady analysis on the instantaneous forces and moment arms acting on a novel Savonius-style wind turbine. Energy Convers. Manag. 121, 281–296. https://doi.org/10.1016/j.enconman.2016.05.044

Roy, S., Mukherjee, P., Saha, U. K., 2014. Aerodynamic performance evaluation of a novel savonius-style wind turbine under an oriented jet, in: ASME 2014 Gas Turbine India Conference. Delhi, India. December 15-17, pp. V001T08A001. https://doi.org/10.1115/GTINDIA2014-8152

Roy, S., Saha, U. K., 2015. Wind tunnel experiments of a newly developed two-bladed Savonius-style wind turbine. Appl. Energy 137, 117–125. https://doi.org/10.1016/j.apenergy.2014.10.022

Roy, S., Saha, U. K., 2013a. Review on the numerical investigations into the design and development of Savonius wind rotors. Renew. Sustain. Energy Rev. 24, 73–83. https://doi.org/10.1016/j.rser.2013.03.060

Roy, S., Saha, U. K., 2013b. Review of experimental investigations into the design, performance and optimization of the Savonius rotor. Proc. Inst. Mech. Eng. Part A J. Power Energy 227, 528–542. https://doi.org/10.1177/0957650913480992

Roy, S., Saha, U. K., 2013c. Investigations on the effect of aspect ratio into the performance of savonius rotors, in: ASME 2013 Gas Turbine India Conference. Bangalore, Karnataka, India. December 5-6, pp. V001T07A002. https://doi.org/10.1115/GTINDIA2013-3729

Rubenstein, D., Koehl, M. A. R., 1977. The mechanisms of filter feeding : Some theoretical considerations. Am. Nat. 111, 981–994. https://www.journals. uchicago.edu/doi/10.1086/283227

Sadeghi, G., Najafzadeh, M., Safarzadeh, H., 2020. Utilizing gene-expression programming in modelling the thermal performance of evacuated tube solar collectors. J. Energy Storage 30, 101546. https://doi.org/10.1016/j.est.2020.101546

Saha, U. K., Rajkumar, M. J., 2006. On the performance analysis of Savonius rotor with twisted blades. Renew. Energy 31, 1776–1788. https://doi.org/10.1016/j.renene.2005.08.030

Saha, U. K., Thotla, S., Maity, D., 2008. Optimum design configuration of Savonius rotor through wind tunnel experiments. J. Wind Eng. Ind. Aerodyn. 96, 1359–1375. https://doi.org/10.1016/j.jweia.2008.03.005

Sargolzaei, J., Kianifar, A., 2009. Modeling and simulation of wind turbine Savonius rotors using artificial neural networks for estimation of the power ratio and torque. Simul. Model. Pract. Theory 17, 1290–1298. https://doi.org/10.1016/j.simpat.2009.05.003

Sarkar, B., Sengupta, A., De, S., Dasgupta, S., 2009. Prediction of permeate flux during electric field enhanced cross-flow ultrafiltration - A neural network approach. Sep. Purif. Technol. 65, 260–268. https://doi.org/10.1016/j.seppur.2008.10.032

Satrio, D., Utama, I. K. A. P., Mukhtasor, 2018. Numerical Investigation of Contra Rotating Vertical-Axis Tidal-Current Turbine. J. Mar. Sci. Appl. 17, 208–215. https://doi.org/10.1007/s11804-018-0017-5

Sharma, S., Sharma, R. K., 2016. Performance improvement of Savonius rotor using multiple quarter blades - A CFD investigation. Energy Convers. Manag. 127, 43–54. https://doi.org/10.1016/j.enconman.2016.08.087

Shaughnessy, B. M., Probert, S. D., 1992. Partially-blocked savonius rotor. Appl. Energy 43, 239-249. https://doi.org/10.1016/0306-2619(92)90024-6

Sheela, K. G., Deepa, S. N., 2013. Review on methods to fix number of hidden neurons in neural networks. Math. Probl. Eng. 2013, 425740. https://doi.org/10.1155/2013/425740

Sheldahl, R. E., Feltz, L. V., Blackwell, B. F., 1978. Wind tunnel performance data for two- and three-bucket Savonius rotors. J. Energy 2, 160–164. https://doi.org/10.2514/3.47966

Shibata, K., Ikeda, Y., 2009. Effect of number of hidden neurons on learning in large-scale layered neural networks, in: ICROS-SICE International Joint Conference 2009. IEEE, Fukuoka International Congress Center, Japan. August 18-21, pp. 5008–5013. https://ieeexplore.ieee.org/document/5334631

Shikha, Bhatti, T. S., Kothari, D. P., 2003. Wind energy conversion systems as a distributed source of generation. J. Energy Eng. 129, 69–80. https://doi.org/10.1061/(asce)0733-9402(2003)129:3(69)

Shimek, R. L., 2011. To pen a tale of pens [WWW Document]. E-Fauna BC, Electron. atlas Wildl. Br. Columbia. URL https://ibis.geog.ubc.ca/biodiversity/efauna/documents/ToPenATaleOfPens.pdf (accessed 10.30.21).

Shimeta, J., Jumars, P. A., 1991. Physical mechanisms and rates of particle capture by suspension-feeders. Oceanogr. Mar. Biol. An Annu. Rev. 29, 191–257. https://doi.org/10.1.1.617.7288&rep=rep1&type=pdf

Siram, O., Kesharwani, N., Sahoo, N., Saha, U. K., 2022. Aerodynamic design and wind tunnel tests of small-scale horizontal-axis wind turbines for low tip speed ratio applications. ASME J. Sol. Energy Eng. 144, 041009. https://doi.org/10.1115/1.4053453

Skillen, A., Revell, A., Pinelli, A., Piomelli, U., Favier, J., 2015. Flow over a wing with leading-edge undulations. AIAA J. 53, 464–472. https://doi.org/10.2514/1.J053142

Slater, J. W., 2011. Examining spatial grid convergence [WWW Document]. NPARC alliance CFD Verif. Valid. web site, NASA. URL https://www.grc.nasa.gox/www/wind/valid/tutorial/spatconv.html (accessed 8.18.22).

Smith, E. H., 1971. Autorotating wings: An experimental investigation. J. Fluid Mech. 50, 513–534. https://doi.org/10.1017/S0022112071002738

Song, L., Yang, Z. X., Deng, R. T., Yang, X. G., 2013. Performance and structure optimization for a new type of vertical axis wind turbine, in: Proceedings of the 2013 International Conference on Advanced Mechatronic Systems. IEEE, Luoyang, China. September 25-27, pp. 687–692. https://doi.org/10.1109/ICAMechS.2013.6681730

Speck, O., Speck, D., Horn, R., Gantner, J., Sedlbauer, K. P., 2017. Biomimetic bio-inspired biomorph sustainable? An attempt to classify and clarify biology-derived technical developments. Bioinspiration and Biomimetics 12. https://doi.org/10.1088/1748-3190/12/1/011004

Squires, K., 2013. Palau nautilus-Nautilus belauensis (CC-BY) [WWW Document]. GBIF-Global Biodivers. Inf. Facil. https://doi.org/10.15468/dl.tuuvcu

Storti, B. A., Dorella, J. J., Roman, N. D., Peralta, I., Albanesi, A. E., 2019. Improving the efficiency of a Savonius wind turbine by designing a set of deflector plates with a metamodel-based optimization approach. Energy 186, 115814. https://doi.org/10.1016/j.energy.2019.07.144

Strazzari, T., 2021. Great sea-pen (Sarcoptilus grandis Gray) (CC-BY-NC) [WWW Document]. GBIF-the Glob. Biodivers. Inf. Facil. https://doi.org/10.15468/dl.9tdvr3

Stringer, C. C., Polagye, B. L., 2020. Implications of biofouling on cross-flow turbine performance. SN Appl. Sci. 2, 464. https://doi.org/10.1007/s42452-020-2286-2

Sun, J., Bhushan, B., 2012. The structure and mechanical properties of dragonfly wings and their role on flyability. Comptes Rendus - Mec. 340, 3–17. https://doi.org/10.1016/j.crme.2011.11.003

Szul, T., Necka, K., Mathia, T. G., 2020. Neural methods comparison for prediction of heating energy based on few hundreds enhanced buildings in four season's climate. Energies 13, 1–17. https://doi.org/10.3390/en13205453

Tabassum, S. A., Probert, S. D., 1987. Vertical-axis wind turbine: A modified design. Appl. Energy 28, 59–67. https://doi.org/10.1016/0306-2619(87)90041-9

Talukdar, P. K., Alom, N., Rathod, U. H., Kulkarni, V., 2022. Alternative blade profile based on Savonius concept for effective wind energy harvesting. ASME J. Energy Resour. Technol. 144, 041304. https://doi.org/10.1115/1.4051675

Tartuferi, M., D'Alessandro, V., Montelpare, S., Ricci, R., 2015. Enhancement of Savonius wind rotor aerodynamic performance: A computational study of new blade shapes and curtain systems. Energy 79, 371–384. https://doi.org/10.1016/j.energy.2014.11.023

Tian, K., Wu, Y., 2020. Design of anti-glare device for freeway with power generation using a vertical axis wind turbine, in: 2020 International Conference on Adv. Mechatronic Sys. Hanoi, Vietnam. December 10-13, pp. 100–103. https://doi.org/10.1109/ICAMechS49982.2020.9310130

Tian, W., Song, B., Van Zwieten, J. H., Pyakurel, P., 2015. Computational fluid dynamics prediction of a modified Savonius wind turbine with novel blade shapes. Energies 8, 7915–7929. https://doi.org/10.3390/en8087915

Tian, Y., 2017. Nautilus equiangular spiral wind wheel electric generator. CN106368896A.

Tran, V. L., Kim, S. E., 2021. A practical ANN model for predicting the PSS of two - way reinforced concrete slabs. Eng. Comput. 37, 2303–2327. https://doi.org/10.1007/s00366-020-00944-w

Trenn, S., 2008. Multilayer perceptrons : Approximation order and necessary number of hidden units. IEEE Trans. neural networks 19, 836–844. https://doi.org/10.1109/TNN.2007.912306

Tudu, P. C., Ray, D., Mohapatra, A., 2018. A checklist of Indian sea pen (Cnidaria: Anthozoa: Pennatulacea). Indian J. Geo-Marine Sci. 47, 1014–1017. http://nopr.niscair.res.in/handle/123456789/44421

Ushiyama, I. I., Nagai, H., Shinoda, J., 1986. Experimentally determining the optimum design configuration for Savonius rotors. Trans. Japan Soc. Mech. Eng. Ser. B 52, 4130–4138. https://doi.org/10.1299/jsme1958.29.4130

Vargas, A., Mittal, R., 2004. Aerodynamic performance of biological airfoils, in: 2nd AIAA Flow Control Conference. Portland, Oregon. June 28-July 1, pp. 2319. https://doi.org/10.2514/6.2004-2319

Verbrugghe, N., Rubinacci, E., Khan, A. Z., 2023. Biomimicry in Architecture: A review of definitions, case studies, and design methods. Biomimetics 8, 107. https://doi.org/10.3390/biomimetics8010107

Versteeg, H., Malalasekra, W., 2009. Methods for dealing with complex geometries, in: An introduction to computational fluid dynamics :The finite volume method. Pearson Education Ltd., Harlow, England, pp. 318–356.

Vogel, S., 1994. The Life in moving fluid - The physical biology of flow, 2nd ed. Princeton University Press, Princeton, New Jersey.

Wainwright, S. A., Dillon, J. R., 1969. On the orientation of sea fans. Biol. Bull. 136, 130–139. https://doi.org/10.2307/1539674

Wang, Y., Cheng, W., Du, R., Wang, S., 2020. Bionic drag reduction for box girders based on ostracion cubicus. Energies 13, 4392. https://doi.org/10.3390/en13174392

Warner, G. F., 1977. On the shape of passive suspension feeders, in: Keegan, B. F., Ceidigh, P. O., Boaden, P. J. S. (Eds.), Biology of benthic organisms, in: 11th European Symposium on Marine Biology. Pergamon Press Ltd., Galway, Republic of Ireland. October, pp. 567–576. https://doi.org/10.1016/B978-0-08-021378-1.50063-4

Watson, S., Moro, A., Reis, V., Baniotopoulos, C., Barth, S., Bartoli, G., Bauer, F., Boelman, E., Bosse, D., Cherubini, A., Croce, A., Fagiano, L., Fontana, M., Gambier, A., Gkoumas, K., Golightly, C., Latour, M. I., Jamieson, P., Kaldellis, J., Macdonald, A., Murphy, J., Muskulus, M., Petrini, F., Pigolotti, L., Rasmussen, F., Schild, P., Schmehl, R., Stavridou, N., Tande, J., Taylor, N., Telsnig, T., Wiser, R., 2019. Future emerging technologies in the wind power sector: A European perspective. Renew. Sustain. Energy Rev. 113, 109270. https://doi.org/10.1016/j.rser.2019.109270

Wenehenubun, F., Saputra, A., Sutanto, H., 2015. An experimental study on the performance of Savonius wind turbines related with the number of blades. Energy Procedia 68, 297–304. https://doi.org/10.1016/j.egypro.2015.03.259

Whitesides, G. M., 2015. Bioinspiration : something for everyone. Interface Focus 5, 20150031. https://doi.org/10.1098/rsfs.2015.0031

Wilamowski, B. M., Irwin, D. J., 2011. The industrial electronics handbook-intelligent system. CRC Press, Taylor and Francis Group, Boca Raton.

Williams, G. C., 2011. The global diversity of sea pens (cnidaria: Octocorallia: Pennatulacea). PLoS One 6, e22747. https://doi.org/10.1371/journal.pone.0022747

Wu, Z., Zhu, M., Kang, Y., Leung, E. L. H., Lei, T., Shen, C., Jiang, D., Wang, Z., Cao, D., Hou, T., 2021. Do we need different machine learning algorithms for QSAR modeling? A comprehensive assessment of 16 machine learning algorithms on 14 QSAR data sets. Brief. Bioinform. 22, bbaa321. https://doi.org/10.1093/bib/bbaa321

WWEA, 2022. WWEA Half-year Report 2022. Bonn, Germany.

Yassin, M. A., Alazba, A. A., Mattar, M. A., 2016. Artificial neural networks versus gene expression programming for estimating reference evapotranspiration in arid climate. Agric. Water Manag. 163, 110–124. https://doi.org/10.1016/j.agwat.2015.09.009

Yazıcı, İ., Yaylacı, E. K., Yalçın, F., 2021. Modified golden section search based MPPT algorithm for the WECS. Eng. Sci. Technol. an Int. J. 24, 1123-1133. https://doi.org/10.1016/j.jestch.2021.02.006

Zhao, Z., Zheng, Y., Xu, X., Liu, W., Hu, G., 2009a. Research on the improvement of the performance of Savonius rotor based on numerical study, in: 2009 Int. Conference Sustainable Power Generation Supply. Nanjing, China. April 6-7, 1–6. https://doi.org/10.1109/SUPERGEN.2009.5348197

Zhao, Z., Zheng, Y., Xu, X., Liu, W., Zhou, D., 2009b. Optimum design configuration of helical Savonius rotor via numerical study. Proc. ASME 2009 Fluids Eng. Div. Summer Conf., Volume 1: Symposia, Parts A, B and C, Colorado, USA. August 2–6, 1273–1278. https://doi.org/10.1115/FEDSM2009-78430

Zhong, J., Feng, L., Ong, Y. S., 2017. Gene expression programming: A survey [review article]. IEEE Comput. Intell. Mag. 12, 54–72. https://doi.org/10.1109/MCI.2017.2708618

Appendix

The data processing and training of the ANN that is used in the Chapter 7 are described in this appendix. The purpose is to evade superfluous repetition of the ANN training procedure already covered in Chapter 6 besides avoiding possible misunderstanding in the reader's mind. The reason behind the need of training another ANN is the implementation of the new data partitioning method proposed in Section 7.2.

A.1 Data Selection and Processing

The research articles from where the experimental dataset is extracted to train ANN, are enlisted in Table A.1. For this dataset, the experimental investigations were carried out to study the influence of different variables such as D, H, p/q, θ_1, θ_2, n_s, e, s, D_o, U, on output variable C_P. In all the experiments, the same wind tunnel setup was used, therefore, wind tunnel cross-sectional area (A_{wt}) is omitted as an input variable, unlike that of Eq. 6.1. Similarly, all the rotors were of two-bladed, therefore, the number of blades (n_b) is also excluded from the list of input variables. Consequently, an equation of C_P is formulated (Eq. A.1) for the task of ANN function approximation. It is important to state that the current study is focussed on using a limited amount of input data unlike the past attempts documented in literature. A total 763 instances (or data entries) are accumulated from the research papers enlisted in Table A.1.

Table A.1 List of research papers used for ANN data extraction

Investigators	Type of blades	Variables
Kamoji et al. (2008)	Semicircular	D, H, n_s, U, e, D_o
Kamoji et al. (2009)	Bach	D, H, s, p/q, θ_1, θ_2, D_o, U

$$C_P = f\left(D, H, \frac{p}{q}, \theta_2, \theta_1, n_S, e, s, D_0, U, \lambda\right) \tag{A.1}$$

Conventionally, the rotor variables are presented in non-dimensional form of parametric ratios such as overlap ratio (e/d), gap ratio (s/d), aspect ratio (H/D) and many others. Still the absolute values of each variables are preferred in order to allow the ANN to decide the mathematical relationships among the variables. However, the shape factor (p/q), remains in non-dimensional form because the individual values of p and q can be calculated using a geometric relationship between D, p/q and e. The effect of shaft diameter is not considered in the present study. The variable U is selected for a given working condition without placing the rotor inside the wind

tunnel. The uncorrected power characteristics are calculated from the corrected power characteristics provided in the research papers for ANN training in order to address the blockage mechanism implicitly by ANN. The minimum and maximum values of all the selected variables are shown in Table A.2. It is important to note that some variables (like n_s) have discrete integer values, while others have real values in the limited range of minimum-maximum bounds. This can easily be observed in many benchmarking datasets and can be used to train ANN model (Dua and Graff, 2019). Thereafter, all the variables of the dataset are normalized upon mapping them between [-1,1] using Eq. A.2, as per the choice of the transfer function in the ANN model.

Table A.2 Approximate minimum-maximum bounds of variables

Sr. No.	Variable	Max Value (x_{max})	Min Value (x_{min})
1	D	0.22 m	0.0966 m
2	H	0.29 m	0.13 m
3	p/q	0.6	0
4	θ_1	150°	90°
5	θ_2	90°	0°
6	n_s	3	1
7	e	0.018 m	0 m
8	s	0.034 m	0 m
9	D_0	0.24 m	0 m
10	U	12 m/s	6 m/s
11	λ	2	0
12	C_p	0.21	0

$$x_{norm} = \frac{x_{\exp} - x_{\min}}{x_{\max} - x_{\min}} \quad \text{(A.2)}$$

where $x_{\exp}$ = experimental value of variable,
$x_{\min}$ = minimum value of variable,
$x_{\max}$ = maximum value of variable

The function approximation using ANN model uses a batch type supervised learning method. The entire dataset thus has to be divided into three categories *viz.* training dataset, validation dataset and testing dataset. The training dataset is used to train the ANN model in order to determine the weights and biases of neurons. The validation dataset is not directly being used for the training purpose, rather being used for stopping the training process and validation. Lastly, the test dataset is reserved for evaluating the trained ANN as this dataset is not used for the training purpose, and hence, it can be considered as completely new dataset for the trained ANN.

A.2 Selection of Optimum ANN Model

As mentioned earlier in Section 6.7.1, the upper and lower limits of n_h are estimated as 6 and 26, respectively. Thus, the remining task is to find the optimum number of n_h by an exhaustive search method using the evaluation parameters such as network performance, correlation co-efficient (R) and mean absolute error (ε). Herein, ε is calculated from the test data using Eq. A.3. It is necessary to state that these quantities are calculated based on the experimental values and the estimated values provided by trained ANN *i.e.* C_P in the present investigation.

$$\varepsilon = \frac{\sum_{1}^{n} \left| x_{\exp} - x_{est} \right|}{n} \tag{A.3}$$

The computer system used to train the ANN models having different numbers of n_h is equipped with processor i5 Intel (R) core (TM) and 7200U CPU running at 2.50 GHz and 8 GB RAM with the Windows 10 operating system under the *MATLAB 2020b* programming environment. The computational time required for each ANN model ranges from 5 to 10 seconds (Zhang et al., 2020).

Table A.3 Performance of different ANN models

n_h	R of test data	R of overall data	ε of test data	ε of overall data
5	0.8768	0.9457	0.0130	0.0121
6	0.6466	0.88098	0.025083	0.01174
7	0.87664	0.94934	0.017859	0.01084
8	0.90962	0.96597	0.01693	0.009493
9	0.9421	0.96869	0.01423	0.009645
10	0.9551	0.974	0.01262	0.009182
11	0.8821	0.9594	0.01856	0.01016
12	0.83986	0.9557	0.01951	0.007977
13	0.9688	0.9831	0.01075	0.006993
14	0.87884	0.964	0.01865	0.007436
15	0.84434	0.95044	0.021443	0.008917
17	0.93758	0.97936	0.01348	0.006773
19	0.8869	0.96772	0.01724	0.007262
21	0.8977	0.9665	0.01886	0.007966

The results obtained for trained ANN models having n_h = 6 to 26 are summarised in Table A.3 in the form of R and ε of both the test and the overall datasets. It can be observed that R values of test as well as overall dataset are not sufficiently close to unity for n_h = 5 to 12. The highest values are found at n_h = 13 demonstrating $R \approx 0.968$ and ≈ 0.983 for test and overall dataset, respectively. It also provides the lowest ε values as compared to the previous models enlisted

in Table A.3. As n_h further increases, it again shows deteriorated R values in addition to increased ε values, indicating diminishment of generalization characteristic in the trained ANN models. Thus, the ANN model with n_h = 13 is selected as the optimum topology in the present investigations (Fakir et al., 2019). The specifications of this optimum ANN model are enlisted in Table A.4.

Table A.4 Specification of optimum ANN topology

Parameters	Specification
Input	11
Output	1
Hidden layer of neural network	1
Number of neurons	13
Training/validation/Test Percentage	60%/20%/20%
Numbers of Epochs/Iterations	50
Back propagation algorithm	Levenberg-Marquardt
Seed value of Marsanne-Twister random number generator	10
Mean Squared error	Range of 10^{-3}
Validation performance	0.000121
Number of the Validation check	20
Activation function for hidden layer	Tansigmoid (*tansig*)
Activation function for output layer	pure linear (*purelin*)

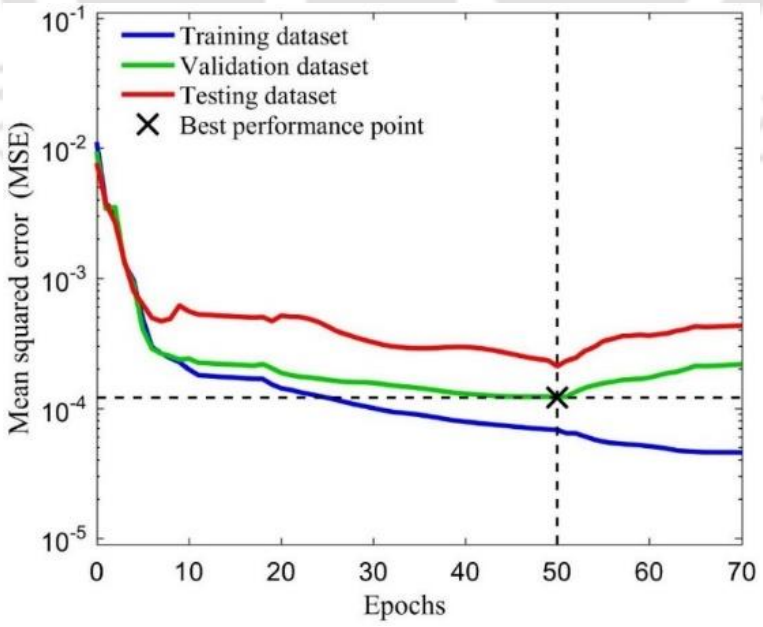

Figure A.1 Performance curve of ANN training

During the training of the aforementioned optimum ANN model, the stopping criteria is set as 'maximum fail of validation check'. The performance of the same is monitored in terms of decrement in Mean Squared Error (MSE) at each epoch (Fig. A.1). The formula of estimating MSE is given in Eq. A.4. After 50th epoch, the training algorithm fails to decrease MSE for 20 times, consecutively. Therefore, 50th epoch is accepted as the best and corresponding weights and biases are finalised as a solution. Above this point, the MSE values of training dataset decreases, while for the test and validation datasets, it increases, thereby clearly indicating the overtraining of ANN.

$$MSE = \frac{1}{n}\sum_{i=1}^{n}\left(x_{est} - x_{\exp}\right)^2 \tag{A.4}$$

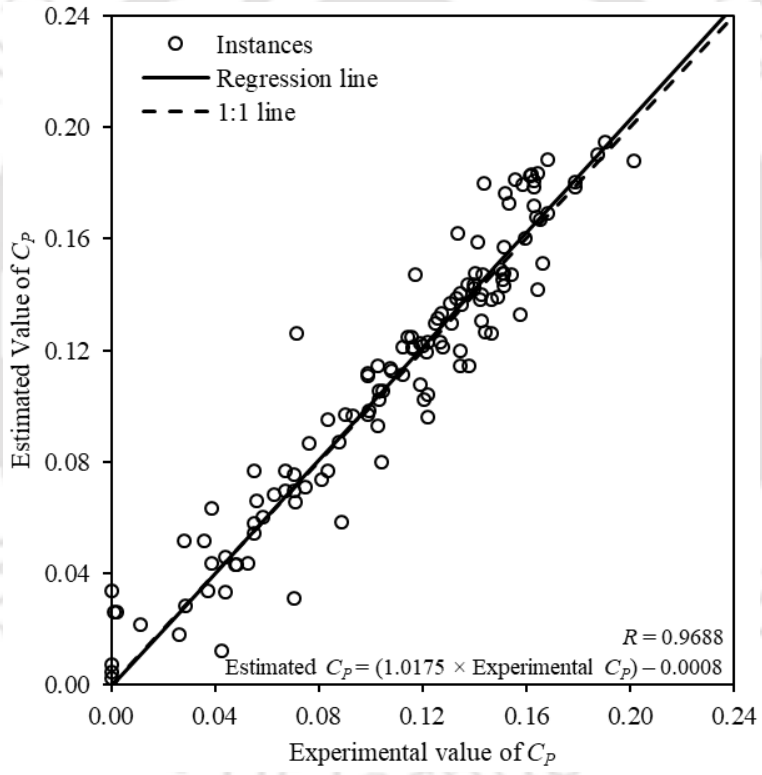

Figure A.2 Estimated vs Experimental C_P value of test data using ANN

A comparison of experimental and estimated values of C_P is presented in Figs. A.2 and A.3 for the test and the overall datasets, respectively. It can clearly be seen that the majority of the points are clustered around 1:1 line. Moreover, the regression lines in both the graphs have approximate slope that is equal to unity with a very small value of interception. This clearly indicates a slight deviation between the regression line and the 1:1 line. This again ensures a very small error between the experimental and the estimated C_P values, which is further

supported by the error histogram provided in Fig. A.4. It is evident from the histogram that majority of the instances are clustered towards zero error line (difference between experimental and estimated C_P value) bounded between ± 10^{-3}. In order to further diminish the errors, necessary steps are discussed in Section 7.4.1.

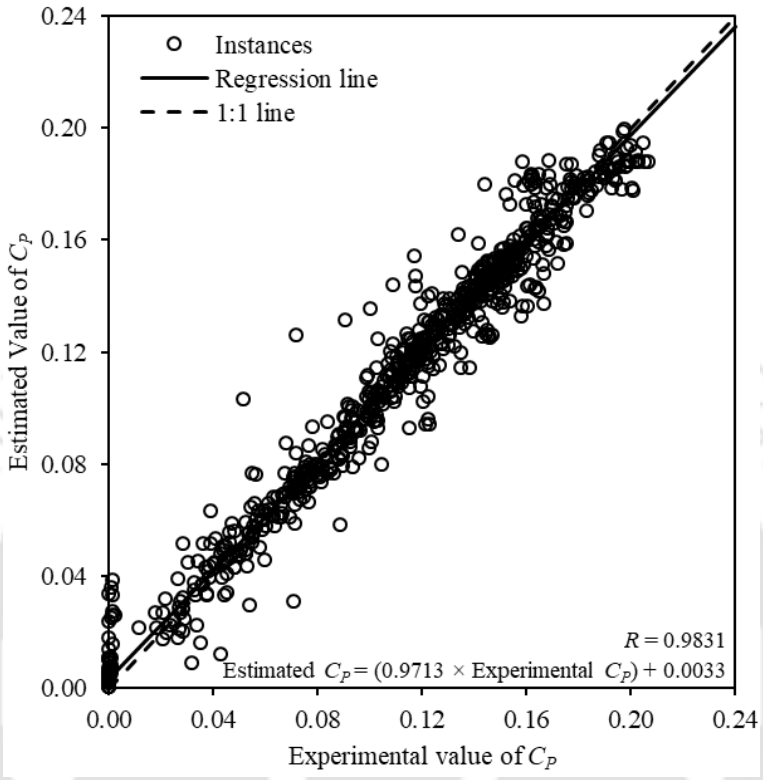

Figure A.3 Estimated vs Experimental (target) C_P value of test data using ANN

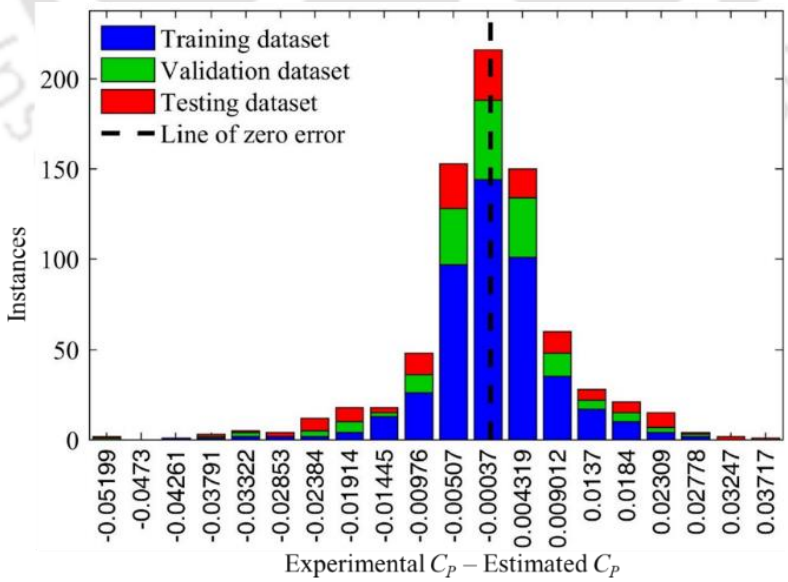

Figure A.4 Error histogram of trained ANN

List of Publications

Peer-reviewed Journals

- **Rathod U. H.**, Saha U. K., Kulkarni V., 2024, 'Bioinspired Fluid Dynamic Designs of Vertical-Axis Turbines: State-of-the-Art Review and the Way Forward', *ASME Journal of Fluids Engineering*, 146(9), pp. 090801. https://doi.org/10.1115/1.4064753
- **Rathod U. H.**, Kulkarni V., Saha U. K., 2023, 'Evolving a Bio-inspired Blade Shape of the Drag-based Vertical-axis Wind Rotor Derived from Orange Sea-pen (*Ptilosarcus Gurneyi*)', *ASME Journal of Solar Energy Engineering*, 145(3), pp. 031007. https://doi.org/10.1115/1.4055914
- **Rathod U. H.**, Kulkarni V., Saha U. K., 2023, 'Predicting the Optimum Performance of a Vertical-axis Savonius Wind Rotor with Parametric Modelling using Artificial Neural Network and Golden Section Method', *ASME Journal of Computing and Information Science in Engineering*, 23(2), pp. 0.21016. https://doi.org/10.1115/1.4054691
- **Rathod U. H.**, Kulkarni V., Saha U. K.,2022, 'On the Application of Machine Learning in Savonius Wind Turbine Technology: An Estimate of Turbine Performance Using Artificial Neural Network and Genetic Expression Programming', *ASME Journal of Energy Resources Technology*, 144(6), pp. 061301. https://doi.org/10.1115/1.4051736

Conference Proceedings

- **Rathod U. H.**, Kulkarni V., Saha U. K., 'Computational Analysis of a Savonius Wind Rotor Using Bio-inspired Corrugated Blades', *ASME Turbomachinery Technical Conference and Exhibition – Turbo Expo 2023*, Boston, Massachusetts, USA, 26-30 June 2023, pp. V014T37A008. https://doi.org/10.1115/GT2023-102801
- **Rathod U. H.**, Nalavade C. H., Saha U. K., Kulkarni V., 'A Systematic Probe into the Starting Torque Characteristics of a Bio-inspired Orange Sea-pen Bladed Savonius Wind Rotor', *ASME Turbomachinery Technical Conference and Exhibition – Turbo Expo 2023*, Boston, Massachusetts, USA, 26-30 June 2023, pp. V014T37A009. https://doi.org/10.1115/GT2023-102811

Book Chapter

- **Rathod U. H.**, Kulkarni V. N., Saha U. K., 2023, 'Development of a Novel Drag-Based Vertical-Axis Wind Rotor Inspired from Orange Sea-Pen', Chapter in: Moholkar V. S., Mohanty K., Goud V. V., (eds) *Sustainable Energy Generation and Storage*, Springer Nature, Singapore. https://doi.org/10.1007/978-981-99-2088-4_1

o0o